ISSN 0911-5730
UVSOR-39
June 2012

UVSOR ACTIVITY REPORT 2011

UVSOR II since 2003

BL3B
HOTRLU

High resOlution Transmission, Reflection, and LUminescence spectroscopies of solids in the VIS-VUV region

UVSOR Facility
Institute for Molecular Science
National Institutes of Natural Sciences

Preface

This Activity Report covers the research activities carried out at the UVSOR Facility in FY2011 (April 2011-March 2012). This is the ninth volume in the new series for the third decade of UVSOR.

After the major upgrade in 2002-2003, we renamed the machine to UVSOR-II. This machine has been serving as the only low-energy third-generation light source in Japan. We are now preparing for the next upgrade. This time, the bending magnets will be replaced with combined-function magnets, to reduce the emittance from 27 nm-rad to around 15 nm-rad. The machine will be operated fully in the top-up mode. Although this operating mode was already established a few years ago, we are going to introduce a more sophisticated injection scheme, in which the perturbation to the stored beam will be greatly reduced. A total of six undulators will be operational. One of them, an in-vacuum undulator, will provide extreme ultraviolet (EUV) light to a new scanning transmission soft X-ray microscope (STXM) beamline.

Construction of all the necessary components for the accelerator and the beamlines was completed by March 2012. The reconstruction work is scheduled to start in April 2012 and be finished in May. The machine commissioning will begin in June. After commissioning, the machine will be referred to as UVSOR-III.

Under the Quantum Beam Technology Program of the Ministry of Education, Culture, Sports, Science and Technology (MEXT), a new coherent light source and its dedicated beamline have been constructed. By using an external laser source, density modulation of various types can be created on the electron beam circulating in the storage ring. Such bunches radiate coherently. A new laser system, new optical klystron, and new terahertz (Thz) beamline have been successfully commissioned. To create the necessary space for this program, two old beamlines, BL1A and BL1B, were moved and renamed to BL2A and BL3B, respectively. In particular, BL3B was completely renewed, with the design and construction work carried out as collaboration between the UVSOR Facility and the user group.

At UVSOR, we have four research positions for accelerator physics (one full professor, one associate professor, and two assistant professors) and four research positions for photophysics and photochemistry (two associate professors and two assistant professors). In June 2011, Dr. Heishun Zen, an assistant professor of the accelerator physics, left IMS. Two new young researchers, Takuji Ohigashi and Taro Konomi joined the Accelerator Physics Group in August 2011 and in April 2012, as assistant professors.

We look forward to further exciting achievements in FY2012 at UVSOR-III.

Masahiro Katoh
Director, UVSOR
April 2012

PASJ Award for Young Scientists Given to Dr. Miho Shimada

Dr. Miho Shimada, an assistant professor at the High Energy Accelerator Research Organization (KEK), who worked at UVSOR with Prof. Masahiro Katoh in 2006-2007, received the PASJ Award for Young Scientists from the Particle Accelerator Society of Japan in 2011 for her study titled “Study on the beam dynamics associated with the coherent synchrotron radiation”. Congratulations, Dr. Shimada!

The Encouragement Award for Students at the 14th XAFS Annual Meeting Given to Mr. Keitaro Eguchi

Mr. Keitaro Eguchi, a Ph.D. candidate at the Graduate University for Advanced Studies (SOKENDAI) working with Prof. Toshihiko Yokoyama, received the Encouragement Award for Student from the Japanese XAFS Society in 2011 for his oral presentation on “Formation and magnetic properties of iron nanoparticles deposited on Si_3N_4/Si(111)”. Congratulations, Mr. Eguchi!

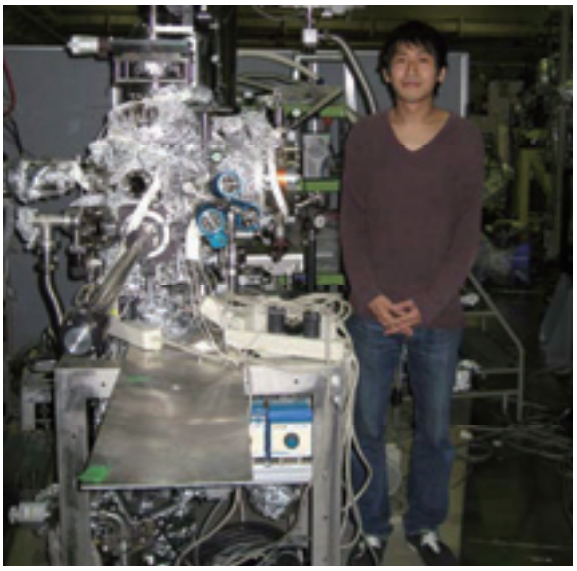

UVSOR Organization

April 2012

IMS OHMINE, Iwao (Director General)
IMS KOSUGI, Nobuhiro (Deputy Director General)

UVSOR Facility: KATOH, Masahiro (Director)

- Users in IMS
- UVSOR Users Association
- UVSOR Steering Commitee

- Accelerator Physics: KATOH, Masahiro (Prof.)
- Photophysics: KIMURA, Shin-ichi (Assoc. Prof.)
- Photochemistry: SHIGEMASA, Eiji (Assoc. Prof.)

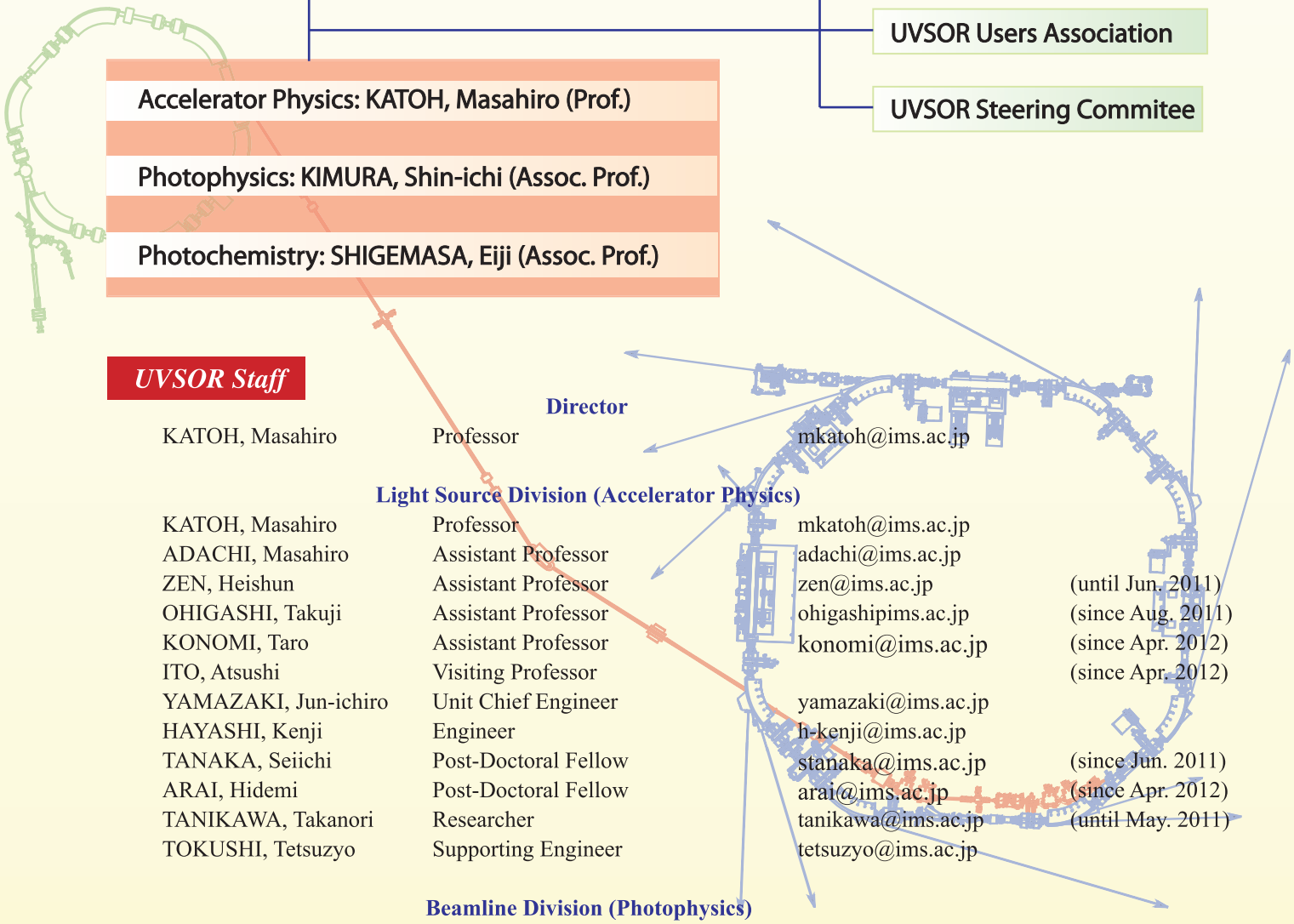

UVSOR Staff

Director

KATOH, Masahiro	Professor	mkatoh@ims.ac.jp	

Light Source Division (Accelerator Physics)

KATOH, Masahiro	Professor	mkatoh@ims.ac.jp	
ADACHI, Masahiro	Assistant Professor	adachi@ims.ac.jp	
ZEN, Heishun	Assistant Professor	zen@ims.ac.jp	(until Jun. 2011)
OHIGASHI, Takuji	Assistant Professor	ohigashipims.ac.jp	(since Aug. 2011)
KONOMI, Taro	Assistant Professor	konomi@ims.ac.jp	(since Apr. 2012)
ITO, Atsushi	Visiting Professor		(since Apr. 2012)
YAMAZAKI, Jun-ichiro	Unit Chief Engineer	yamazaki@ims.ac.jp	
HAYASHI, Kenji	Engineer	h-kenji@ims.ac.jp	
TANAKA, Seiichi	Post-Doctoral Fellow	stanaka@ims.ac.jp	(since Jun. 2011)
ARAI, Hidemi	Post-Doctoral Fellow	arai@ims.ac.jp	(since Apr. 2012)
TANIKAWA, Takanori	Researcher	tanikawa@ims.ac.jp	(until May. 2011)
TOKUSHI, Tetsuzyo	Supporting Engineer	tetsuzyo@ims.ac.jp	

Beamline Division (Photophysics)

KIMURA, Shin-ichi	Associate Professor	kimura@ims.ac.jp	
MATSUNAMI, Masaharu	Assistant Professor	matunami@ims.ac.jp	
HASUMOTO, Masami	Unit Chief Engineer	hasumoto@ims.ac.jp	
SAKAI, Masahiro	Engineer	sakai@ims.ac.jp	
IMURA, Keiichiro	Post-Doctoral Fellow	imura@ims.ac.jp	(until Dec. 2011)
TAKAHASHI, Toshiharu	Visiting Associate Professor		(until Mar. 2012)
NISHI, Tatsuhiko	Guest Researcher	tnishi@ims.ac.jp	(until Jun. 2011)
OZKENDIR, Osman Murat	Guest Researcher	ozkendir@ims.ac.jp	(until Nov. 2011)
IIZUKA, Takuya	Researcher	takuizk@ims.ac.jp	(since Apr. 2012)

Beamline Division (Photochemistry)

SHIGEMASA, Eiji	Associate Professor	sigemasa@ims.ac.jp	
IWAYAMA, Hiroshi	Assistant Professor	iwayama@ims.ac.jp	
HORIGOME, Toshio	Facility Chief Engineer	horigome@ims.ac.jp	
NAKAMURA, Eiken	Unit Chief Engineer	eiken@ims.ac.jp	(until Mar. 2012)
KONDO, Naonori	Engineer	nkondo@ims.ac.jp	
ISHIKAWA, Lisa	Post-Doctoral Fellow	ishikawa@ims.ac.jp	

Secretary

HAGIWARA, Hisayo		hagiwara@ims.ac.jp
KAWAI, Shigeko		kawai@ims.ac.jp

UVSOR Steering Committee

KATOH, Masahiro	UVSOR, IMS	Chair
KIMURA, Shin-ichi	UVSOR, IMS	
SHIGEMASA, Eiji	UVSOR, IMS	
TAKAHASHI, Toshiharu	Kyoto Univ. (Visiting Assoc. Prof., IMS)	(until Mar. 2012)
ITO, Atsushi	Tokai Univ. (Visiting. Prof., IMS)	(since Apr. 2012)
YOKOYAMA, Toshihiko	IMS	
MITSUKE, Koichiro	IMS	(until Mar. 2012)
OHSHIMA, Yasuhiro	IMS	
TADA, Mizuki	IMS	
FUJI, Takao	IMS	(since Apr. 2012)
FUKUI, Kazutoshi	Fukui Univ.	(until Mar. 2012)
MATSUDA, Iwao	Univ. of Tokyo	(until Mar. 2012)
YOSHIDA, Tomoko	Nagoya Univ.	(until Mar. 2012)
KINOSHITA, Toyohiko	JASRI	
KOBAYASHI, Yukinori	KEK-PF	
KONDOH, Hiroshi	Keio Univ.	
SHIMADA, Kenya	Hiroshima Univ.	
HARADA, Yoshihisa	Univ. of Tokyo	(since Apr. 2012)
NAKAGAWA, Kazumichi	Kobe Univ.	(since Apr. 2012)
SODA, Kazuo	Nagoya Univ.	(since Apr. 2012)

UVSOR Users Association

SODA, Kazuo	Chair, Nagoya Univ.	
FUKUI, Kazutoshi	Fukui Univ.	(until Mar. 2012)
NAKAGAWA, Kazumichi	Kobe Univ.	(until Mar. 2012)
YOSHIDA, Tomoko	Nagoya Univ.	(until Mar. 2012)
URISU, Tsuneo	Nagoya Univ.	(since Apr. 2012)
TANAKA, Shin-ichiro	Osaka Univ.	(since Apr. 2012)
KERA, Satoshi	Chiba Univ.	(since Apr. 2012)
ITO, Takahiro	Nagoya Univ.	

Graduate Students

IIZUKA, Takuya	Grad. Univ. Adv. Studies	takuizk@ims.ac.jp	(until Mar. 2012)
TAIRA, Yoshitaka	Nagoya Univ.		(until Mar. 2012)
HAJIRI, Tetsuya	Nagoya Univ.		
NIWA, Ryosuke	Nagoya Univ.		(until Sep. 2011)
UEMATSU, Yohei	Nagoya Univ.		(since Oct. 2011)
HIDA, Yohei	Nagoya Univ.		(since Oct. 2011)
NIWA, Takahiro	Nagoya Univ.		(since Oct. 2011)
SHIMURA, Yusuke	Nagoya Univ.		(since Oct. 2011)
HIRATE, Satoshi	Nagoya Univ.		(since Oct. 2011)

Visiting Scientists

OZKENDIR, Osman Murat	Mersin Univ.	Apr. - Nov. 2011
KWON, Yong-Seung	Sungkyunkwan Univ.	Jun. - Jul. 2011, Jan. 2012
HONG, Jeong-Beom	Sungkyunkwan Univ.	Jun. - Jul. 2011
MIN, Gyeong-Im	Sungkyunkwan Univ.	Jun. - Jul. 2011
KIM, Beom-Young	Yonsei Univ.	Jul. - Aug. 2011, Feb. - Mar. 2012
KYUNG, Won-Shik	Yonsei Univ.	Jul. - Aug. 2011
KOH, Yoon-Young	Yonsei Univ.	Jul. - Aug. 2011
LABLANQUIE, Pascal	LCPMR, Univ. Pierre et marie Curie	Sep. 2011, Mar. 2012
GURITAMU, Violeta	Univ. of Geneva Faculity of Science	Oct. - Nov. 2011
CHEN, Fei	Fudan Univ.	Nov. - Dec. 2011
GE, Qingqin	Fudan Univ.	Nov. - Dec. 2011
LEE, Chul	Univ. of Seoul	Dec. 2011
KIM, Jooyun	Univ. of Seoul	Dec. 2011
UFUKTEPE, Yulsel	Univ. of Cukurova	Jan. - Mar. 2012
MIN, Byeon-Hun	Sungkyunkwan Univ.	Jan. 2012
SONG, Yun Young	Sungkyunkwan Univ.	Jan. 2012
LIU, Hsiang-Lin	National Taiwan Normal Univ.	Feb. 2012
SIMON, Marc	Univ. Pierre et Marie Curie	Feb. 2012
GUILLEMIN, Renaud	Univ. Pierre et Marie Curie	Feb. 2012
PIANCASTELLI, Maria-N.	Univ. Pierre et Marie Curie	Feb. 2012
SEO, Jeong Jin	Yonsei Univ.	Feb. - Mar. 2012
KYUNG, Won Shik	Yonsei Univ.	Feb. - Mar. 2012
SZWAJ, Christophe	Univ. des sciences et technologies de Lille	Mar. 2012
BIELAWSKI, Serge	Univ. des sciences et technologies de Lille	Mar. 2012
ROUSSEL, Eleonore	Univ. des sciences et technologies de Lille	Mar. 2012
PROBST, Petra	The Karksruhe Institute of Technology	Mar. 2012

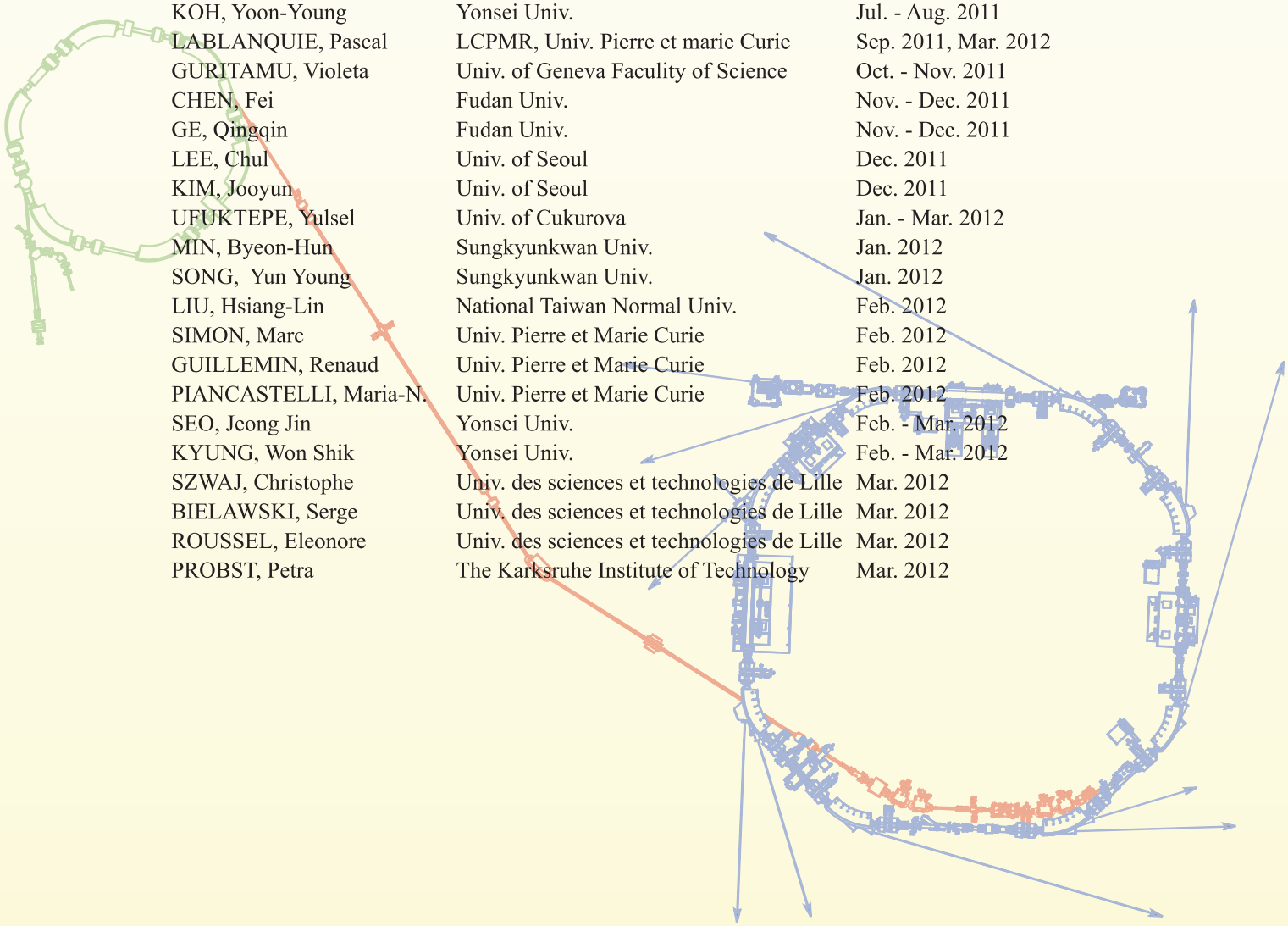

Light Sources in 2011

1. Status of UVSOR Accelerators

In FY2011, the UVSOR-II accelerators were in operation from May 2011 to March 2012. A total of 36 weeks were devoted to user operations, consisting of 34 weeks in multi-bunch mode and two weeks in single-bunch/multi-bunch hybrid mode, in which the machine is operated in single-bunch mode during the daytime and in multi-bunch mode at night. Four weeks were dedicated to machine studies this year. We had a two-month shutdown starting from April 2011, for the installation of a new undulator and construction of two new beamlines. There was also a one-week shutdown in September and a two-week shutdown around the New Year period.

The monthly statistics of the operation time and the integrated beam current are shown in Fig. 1. The high integrated beam current in June was due to vacuum conditioning.

Fig. 1. Monthly statistics in FY2011 (upper) for the operation time (red bars) and integrated beam current (blue dashed bars).

The weekly operation schedule is as follows. On Monday, the machine is operated for machine studies from 9 a.m. to 9 p.m. On Tuesday and Wednesday, the machine is operated for users from 9 a.m. to 9 p.m. From Thursday 9 a.m. to Friday 9 p.m., the machine is operated for 36 hours continuously for users. Thus, the beam time available to users is 60 hours per week. Since last year, we have been operating the machine in top-up mode for 100% of the users' time. The beam current is maintained at 300 mA in multi-bunch mode and 50 mA in single-bunch mode.

This fiscal year, we had a few problems with the pulse magnet power supplies for the booster synchrotron, which may have been due to the increased operation time of the beam injection system caused by the start of the top-up operation. We also encountered a problem with the programmable logic controller (PLC) for the magnet power supplies in the storage ring, which was caused by an instantaneous electricity shortage. Fortunately, in all cases the beam time for users could be secured by extending the operation time in the same weeks.

2. Improvements and Developments

New bending magnet for UVSOR-III

The magnetic lattice of UVSOR was modified in 2003, by replacing all the focusing magnets (quadrupoles and sextupoles). In 2012, we are going to replace all of the bending magnets (dipoles) with newly designed combined-function magnets. The new

Fig. 2. New combined-function bending magnet (a lower half is shown).

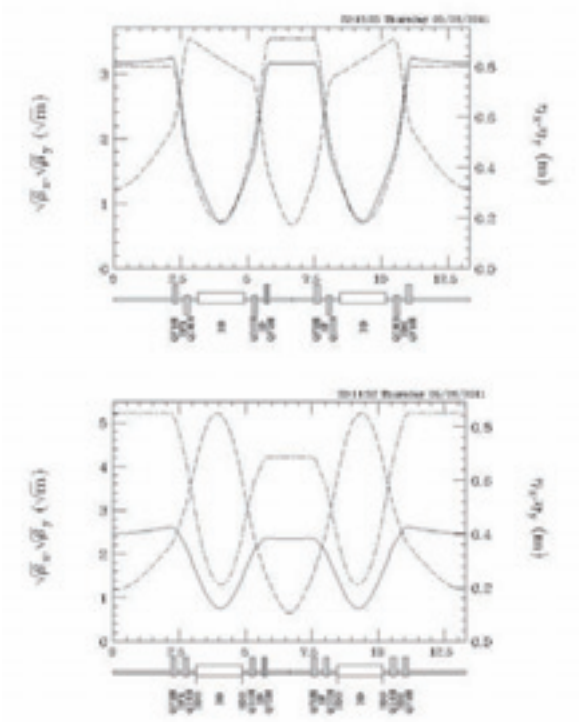

Fig. 3. Lattice functions of UVSOR-II (upper) and UVSOR-III (lower). The emittance is 27nm-rad and ~15nm-rad, respectively.

magnets have specially designed pole shapes and edge shapes as shown in Fig. 2, to produce dipole, quadrupole, and sextupole fields.

By this lattice modification, the emittance will be reduced from 27 nm-rad to around 15 nm-rad. The old and new lattice functions are shown in Fig. 3. The construction of the bending magnets and the field measurements were completed by the middle of March, 2012. In April 2012, the reconstruction work is scheduled to start. The commissioning of the new lattice will begin in June. After commissioning has been successfully completed, the ring will be called UVSOR-III.

Design and construction of in-vacuum undulator for STXM beamline

We designed and constructed an in-vacuum undulator for the new scanning transmission soft X-ray microscope (STXM) beamline (BL4U), which will be constructed in 2012. The magnetic period length is 38 mm and the pole length is about 1 m. This will be the third in-vacuum device in this ring. The basic design is similar to that of the U3 and U6 devices. The undulator will be installed in the ring in May 2012.

Fig. 4. New in-vacuum undulator for BL4U STXM beamline.

Design and construction of optical klystron

We installed a new undulator system (optical klystron) at the 4 m-long straight section (S1), which was newly created by moving the injection point in 2010. The optical klystron consists of two identical helical undulators (APPLE-II type) of 1 m in length, with a buncher (wiggler) in between. Because of the delay in the construction of these devices due to the earthquake last year, one undulator was installed in May and the other in September. The installation of the buncher took place in December.

This optical klystron will be used for generating coherent synchrotron radiation in the terahertz (THz) region and coherent harmonics in the vacuum ultraviolet (VUV) region, as well as for driving a free electron laser in the visible and UV regions. The first experiment on THz coherent synchrotron radiation was successfully carried out in February 2012.

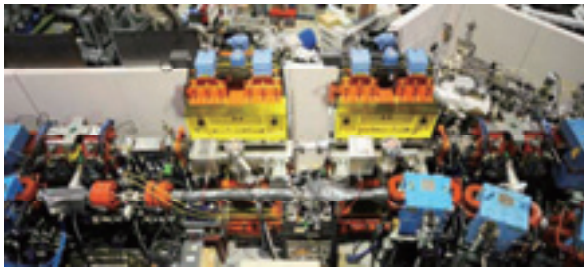

Fig. 5. New undulator system for coherent light source development installed at the straight section, S1.

Laser Compton scattering of gamma rays

Generation of polarized gamma rays based on the laser Compton scattering technique has been investigated, in which polarized laser photons are injected into the storage ring and Compton back-scattered. The photon energy was increased by the square of the Lorentz factor (~1500 for UVSOR-II), while preserving the polarity of the photons. By controlling the polarity of the laser photons, we can control that of the gamma rays. We have succeeded in observing the changes in the special distribution of the gamma rays depending on the polarization, which was well reproduced by numerical simulation [1]. Direct measurement of the polarization will be carried out in the future.

References

[1] Y. Taira *et al.*, in this report.

Masahiro Katoh (UVSOR Facility)

UVSOR Accelerator Complex

Injection Linear Accelerator

Energy	15 MeV
Length	2.5 m
Frequency	2856 MHz
Accelerating RF Field	2π/3 Traveling Wave
Klystron Power	1.8 MW
Energy Spread	~1.6 MeV
Repetition Rate	2.6 Hz

Booster Synchrotron

Energy	750 MeV
Injection Energy	15 MeV
Beam Current	32 mA (uniform filling)
Circumference	26.6 m
RF Frequency	90.1 MHz
Harmonic Number	8
Bending Radius	1.8 m
Lattice	FODO×8
Betatron Tune	
Horizontal	2.25
Veritcal	1.25
Momentum Compaction	0.138
Repetition Rate	1 Hz (750 MeV)

UVSOR-II Storage Ring

Energy	750 MeV
Injection Energy	750 MeV
Maximum Stored Current	500 mA (multi bunch) 100 mA (single bunch)
Natural Emittance	27.4 nm-rad
Circumference	53.2 m
RF Frequency	90.1 MHz
Harmonic Number	16
Bending Radius	2.2 m
Lattice	Extended DBA×4
Straight Section	(4 m×4)+(1.5 m×4)
RF Voltage	100 kV
Betatron Tune	
Horizontal	3.75
Veritcal	3.20
Momentum Compaction	0.028
Natural Chromaticity	
Horizontal	-8.1
Vertical	-7.3
Energy Spread	4.2×10^{-4}
Natural Bunch Length	108 ps

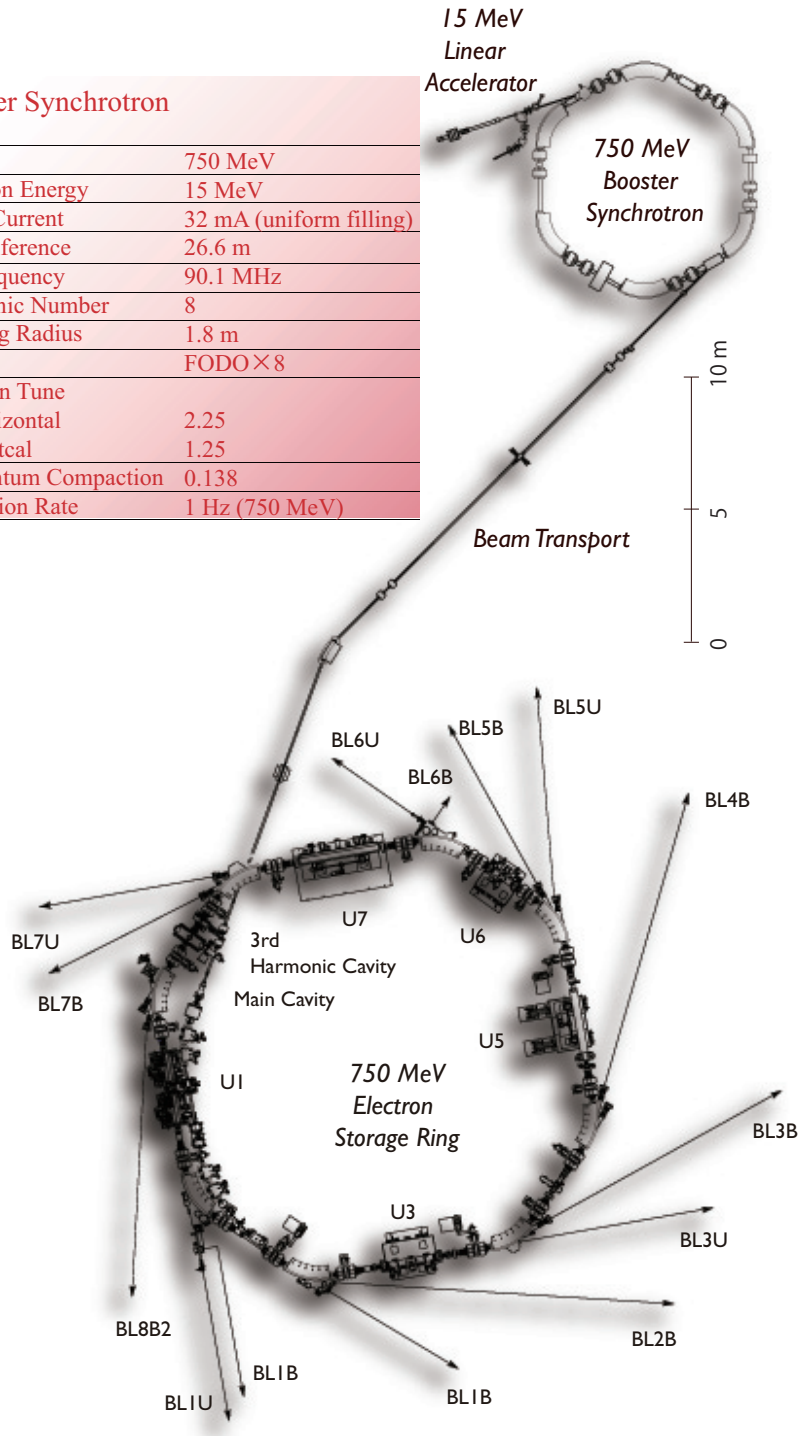

Electron Beam Optics of UVSOR-II Storage Ring

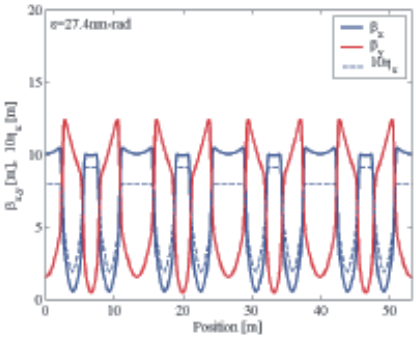

Horizontal /vertical
betatron functions
and dispersion function

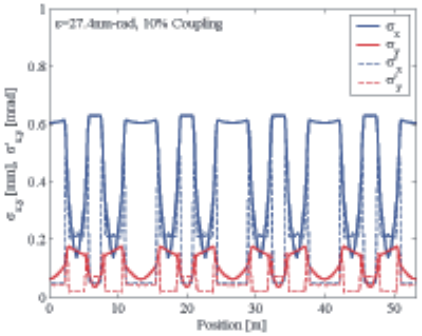

Horizontal /vertical
electron bem sizes
and beam divergences

Insertion Devices

Brilliance of Radiation

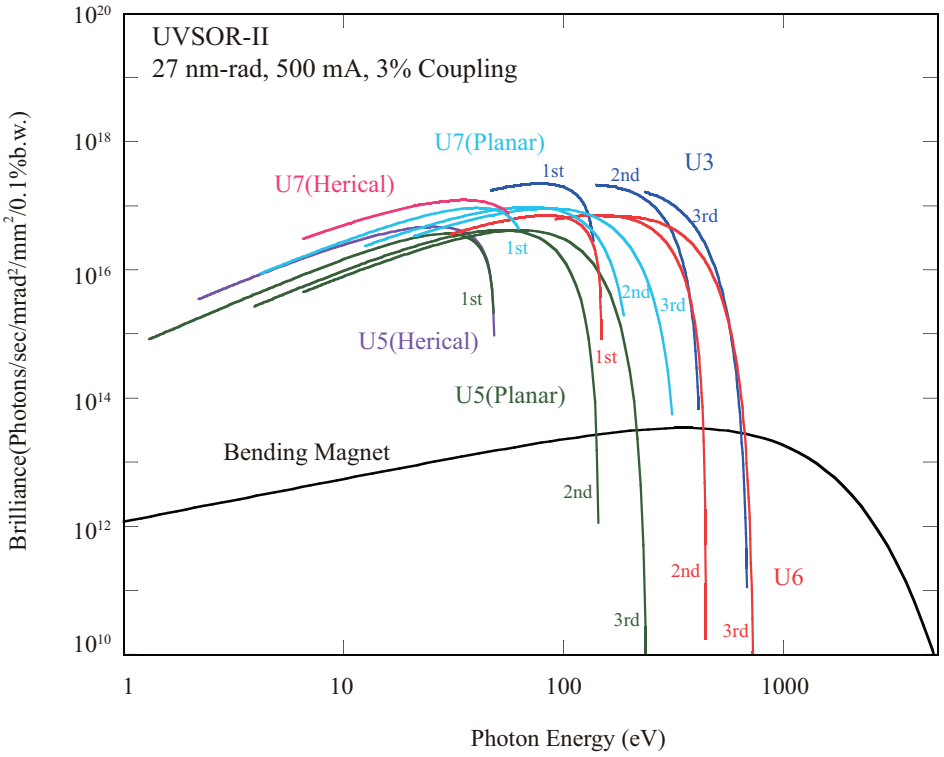

Brilliance of radiation from the insertion devices (U3, U5, U6 and U7) and a beding magnet of UVSOR-II

U3 In-vacuum Undulator

Number of Periods	50
Period Length	38 mm
Pole Length	1.9 m
Pole Gap	15 - 40 mm
Deflection Parameter	2.00 - 0.24

U6 In-vacuum Undulator

Number of Periods	26
Period Length	36 mm
Pole Length	0.94 m
Pole Gap	15 - 40 mm
Deflection Parameter	1.78 - 0.19

U5 Herical Undulator / Optical Klystron

Number of Periods	21 / 9+9 (Opt. Kly.)
Period Length	110 mm
Pole Length	2.35 m
Pole Gap	30 - 150 mm
Deflection Parameter	4.6 - 0.07 (Helical) 8.5 - 0.15 (Linear)

U7 Apple-II Variable Polarization Undulator

Number of Periods	40
Period Length	76 mm
Pole Length	3.04 m
Pole Gap	24 - 200 mm
Deflection Parameter	5.4 (Max. Horizontal) 3.6 (Max. Vertical) 3.0 (Max. Helical)

Bending Magnets

Bending Radius	2.2 m
Critical Energy	425 eV

Beamlines in 2011

The UVSOR facility has been widely recognized as one of the highest brilliance extreme ultraviolet (EUV) radiation sources among synchrotron radiation facilities with an electron energy of less than 1 GeV, after the successful accomplishment of the upgrade project on the storage ring (UVSOR-II Project). Eight bending magnets and four insertion devices are available for the utilization of synchrotron radiation at UVSOR. There has been a total of twenty operational beamlines in 2011, which are classified into two categories. A total of 14 beamlines were operational in 2011, classified into two categories. Nine are so-called "open beamlines," which are open to scientists of universities and research institutes belonging to the government, public organizations, private enterprises, and those of foreign countries. The remaining five beamlines are so-called "in-house beamlines," which are dedicated to the use of research groups within IMS.

The improvements and upgrades of the beamlines at UVSOR have been continuously discussed with users in a series of UVSOR workshops. The newly constructed (BL3U, BL7U, and BL6U) as well as upgraded (BL5U and BL6B) beamlines synchronized with the UVSOR-II Project have been routinely operated, and a number of outcomes have emerged through the utilization of these beamlines. We had one soft X-ray station equipped with a double-crystal monochromator, seven EUV and soft X-ray stations with a grazing incidence monochromator, three vacuum ultraviolet (VUV) stations with a normal incidence monochromator, and one infrared (IR) station equipped with Fourier-transform interferometers, as shown in the appended table (next page) for all available beamlines at UVSOR in 2011.

“Development and Application of Light Source Technology Based on Electron Storage Ring and Laser” proposed by the UVSOR Machine Group was accepted in 2008 as a research program in the Quantum Beam Technology Project conducted by the Japan Science and Technology Agency (JST) of the Ministry of Education, Culture, Sports, Science and Technology (MEXT). In this connection, the straight section U1 will be used for generating coherent terahertz (THz) and VUV radiation, with two beamlines to be constructed there. As a consequence of this, BL1A and BL1B must be moved to vacant sites. Since spectroscopic research work on solids has been carried out very actively at these beamlines, it is essential that all of the users’ activities there be continued smoothly at their new locations. Based on the results of discussions at the users’ meetings, which were organized by the UVSOR User’s Union, it was decided that BL1A will be moved to the location of the previous BL2A without any changes to the beamline components, and that BL1B will be newly constructed at the site of the previous BL3B. For the monochromator at BL3B, a 2.5 m off-plane Eagle type has been chosen. The relocation and construction of the related beamlines, as well as the relocation of the Ti:Sa laser system for the Machine Group to the downstream site of BL8B, were successfully completed in 2011. Actual operation of the new BL3B for users was initiated in January 2012.

A supplementary budget for upgrading the UVSOR Facility, which had been originally submitted as one of the budget requests of NINS, was approved in the autumn of 2010. The supplementary budget includes the cost for constructing a new soft X-ray microscopy beamline at BL4U, where a short in-vacuum type undulator with a total length of about 1 m is available as a light source. The period length chosen for this undulator, U4, is 38 mm, which is the same value as that for U3. The spectral region from 60 eV to 800 eV will be covered by the first and higher harmonic radiation. In order to cover a wide photon energy region with one single grating, and to keep the monochromator throughput as high as possible, a variable-included-angle Monk-Gillieson mounting with an entrance slit-less configuration has been selected. A scanning transmission soft X-ray microscope (STXM) will be installed at the exit slit position of the new BL4U. A new assistant professor, who is in charge of the installation, commissioning, and maintenance of the STXM beamline, arrived in the summer of 2011. The installation of the beamline components including STXM will start during the shutdown term before the summer of 2012, and practical operation of BL4U is due to begin around the end of the year. The introduction of photoemission electron microscopy to a branch beamline of BL4U as well as upgrades of the undulator U5 and the SGM-TRAIN monochromator at BL5U are still at the planning stage. Further discussions will be continued toward formulating a basic plan for beamline construction with users.

All users are required to refer to the beamline manuals and the UVSOR guidebook (the latest revision in PDF format uploaded on the UVSOR website in June 2010), at the time of conducting actual experimental procedures. Those wishing to use the open and in-house beamlines are recommended to contact the relevant beamline master (see next page). For updated information on UVSOR, please see the following site: http://www.uvsor.ims.ac.jp

Eiji Shigemasa (UVSOR Facility)

Beamline List

Beamline	Monochromator/ Spectrometer	Energy Range	Targets	Techniques	Contact
BL1U*	Free electron laser	1.6-13.9 eV			M. Katoh mkatoh@ims.ac.jp
BL1B	Martin-Puplett FT-FIR	0.5-30 meV	Solids	Reflection Absorption	S. Kimura kimura@ims.ac.jp
BL2A	Double crystal	585 eV-4 keV	Solids	Reflection Absorption	N. Kondo nkondo@ims.ac.jp
BL2B*	18 m spherical grating (Dragon)	24-205 eV	Gases	Photoionization Photodissociation	H. Katayanagi kata@ims.ac.jp
BL3U*	Varied-line-spacing plane grating (Monk-Gillieson)	60-800 eV	Gases Liquids Solids	Absorption Photoemission Photon-emission	N. Kosugi kosugi@ims.ac.jp
BL3B	2.5 m off-plane Eagle	1.7-30 eV	Solids	Reflection Absorption	M. Hasumoto hasumoto@ims.ac.jp
BL4B*	Varied-line-spacing plane grating (Monk-Gillieson)	25 eV-1 keV	Gases Solids	Photoionization Photodissociation Photoemission	E. Shigemasa sigemasa@ims.ac.jp
BL5U	Spherical grating (SGM-TRAIN†)	5-250 eV	Solids	Photoemission	M. Sakai sakai@ims.ac.jp
BL5B	Plane grating	6-600 eV	Solids	Calibration Absorption	M. Hasumoto hasumoto@ims.ac.jp
BL6U*	Variable-included-angle varied-line-spacing plane grating	30-500 eV	Gases Solids	Photoionization Photodissociation Photoemission	E. Shigemasa sigemasa@ims.ac.jp
BL6B	Michelson FT-IR	3 meV-2.5 eV	Solids	Reflection Absorption	S. Kimura kimura@ims.ac.jp
BL7U	10 m normal incidence (modified Wadsworth)	6-40 eV	Solids	Photoemission	M. Matsunami matunami@ims.ac.jp
BL7B	3 m normal incidence	1.2-25 eV	Solids	Reflection Absorption	M. Hasumoto hasumoto@ims.ac.jp
BL8B	Plane grating	1.9-150 eV	Solids	Photoemission	S. Kimura kimura@ims.ac.jp

BL4U is under construction.
Yellow columns represent undulator beamlines.
* In-house beamline.
† Spherical grating monochromator with translating and rotating assembly including normal incidence mount.

BL1U

Free Electron Laser

The free electron laser (FEL) at UVSOR-II is being moved to a dedicated long straight section (S1). The FEL is equipped with a variably polarized optical klystron of 3 m in length and an optical cavity of 13.3 m in length. By using various multilayer mirrors for the cavity, the FEL can provide coherent light in a wide wavelength range from 800 nm to 199 nm. The pulse duration is typically several tens of picoseconds. The repetition rate is approximately 11 MHz. The average output power depends on the wavelength but its typical value is several hundred milliwatts. Output power higher than 1 W was recorded at 230 nm and 570 nm. The FEL can be operated in top-up injection mode. Users can use the FEL for several hours with quasi-constant output power. The laser pulses are naturally synchronized with the synchrotron radiation pulses that are provided at other synchrotron radiation beamlines. The laser beam can be transported to the beamlines using a mirror system for pump and probe experiments if requested.

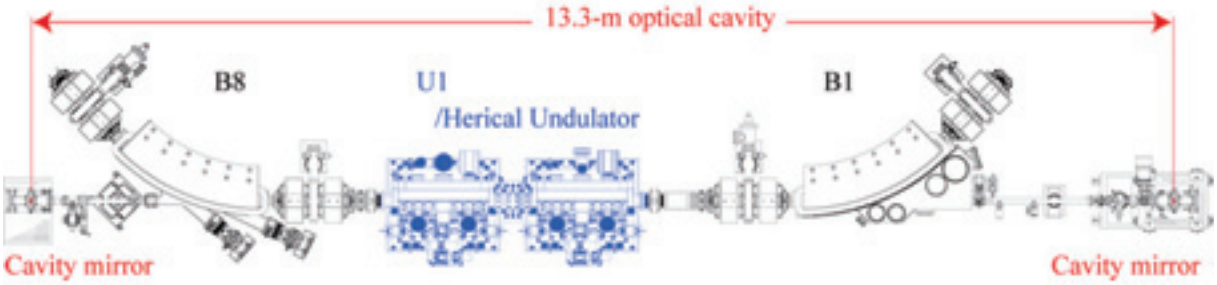

Fig. 1. Schematic of the 13.3 m-long optical cavity.

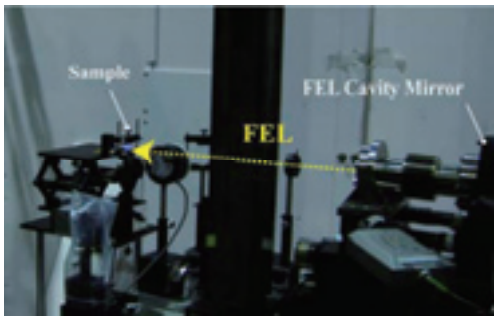

Fig. 2. Left and right circularly polarized FEL being delivered to B4 for an application experiment.

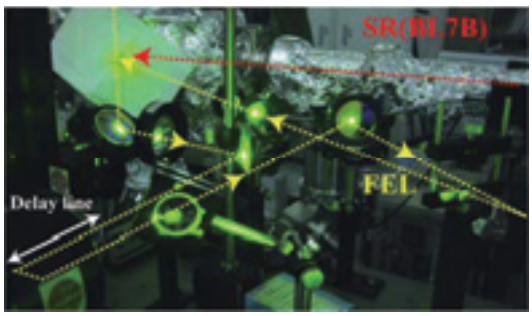

Fig. 3. The FEL is delivered to BL7B. The FEL is irradiated on a target simultaneously with the SR .

FEL Specifications

Wavelength	199-800 nm
Spectral band width	~10^{-4}
Polarization	Circular/linear
Pulse rate	11.26 MHz
Max. average power	~1 W
Cavity type	Fabry-Perot
Cavity length	13.3 m
Cavity mirror	HfO_2, Ta_2O_5, Al_2O_3 multilayer

BL1B

Terahertz Spectroscopy Using Coherent Synchrotron Radiation

Coherent synchrotron radiation (CSR) is a powerful light source in the terahertz (THz) region. This beamline has been constructed for basic studies on the properties of THz-CSR. However, it can be also used for measurements of reflectivity and transmission spectra of solids using conventional synchrotron radiation.

The emitted THz light is collected by a three-dimensional magic mirror (3D-MM, M0) of the same type as those already successfully installed at BL43IR in SPring-8 and BL6B in UVSOR-II. The 3D-MM was installed in bending-magnet chamber #1 and is controlled by a 5-axis pulse motor stage (x, z translation; θ_x, θ_y, θ_z rotation). The acceptance angle was set at 17.5-34 degrees (total 288 mrad) in the horizontal direction. The vertical angle was set at ±40 mrad to collect the widely expanded THz-CSR.

The beamline is equipped with a Martin-Puplett type interferometer (JASCO FARIS-1) to cover the THz spectral region from 4 to 240 cm^{-1} ($h\nu$ = 500 μeV-30 meV). There is a reflection/absorption spectroscopy (RAS) end-station for large samples (~ several mm). At the RAS end-station, a liquid-helium-flow type cryostat with a minimum temperature of 4 K is installed.

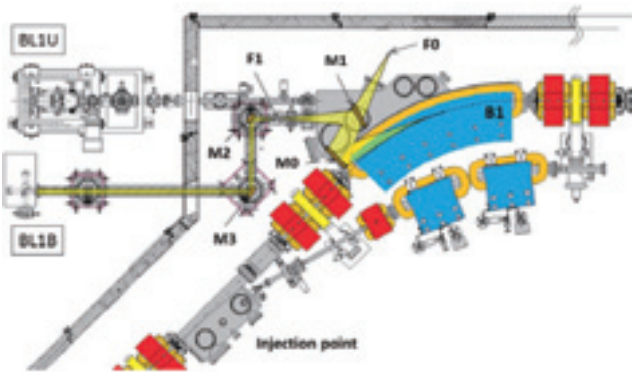

Fig. 1. Schematic top view of the beam extraction part of the THz-CSR beamline, BL1B. The three-dimensional magic mirror (3D-MM, M0) and a plane mirror (M1) are located in the bending-magnet chamber. A parabolic mirror (M2) is installed to form a parallel beam. The straight section (BL1U) is used for coherent harmonic generation (CHG) in the VUV region.

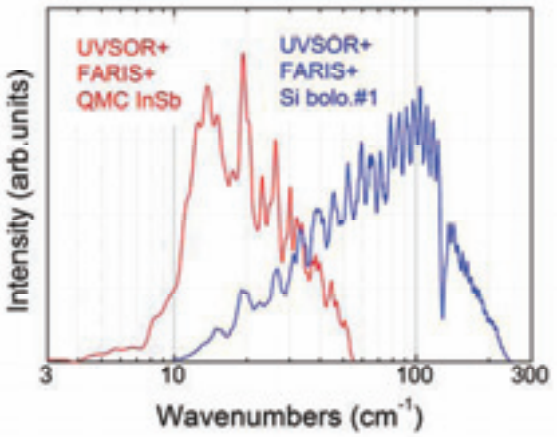

Fig. 2. Obtained intensity spectra with the combination of a light source (UVSOR), interferometer (FARIS-1), and detectors (Si bolometer and InSb hot-electron bolometer).

Beamline Specifications

Interferometer	Martin-Puplett (JASCO FARIS-1)
Wavenumber range (Energy range)	4-240 cm^{-1} (500 μeV-30 meV)
Resolution in cm^{-1}	0.25 cm^{-1}
Experiments	Reflection/transmission spectroscopy
Miscellaneous	Users can use their experimental system in this beamline.

BL2A

Soft X-Ray Beamline for Photoabsorption Spectroscopy

BL2A, which was moved its previous location as BL1A in 2011, is a soft X-ray beamline for photoabsorption spectroscopy. The beamline is equipped with a focusing premirror and a double-crystal monochromator [1]. The monochromator serves soft X-rays in the energy region from 585 to 4000 eV using several types of single crystals, such as β-Al_2O_3, beryl, KTP ($KTiOPO_4$), quartz, InSb, and Ge. The throughput spectra measured using a Si photodiode (AXUV-100, IRD Inc.) are shown in Fig. 1. The typical energy resolution (E / ΔE) of the monochromator is approximately 1500 for beryl and InSb. There are no experimental setups that are specific to this beamline, except for a small vacuum chamber equipped with an electron multiplier (EM) detector. Photoabsorption spectra for powdery samples are usually measured in total electron yield mode, with the use of the EM detector.

[1] Hiraya *et al.*, Rev. Sci. Instrum. **63** (1992) 1264.

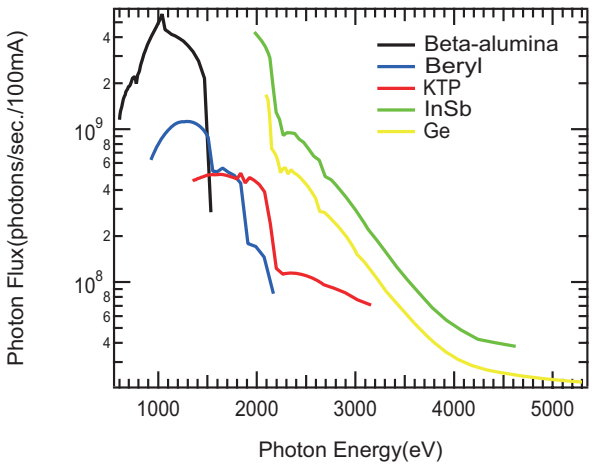

Fig. 1. Throughput spectra of the double-crystal monochromator at BL2A.

Fig. 2. Side view of BL2A.

Beamline Specifications

Monochromator	Double crystal monochromator
Monochromator crystals: (2d value, energy range)	β-Al_2O_3 (22.53 Å, 585–1609 eV), beryl (15.965 Å, 826–2271 eV), KTP (10.95 Å, 1205–3310 eV), quartz (8.512 Å, 1550–4000 eV), InSb (7.481 Å, 1764–4000 eV), Ge (6.532 Å, 2094–4000 eV)
Resolution	$E/\Delta E$ = 1500 for beryl and InSb
Experiments	Photoabsorption spectroscopy

BL2B

Beamline for Gas Phase Photoionization and Reaction Dynamics

This beamline has been developed to study ionization, excitation, and decay dynamics involving inner-valence electrons, 2*p* electrons of the third row atoms, and 4d electrons of the lanthanides. The monochromator is a spherical grating Dragon type with 18-m focal length. High throughput (1×10^{10} photons s^{-1}) and high resolution ($E/\Delta E$ = 2000 - 8000) are achieved simultaneously under the condition of the ring current of 100 mA [1]. The optical system consists of two pre-focusing mirrors, an entrance slit, three spherical gratings (G1 - G3), two folding mirrors, a movable exit slit, and a refocusing mirror [2]. The monochromator is designed to cover the energy range of 23–205 eV with the three gratings: G1 (2400 lines mm^{-1}, R = 18 m) at 80–205 eV; G2 (1200 lines mm^{-1}, R = 18 m) at 40–100 eV; G3 (2400 lines mm^{-1}, R = 9.25 m) at 23–50 eV. The percentage of the second-order light contamination at $h\nu$ = 45.6 eV is 23% for G2 or 7% for G3.

We have been measuring the yield curves of various fullerene ions [3]. Geometrical structures and electronic properties of fullerenes have attracted widespread attention because of their novel structures, novel reactivity, and novel catalytic behaviors as typical nanometer-size materials. However, spectroscopic information was very limited in the extreme UV region, owing to difficulties in acquiring sufficient sample amounts. This situation has rapidly changed since the start of this century, because the techniques related to syntheses, isolation, and purification have advanced so rapidly that an appreciable amount of fullerenes can now be readily obtained.

[1] M. Ono, H. Yoshida, H. Hattori and K. Mitsuke, Nucl. Instrum. Meth. Phys. Res. A **467-468** (2001) 577.
[2] H. Yoshida and K. Mitsuke, J. Synchrotron Radiation **5** (1998) 774.
[3] J. Kou, T. Mori, Y. Kubozono and K. Mitsuke, Phys. Chem. Chem. Phys. **7** (2005) 119.

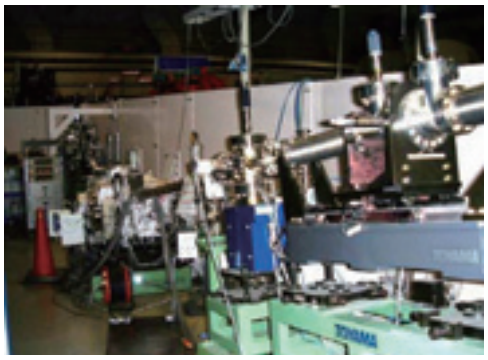

Fig. 1. 18 m spherical grating monochromator at BL2B.

Fig. 2. End station of BL2B for gas phase spectroscopy of refractory materials.

Beamline Specifications

Monochromator	18 m spherical grating Dragon-type
Wavelength Range	6-55 nm; 24-205 eV
Resolution	2000–8000 depending on the gratings
Experiments	Mass spectrom.; photoelectron spectrosc.; momentum imaging spectrosc.; e^--ion coincidence spectrosc.; fullerene beam source

BL3U

Varied-Line-Spacing Plane Grating Monochromator for Molecular Soft X-Ray Spectroscopy

The beamline BL3U is equipped with an in-vacuum undulator composed of 50 periods of 3.8 cm period length. The emitted photons are monochromatized by the varied-line-spacing plane grating monochromator (VLS-PGM) designed for various spectroscopic investigations in the soft X-ray range including soft X-ray emission studies. Three holographically ruled laminar profile plane gratings are designed to cover the photon energy range from 60 to 800 eV. The beamline has two endstations, namely, XES setup and multi-purpose setup. The XES setup is used for soft X-ray emission spectroscopy. The beam is horizontally focused onto the sample position by a plane-elliptical mirror, M2X. In the multi-purpose setup, the beam is focused by the toroidal mirror M2. Between the sample position and M2, the differential pumping is placed.

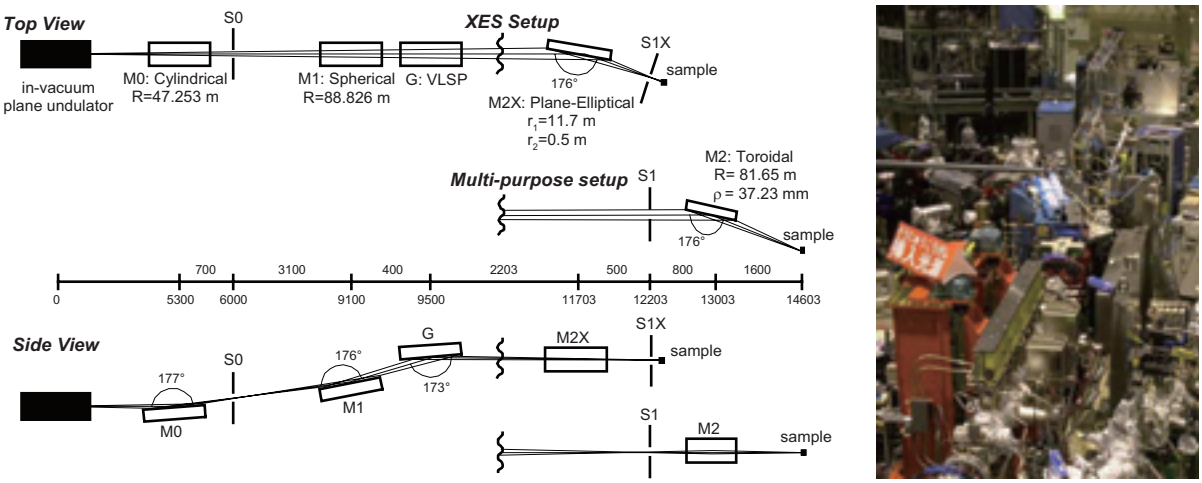

Fig. 1. Schematic layout (left) and the photography (right) of the BL3U. The distances along the beam from the center of the in-vacuum plane undulator are shown in millimeters. S1X and M2X can be replaced with the other exit slit S1 so that experiments can be carried out at either the XES or the multipurpose endstation. In the XES setup, the sample is placed 5–10 mm downstream of S1X.

Beamline Specifications

Monochromator	Varied-line-spacing plane grating monochromator
Energy Range	60-800 eV
Resolution	$E / \Delta E > 10\,000$
Experiments	Soft X-ray spectroscopy (XPS, XES, XAS)
Beam Size (XES Endstation)	Gaussian shape Vertical 5-20 μm; Horizontal 41 μm (FWHM)

BL3B (HOTRLU)

VIS-VUV Photoluminescence and Reflection/Absorption Spectroscopy

BL3B has been constructed to study photoluminescence (PL) in the visible (VIS) to vacuum ultraviolet (VUV) region. This beamline consists of a 2.5 m off-plane Eagle type normal-incidence monochromator, which covers the VUV, UV, and VIS regions, i.e., the energy (wavelength) region of 1.7-31 eV (40-730 nm), with three spherical gratings having constant grooving densities of 1200, 600, and 300 l/mm optimized at the photon energies of ~20, ~16, and ~6 eV, respectively. The schematic side view and top view layouts are shown in Figs. 1(a) and 1(b), respectively. The FWHM of the beam spot at the sample position is 0.25 mm (V) × 0.75 mm (H). Low energy pass filters (LiF, quartz, WG32, OG53) can be inserted automatically to maintain the optical purity in the G3 (300 l/mm) grating region (1.7~11.8 eV). Figure 2 shows the throughput spectra (photon numbers at a beam current of 300 mA) for each grating with entrance and exit slit openings of 0.1 mm (resolving power E / ΔE of ~2000 (G3, ~6.8 eV)). Since both slits can be opened up to 0.5 mm, a monochromatized photon flux of 10^{10} photons/s or higher is available for PL measurements in the whole energy region.

The end station is equipped with a liquid-helium-flow type cryostat for sample cooling and two detectors; one of which is a photomultiplier with sodium salicylate and the other a Si photodiode for reflection/absorption measurement. For the PL measurements in the wide energy region from VIS to VUV, two PL monochromators, comprising not only a conventional VIS monochromator but also a VUV monochromator with a CCD detector, are installed at the end station.

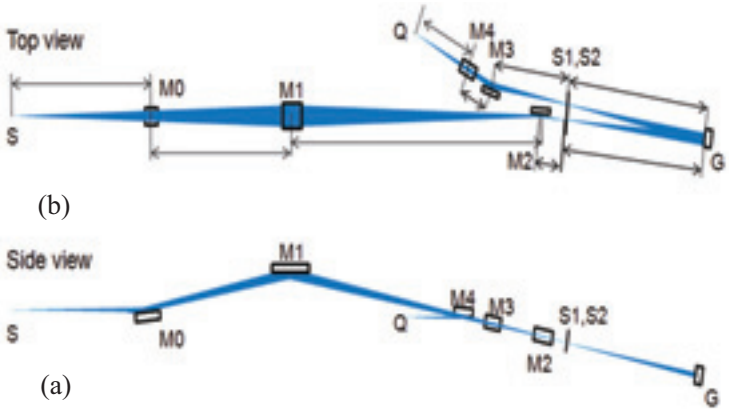

Fig. 1. Schematic layout of the BL3B (a) side view and (b) top view.

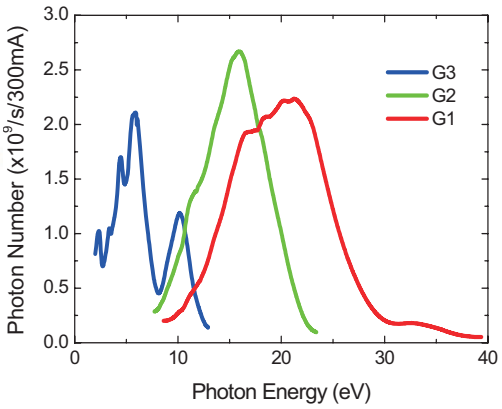

Fig. 2. Throughput spectra for each grating (G1:1200 l/mm, G2:600 l/mm and G3:300 l/mm) with S1 = S2 = 0.1 mm.

Beamline Specifications

Monochromator	-2.5 m normal-incidence monochromator
Energy range	1.7-31 eV (40~730 nm)
Resolution (Δhν/ hν)	≥ 12000 (at ~ 6.9 eV, 0.02 mm slits, G1 (1200 l/mm)
Experiments	Photoluminescence, reflection, and absorption spectroscopy, mainly for solids

BL4B

Varied-Line-Spacing Plane Grating Monochromator for Molecular Soft X-Ray Spectroscopy

The beamline BL4B equipped with a varied-line-spacing plane grating monochromator (VLS-PGM) was constructed for various spectroscopic investigations in a gas phase and/or on solids in the soft X-ray range. Three holographically ruled laminar profile plane gratings with SiO_2 substrates are designed to cover the photon energy range from 25 to 800 eV. The gratings with groove densities of 100, 267, and 800 l/mm cover the spectral ranges of 25–100, 60–300, and 200-1000 eV, respectively, and are interchangeable without breaking the vacuum. Fig. 1 shows the absolute photon flux for each grating measured using a Si photodiode (IRD Inc.), with the entrance- and exit-slit openings set at 50 and 50 μm, respectively. The maximum resolving power ($E/\Delta E$) achieved for each grating exceeds 5000.

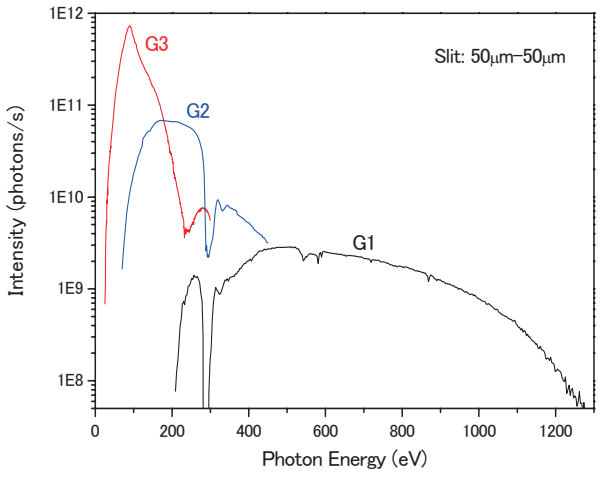

Fig. 1. Throughput from the VLS-PGM monochromator on BL4B.

Fig. 2. Photo of BL4B.

Beamline Specifications

Monochromator	Varied-line-spacing Plane Grating Monochromator
Energy range	25-1000 eV
Resolution	$E / \Delta E > 5000$ (at maximum)
Experiments	Soft X-ray spectroscopy (mainly, angle-resolved photoion spectroscopy for gaseous targets and photoelectron spectroscopy for gaseous and solid targets)

BL5U

Photoemission Spectroscopy of Solids and Surfaces

This beamline is designed for high-resolution angle-resolved photoemission study of solids and surfaces with horizontal-linearly and circularly (CW, CCW) polarized synchrotron radiation from a helical undulator. The beamline consists of a Spherical Grating Monochromator with a Translational and Rotational Assembly Including a Normal incidence mount (SGM-TRAIN) and a high-resolution angle-resolved photoemission spectrometer.

The SGM-TRAIN is an improved version of a constant-length SGM that aims at realizing the following points: (1) covering the wide energy range of 5–250 eV, (2) high energy resolving power, (3) use of linearly and circularly polarized undulator light, (4) reduction of higher-order light, and (5) two driving modes (rotation and translation of gratings) by computer control. The second-order light is well suppressed using laminar profile gratings and combinations of mirrors and gratings.

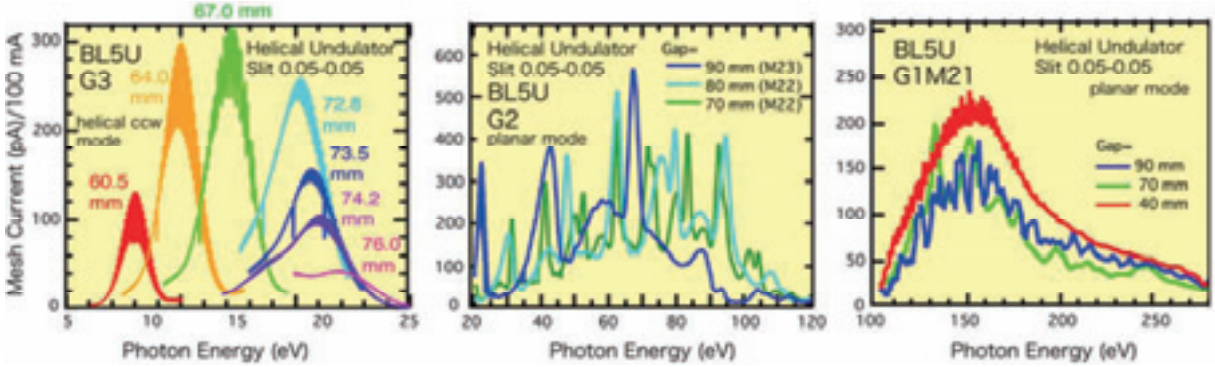

Fig. 1. Throughput spectra from the SGM-TRAIN monochromator at BL5U.

Beamline Specifications

Monochromator	SGM-TRAIN
Energy Range	5-250 eV
Resolution	$h\nu$ / ΔE > 2,000 for < 40 μm slits
Experiment	ARPES, AIPES, XAS
Flux	$<10^{11}$ photons/s for <40 μm slits (in the sample position)
Main Instruments	Hemispherical photoelectron analyzer (MBS-Toyama 'Peter' A-1), LEED of reverse type (OMICRON), Liq-He flow cryostat (5-400 K)

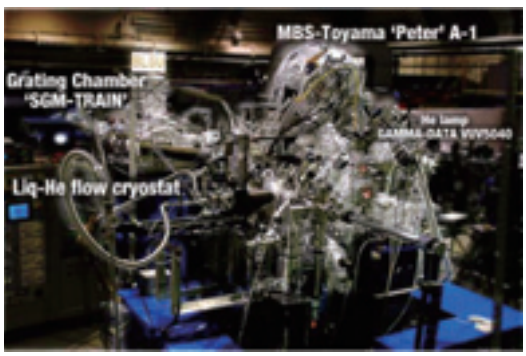

Fig. 2. High-resolution angle-resolved photoemission apparatus at BL5U.

BL5B

Calibration Apparatus for Optical Elements and Detectors

BL5B has been constructed to perform calibration measurements for optical elements and detectors. This beamline is composed of a plane grating monochromator (PGM) and three endstations in tandem. The most upstream station is used for the calibration measurements of optical elements, the middle one for optical measurements for solids, and the last for photo-stimulated desorption experiments. The experimental chamber at the most downstream station is sometimes changed to a chamber for photoemission spectroscopy. The calibration chamber shown in Fig. 2 is equipped with a goniometer for the characterization of optical elements, which has six degrees of freedom, X-Y translation of a sample, and interchanging of samples and filters. These are driven by pulse motors in vacuum. Because the polarization of synchrotron radiation is essential for such measurements, the rotation axis can be made in either the horizontal or vertical direction (s- or p-polarization).

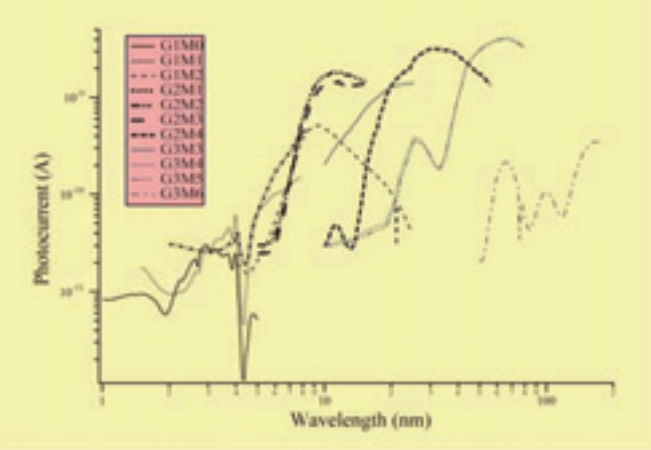

Fig. 1. Throughput spectra for possible combinations of gratings and mirrors at BL5B measured by a gold mesh.

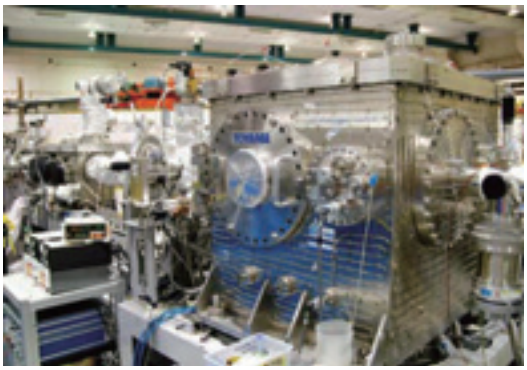

Fig. 2. A side view of the experimental chamber for calibration measurements.

Beamline Specifications

Monochromator	Plane Grating Monochromator
Energy range	6-600 eV (2-200 nm)
Resolution	E / ΔE~500
Experiments	Calibration of optical elements, absorption of solids, photo-stimulated desorption from rare-gas solids

BL6U

Variable-Included-Angle VLS-PGM for Molecular Soft X-Ray Spectroscopy

The beamline BL6U equipped with a variable-included-angle Monk-Gillieson mounting monochromator with a varied-line-spacing plane grating was constructed for various spectroscopic investigations requiring high-brilliance soft X-rays in a gas phase and/or on solids. Through a combination of undulator radiation and sophisticated monochromator design (entrance slit-less configuration and variable-included-angle mechanism), using a single grating, the monochromator can cover the photon energy ranging from 30 to 500 eV, with resolving power of greater than 10000 and photon flux of more than 10^{10} photons/s. Figure 1 shows an example of the monochromator throughput spectra measured using a Si photodiode, with the exit-slit opening set at 30 μm, which corresponds to the theoretical resolving power of 10000 at 80 eV.

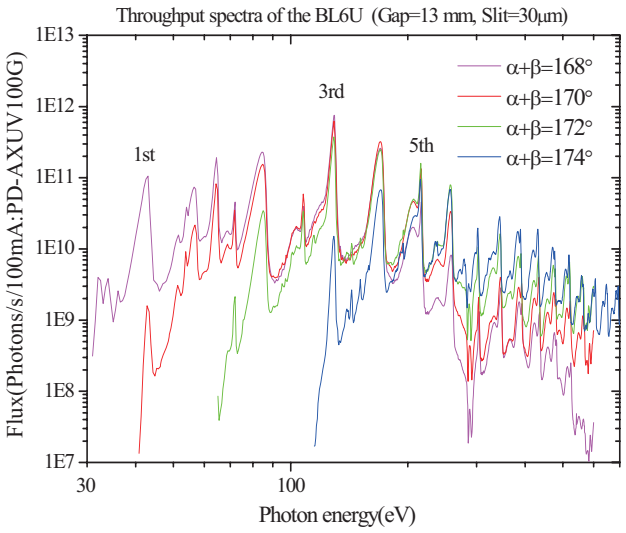

Fig. 1. Throughput spectra of the BL6U monochromator at various included angles.

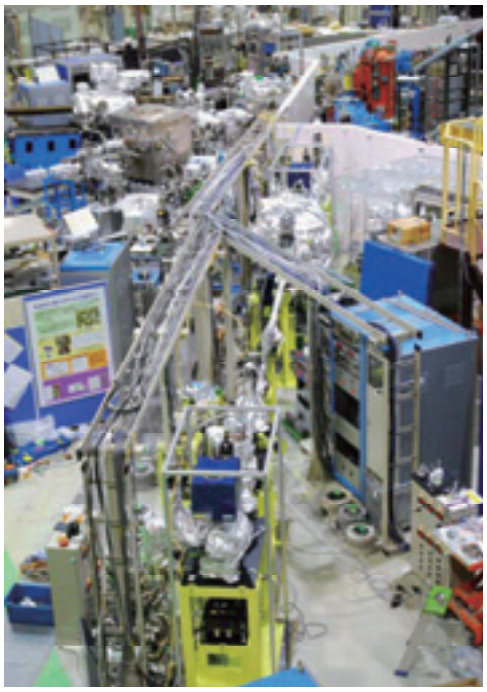

Fig. 2. Photo of BL6U

Beamline Specifications

Monochromator	Variable-included-angle Varied-line-spacing Plane Grating Monochromator
Energy range	40-500 eV
Resolution	$E / \Delta E > 10000$ (at maximum)
Experiments	High-resolution soft X-ray spectroscopy (mainly photoelectron spectroscopy for gaseous and solid targets)

BL6B

Infrared and Terahertz Spectroscopy of Solids

Synchrotron radiation (SR) has good performance (high brilliance and high flux) not only in the VUV and soft X-ray (SX) regions but also in the infrared (IR) and THz regions. BL6B covers the IR and THz regions. The previous beamline, BL6A1, which was constructed in 1985, was the pioneer in IRSR research. The beamline was deactivated at the end of FY2003 and a new IR/THz beamline, BL6B (IR), was constructed in FY2004. The front-end part including bending duct #6 was replaced with a new part having a higher acceptance angle (215 (H) × 80 (V) mrad^2) using a magic mirror, as shown in Fig. 1 [1].

The beamline is equipped with a Michelson type (Bruker Vertex70v) interferometer to cover a wide spectral region from 30 to 20,000 cm^{-1} ($h\nu$ = 4 meV-2.5 eV), as shown in Fig. 2. There are two end-stations; one for reflection/absorption spectroscopy (RAS) of large samples (up to several mm) and the other for IR/THz microscopy (transmission microscopy: TM) of tiny samples (up to several tens of μm). At the RAS end-station, a liquid-helium-flow type cryostat with a minimum temperature of 10 K is installed. At the TM end-station, pressure- and temperature-dependent THz spectroscopy can be performed. A superconducting magnet with a maximum field of 6 T can be installed by the exchange with the TM end-station.

[1] S. Kimura, E. Nakamura, T. Nishi, Y. Sakurai, K. Hayashi, J. Yamazaki, M. Katoh, "Infrared and terahertz spectromicroscopy beam line BL6B(IR) at UVSOR-II," Infrared Phys. Tech. **49** (2006) 147.

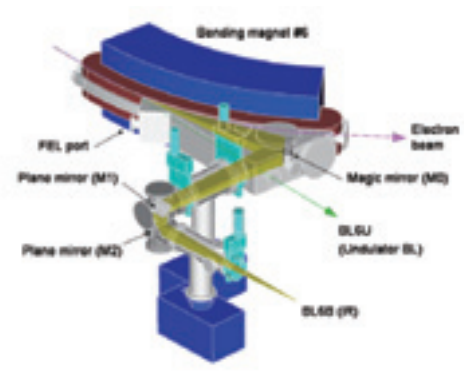

Fig. 1. Design of the optics and front end of BL6B.

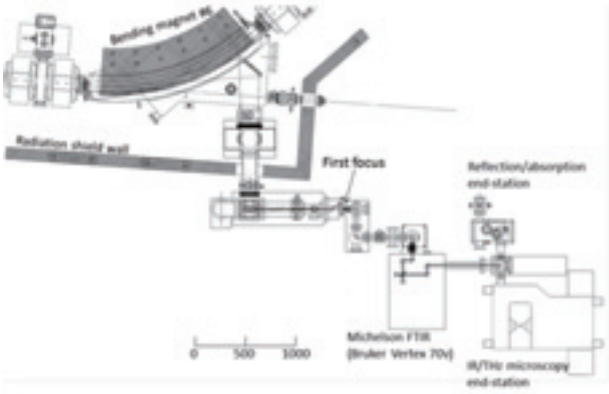

Fig. 2. Schematic top view of BL6B.

Beamline Specifications

Interferometer	Michelson (Bruker Vertex70v)
Wavenumber Range (Energy range)	30-20,000 cm^{-1} (4 meV-2.5 eV)
Resolution in cm^{-1}	0.1cm^{-1}
Experiments	Reflectivity and transmission Microspectroscopy Magneto-optics
Miscellaneous	Users can use their experimental system in this beamline.

BL7U (SAMRAI)

Angle-Resolved Photoemission of Solids in the VUV Region

Beamline 7U, named the Symmetry- And Momentum-Resolved electronic structure Analysis Instrument (SAMRAI) for functional materials, was constructed to provide a photon flux with high energy resolution and high flux mainly for high-resolution angle-resolved photoemission spectroscopy of solids [1]. An APPLE-II-type variable-polarization undulator is installed as the light source. The undulator can produce intense VUV light with horizontal/vertical linear and right/left circular polarization. The undulator light is monochromatized by a modified Wadsworth type monochromator with three gratings (10 m radius; 1200, 2400, and 3600 lines/mm optimized at $h\nu$ = 10, 20, and 33 eV). The energy resolution of the light ($h\nu$ / $\Delta h\nu$) is more than 10^4 with a photon flux of 10^{11}-10^{12} ph/s or higher on samples in the entire energy region.

The beamline has a photoemission end-station equipped with a 200 mm-radius hemispherical photoelectron analyzer (MB Scientific AB, A-l analyzer) with a wide-angle electron lens and a liquid-helium-cooled cryostat with 6-axis pulse motor control (AVC Co., Ltd., i-GONIO). The main function of the beamline is to determine the three-dimensional Fermi surface and electronic structure of solids at low temperatures and their temperature dependence in order to reveal the origin of their physical properties.

[1] S. Kimura, T. Ito, M. Sakai, E. Nakamura, N. Kondo, K. Hayashi, T. Horigome, M. Hosaka, M. Katoh, T. Goto, T. Ejima, K. Soda, "SAMRAI: A variably polarized angle-resolved photoemission beamline in the VUV region at UVSOR-II," Rev. Sci. Instrum. **81** (2010) 053104.

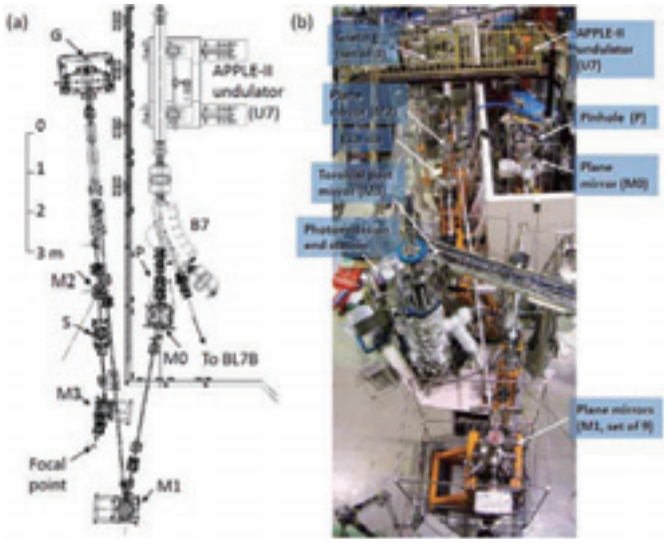

Fig. 1. Layout (a) and photograph (b) of the SAMRAI beamline consisting of an APPLE-II type undulator (U7), a modified Wadsworth type monochromator (M0-S), and a high-resolution photoemission analyzer at the focal point. The monochromator has five major optical components: two plane mirrors (M0 and M1) with water cooling, one set of three spherical gratings (G), an exit slit (S), and one toroidal refocusing mirror (M3). The spherical gratings have a radius of 10 m and are located 22 m from the center of the undulator. There is no entrance slit. S is located 6.47 m from G. A second branch for a VUV microscope end-station is planned to be constructed after the plane mirror (M2) located between G and S.

Beamline Specifications

Light source	APPLE-II type undulator (λ_u = 76 mm, N = 36) vertical/horizontal linear, right/left circular
Monochromator	10 m normal-incidence monochromator (modified Wadsworth type)
Photon energy range	6~40 eV (λ = 30~200 nm)
Resolution ($h\nu/\Delta h\nu$)	1×10^4-5×10^4
Photon flux on sample	$\geq 10^{12}$-10^{11} ph/s (depending on $h\nu$)
Beam size on sample	200 (H) × 50 (V) μm^2
Experiments	Angle-resolved photoemission of solids (MB Scientific A-1 analyzer, acceptance angle: ± 18 deg)

BL7B

3 m Normal-Incidence Monochromator for Solid-State Spectroscopy

BL7B has been constructed to provide sufficiently high resolution for conventional solid-state spectroscopy, sufficient intensity for luminescence measurements, wide wavelength coverage for Kramers–Kronig analyses, and minimum deformation to the polarization characteristic of incident synchrotron radiation. This beamline consists of a 3-m normal incidence monochromator, which covers the vacuum ultraviolet, ultraviolet, visible, and infrared, i.e., the wavelength region of 40–1000 nm, with three gratings (1200, 600, and 300 l/mm). Two interchangeable refocusing mirrors provide two different focusing positions. For the mirror with the longer focal length, an LiF or a MgF_2 window valve can be installed between the end valve of the beamline and the focusing position. Fig.1 shows the absolute photon intensity for each grating with the entrance and exit slit openings of 0.5 mm. A silicon photodiode (AXUV-100, IRD Inc.) was utilized to measure the photon intensity and the absolute photon flux was estimated, taking the quantum efficiency of the photodiode into account.

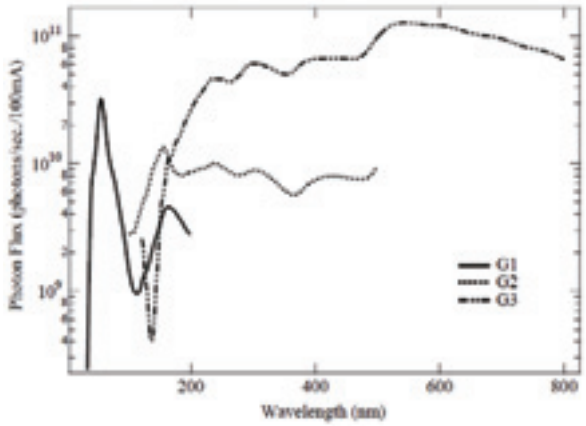

Fig. 1. Throughput spectra of BL7B measured using a silicon photodiode.

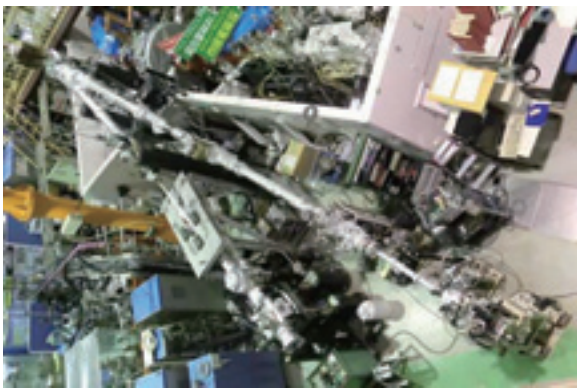

Fig. 2. Photo of BL7B.

Beamline Specifications

Monochromator	3 m Normal-Incidence Monochromator
Wavelength Range	50-1000 nm (1.2-25 eV)
Resolution	E / ΔE = 4000-8000 for 0.01 mm slits
Experiments	Absorption, reflection, and fluorescence spectroscopy, mainly for solids

BL8B

Angle-Resolved Ultraviolet Photoelectron Spectrometer for Solids

BL8B is a beamline for the angle-resolved ultraviolet photoemission spectroscopy (ARUPS) system, which is designed to measure various organic solids such as molecular crystals, organic semiconductors, and conducting polymers. This beamline consists of a plane-grating monochromator (PGM), a sample preparation chamber with a fast-entry load-lock chamber, a measurement chamber (base pressure 1×10^{-10} Torr), a cleaning chamber (base pressure 1×10^{-10} Torr), and a sample evaporation chamber (base pressure 3×10^{-10} Torr). The cleaning chamber is equipped with a back-view LEED/AUGER, an ion gun for Ar^+ sputtering, and an infrared heating unit. The PGM consists of premirrors, a plane grating, focusing mirror, and a post-mirror, with an exit slit. It covers the wide range from 2 to 130 eV with two exchanging gratings (G1: 1200 l/mm, G2: 450 l/mm) and five cylindrical mirrors. The toroidal mirror focuses the divergent radiation onto the sample in the measurement chamber. The spot size of the zeroth-order visible light at the sample surface is approximately 1×1 mm^2. Figure 1 shows the throughput spectra of PGM (slit = 100 μm). The energy resolution at a slit width of 100 μm was found to be $E/\Delta E$ = 1000 in the wavelength range from 2 to 130 eV. A hemispherical electron energy analyzer of 75 mm mean radius with an angular resolution less than 2° can be rotated around the vertical and horizontal axes. The sample mounted on a manipulator (temperature range 14–320 K) can also be rotated around two axes.

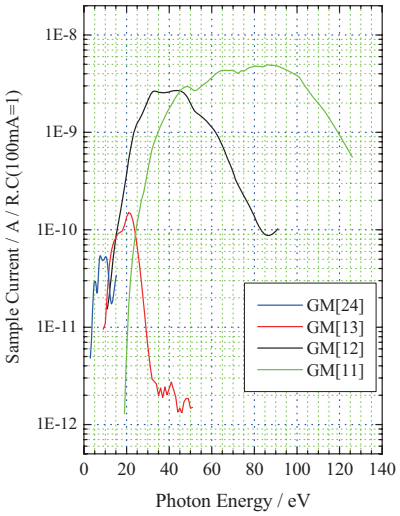

Fig. 1. Throughput spectra of plane-grating monochromator at BL8B (slit = 100 μm).

Fig. 2. A photo of BL8B.

Beamline Specifications

Monochromator	Plane-grating monochromator
Wavelength Range	9-600 nm
Resolution	$E / \Delta E$ = 1000
Experiments	Angle-resolved ultraviolet photoemission spectroscopy

Electric Field of Coherent Synchrotron Radiation Generated Using Laser Bunch Slicing Technique

I. Katayama[1], H. Shimosato[2], M. Bito[2], K. Furusawa[2], M. Adachi[3, 4], M. Shimada[5], H. Zen[3, 4], S. Kimura[3, 4], N. Yamamoto[6], M. Hosaka[6], M. Katoh[3, 4] and M. Ashida[2, 7]

[1]*Interdisciplinary Research Center, Yokohama National Univ., Yokohama 240-8501, Japan*
[2]*Graduate School of Engineering Science, Osaka University, Toyonaka 560-8531, Japan*
[3]*UVSOR, Institute of Molecular Science, Okazaki 444-8585, Japan*
[4]*GraduateUniversities for Advanced Studies (SOKENDAI), Okazaki 444-8585, Japan*
[5]*High Energy Accelerator Research Organization (KEK), Tsukuba 305-0801, Japan*
[6]*Graduate School of Engineering, Nagoya University, Nagoya 464-8603, Japan*
[7]*PRESTO JST, Tokyo 102-0075, Japan*

Terahertz region has been attracting much attention in the viewpoints of solid-state physics, chemistry, and even biology, because its energy scale is of fundamental importance for the phenomena occurring at or slightly below the room temperature. Recent development of the ultrashort laser technology enables us the generation and detection of phase-locked terahertz waves, which is now applied to the coherent spectroscopy such as terahertz time-domain spectroscopy, and nonlinear terahertz spectroscopy. Especially, the nonlinear terahertz spectroscopy was difficult before the invention of recent laser-based terahertz technologies [1], which requires intense and tunable terahertz light sources.

Coherent terahertz synchrotron radiation (CSR) is a promising light source for such nonlinear terahertz spectroscopy because it potentially has ultrahigh power, and the spectrum can be tuned from broadband to monochromatic in low-terahertz region [2]. In UVSOR, we recently demonstrated generation of CSR by applying the laser bunch slicing technique [2, 3]. However, the electric field detection of the CSR from laser bunch slicing has not been realized. In this report, we show that the electric field of CSR can be observed by using electro-optic sampling method, and that the longitudinal density profile of electron bunches can be characterized by using the electric field waveform [4].

We used a large mode-area photonic-crystal fiber to deliver the probe pulses to the detection port from the laser systems for the laser bunch slicing. The output of the seed oscillator was sent through the fiber and then compressed to about 180 fs by using a grating-pair compressor. The probe and CSR were focused on an electro-optic crystal (ZnTe), and the polarization rotation due to the CSR electric field was detected with electro-optic sampling method.

By using this method, it becomes possible to measure the electric field of the terahertz pulses as shown in Fig. 1(a). The observation of the pulsed electric field means that phase of the CSR is indeed very stable, which is a promising characteristic for the coherent nonlinear terahertz spectroscopy. The Fourier transform of the waveform is in good agreement with the FTFIR measurement of the same radiation at the same port [3, 4].

Because the generated CSR reflects the longitudinal density profile of the electron bunch, we can estimate it from the observed electric field profile. Fig. 1(b) is the result of such calculation, illustrating the formation of a dip structure in the electron bunch. We reproduced the symmetric structure of the dip expected in the theory [3], and showed that the duration of the dip depends on the duration of the slicing laser pulse [4].

In summary, we have demonstrated the electric field detection of the CSR generated by using the laser bunch slicing technique. From the observed electric field waveform, it becomes possible to estimate the longitudinal density distribution of electron bunches. Therefore, the technique demonstrated in this study is promising for monitoring bunch profiles, as well as for coherent terahertz spectroscopy using CSR.

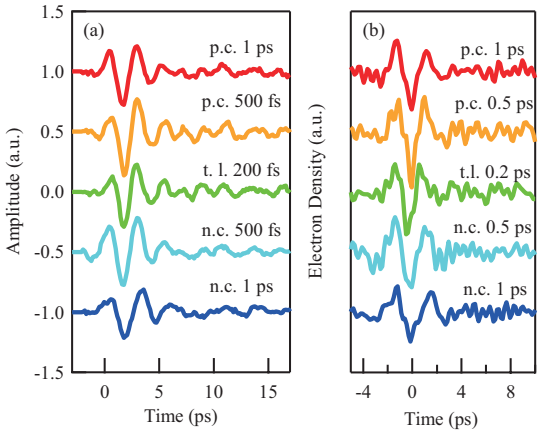

Fig. 1. (a) Observed electric field waveforms of the CSR generated with various pulses of different chirp and pulse durations: p.c.: positive chirp, t.l.: transfer limited and n.c.: negative chirp. (b) Reconstructed electron density profile of electron bunches.

[1] I. Katayama *et al.,* Phys Rev. Lett. **108** (2012) 097401.
[2] S. Bielawski *et al.,* Nat. Phys. **4** (2008) 390.
[3] M. Shimada *et al.,* Jpn. J. Appl. Phys. **46** (2007) 7939.
[4] I. Katayama *et al.*, Appl. Phys. Lett. **100** (2012) 111112.

Generation of Polarized Gamma Rays by Laser Compton Scattering

Y. Taira[1, 2], M. Adachi[3], H. Zen[3], N. Yamamoto[1], M. Hosaka[1], K. Soda[1] and M. Katoh[3]
[1]*Graduate School of Engineering, Nagoya University, Nagoya 464-8603, Japan*
[2]*The Japan Society for the Promotion of Science, Chiyoda-ku, Tokyo 102-8472, Japan*
[3]*UVSOR, Institute for Molecular Science, Myodaiji-cho, Okazaki 444-8585, Japan*

Gamma rays with excellent features can be generated via laser Compton scattering (LCS [1]), where incident laser photons are scattered by a relativistic electron beam circulating in an electron storage ring. LCS gamma rays are tunable in energy, quasi-monochromatic, intense, and highly polarized. Highly polarized gamma rays can be generated via LCS because gamma rays preserve polarization of an incident laser. Circularly polarized gamma rays are used in development polarized positron beam for future electron-positron linear colliders and solid state physics using magnetic Compton scattering. Linearly polarized gamma rays are used in nuclear science.

In this paper, we have demonstrated that the spatial image of the polarized gamma rays is reflected in the polarization effect and have evaluated the degree of linear polarization of LCS gamma rays.

The point of collision between the electron beam and the laser was in a vacuum chamber along a straight section. Linearly and circularly polarized laser was injected into the electron beam from the horizontal 90-degree direction. The polarization was controlled by a wave plate. The spatial profile of the gamma rays was recorded with an imaging plate (BAS-IP MS) located 5.4 m away from the collision point.

Figures 1 and 2 show the spatial images of LCS gamma rays generated by linearly (horizontal direction) and circularly polarized laser, respectively. For the linear polarization, the root mean square (rms) of the LCS gamma rays is 0.245 mrad and 0.300 mrad along the horizonrtal (x) and vertical (y) direction, respectively. For the circular polarization, the rms of the LCS gamma rays is 0.294 mrad and 0.261 mrad along the x and y direction, respectively.

The spatial distribution was calculated using a Monte Carlo simulation code, EGS5. In this simulation, the divergence, and spatial distribution of the electron beam were included in the calculation. The rms of the linearly polarized gamma rays is 0.227 mrad and 0.282 mrad along the x and y direction, respectively. The divergence is lower along the horizontal direction due to polarization effects. The rms of the circularly polarized gamma rays is 0.261 mrad and 0.230 mrad along the x and y direction, respectively. The divergence is lower along the vertical direction due to spatial distribution of the electron beam.

We also calculated the spatial distribution of LCS gamma rays with different degree of linear polarization. The degree of linear polarization of LCS gamma rays shown in Fig. 1 was found to be further than 88 % by comparing the ratio of the rms along the x and y directions between the experimental data and calculated values.

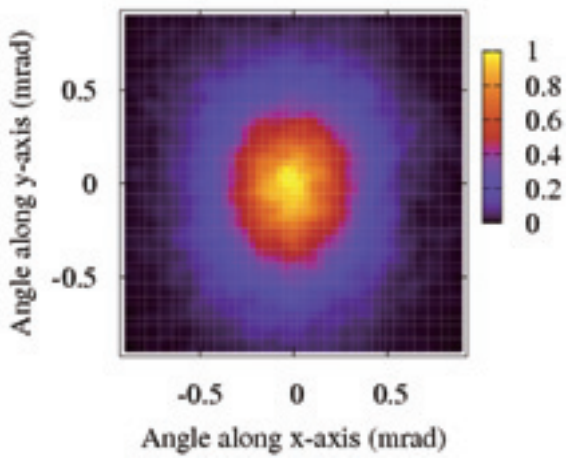

Fig. 1. Spatial image of LCS gamma rays generated by linearly polarized laser.

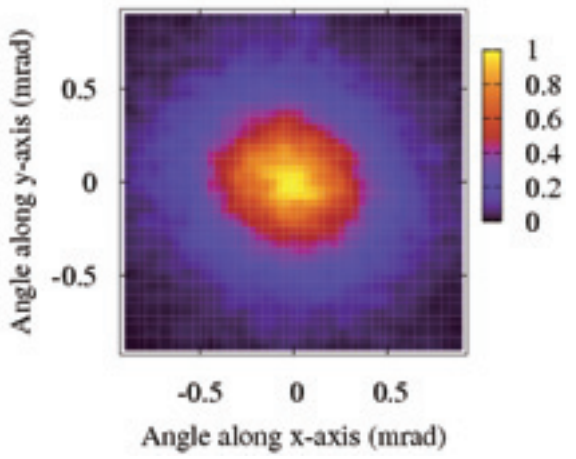

Fig. 2. Spatial image of LCS gamma rays generated by circularly polarized laser.

[1] J. Stepanek, Nucl. Instr. and Meth. A **412** (1998) 174.

Consideration on Using Higher Harmonics of Ti:Sa Laser for Coherent Harmonic Generation at UVSOR

N. Wasa[1], M. Hosaka[2], Y. Uematsu[1], S. Sekita[1], N. Yamamoto[2], Y. Takashima[1, 2], M. Adachi[3], H. Zen[3], S. Tanaka[3] and M. Katoh[3]

[1]*Graduate School of Engineering, Nagoya University, Nagoya 464-8603, Japan*
[2]*Nagoya University Synchrotron Radiation Research Center, Nagoya 464-8603, Japan*
[3]*UVSOR, Institute for Molecular Science, Myodaiji-cho, Okazaki 444-8585, Japan*

Development of new coherent light sources using a relativistic electron beam and laser is underway at the UVSOR storage ring. We have already succeeded in generation of coherent synchrotron radiation (CSR) in THz region [1] and coherent harmonic generation (CHG) [2]. So far fundamental wave of a mode-lock Ti:Sa laser is employed as a seed for the CHG experiment. In parallel with those experiments, we are considering using high harmonics of the laser as a seed for the CHG experiment and made numerical calculations and basic experiments.

CHG is a method to produce coherent harmonics of laser light by using a relativistic electron beam and an optical klystron type undulator. With increasing harmonic number of the CHG, the conversion efficiency rapidly decreases and therefore short-wavelength coherent light is difficult to obtain. On the other hand, if higher harmonics of the laser is applied for the seed, the harmonic number can be much reduced and generation of shorter wavelength coherent light up to soft-X ray region can be expected. In order to evaluate the effectiveness, we made numerical calculations. The spectral intensity of CHG is approximately expressed using the CHG form factor f_n as:

$$P_{CHG}(n) \approx N f_n P_{Sp}(n),$$

where N is number of electrons interacted with the laser and $P_{Sp}(n)$ is spectral intensity of incoherent spontaneous radiation. As CHG spectral intensity is proportional to the form factor, we estimate efficiency of the CHG via the form factor. Figure 1 shows calculated form factor as a function of the harmonic number of the fundamental laser (not of the seed laser) under various conditions of the seed laser [3]. Parameters of electron beam from UVSOR-II storage ring and of the new optical klystron are employed in the calculation. For 2nd and 4th harmonics generation, we assume 200 μJ pulse energy and 100 fsec-FWHM pulse width, which can be provided by harmonic generation with a nonlinear crystal. For 15th harmonics of laser, we assume the high harmonic is produced with Gas and much reduced pulse energy of 5 μJ. As seen in the figure, 2nd and 4-th harmonics of laser has advantages in producing coherent light in the VUV and soft X-ray region over fundamental wave and 15-th harmonics.

We performed experiment to deduced conversion efficiency and properties of the 2nd harmonics from non-linear crystal. No-linear crystals of BBO of thickness of 0.1 mm, 0.5 mm, 1 mm and 2 mm are irradiated by a mode-lock Ti:Sa laser with 2.5 mJ pulse energy and 100 fsec. The measured efficiency of 2nd harmonics is around 50 % for crystals with thickness more than 0.5 mm. We constructed a compact auto-correlator system to measure pulse width of the 2nd harmonics [4]. Slightly increase of pulse width is observed in the second harmonics, but degradation to the peak power is small. We also measured spectra of the 2nd harmonics using the crystals and conclude that 0.5 mm thickness BBO is the most suitable for our CHG experiment.

Near future we plan to make the CHG experiment using 2nd harmonics of the Ti:Sa laser. We also plan to make basic experiment on production of 3rd and 4th harmonics for the CHG experiment.

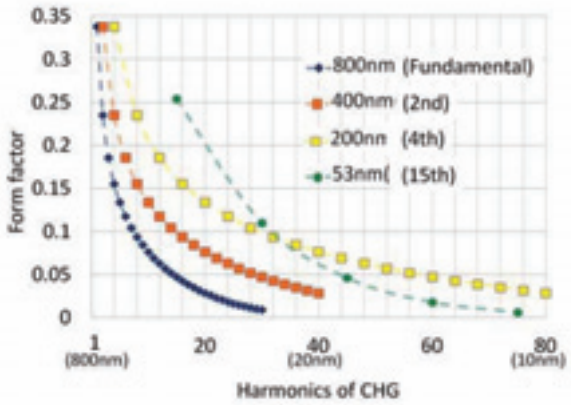

Fig. 1. Calculated CHG form factor as a function of harmonic number.

[1] M. Shimada *et al.*, Phys. Rev. Lett. **103** (2009) 144802.
[2] M. Labat *et al.*, Phys. Rev. Lett. **101** (2008) 164803.
[3] N. Wasa, Master's Thesis, Nagoya University (2012).
[4] S. Sekita, Graduation Thesis, Nagoya University (2012).

Chirality Formation of Amino Acids by Circularly Polarized UV Irradiation

P. K. Sarker[1], J. Takahashi[2], Y. Obayashi[1], T. Kaneko[1], K. Kobayashi[1] H. Mita[2], J. Takahashi[3], K. Matsuo[4], M. Hosaka[5], M. Adachi[6], H. Zen[6] and M. Kato[6]

[1]*Department of Chemistry and Biotechnology, Faculty of Engineering, Yokohama National University, Yokohama 240-8501, Japan*

[2]*NTT Microsystem Integration Laboratories, Atsugi 243-0198, Japan*

[3]*Faculty of Engineering, Fukuoka Institute of Technology, Fukuoka 811-0295, Japan*

[4]*Hiroshima Synchrotron Radiation Center, Hiroshima University, Higashi-Hiroshima 739-0046, Japan*

[5]*Graduate School of Engineering, Nagoya University, Nagoya 464-8601, Japan*

[6]*Institute for Molecular Science, Okazake 444-8585, Japan*

Science obtaining the first evidence of extraterrestrial amino acids in a carbonaceous chondrite (*e.g.*, Murchison meteorite), a great number of laboratory experiments have been reported to study possible abiotic formation of bioorganic compounds including amino acids and their precursors from possible astrophysical media by irradiation with high-energy particles [1] or ultraviolet (UV) light [2]. It is plausible that considerable number of organic compounds, including amino acids and their precursors, were brought to primitive planets by micrometeorites (MMs), comets, and interplanetary dust particles (IDPs). Moreover, amino acids in several meteorites (*e.g.,* Murchison, Murray, Orgueil) have been found to have L-enantiomeric excess, the same handedness as observed in some biological amino acids. Therefore, it has been suggested that life on Earth was seeded by the delivery of organic compounds from outer space during the intense bombardment period of the primitive Earth [3]. On the other hand, the origin of homochirality in terrestrial biological molecules (dominant L-body amino acids and D-body sugars) remains an unresolved important problem in the study for the origins of life. One of the most attractive hypotheses for the origin of homochirality is nominated as "Cosmic Scenario"; some chiral impulses from asymmetric excitation sources in space triggered asymmetric reactions on the surfaces of such space materials as meteorites or interstellar dusts. According to this scenario, the enantiomeric excesses in terrestrial amino acids can be advocated that asymmetric reactions of complex organic molecules including amino acid precursors were induced by circularly polarized light (CPL) from synchrotron radiation (SR) source in space prior to the existence of terrestrial life. Recently, a wide-field and deep near-infrared circularly polarized light has been observed in the Orion nebula, where massive stars and many low-mass stars are forming [4]. This observation results strongly support the "Cosmic Scenario" with CPL in space for the origin of homochirality in terrestrial bioorganic compounds.

Currently, ground simulation experiments for the extraterrestrial scenario by using CPL from SR facilities as a simulating polarized energy source is being conducted. Aqueous solutions of DL-isovaline (Ival), DL-histidine (His) and DL-5-ethyl-5methylhydantoin (EM-Hyd, a precursor of Ival) were irradiated with UV-CPL at 215 nm from an free electron laser source of UVSOR-II (IMS, Japan). Now, the circular dichroism (CD) spectra of the UV-CPL irradiated compounds are being measured at the beamline-15 of Hiroshima Synchrotron Radiation Center (HiSOR, Hiroshima University, Japan).

After UV-LCPL and UV-RCPL irradiation of His, Ival and EM-Hyd, no D- and L-excess was observed (Fig. 1), although very small D- and L-excess was investigated by high performance liquid chromatography. As it is very difficult to examine the asymmetric photodecomposition of UV-CPL irradiated amino acids in aqueous state, we are now planning to enlarge their enantiomeric excess (e.e.) which will be investigated in near future.

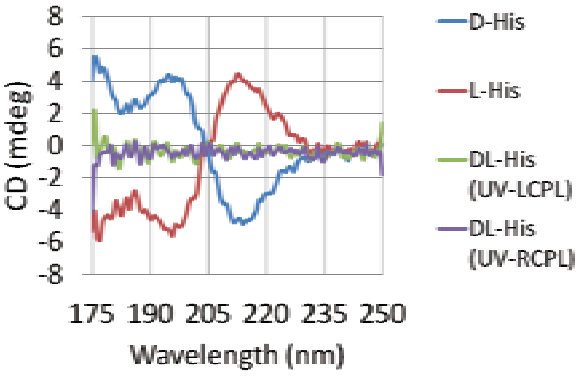

Fig. 1. CD spectra of non-irradiated and irradiated (UV-CPL) Histidine.

[1] K. Kobayashi *et al*., Adv. Space Res. **16** (1995) 21.
[2] P. de Marcellus *et al.*, Astrobiology **11** (2011) 847.
[3] J. Bailey, Orig. Life Evol. Biosph. **31** (2001) 167.
[4] T. Fukue *et al.*, Orig. Life Evol. Biosph. **40** (2010) 335.

BL1B: A Dedicated THz Coherent Synchrotron Radiation Beamline

S. Kimura[1, 2], E. Nakamura[1], K. Imura[1], M. Hosaka[3], T. Takahashi[4] and M. Katoh[1, 2]

[1]*UVSOR Facility, Institute for Molecular Science, Okazaki 444-8585, Japan*

[2]*School of Physical Sciences, The Graduate University for Advanced Studies (SOKENDAI), Okazaki 444-8585, Japan*

[3]*Synchrotron Radiation Research Center, Nagoya University, Nagoya 463-8603, Japan*

[4]*Research Reactor Institute, Kyoto University, Kumatori, Osaka 590-0494, Japan*

Infrared (IR) and terahertz (THz) spectroscopies have now become conventional methods for the measurement of vibration modes and low-energy electronic structures. IR/THz synchrotron radiation (SR) is also used as a light source for spectroscopy and microscopy throughout the world. So far, many advanced types of spectroscopy have been developed such as IR imaging, pressure-dependent and magnetic-field-dependent THz spectroscopy, and so on. However, to realize further advances in spectroscopy, intense tunable light sources must be developed. One candidate for an intense broadband THz source is coherent synchrotron radiation (CSR). Then we planned to construct a dedicated beamline for THz coherent radiation at BL1B.

A top view of the THz beamline is shown in Fig. 1. The emitted THz light is collected by a three-dimensional magic-mirror (3D-MM, M0) of the same type as those already successfully installed at BL43IR in SPring-8 [1] and BL6B in UVSOR-II [2]. The 3D-MM was installed in the bending-magnet chamber and is controlled by a 5-axis pulse motor stage (x, z translation; θ_x, θ_y, θ_z rotation). To extract the emission at 34 degrees, the 3D-MM is located at the short distance of 55 mm from the electron orbit. The 3D-MM is made of aluminum and was fabricated by an NC length milling machine at the Equipment Development Center of Institute for Molecular Science. The surface roughness is less than ±1 μm, which is comparable to the visible wavelength but much smaller than the wavelength of THz light. Visible light is scattered by the surface of the 3D-MM, but THz light can be focused.

To eliminate the heat load from the SR, we employed a copper rod (6 mm in diameter) with water cooling on the emission plane because the power from the SR is concentrated in the emission plane.

The 3D-MM, which is located 880 mm from the center of the source, reflects the THz-CSR to the focal point (F0) on the outside of the bending-magnet chamber, as shown in Fig. 1 (1200 mm from M0). The THz-CSR collected by the 3D-MM is intercepted by a plane mirror (M1) located in the bending-magnet chamber and guided to the beamline. The focal point (F1) is located on the outside of the bending-magnet chamber through a tapered z-cut quartz window (24 mm in diameter and 5 mm thickness at the center). After F1, the light is formed into a parallel beam by a parabolic mirror (M1) and guided to the outside of the radiation shielding wall. The emitted THz-CSR and normal THz-SR light are measured by a Martin-Puplett type Fourier transform interferometer (FARIS-1, JASCO ltd.) installed. Reflection and transmission measurements can be performed in the beamline.

[1] S. Kimura *et al.*, Nucl. Instrum. & Meth. Phys. Res. A **467-468**, (2001) 437.
[2] S. Kimura *et al.*, Infrared Phys. Tech. **49** (2006) 147.

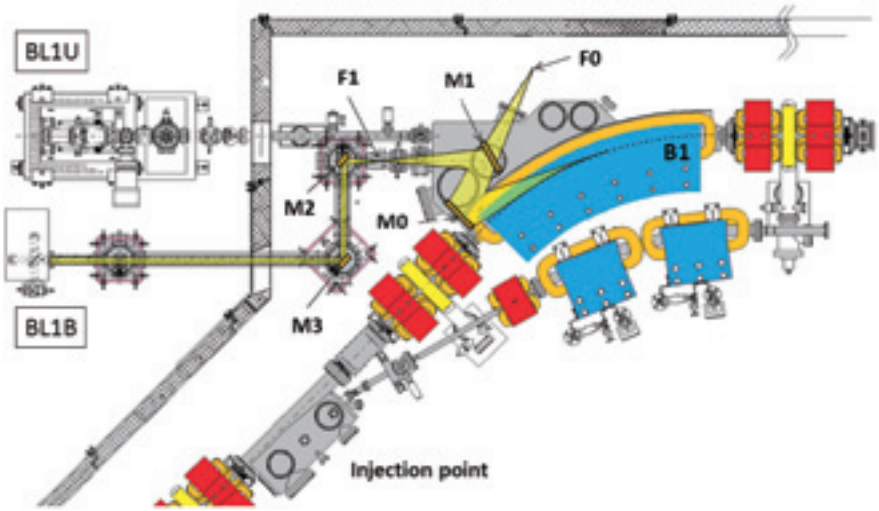

Fig. 1. Schematic top view of the beam extraction part of the THz-CSR beamline, BL1B. The three-dimensional magic mirror (3D-MM, M0) and a plane mirror (M1) are located in the bending-magnet chamber. A parabolic mirror (M2) is installed to form a parallel beam. The straight section (BL1U) is used for coherent harmonic generation (CHG) in the VUV region.

Present Status of a New VIS-VUV Photoluminescence Beamline BL3B

K. Fukui[1], Y. Imoto[1], M. Kitaura[2], K. Nakagawa[3], T. Ejima[4], E. Nakamura[5], N. Kondo[5], M. Sakai[5], M. Hasumoto[5] and S. Kimura[5]

[1]*Fac. Engi., Univ. Fukui, Fukui 910-8507, Japan*
[2]*Fac. Sci., Yamagata Univ., Yamagata 990-8560, Japan*
[3]*Grad. Sch. Human Dev. Enviro., Kobe Univ., Kobe 657-8501, Japan*
[4]*IMRAM, Tohoku Univ., Sendai 980-8577, Japan*
[5]*UVSOR facility, Institute for Molecular Science, Okazaki 444-8585, Japan*

The solid-state optical devices in ultraviolet (UV) region will bring dramatic improvements in not only the telecommunication applications but also the illuminating, environmental and medical applications. To achieve both technological and scientific investigations on such industrially important materials, the light sources which cover a wide photon energy region from visible (VIS) to vacuum ultraviolet (VUV) are required. In order to study photoluminescence (PL) of such materials in the VIS-VUV regions, a new bending-magnet beamline BL3B with a 2.5 m normal incidence monochromator (NIM) has been constructed. For the PL measurements in the wide energy region from VIS to VUV, two PL monochromators, one covers the VIS – UV regions and the other VUV region, are equipped.

The schematic layout of the BL3B which mainly consists of a 2.5 m off-plane Eagle-type monochromator is shown in Figs. 1(a) and 1(b). The actual parameters of the mirrors and gratings are listed in Table 1. The design concept has been reported in the previous report [1]. Fig. 2 shows the throughput using a Si photodiode (IRD AX-UV100), with S1 (entrance slit) = S2 (exit slit) = 100 μm. Fig. 3 shows the beam spot profile at the sample position (Q in Figs. 1(a) and 1(b)) using the G2 grating (at ~12 eV) with S1 = S2 = 100 μm. The FWHM of this spot is 0.25 mm (V) × 0.75 mm (H). The present status of the BL3B is as follows: photon energy coverage range: 1.7 ~ 31 eV, E/ΔE > 12000 (G1, ~ 7 eV), 0.8 ~ 2.8 × 10^{10} photons/s (E/ΔE ≈ 1000, G3), beam size (at Q) 0.25 mm (V) × 0.75 mm (H).

Table 1. Actual parameters of the mirrors and gratings.

Pre-mirrors	Incidence angle	Radius (mm)	Dimension (mm)	Coat
M0	85°	∞ (plane)	110 × 300	Au
M1	88.1°	77360 × 32300 (toroidal)	210 × 280	Au
M2	87°	∞ (plane)	30 × 440	Au

Gratings	Deviation angle	Radius (mm)	Dimension (mm)	Coat	Grooves (mm^{-1})
G1	4°	2500	40 × 110	Au	1200
G2	4°	2500	40 × 110	Pt	600
G3	4°	2500	40 × 110	Al	300

Post-mirrors	Incidence angle	Radius (mm)	Dimension (mm)	Coat
M3	82°	9390	40 × 400	Au
M4	86.49°	17890	50 × 270	Au

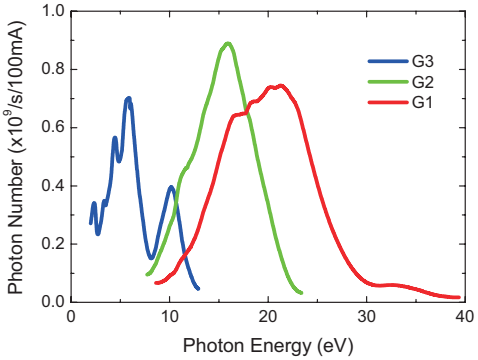

Fig. 2. Throughput from the off-plane Eagle type normal incidence monochromator beamline on BL3B.

[1] R. Ikematsu, K. Fukui, T. Ejima, E. Nakamura, M. Hasumoto and S. Kimura, UVSOR Activity Report **38** (2011) 44.

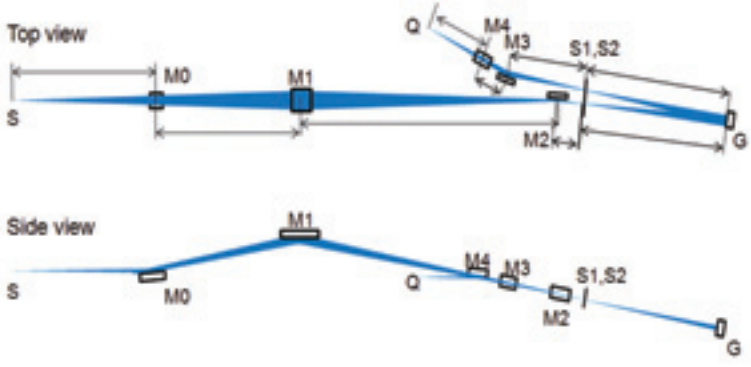

Fig. 1. Schematic layout of the BL3B: top view and side view.

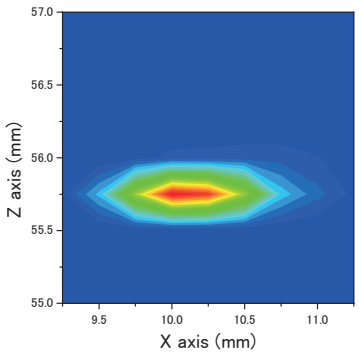

Fig. 3. Beam spot profile at the sample position [the point Q in Figs. 1(a) and 1(b)].

BL3B

Estimation of High Energy Limit of the 2.5 m Normal Incidence Monochromator Constructed at BL3B by Reflectivity Measurements

Y. Imoto[1], S. Watanabe[2], M. Kitaura[3], K. Fukui[1], K. Nakagawa[4], T. Ejima[5], E. Nakamura[6], M. Sakai[6], M. Hasumoto[6] and S. Kimura[6]

[1]*Department of Electric and Electronics Engineering, University of Fukui, Fukui 910-8507, Japan*
[2]*EcoTopia Science Institute, Nagoya University, Nagoya 464-8603, Japan*
[3]*Department of Physics, Faculty of Science, Yamagata University, Yamagata 990-8560, Japan*
[4]*Graduate School of Human Development and Environment, Kobe University, Kobe 657-8501, Japan*
[5]*IMRAM, Tohoku University, Sendai 980-8577, Japan*
[6]*UVSOR facility, Institute for Molecular Science, Okazaki 444-8585, Japan*

The 2.5-m normal incidence monochromator for the photoluminescence spectroscopy was newly constructed at the BL3B beamline. This monochromator was designed to cover the photon energy range from 2 eV to 30 eV. It is necessary to evaluate whether the monochromator works as expected or not. We have investigated the actual high-energy limit of this monochromator through the reflectivity measurements of alkaline and alkali-earth halides. It is well known that these materials exhibit the sharp peaks in the vacuum ultraviolet region spectra [1, 2]. These sharp peaks are due to the absorption of the cation's n*p* core excitons (n = 2-5). An observation of such core exciton peaks is expected to be an indication to grasp the high-energy limit that can be measured with a monochromator.

The single crystals of alkali and alkali-earth halides were cleaved in air, and quickly placed in a vacuum. The samples were attached at the cold finger of a liquid helium flow-type cryostat, and cooled down at 10 K. Both incident and reflected light were detected using a calibrated silicon photodiode sensor in the measurement chamber. The incident and reflected angles were fixed to be 15° for the direction perpendicular to the surface of samples.

Figure 1 shows the reflectivity spectrum of a $PbCl_2$ single crystal measured in the 5-30 eV range. There are three peaks between 21-25 eV, and the feature of these peaks is seen at two places in the low energy side. Since these values are about one half and one third, this result shows that the higher-order light has been observed, which was also observed with KCl single crystal. Therefore, we need to note the higher-order light, especially in the G1 and G2 grating regions.

Figure 2 shows the reflectivity spectrum of a MgF_2 single crystal measured in the 50-60 eV range. One can see two peaks split by 0.34 eV, which are of Mg 2*p* core excitons. From this result, the higher side limit of the photon energy coverage is set to be at least 55 eV at present.

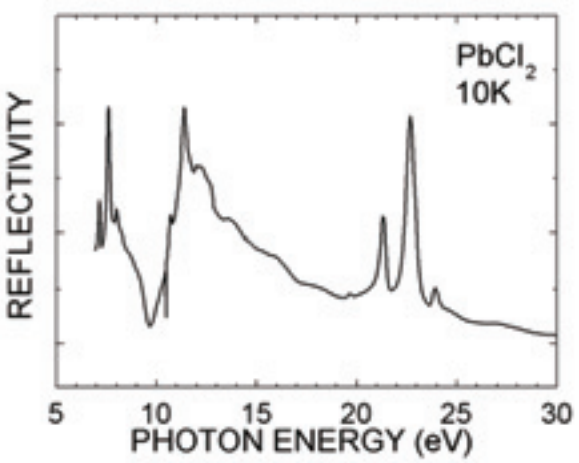

Fig. 1. Reflection spectrum of a $PbCl_2$ single crystal measured at 10 K.

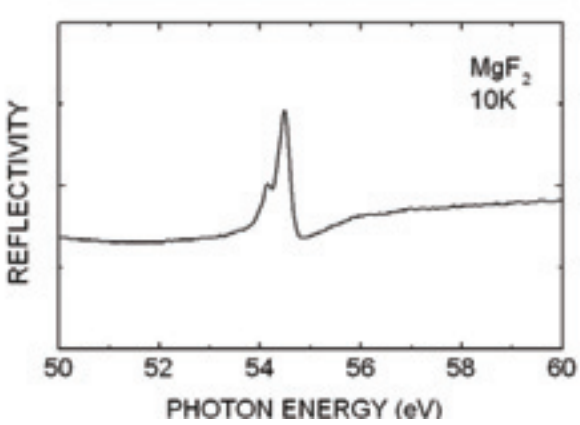

Fig. 2. Reflection spectrum of a MgF_2 single crystal measured at 10 K.

[1] G. W. Rubloff, Phys. Rev. B **5** (1972) 662.
[2] O. Aita *et al*., Phys. Rev. B **93** (1989) 10266.

Many thanks to Prof. M. Itoh (Shinshu Univ.) for providing alkali and alkali-earth halides single crystals.

Scanning Transmission X-ray Microscope Project at BL4U

T. Ohigashi[1], T. Araki[2], E. Nakamura[1], N. Kondo[1], E. Shigemasa[1], N. Kosugi[1] and M. Kato[1]
[1]*Institute for Molecular Science, Okazaki 444-8585, Japan*
[2]*TOYOTA Central R&D Labs., Inc. Nagakute Aichi 480-1192, Japan*

The soft x-ray spectroscopy gives plenty of information about the electronic structure of materials containing low Z elements and metals. By analyzing the photoabsorption and photoionization cross section near the soft X-ray absorption edges in detail, the chemical states of molecules and solids can be determined. Since a high brilliant soft X-ray source and advanced focusing optical elements have progressed in recent years, several microscopic methods have been combined with soft X-ray spectroscopy, such as XAFS (X-ray Absorption Fine Structure) and XPS (X-ray photoelectron spectroscopy), to obtain the 2-dimentional (2D) mapping of the chemical states with high spatial resolution. A scanning transmission X-ray microscopy (STXM) combined with XAFS is one of the promising tools in the soft X-ray spectroscopy.

In the STXM system, the incident X-rays are focused onto the sample by using a focusing optical element, such as a Fresnel zone plate (FZP), and the intensities of the transmitted X-rays through the sample are monitored by using a detector. By scanning the sample, the 2D mappings are obtained. The advantages of the STXM are the high penetrating power and the non-destructive property of the X-rays. That enables the STXM to apply to rather thick and/or rather radiation-sensitive samples in comparison with the electron-based microscopy. Therefore, even the 3-dimensional structural analysis of the sample can be performed by using the tomographic technique without any destructive process. The high penetrating power of the X-rays also allows us to observe the sample in air or wet condition (*i.e.* the vacuum is not necessary). Especially, the soft X-ray energy region from 282 to 540 eV, between the K edges of carbon and oxygen, is called the “water window” region. By using the X-rays in this energy region, carbon-based samples in water, such as living cells, can be observed without any staining. The STXM could be a unique technique to observe a living biological sample like cells in water with high resolution. Thanks to these features, the STXM has advantages over the electron microscopy and the optical one.

In 2011, the STXM beamline project has been launched with the upgrade project from the UVSOR-II ring to the UVSOR-III ring. A schematic image of the beamline is shown in Fig. 1. The soft X-ray source of the BL4U is equipped with an in-vacuum undulator. This undulator has 26 magnetic periods and the period length of 38 mm pitch and its gap width can be set from 13 to 40 mm. The monochromator is a Monk-Gillieson type with a varied line spacing plane grating. The energy range from 100 to 700 eV is available. The theoretical resolving power (E/ΔE) is 10000 at a maximum. In practical use for spectromicroscopy, the resolving power of 2000~4000 will be routinely utilized. The fixed exit slit is used as a virtual source of the focusing optics of the STXM (the third Bruker system following SLS and BESSY) and the FZP is placed at 1334 mm downstream from the slit. Two focusing FZPs of different pattern materials are in preparing. One is made of gold supported by Si_3N_4 membrane of 100 nm thick, and the other is made of hydrogen silsesquioxane (HSQ) supported by Si_3N_4 membrane of 50 nm thick. Their calculated efficiencies of +1 order diffraction including the absorption by the support membranes are plotted against the photon energy in Fig. 2. These plots show that better efficiencies are available by using the HSQ FZP for the carbon K-edge (around 285 eV) and the gold one for the oxygen K-edge (around 540 eV), respectively.

Operation of the BL4U is due to start in the end of 2012. Carbon nanotube will be used as a first reference sample to estimate the characteristics of the beamline; spectral resolution, spatial resolution, and polarization of the monochromatized radiation.

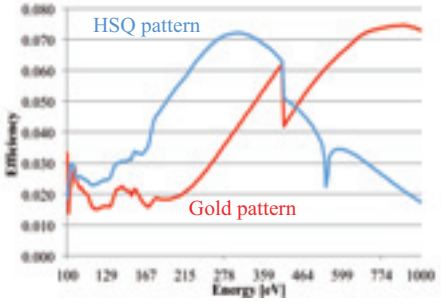

Fig. 2. Calculated efficiencies of the Fresnel zone plates of gold pattern and HSQ pattern.

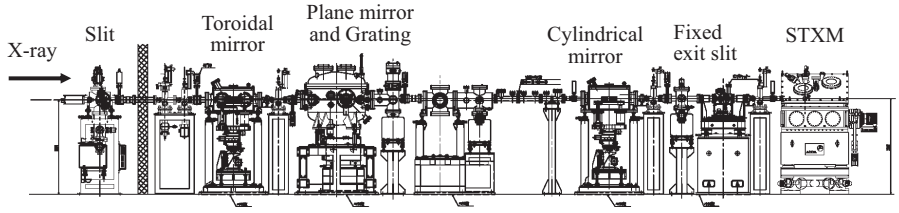

Fig. 1. Schematic image of the optical system of BL4U

BL7B

Measurement of Transmissivity and Ghost Image Created by Ly-Alpha Filters for CLASP Slit-Jaw Unit

M. Kubo[1], Y. Katsukawa[1], N. Narukage[2], R. Kano[1], T. Bando[1], T. Kobiki[1], R. Ishikawa[1] and S. Tsuneta[1]

[1]*National Astronomical Observatory of Japan, Osawa, Mitaka, Tokyo 181-8588, Japan*
[2]*Institute of Space and Astronautical Science, Japan Aerospace Exploration Agency, 3-1-1 Yoshinodai, Chuo-ku, Sagamihara, Kanagawa 252-5210, Japan*

A sounding rocket program called the Chromospheric Lyman-Alpha Spectro-Polarimeter (CLASP) will observe the upper solar chromosphere in Ly-alpha (121.567 nm), aiming to detect the linear polarization signal produced by scattering processes and the Hanle effect for the first time [1,2]. The solar image is focused at a slit by telescope mirrors, and the spectropolarimeter that measures the linear polarization with high accuracy of 0.1% order is located after the slit [3]. The solar image outside the slit is reflected to the slit-jaw unit and is monitored during flight. It is used to confirm the instrument pointing during flight and to obtain Ly-alpha context images for the interpretation of the data obtained by the spectropolarimeter. The images are also needed for co-alignment with other observations.

The slit-jaw unit consists of a fold mirror, a matched pair of off-axis parabolic mirrors, a pair of Ly-alpha narrow band filters, and a CCD detector. The Ly-alpha filter is the key to good quality Ly-alpha images. The prime candidate of the Ly-alpha filter is a 122-XN-1D developed by the Acton Optics & Coatings.

First of all, we have to know the transmissivity of the 122-XN-1D filter and its visible light rejection performance. Figure 1 shows the transmissivity of the 122-XN-1D filter as measured with the synchrotron radiation at the UVSOR BL7B. The transmission profile from 115nm to 200nm is consistent with that provided by the Acton Optics & Coatings, and the transmissivity is 7% in the wavelength of Ly-alpha (121.567nm). We find the transmissivity for the visible light is 0.01%. It is highest visible light rejection performance in the three types of 122nm narrowband filters developed by the Acton Optics & Coatings. From this measurements, we conclude that two 122-XN-1D filters are necessary for the slit-jaw unit to have the visible light contamination less than 1% in the Ly-alpha image.

Another issue on the Ly-alpha filter is a ghost image created by the filters. The ghost images are created by the reflection on the back and front surfaces of a filter and by the reflection between two filters. We take images of a main beam and ghost beams by using CCD camera. We plan to use the two Ly-alpha filters at the angle of incidence (AOI) of 0 degree in the slit-jaw unit. We have confirmed neither unexpected ghost image nor strange pattern created by the two filters at the AOI of 0 degree. Furthermore, we take images at some AOIs of the two filters in order to obtain the intensity ratios of the ghost beams to the main beam (Fig. 2), although it is a different configuration with the filters in the slit-jaw unit. The intensity ratio is less than 4% in every case, which is consistent with the expected value in our investigation of ghost images.

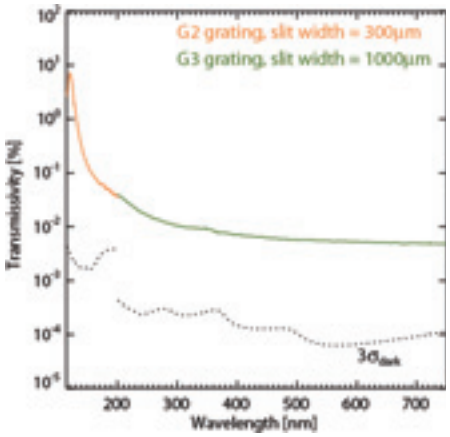

Fig. 1. Transmissivity of the 122-XN-1D filter.

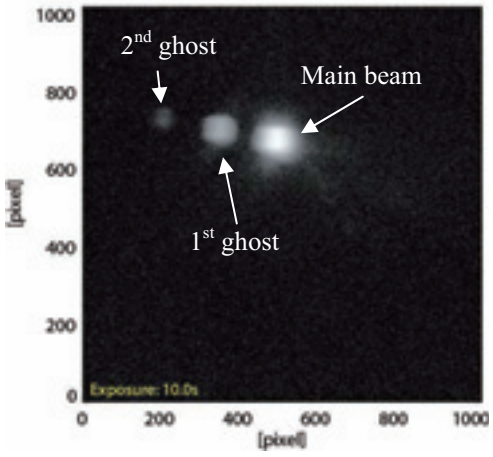

Fig. 2. Main beam and ghost beams created by two Ly-alpha filters at the AOI of 10 degree.

[1] R. Ishikawa *et al.*, ASP Conference Series, **287** (2011) 437.
[2] N. Narukage *et al.*, SPIE, **8148** (2011) 81480H.
[3] H. Watanabe *et al.*, SPIE, **8148** (2011) 81480T.

BL7B

Verifications of CLASP Polarimeter at an Oblique Incidence

R. Ishikawa[1], M. Kubo[1], D. Song[2], N. Narukage[3], T. Bando[1], R. Kano[1], T. Kobiki[1], S. Tsuneta[1] and H. Watanabe[4]

[1]*National Astronomical Observatory of Japan, Osawa, Mitaka, Tokyo 181-8588, Japan*
[2]*Department of Physics and Astronomy, Seoul National University, Gwanak-gu, Seoul 151-742, Korea*
[3] *Institute of Space and Astronautical Science, Japan Aerospace Exploration Agency, 3-1-1 Yoshinodai, Chuo-ku, Sagamihara, Kanagawa 252-5210, Japan*
[4]*Kwasan and Hida observatories, Kyoto University, Yamashina-ku, Kyoto 607-8417, Japan*

A team consisting of Japan, USA, Spain, France, and Norway is developing a high-throughput Chromospheric Lyman-Alpha Spectro-Polarimeter (CLASP), which is proposed to fly with a NASA sounding rocket [1, 2]. CLASP will explore the magnetic fields of the upper chromosphere and transition region via the Hanle effect of the Ly-alpha line (121.567 nm) for the first time. This experiment requires specrtopolarimetric observations with high polarimetric sensitivity (<0.1%) and wavelength resolution of 0.01 nm.

CLASP polarimeter consists of a rotating MgF_2 half-waveplate and MgF_2 polarization analyzers at Brewster's angle [3]. The linear polarization in the Ly-alpha line is measured as the intensity modulation by the rotation of the waveplate. The CLASP polarimeter is located in the converging beam with a cone angle of 3-4 degree. Due to the oblique incidence, the retardation angle (δ) of the half-waveplate slightly deviates from 180 degree. As to polarization analyzer, the purity of s-polarization is reduced and the direction of s-polarization slightly rotates from that for a normal incidence. These effects will appear on the modulation patterns.

We developed a prototype of the CLASP polarimeter in 2010 [4] (Fig. 1). In this time we verified its response to an oblique incidence at the UVSOR BL7B. Using a MgF_2 plate mounted at Brewster's angle, we created a source beam which is highly linearly polarized in the horizontal direction, and the output signal was measured with a silicon photodiode or CCD camera. At a normal incidence, with the waveplate of δ=180 degree and the polarization analyzer at the Brewster's angle, the sinusoidal modulation must be observed as shown in Fig.2 (a). The minimum value in the modulation at a normal incidence is ~0 (comparable to the noise level) as expected [Fig. 2 (b)]. However, when we rotate the whole polarimeter by 3 degree horizontally, the minimum value becomes non-zero. This is due to the incident angle into the analyzer different from Brewster's angle and non-180 degree retardation angle of the waveplate. When we tilt the elevation angle of polarization analyzer by 6 degree (blue arrow in Fig. 1) without rotating the whole polarimeter, the phase is shifted by 3.7 degree from the normal incidence case [Fig. 2 (d)]. This is caused by the change of direction of s-polarization due to the oblique incidence to the polarizer.

Based on this experiment, we investigate the greater detail of the effect of an oblique incidence on the polarimetric observation with <0.1% accuracy, and refine the final design of the CLASP polarimeter.

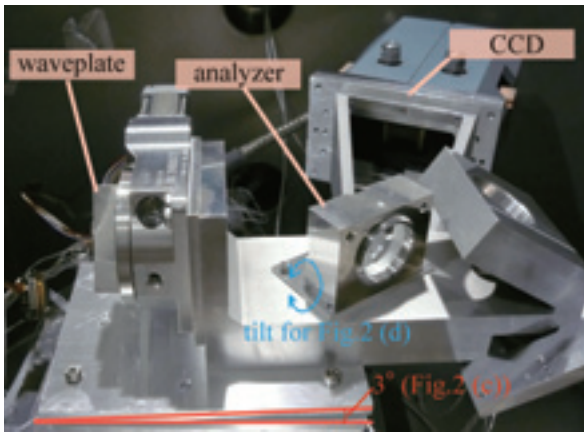

Fig. 1. Prototype of CLASP polarimeter.

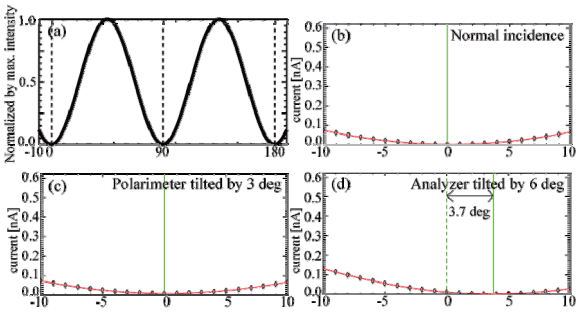

Fig. 2. (a) Ideal modulation in our experiment with normal incidence. Observed modulations around 0 degree at normal (b) and oblique (c, d) incidences. X-axis represents a rotation angle of the waveplate.

[1] R. Ishikawa *et al*., ASP Conference Series, **287** (2011) 437.
[2] N. Narukage *et al*., SPIE, **8148** (2011) 81480H.
[3] H. Watanabe *et al*., SPIE, **8148** (2011) 81480T.
[4] H. Watanabe *et al*., UVSOR Activity Report **38** (2010) 49.

BL2B

Measurement of Kinetic Energies of Fragments Produced by the Photodissociation of C_{70} Using Velocity Map Imaging

H. Katayanagi[1,2] and K. Mitsuke[1,2]

[1]*Dept. of Photo-Molecular Science, Institute for Molecular Science, Okazaki 444-8585, Japan*

[2]*Graduate University for Advanced Studies, Okazaki 444-8585, Japan*

We have developed a photofragment imaging spectrometer suitable for synchrotron radiation excitation of gaseous molecules of refractory materials [1]. Using this apparatus we have observed the scattering distributions of the fragments produced by the photodissociation of C_{60} [2]. We have recently performed a same kind of experiment using C_{70} as a sample [3]. This series of the experiments on the fullerenes is the first attempt of applying our imaging technique to the energetics and dynamics of comprehensive decay chain starting from large clusters.

The experiments were performed at BL2B in UVSOR. Fullerene (C_{70}) powder was loaded in a quartz tube and heated up by an electric heater in vacuum. The C_{70} vapor passed through two apertures and reached the ionization region, where the C_{70} molecular beam (x axis) intersected the monochromatized synchrotron radiation (y axis) at right angles. Ions produced at the ionization region were extracted by a velocity map imaging electrode assembly and projected along z axis on to a position sensitive detector (PSD). Photoelectrons were extracted to the opposite direction to the ions and detected by a microchannel plate detector. Time of flight (t) and arrival position (x, y) of ions on the PSD were recorded using the signal of photoelectrons as a start trigger. Three-dimensional (3D) lists of data, (x, y, t), were thus obtained. Integration of the 3D listdata with respect to x, 2D y-t distributions (y-t maps) were obtained (not shown here, see Ref. 3). Distributions along y-direction on the y-t map with limited t ranges which correspond to mass-to-charge ratios (m/z) of fragments were then extracted. The y-distribution of a fragment is 1D projection of 3D velocity distribution and is converted to a translational temperature.

The translational temperatures were converted to the kinetic energy release (KER) in each C_2 ejection step such as $C_{70-2n+2} \rightarrow C_{70-2n} + C_2$. The values of KER at the nth step of the reaction are shown in Fig. 1. The values of KER are found to be approximately 0.4 eV at 110 eV except for the n=5 (C_{60}^{2+} production) step. The KER for the n=5 step is exceptionally smaller than those for the n=1～4 steps.

We performed an analysis based on the finite-heat-bath theory to interpret the above KER values. The analysis predicts minimum cluster sizes which are detectable in these photon energies and the values of KER for these clusters. Figure 2 shows the theoretical (filled symbols) and experimental (open symbols) values of KER. The theoretical values agreed with the experimental values if we assume the excess energy in the parent ion is smaller by 15 eV than the maximum available energy. This shift can be ascribable to the energy of photoelectrons. In Fig. 2 we can recognize that C_{60}^{2+} fragments are produced with small kinetic energy release, in contradiction to theoretical predictions. This may suggest that other fragmentation mechanisms are involved in the formation of C_{60}^{2+}.

We are now improving this apparatus to be applicable to functional materials such as carbon nanotubes and ionic liquids, which are indispensable in the development of renewable energy technology.

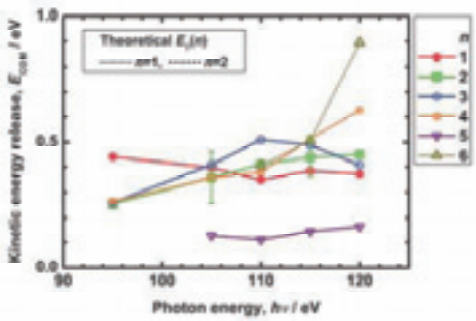

Fig. 1. Excitation photon energy dependence of average KER generated at the n-th reaction step to produce C_{70-2n}^{2+}. Error bars show the uncertainty caused in the fitting procedure.

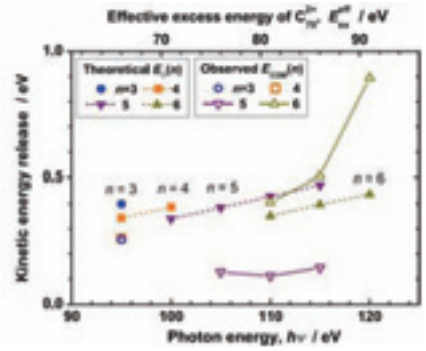

Fig. 2. Theoretical (filled symbols) and experimental (open symbols) kinetic energy release generated at the nth reaction step.

[1] Md. S. I. Prodhan *et al.*, Chem. Phys. Lett. **469** (2009) 19.

[2] H. Katayanagi and K Mitsuke, J. Chem. Phys. **133** (2010) 081101.

[3] H. Katayanagi and K. Mitsuke, J. Chem. Phys. **135** (2011) 144307.

BL2B

Dissociative Photoionization of Perfluorocyclobutane Studied by Mass-Resolved Photoion Imaging

K. Okada[1], T. Nakashima[1], Y. Fukuoka[1], A. Suemitsu[1], H. Katayanagi[2, 3] and K. Mitsuke[2, 3]

[1]*Department of Chemistry, Hiroshima University, Higashi-Hiroshima 739-8526, Japan*

[2]*Institute for Molecular Science, Okazaki 444-8585, Japan*

[3]*School of Physical Sciences, The Graduate University for Advanced Studies (SOKENDAI), Okazaki 444-8585, Japan*

Molecular photoionization and ionic fragmentation processes are of fundamental importance in the upper-atmospheric chemistry and plasma physics. Perfluorocyclobutane (*c*-C_4F_8) is extensively used as a reagent for dry etching of semiconductors. The accurate knowledge of its chemical processes is required to evaluate the role in the upper atmosphere. In our previous study [1] we have reported yield spectra of the fragment ions of *c*-C_4F_8 in the photon energy range of 25–170 eV. Measurements by use of a photoelectron–photoion–photoion coincidence (PEPIPICO) technique were also conducted to study the breakdown pathways. From coincidence islands found in the PEPIPICO spectra, several deferred charge separation processes were identified.

This study is a continuation of the previous report. We particularly focus on the kinetic energy of CF_2^+ to get more insight concerning the dissociation energetics of the *c*-C_4F_8 system.

The experiments have been performed on the beamline BL2B at the UVSOR facility. The experimental setup has been described in a previous paper [1]. Arrangement of the electrostatic lens system employed in this study was described in Ref. [2]. The photoions traveling through the flight tube were detected with a position sensitive detector (Quantar Technology, 3394A). Position signals of the photoion arrival were fed into a multi-parameter data acquisition system (FAST ComTec, MPA) together with photoelectron signals for triggering the real time clock. The list of a data set (*x*,*y*,*t*) was stored in a personal computer as a list-mode file. The data were acquired at the excitation energies of 40.0, 55.0, 60.0 and 80.0 eV. A series of time-of-flight (TOF) spectra were also measured separately while scanning the photon energy in the range of 35–55 eV.

The upper panel of Fig. 1 depicts a typical *y*–*t* map of the photofragment ions, measured at the excitation energy of 40.0 eV. It is obtained by integrating the (*x*,*y*,*t*) data with respect to *x*. The ion counts are displayed in color. Intense bar-shaped spots with different lengths can be found in the map. The length reflects the departing velocity of each fragment ion. Summation of the counts of the map over all *y* yields a familiar TOF spectrum. The resulting spectrum is given in the lower panel of Fig. 1, being in perfect agreement with the previous measurement [1].

We found that for the CF_2^+ ion the bar length depends on the photon energy. The velocity distribution of the ion was derived from the signal counts of the *y*–*t* map over the time range corresponding to the CF_2^+ peak. The kinetic energy at the half-maximum intensity is 1.7 times as high in the 60.0-eV data as in the 40.0-eV data. This result can be qualitatively understood in such a way that with increasing the photon energy the CF_2^+ ion is released with higher kinetic energy due to a lighter ion forming at an early step of the fragmentation mechanism.

More detailed analysis of the imaging data is in progress and the results will be published in the near future.

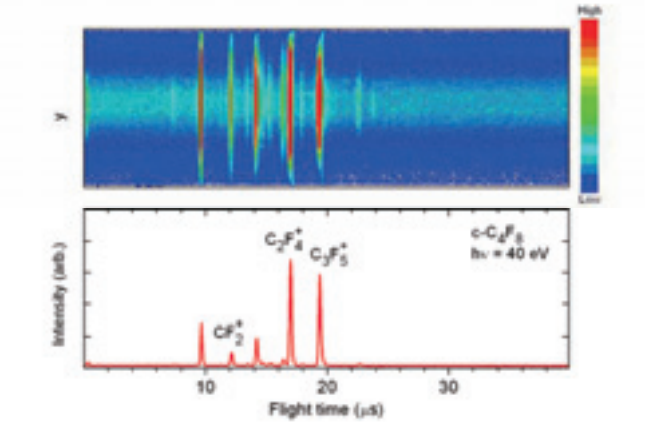

Fig. 1. A typical *y*–*t* map of the photofragment ions of *c*-C_4F_8 acquired at 40.0 eV (the upper panel) and its corresponding TOF spectrum (the lower panel). On the *y*–*t* map the signal counts are plotted as a function of the arrival time *t* and the *y* coordinate of the position on the ion detector. Summation of the counts over the whole *y* gives the TOF spectrum.

[1] K. Okada, T. Nakashima, M. Sakai, A. Suemitsu, C. Huang, H. Yagi, H. Katayanagi, K. Mitsuke and K. Tabayashi, J. Phys. Conf. Ser. **288** (2011) 012021.

[2] H. Katayanagi and K. Mitsuke, J. Chem. Phys. **133** (2010) 081101.

BL3U

Development of a Novel Nozzle for Probing Large Molecules in Vacuum Chamber by Photoelectron Spectroscopy

T. Gejo[1], T. Tajiri[1], K. Honma[1], M. Nagasaka[2] and N. Kosugi[2]
[1]*Univ. of Hyogo, Koto 3-2-1, Kamigori-cho, Hyogo 678-1205, Japan*
[2]*Institute for Molecular Science, Okazaki 444-8585, Japan*

The liquid water has been regarded as fundamental material and has been investigated for many years. Particularly interest is the hydrogen network in liquid water, which were investigated by many spectroscopic studies. Since then, many models have been proposed. Recently, in order to investigate the electronic states of liquid water with hydrogen networks, photoelectron spectroscopy and soft x-ray emission spectra have been investigated. To obtain those spectra, liquid phase in vacuum chamber is necessary. Therefore, liquid water beam technique [1] has been employed.

For this experimental, we have developed the device that utilizes ultrasonic atomization to produce a dense aerosol microdroplet of water. The ultrasonic atomization technique has been used for generate the microdroplets in mist: The size of liquid droplets was distributed around the micrometer scale. Therefore one can achieve micro droplet of liquid water in vacuum chamber by the injecting them directly.

The experiments were carried out on the undulator beamline BL3U at the UVSOR facility in IMS. The experimental set-up consists of three parts: a mist generation part, a transportation part and a nozzle. The microdroplets are generated via ultrasonic atomization. Ultrasonic oscillators (HM2412, Honda Electronics Co., Ltd) operating at 2.4 MHz were installed at the bottom of the water bath. The micro droplet were carried by Ar and pumped out to obtain a stable stream. Figure 1 shows the picture of the stream of mist. A 0.5 mm diameter nozzle hole has been placed just before pumping system and the leaked microdroplet go into the vacuum chamber. After the skimmer, 100 eV VUV photons have been radiated to the microdroplets and the photoelectron spectra has been measured by SIENTA installed.

The water molecule has C_{2v} symmetry with electronic configuration $1a_1 2a_1 1b_2 3a_1 1b_1$. $1a_1$ and $2a_1$ orbitals correspond to the oxygen 1s and 2s orbitals. $1b_1$ and $3a_1$ valence orbitals are mainly responsible for the O-H bond. The $1b_1$ valence orbital is the lone pair orbital with almost pure O 2p character.

Figure 2 shows the photoelectron spectra of water when the ultrasonic atomization apparatus was on and off. Three major peaks arise from $1b_2$, $3a_1$ and $1b_1$ electronic states. Although a small peak due to large cluster of water can be found at 87 eV kinetic energy region, two spectra are almost identical, which suggests that the generation of microdroplets was quite few in comparison with the water molecule. This is presumably due to low conductance of the nozzle, which prevent the microdroplets to pass without condensation.

We are planning a modified nozzle, in which pulsed valve with high conductance and high repetition rate is used.

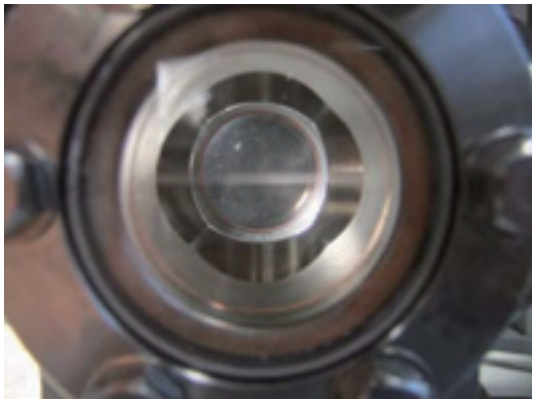

Fig. 1. The picture of mist stream of microdroplets in the view port chamber.

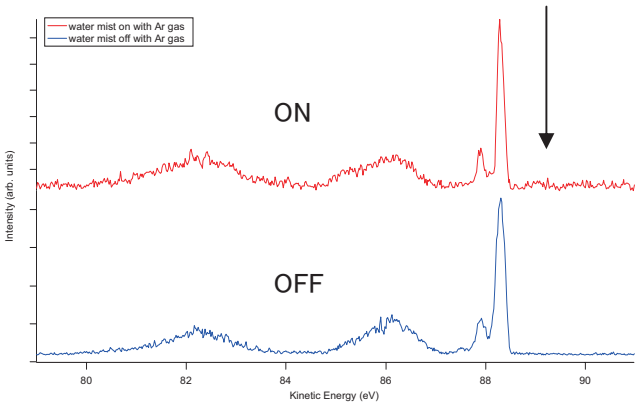

Fig. 2. The photoelectron spectra of water when the ultrasonic atomization is on and off. An arrow shows the peak position due to clusters or microdroplets.

[1] B. Winter *et al*., J. Phys. Chem. A **108** (2004) 2625.

BL3U

Local Structures of Methanol-Water Binary Solutions. I. Oxygen K-Edge Soft X-Ray Absorption Spectra

M. Nagasaka and N. Kosugi
Institute for Molecular Science, Myodaiji, Okazaki 444-8585, Japan

A water molecule has two hydrogen-accepting ('acceptor') and hydrogen-donating ('donor') sites, and liquid water forms three dimensional hydrogen bonding networks. On the other hand, a methanol molecule has one donor and acceptor sites due to a hydrophobic methyl group, and liquid methanol forms one or two dimensional hydrogen bonding networks, such as chains and rings of 6-8 methanol molecules [1]. It is known that methanol-water binary solution shows three dimensional cluster formations by interactions between water and methanol molecules [2]. But the local structures of the methanol-water mixtures are still unknown. X-ray absorption spectroscopy (XAS) is a promising method to investigate the local structure of liquid. Recently, we have developed a liquid cell for the measurements of XAS in a transmission mode [3]. In this work, the local structures of the methanol-water binary solutions at different concentrations were studied by using oxygen K-edge XAS.

The experiments were performed at BL3U. The liquid thin layer was sandwiched between two 100 nm-thick Si_3N_4 membranes (NTT AT Co.). The thickness of the liquid layer was optimized from 50 to 1000 nm by changing the He backpressure [3]. The photon energy was calibrated by the oxygen 1s – π* peak (530.8 eV) of O_2 gas mixture in He.

Figure 1 shows oxygen K-edge XAS spectra of the methanol-water solutions at different concentrations. The previous work observed the peak around 532 eV in the methanol-water mixtures [4], but it is not observed in our measurements. The pre-edge peak (535 eV) corresponds to a transition from oxygen 1s to $4a_1$* unoccupied orbital, which is mainly distributed at the oxygen atom in the water molecule, and reflect the interaction in the hydrogen bonding [5]. The intensities of the pre-edge peaks decrease with the higher mixing ratio of water. The isosbestic points are observed in the pre-edge region, which mean only the contributions of the liquid methanol and water in the XAS spectra. In order to confirm this result, the intensities of the pre-edge regions are plotted with the different concentrations, as shown in Fig. 2. We confirmed that the intensities of the pre-edge regions decrease almost linearly by increasing the mixing ratio of water. It means the interactions around the oxygen atoms in the hydrogen bonding networks are not changed at different concentrations of the methanol-water mixtures. These results suggested that the hydrogen bonding of the CH_3OH-H_2O pair is nearly the same as that of both the H_2O-H_2O and CH_3OH-CH_3OH pairs.

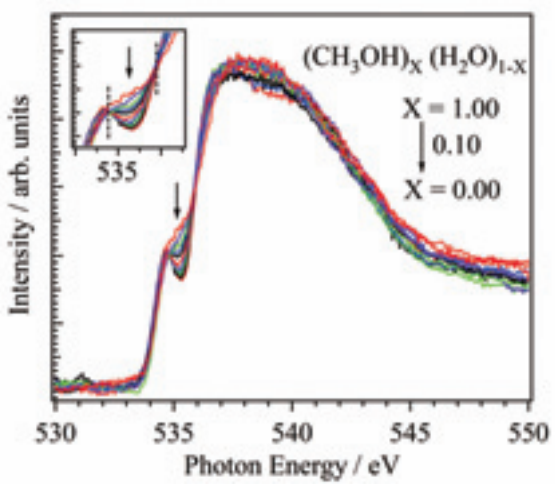

Fig. 1. Oxygen K-edge XAS spectra of the methanol-water binary solutions at the different concentrations at 25 ºC. The mixing ratio of water in the solution is increased along indicated arrows. The inset shows the isosbestic points (dashed lines) in the pre-edge region.

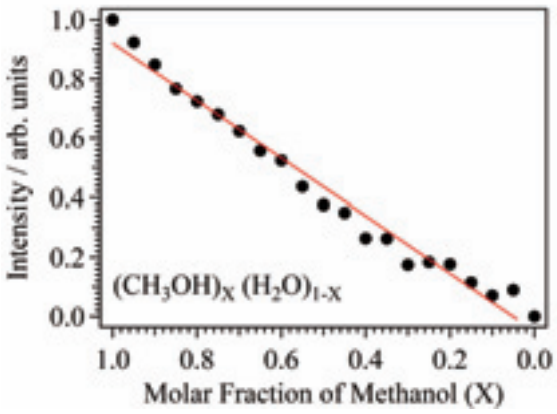

Fig. 2. Intensities of the pre-edge regions as a function of molar fraction of methanol (X) in the methanol-water mixtures $(CH_3OH)_X(H_2O)_{1-X}$. The intensities of methanol and water are normalized to one and zero, respectively.

[1] S. Sarkar and R. N. Joarder, J. Chem. Phys. **99** (1993) 2032.
[2] S. Dixit *et al*., Nature **416** (2002) 829.
[3] M. Nagasaka *et al*., J. Electron Spectrosc. Relat. Phenom. **177** (2010) 130.
[4] J.-H. Guo *et al*., Phys. Rev. Lett. **91** (2003) 157401.
[5] Ph. Wernet *et al*., Science **304** (2004) 995.

BL3U

Local Structures of Methanol-Water Binary Solutions. II. Carbon K-Edge Soft X-Ray Absorption Spectra

M. Nagasaka and N. Kosugi
Institute for Molecular Science, Myodaiji, Okazaki 444-8585, Japan

Oxygen K-edge X-ray absorption spectroscopy (XAS) of methanol-water binary solutions has revealed that hydrogen bonding is not changed at different concentrations [1]. On the other hand, the neutron diffraction studies suggested the formations of three dimensional clusters by interactions between water and methanol molecules [2]. In this work, we have measured carbon K-edge XAS spectra of the methanol-water binary solutions at different concentrations to investigate not only the hydrogen bonding but also the interactions between the methyl groups in the methanol molecules.

The experiments were performed at BL3U. The details of the experimental setups were described previously [3]. The photon energy was calibrated by the first peak (287.96 eV) of methanol gas mixture in He.

Figure 1 shows the carbon K-edge XAS spectra of the methanol-water binary solutions at the different concentrations. Because the carbon atom is contained only in the methanol molecule, carbon K-edge XAS spectra include the core excitations of the methanol molecules. The peak around 288.5 eV is mainly distributed at the hydroxyl group in the methanol molecule, and reflects the hydrogen bonding. The intensity of this peak is not changed so much at different concentrations. It is consistent with the result of the oxygen K-edge XAS, in which the hydrogen bonding is not changed irrespective of the mixing ratios [1]. On the other hand, the peak around 290 eV is mainly distributed at the methyl group in the methanol molecules. This peak is shifted to the higher photon energy by increasing the mixing ratio of water. It means that the methyl groups approach with each other and the interaction between the methyl groups increase. Liquid methanol forms chains or rings of 6-8 methanol molecules [4], and the methyl groups are apart from each other. When the water molecules join the hydrogen bonding networks, three dimensional mixed clusters are formed in the solution, and the distance between the methyl groups becomes small. The intensities of the valleys around 289 eV decrease by the higher photon energy shifts of the peak around 290 eV. Figure 2 shows the intensities of these valleys at the different mixing ratios. The intensities are changed nonlinearly, and are able to separate three regions. The intensities are not changed so much in the region I, where the mixing ratio of water is below 25 %. The intensity suddenly decrease at 25 %, and the slow decrease is continued (II). When the mixing ratio of water exceeds above 70 %, the intensity decrease becomes fast (III). The different growth mechanism of the mixed methanol-water clusters occurs at the different concentrations.

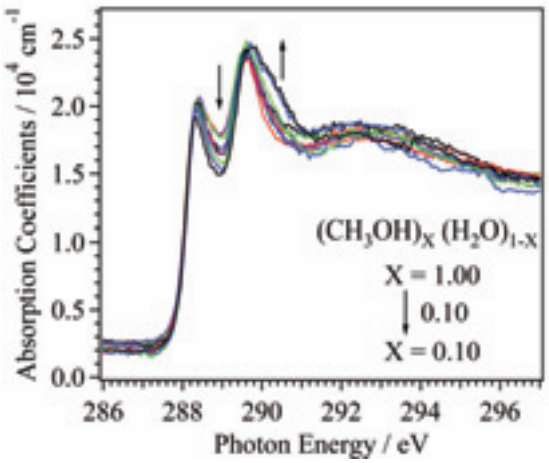

Fig. 1. Carbon K-edge XAS spectra of the methanol-water solutions at different concentrations at 25 ºC. The mixing ratio of water in the solution is increased along indicated arrows.

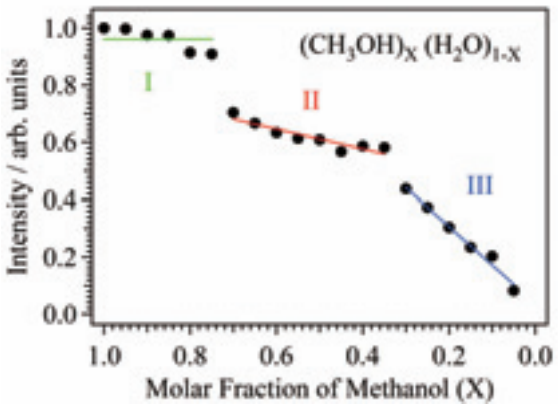

Fig. 2. Intensities of the valleys around 289 eV as a function of molar fraction of methanol (X) in the methanol-water mixtures $(CH_3OH)_X(H_2O)_{1-X}$. The intensities of methanol and water are normalized to one and zero, respectively. Three characteristic regions are found at the different molar fractions.

[1] M. Nagasaka and N. Kosugi, in this volume.
[2] S. Dixit *et al*., Nature **416** (2002) 829.
[3] M. Nagasaka *et al*., J. Electron Spectrosc. Relat. Phenom. **177** (2010) 130.
[4] S. Sarkar and R. N. Joarder, J. Chem. Phys. **99** (1993) 2032.

Absorption Spectra of L-Alanyl-L-Alanine Film from 3 eV to 250 eV

M. Iwai[1], Y. Izumi[2,*], Y. Tanigawa[2], S. Takahara[1], K. Sugiki[2] and K. Nakagawa[1,2]
[1]*Faculty of Human Development, Kobe University, Kobe 657-8501, Japan*
[2]*Graduate school of Human Development and Environment, Kobe University, Kobe 657-8501, Japan*

Absorption spectra of thin films of L-alanyl-L-alanine $C_6H_{12}N_2O_3$ were measured at the photon energy region from 3 eV to 250 eV and discussed in comparison with that of L-alanine.

Powder of L-alanyl-L-alanine was purchased from SIGMA Chemical Company. Thin films of L-alanyl-L-alanine were prepared with vacuum evaporation technique in which heater temperature was set at about 370 K. Collodion films and SiO_2 plates were used as substrate.

Spectral measurement was carried out at the beamlines 3B, 5B and 7B. Photon energy region used for measurements were 3.5 to 37 eV at BL3B and BL7B and 30 to 250 eV at BL5B. Optical density $OD(E)$ was obtained as a function of photon energy E for various samples with different thickness because magnitude of OD(E) around 20 eV was one order larger than that around 90 eV or at higher energies.

Values of absorption cross section $\sigma(E)$ was calibrated around 7 eV for thick films evaporated on SiO_2 substrate, of which $\sigma(E)$ was directly determined by high performance liquid chromatography (HPLC) technique for water solution of the evaporated film.

Because we calibrated the absolute values of $\sigma(E)$ around 7 eV where σ was one order smaller than that around 20 eV, we thought that obtained $\sigma(E)$ values might be erroneous. Thus we used the Tohmas-Reihe-Kuhn sum rule [1] of oscillator strength distribution $df(E)/dE$ in order to calibrate our values of $\sigma(E)$,

$$\int_{E_1}^{E_2} \frac{df(E)}{dE} dE = N_e \quad ,$$

where, N_e is the number of electrons responsible to the optical transition within the photon energy region from E_1 to E_2 . The relation between $\sigma(E)$ and $df(E)/dE$ is known to be

$$\sigma(E)[\mathrm{Mb}] = 1.098 \times 10^2 \cdot \frac{\mathrm{d}\, f(E)}{\mathrm{d}E} [\mathrm{eV}^{-1}] \quad .$$

Since the integration of df/dE yielded the value of N_e to be 84 which is larger than the real number N_e=64, we finally calibrated the $\sigma(E)$ to be multiplied 64/84=0.76.

The calibrated values of $\sigma(E)$ were plotted in the curve A in Fig. 1. In the figure curve B is the $\sigma(E)$ of atomic mixture 6C+12H+2N+3O calculated with the atomic absorption coefficients compiled by Henke[3].

Form the comparison of the curve A , B and C, we can point out following;

(1) Above 30 or 40 eV, experimental spectrum (curve A) is well reproduced by the atomic mixture model (curve B), which means that at higher energies, nature of optical absorption is similar with the atomic mixture.

(2) At lower photon energy region than 30 eV, optical spectrum is of molecular natures.

(3) Clear difference in optical absorption spectrum of L-alanyl-L-alanine appears at 6.3 eV at which energy the peptide bond was reported. No other sharp peaks were found in this work.

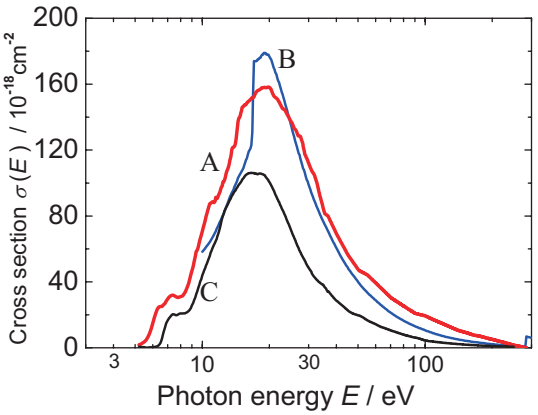

Fig. 1. Absorption cross section spectra $\sigma(E)$ of L-alanyl-L-alanine obtained by experiment (curve A) and by calculation (curve B). Curve C is $\sigma(E)$ of L-alanine reported by Kamohara *et al*. [2].

This work is supported by the Use-of-UVSOR Facility program (2011, 23-817, 23-819, 23-824) of the Institute for Molecular Science.

*Present address: JASRI/SPring-8.

[1] J. O. Hirschfelder, C. F. Curtiss, R. B. Bird, 1954. Molecular Theory of Gases and Liquids. Wiley, New York, p. 890.
[2] M. Kamohara, Rad. Phys. Chem. **77** (2008) 1153.
[3] http://henke.lbl.gov/optical_constants/

BL6U

Ultrafast Molecular Dissociation as a Tool for Dissociative Potential Energy Surface Mapping

R. Guillemin[1], M. N. Piancastelli[1], M. Simon[1], H. Iwayama[2] and E. Shigemasa[2]
[1]*LCPMR, Université Pierre et Marie Curie, 75231 Paris Cedex 05, France*
[2]*UVSOR Facility, Institute for Molecular Science, Okazaki 444-8585, Japan*

In quantum mechanics, potential energy surfaces (PES) are a representation of the structural and dynamical properties of molecular systems. As such, they are essential tool to describe and predict chemical properties and chemical reactivity.

The motivation behind this study is to provide an experimental determination of PES, i.e. the change of potential energy with the inter-atomic distance. A way to achieve this is to perturb the system in such a way that it will respond by a change in geometry, and monitor the spectral variation while the electronic wave packet explores the PES. It was suggested that this could be achieved by electron core excitation and radiative decay monitoring [1]. Recently, it was shown that in the case of bond states, vibrational core excitation provides a way to map PES efficiently [2].

Here, we take advantage of ultrafast dissociation following C 1s core excitation in CF_4 [3] and ultrahigh resolution measurements of the subsequent Auger decay to explore dissociative PES.

The experiment was performed on the soft X-ray beamline BL6U at UVSOR. The radiation from an undulator was monochromatized by a variable included angle varied line-spacing plane grazing monochromator. The photon energy resolution E/ΔE was set to 5000. The monochromatized radiation was introduced into a cell with sample gases. Kinetic energies of the emitted electrons were measured by a hemispherical electron energy analyzer (MBS-A1) placed at a right angle with respect to the photon beam direction. The degree of the linear polarization of the incident light was essentially 100%, and the direction of the electric vector was set to be parallel to the axis of the electrostatic lens of the analyzer. The kinetic energy resolution of the analyzer was set to 60 meV.

Figure 1 (top) shows the absorption spectrum of CF_4 around the $\sigma^*(t_2)$ resonance below the C 1s ionization threshold, and the 2D map of the associated Auger decay spectrum in the region of the participator decay (bottom) as a function of photon energy. The spectrum shows dispersive lines that correspond to the direct photoionization of the valence states of CF_4. These lines are overlapping with the resonant Auger decay of the molecule that can be revealed by subtracting at each photon energy, the direct photoionization lines, as shown in Fig. 2. Two features in this spectrum reveal the dynamics of ultrafast dissociation of the molecule.

On the high-energy side, a non-dispersive electron emission is interpreted as the decay from the core-excited CF_3^* dissociated fragment.

On the low-energy side, the dispersive electron emission shows a large asymmetric tail that reveals the elongation of the C-F bond in competition with the Auger decay. The change of kinetic energy in this dynamical Auger emission correlates directly to the potential energy difference between the PES of the intermediate core-excited state and the PES of the final dissociated ionic state, effectively mapping the PES. Theoretical analysis of the experimental data is underway.

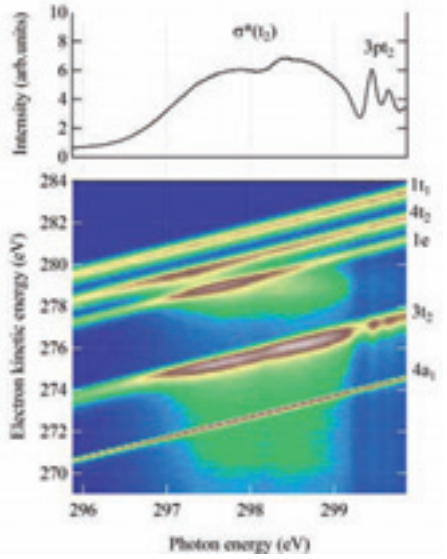

Fig. 1. Full decay spectrum measured at the $\sigma^*(t_2)$ resonance of CF_4.

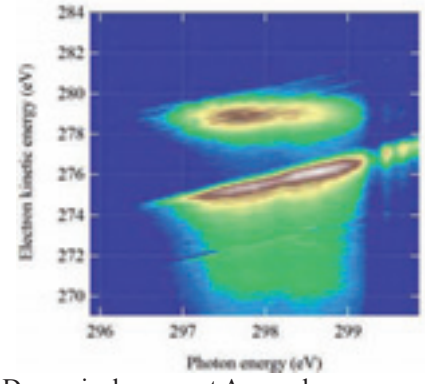

Fig. 2. Dynamical resonant Auger decay.

[1] S. Carniato *et al.*, Chem. Phys. Lett. **439** (2007) 402.
[2] C. Miron *et al.*, Nature Phys. **8** (2011) 135.
[3] K. Ueda *et al.*, Phys. Rev. Lett. **83** (1999) 3800.

BL6U

Ultrafast Molecular Dissociation of Core-Excited HBr Studied by High-Resolution Electron Spectroscopy

E. Shigemasa[1], H. Iwayama[1], K. Soejima[2] and P. Lablanquie[3]
[1]*UVSOR Facility, Institute for Molecular Science, Okazaki 444-8585, Japan*
[2]*Department of Enviromental Science, Niigata University, Niigata 950-2181, Japan*
[3]*LCPMR, Université Pierre et Marie Curie, 75231 Paris Cedex 05, France*

Soft X-ray absorption spectra of molecules exhibit rich structures in the region below the ionization thresholds, which are due to the excitations of a core electron to unoccupied valence or Rydberg orbitals. The core excited states are predominantly relaxed via Auger electron emission, in the case of the molecules composed of light elements, and subsequently fragmentation follows. As demonstrated by Morin and Nenner, however, a fast neutral dissociation could precede the resonant Auger decay [1]. In other words, the electronic decay of the core hole takes place after the constituent atoms come apart. Since then, many research works have been conducted to identify such ultrafast dissociation processes in various different systems. Recent works on high-resolution resonant Auger electron spectroscopy have revealed that the nuclear motion of the molecular core-excited states is promoted in competition with the Auger decay. Here, we revisit the first discovery of ultrafast dissociation following the Br 3d core excitation in HBr [1]. High-resolution electron spectroscopy for the subsequent Auger decay has been applied.

The experiments were carried out on the soft X-ray beamline BL6U at UVSOR. The radiation from an undulator was monochromatized by a variable included angle varied line-spacing plane grazing monochromator. The exit slit opening was set to 300 μm, which corresponds to the photon energy resolution E/ΔE of ~1500 at 70 eV. The monochromatized radiation was introduced into a gas cell with sample gases. Kinetic energies of the emitted electrons were measured by a hemispherical electron energy analyzer (MBS-A1) placed at a right angle relative to the photon beam direction. The degree of the linear polarization of the incident light was essentially 100%, and the direction of the electric vector was set to be parallel to the axis of the electrostatic lens of the analyzer. The energy resolution of the analyzer was set to ~12 meV. Under these experimental conditions, the full width at half maximum of the vibrational fine structure for the X state of HBr^+ was measured to be ~50 meV.

Figure 1 shows the total ion yield spectrum of HBr in the vicinity of the Br 3d ionization threshold. The broad feature centered at around 71 eV is assigned to the 3d → σ* resonance, which has two components $3d_{5/2}$, $3d_{3/2}$ of the initial core hole states. Figure 2 represents a resonant Auger spectrum taken at 70.4 eV, where the $3d_{5/2}$ core-hole states are mainly populated. The vertical scale of the red line spectrum is magnified by the five times. The most marked feature in Fig. 2 is the numerous sharp peaks, due to the vibrational structures for the HBr^+ states and the atomic Auger lines from the Br fragments with a 3d core-hole. In the previous work [1], only five atomic lines indicated by the blue arrows in Fig. 2 have been identified, owing to the limited resolution. In contrast, at least ten more atomic Auger peaks and some molecular peaks with vibrational structures are clearly resolved in the present work. The detailed analyses for the spectral features observed are just beginning to be performed.

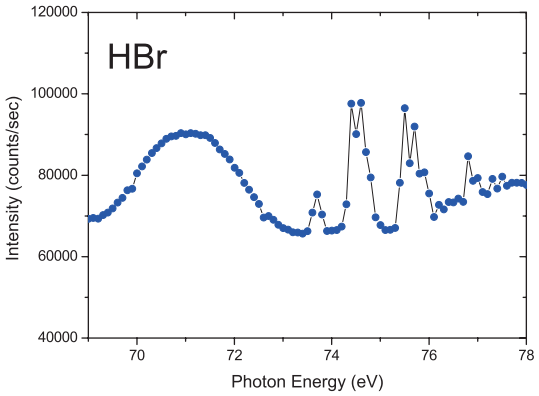

Fig. 1. Total-ion yield spectrum (E/ΔE ~1500) in the Br 3d excitation region of HBr.

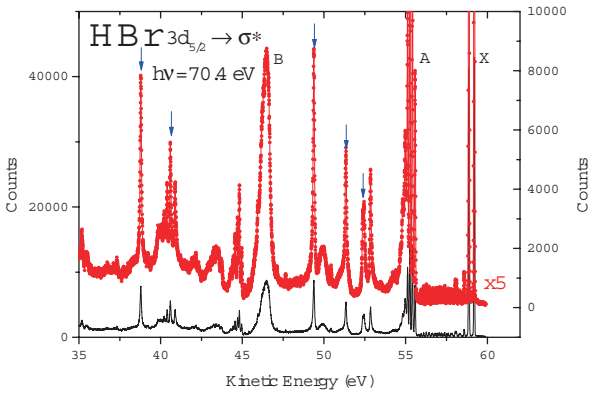

Fig. 2. Resonant Auger spectrum taken at the Br $3d_{5/2}$ → σ* resonance.

[1] P. Morin and I. Nenner, Phys. Rev. Lett. **56** (1986) 1913.

BL6U

Double Auger Decays after 3d Core Ionization or Excitation in HBr Studied by High-Resolution Electron Spectroscopy

P. Lablanquie[1], H. Iwayama[2], K. Soejima[3] and E. Shigemasa[2]
[1]*LCPMR, Université Pierre et Marie Curie, 75231 Paris Cedex 05, France*
[2]*UVSOR Facility, Institute for Molecular Science, Okazaki 444-8585, Japan*
[3]*Department of Environmental Science, Niigata University, Niigata 950-2181, Japan*

Shallow inner shell holes such as 3d in Kr usually decay by emission of a single Auger electron. However, with a probability of ~10%, two Auger electrons can also be released, mainly sequentially [1]. In the HBr isoelectronic molecule, it was found that the molecule can dissociate during this sequential emission of Auger electrons [2]. More precisely, the first emitted Auger electron e_{A1} populates an HBr^{2+} state that dissociates before the second Auger electron e_{A2} is emitted from the Br^{+*} fragment:

$$HBr^{+}(3d^{-1}) \rightarrow HBr^{2+} + e_{A1} \rightarrow H^{+} + Br^{+*}$$
$$\text{followed by: } Br^{+*} \rightarrow Br^{2+} + e_{A2}$$

In this study, we have used a high resolution electron analyser to examine in fine detail these secondary 'atomic' Auger electrons e_{A2}.

The experiments were carried out on the soft X-ray beamline BL6U. The radiation from an undulator was monochromatized by a variable included angle varied line-spacing plane grazing monochromator. The monochromatized radiation was introduced into a gas cell with sample gases. Kinetic energies of the emitted electrons were measured by a hemispherical electron energy analyzer (MBS-A1) placed at a right angle relative to the photon beam direction. The degree of linear polarization of the incident light was essentially 100%, and the direction of the electric vector was set to be parallel to the analyzer axis.

Figure 1 compares the high resolution electron spectrum (in blue) obtained here above the 3d ionization threshold at hν = 90 eV, with the one of reference [2] (red). The latter implied the coincident detection of the associated 3d photoelectron and e_{A1} Auger electron, thus providing an unambiguous identification of the process. It is seen that the present non coincident measurement probes the same process but with a much higher resolution, and demonstrates clearly that the atomic decay involves autoionization of two Rydberg series of Br^{+*} $4p^4(^2D_J)nl$ configurations (with J = 3/2 or 5/2) to the Br^{2+} (^4S) ground state.

Figure 2 shows that the same atomic lines appear also upon excitation of the 3d → σ* resonance. This resonance is well known for the associated ultrafast dissociation producing H and Br* $3d^{-1}4s^24p^6$ fragments. Single Auger decay of this Br* fragment is well documented (see associated Activity Report); the present results demonstrate that double Auger decay of the Br* fragment also occurs.

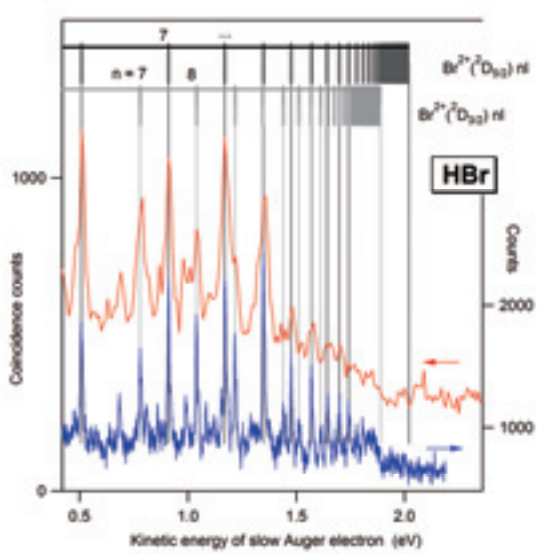

Fig. 1. (blue) High resolution spectrum of low energy electrons measured at hν = 90 eV, and compared to the lower resolution one from reference [2] (red). The energy resolution of the analyzer was set to ~5 meV.

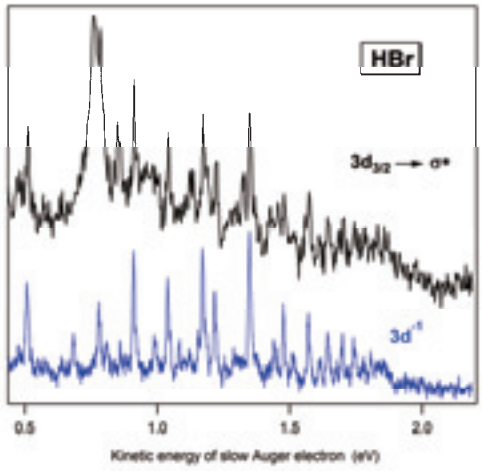

Fig. 2. Comparison of the high resolution electron spectra measured above the 3d threshold (blue, as in Fig. 1) and on the $3d_{3/2} \rightarrow \sigma^*$ resonance at hν = 72 eV.

[1] J. Palaudoux *et al.*, Phys. Rev. A **82** (2010) 043419.
[2] F. Penent *et al.*, Phys. Rev. Lett. **106** (2011) 103002.

BL6U

Doppler Effect in Fragment Autoionization Following Core-to-Valence Excitation of OCS

H. Iwayama and E. Shigemasa
UVSOR Facility, Institute for Molecular Science, Okazaki 444-8585, Japan

When the source and observer are in motion relative to each other, the Doppler effect is known to occur, leading to an apparent change in the observed frequency of the propagating wave. This effect has a wide variety of applications in many fields, relating to the sensing of movement. Since Gel´mukhanov and co-workers predicted in 1997 [1] that the nuclear motion in 'ultrafast dissociation' following molecular core-level photoexcitation can be probed by the Doppler effects in emitted Auger electron, many research works have been conducted. Ultrafast dissociation is a process in which the molecular dissociation at the core-excited state precedes the Auger decay and then an atomic fragment emits an Auger electron [2]. The atomic Auger electron can possess the opposite Doppler shift depending on the direction approaching the detector or moving away from it.

Recently, the electronic Doppler effects after the core-to-Rydberg excitations in N_2 and the core-to-valence excitations in O_2 have been revealed [3,4]. In the present work, experiments for observing the electronic Doppler effects in atomic Auger-electron emissions from S fragments have been performed in the S 2p excitation region of OCS.

The experiment was performed on the soft X-ray beamline BL6U. The radiation from an undulator was monochromatized by a variable included angle varied line-spacing plane grazing monochromator. The photon energy resolution E/ΔE was set to 1000. The monochromatized radiation was introduced into a cell with sample gases. Kinetic energies of the emitted electrons were measured by a hemispherical electron energy analyzer (MBS-A1) placed at a right angle with respect to the photon beam direction. The degree of the linear polarization of the incident light was essentially 100%, and the direction of the electric vector was set to be either parallel or perpendicular to the axis of the electrostatic lens of the analyzer. The kinetic energy resolution of the analyzer was set to 12 meV.

Figure 1 represents the blowup of an atomic Auger line following the ultrafast dissociation [2] in the resonant Auger spectrum obtained at 165.5 eV, where the S $2p_{1/2} \rightarrow \pi^*$ and S $2p_{3/2} \rightarrow \sigma^*$ resonances lie. The observed atomic Auger line clearly demonstrates the Doppler profile, depending on the polarization direction. On the basis of the symmetry-resolved photoion yield spectra [5], the photoion anisotropy parameter β at 165.5 eV can be estimated to be about -0.29. Assuming that the axial recoil approximation is well valid, and the lifetime broadening and instrumental resolution are equal to 65 and 12 meV, respectively, the kinetic energy release in the present study is determined to be about 1.7 eV. The detailed data analysis is now in progress.

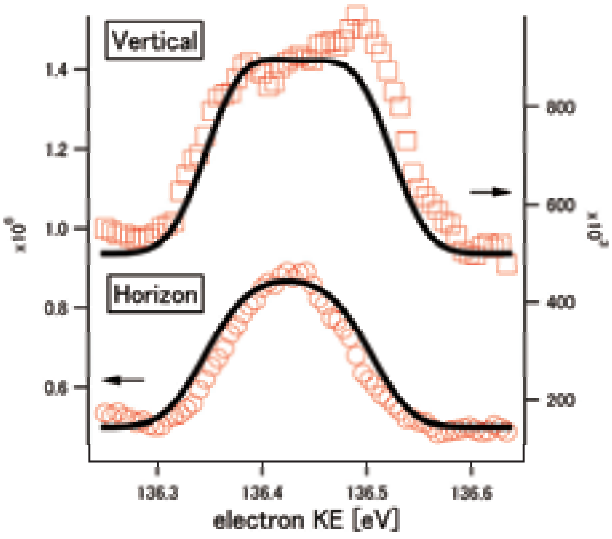

Fig. 1. Doppler profile of atomic Auger line measured at the S $2p_{1/2} \rightarrow \pi^*$ and S $2p_{3/2} \rightarrow \sigma^*$ resonance position of OCS. Solid circles and solid squares in red are experimental data points measured at horizontal and vertical polarization, respectively. Solid lines denote the fitting results.

[1] F. Gel´mukhanov, H. Ågren and P. Sałek, Phys. Rev. A **57** (1998) 2511.
[2] P. Morin and I. Nenner, Phys. Rev. Lett. **56** (1986)1913.
[3] E. Shigemasa *et al.*, New J. Phys. **12** (2010) 063030.
[4] R. Guillemin *et al.*, Phys. Rev. A **82** (2010) 051401(R).
[5] S. Masuda, T. Hatsui and N. Kosugi, J. Electron Spectrosc. Relat. Phenom. **137-140** (2004) 351.

BL6U

Ultrafast Dissociation of Core-Excited OCS Studied by Two Dimensional Electron Spectroscopy and Electron–Ion Coincidence Spectroscopy

L. Ishikawa, H. Iwayama and E. Shigemasa
UVSOR Facility, Institute for Molecular Science, Okazaki 444-8585, Japan

Coincidence detection and correlation analysis among the particles ejected during the relaxation processes of core-excited molecules bring a deeper insight into the molecular inner-shell processes. When both an Auger electron and fragment ions are analyzed in energy, one can give access to the state-to-state dissociation dynamics of the core-excited molecules. In the previous work [1], the correlation between the resonant Auger electrons with their biding energy ranging from 14.5 to 19 eV and subsequent molecular dissociation following the S $2p_{3/2} \rightarrow \pi^*$ excitation of OCS molecules has been investigated. Here, we take advantage of ultrafast dissociation processes following the S 2p core excitations in OCS. Auger-electron–ion coincidence spectroscopy as well as high-resolution 2 dimensional (2D) electron spectroscopy has been applied.

The experiments were carried out on the soft X-ray beamline BL6U. For the 2D electron spectroscopy, the monochromator bandwidth was set to $E/\Delta E$ ~1000 at $h\nu$=165eV. Kinetic energies of the emitted electrons were measured by a hemispherical electron energy analyzer (MBS-A1) placed at a right angle relative to the photon beam direction. The direction of the electric vector was set to be either parallel or perpendicular to the axis of the electrostatic lens of the analyzer. The resonant Auger spectra with kinetic energies ranging from 135 to 155 eV were recorded as a function of the photon energy in the S 2p excitation region.

For the coincidence experiment, the monochromator bandwidth was set to $E/\Delta E$ ~10000 at $h\nu$=165eV. The electrons ejected at 54.7° relative to the electric vector of the light were analyzed in energy by the double toroidal electron analyzer (DTA), while ions were extracted from the interaction region into the momentum spectrometer by a pulsed electric field according to the electron detection. The pass energy of the DTA was set to 100 eV for observing resonant Auger electrons in a binding energy range from 29 to 31 eV. It has been confirmed in the separate experiment that there is a sharp peak due to the atomic Auger line from the core excited S atoms in the corresponding energy region. The coincidence data set was recorded at $h\nu$=165.5 eV, which corresponds to the S $2p_{1/2} \rightarrow \pi^*$ and S $2p_{3/2} \rightarrow \sigma^*$ excitations.

Figure 1 shows the 2D map of resonant Auger electron spectra following the S 2p excitation of OCS measured in horizontal direction. The diagonal lines in Fig. 1 are due to the valence photoelectrons, while the vertical lines seen in the lower kinetic energy region are owing to the atomic Auger lines. The atomic line widths show clear polarization dependence, which may reflect the anisotropic photoexcitation process. According to the symmetry-resolved photoion yield spectra [2], the photoion anisotropy parameter β at 165.5 eV is estimated to be about -0.29. Figure 2 represents the angular distribution of the S^+ ions taken in coincidence with the atomic Auger line. The β value of -0.24 estimated through a fitting procedure is in reasonably good agreement with the above value. This means that the initial molecular orientation induced by photoexcitation is kept in the present case.

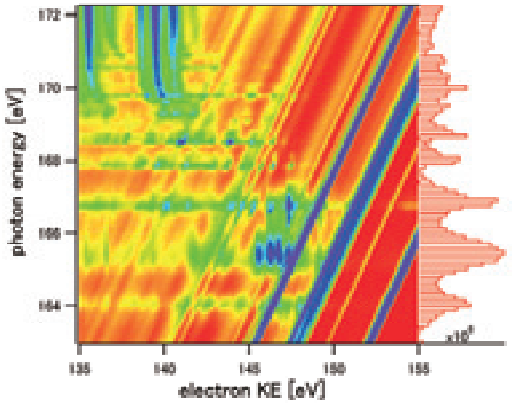

Fig. 1. 2D map of resonant Auger electron spectra following the S 2p excitation of OCS.

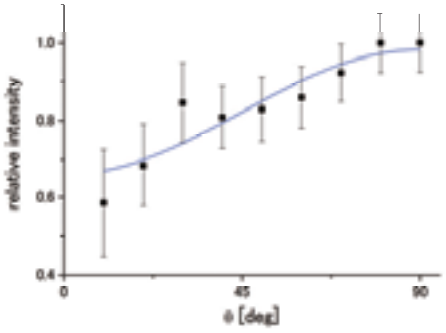

Fig. 2. Angular distributions of S^+ ions taken in coincidence with the atomic Auger electrons.

[1] T. Kaneyasu, M. Ito, Y. Hikosaka and E. Shigemasa, UVSOR Activity Report **34** (2007) 59.
[2] S. Masuda, T. Hatsui and N. Kosugi, J. Electron Spectrosc. Relat. Phenom. **137-140** (2004) 351.

BL5U

Interfacing 2D and 3D Topological Insulators: Bi(111) Bilayer on Bi_2Te_3

T. Hirahara[1], G. Bihlamyer[2], Y. Sakamoto[1], M. Yamada[1], H. Miyazaki[3], S. Kimura[3], S. Blügel[2] and S. Hasegawa[1]

[1]*Department of Physics, University of Tokyo, 7-3-1 Hongo, Bunkyo-ku, Tokyo 113-0033, Japan*
[2]*Peter Grünberg Institut and Institute for Advanced Simulation, Forschungszentrum Jülich and JARA, 52425 Jülich, Germany*
[3]*UVSOR Facility, Institute for Molecular Science, Okazaki 444-8585, Japan*

Topological insulators (TI) are a novel state of quantum matter in three dimensions (3D) that have been gaining increased attention. Along with its two-dimensional (2D) counterpart, the quantum spin Hall (QSH) phase, they are mathematically characterized by the so-called Z_2 topological number [1]. While the bulk is insulating with an inverted gap, there is a metallic edge or surface state which is topologically protected and hence robust against weak perturbation or disorder.

While there have been a large number of reports on 3D TI, only few works have been done in terms of 2D QSH. The most extensively studied system is the HgTe/CdTe quantum well [2]. Another important system predicted to be a 2D QSH is the single bilayer (BL) Bi [3]. But since it is the thinnest limit for a 2D system similar to graphene, it has not been realized experimentally.

In the present research, we succeeded in fabricating a single bilayer of Bi(111) on Bi_2Te_3(111) since they both form in layers with a hexagonal lattice. We have investigated how the surface Dirac cone of Bi_2Te_3 is affected by this Bi termination. Figures 1 (a) and (b) show the band dispersion for the 18 QL (quintuple layer, stack of Te-Bi-Te-Bi-Te) Bi_2Te_3(111) film on silicon and a bilayer of Bi(111) on top of it, respectively, measured by angle-resolved photo-emission spectroscopy. The Dirac cone as well as the bulk conduction/valence bands can be seen in Fig. 1(a). We should note that due to the overlap of the bulk valence band and the Dirac cone near the Dirac point, the photoemission intensity is strongly suppressed near the Γ point. The Dirac cone does not vanish upon Bi adsorption as can be clearly seen in Fig. 1(b), which is a direct evidence that the the Dirac cone is actually robust against nonmagnetic perturbations. However, the intensity at the Dirac point is enhanced and it seems that the Dirac cone has changed its nature. Comparison of the present experimental data with *ab initio* calculations showed that the electronic structure of the Bi/Bi_2Te_3 system can be understood as an overlap of the band dispersions of bilayer Bi and Bi_2Te_3. But whereas the Dirac cone of Bi_2Te_3 is localized at the topmost QL, the Dirac cone in Fig. 1(b) was mostly localized at the topmost Bi and this change induced the change in the experimental observation. Our results show a unique situation where the topologically protected one- and two-dimensional edge states are coexisting at the surface [4].

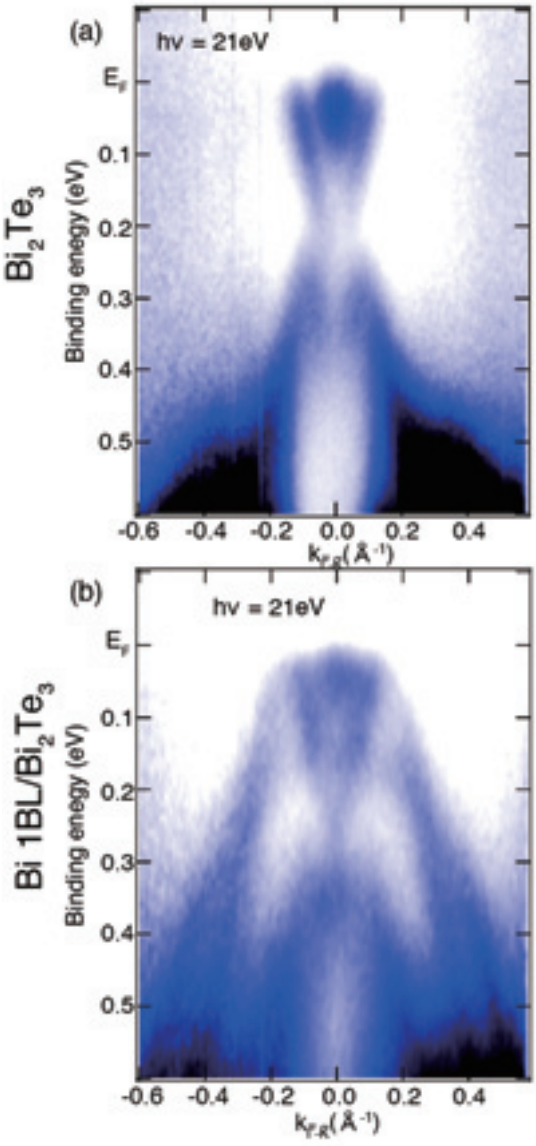

Fig. 1. Band dispersion image of a 18 QL thick Bi_2Te_3 (a), and that for a single-bilayer Bi(111) terminated Bi_2Te_3 (b).

[1] M. Z. Hasan and C. L. Kane, Rev. Mod. Phys. **82** (2010) 3045.
[2] M. König *et al.,* Science **318** (2007) 766.
[3] S. Murakami, Phys. Rev. Lett. **97** (2006) 236805.
[4]T. Hirahara *et al.,* Phys. Rev. Lett. **107** (2011) 166801.

BL3U, BL6U

Polarized NEXAFS Study on Nitrogen Dopant in Rutile TiO_2(110)

Y. Monya[1], M. Nagasaka[2], H. Yamane[2], N. Kosugi[2] and H. Kondoh[1]
[1]*Graduate School of Science and Technology, Keio University, Yokohama 223-8522, Japan*
[2]*Institute for Molecular Science, Okazaki 444-8585, Japan*

Nitrogen doped TiO_2, which is one of most promising visible-light-response photocatalysts, has been extensively studied to understand the mechanism of visible-light-response. Although many structural studies on nitrogen dopants in TiO_2 have been conducted with various techniques, neither site nor chemical state of the nitrogen dopant is clear yet. In this work, we measured polarized NEXAFS spectra for nitrogen-doped rutile TiO_2(110) to elucidate the structure of the nitrogen dopants.

The samples were prepared by heating TiO_2(110) substrates under NH_3 atmosphere. Polarized NEXAFS experiments were performed at BL3U with using the partial electron yield method.

Figure 1 shows O-K edge NEXAFS spectra of rutile TiO_2(110) with different polarization angles. For example, NI [001] indicates that x-ray incidence angle is 90° from the surface parallel and its electric vector is lying along [001] direction (see Fig. 2). In the grazing incidence (GI) geometry, the incidence angle was 30°. For the O-K NEXAFS spectra, we observe seven peaks (a-g) depending on the polarization. Considering the polarization dependence and previous assignments for these peaks [1,2], peaks a, b and d can be attributed to excitations to three unoccupied states: (Ti 3d + O 2pπ), (Ti 3d + O 2pσ) and (Ti 4s + O 2p), respectively. Peaks e and f are assigned to (Ti 4p + O 2pπ and σ). Peaks c and g seem to be associated with of a surface oxygen species shown in Fig. 2. The peak c is attributed to the combination of Ti 3d orbital and O 2p orbital of the surface oxygen species bridging two titanium atoms. Similarly, Peak g is attributed to the combination of Ti 4sp orbitals and O 2p orbital of the same oxygen species.

Figure 3 shows N-K edge NEXAFS spectra of the nitrogen dopants in the rutile TiO_2(110). Here the incidence angle was 15° for GI and 90° for NI. As a result, seven peaks (a'-f' and X) were observed and the peaks a'-f' well correspond to a-f in the O-K NEXAFS with respect to both polarization dependence and the order in energy. The counterpart of peak g is not clearly discernible due to a poor S/N ratio. From these results, the nitrogen dopants in rutile TiO_2 are likely to occupy the lattice oxygen sites via substitution.

It should be noted that peak X appears exclusive in the N-K edge spectra. Based on the results of XPS measured at BL6U and a previous report [3], it is proposed that the nitrogen dopants are in the form of NH. Thus, peak X might be attributed to an excitation to a NH-relating unoccupied orbital. The fact that peak X is enhanced in the GI geometry suggests that the N-H bond is aligned closely along the surface normal.

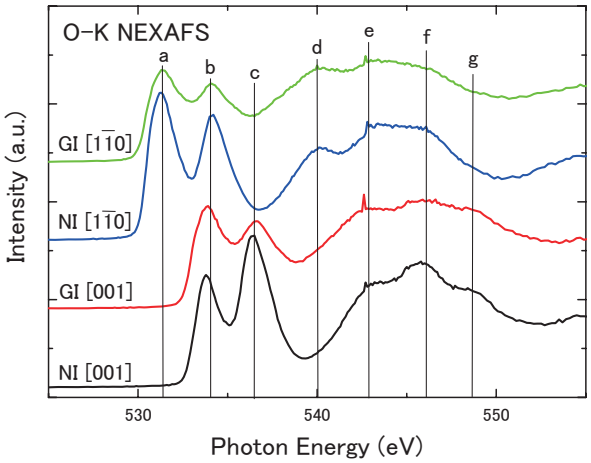

Fig. 1. O-K NEXAFS spectra of rutile TiO_2(110).

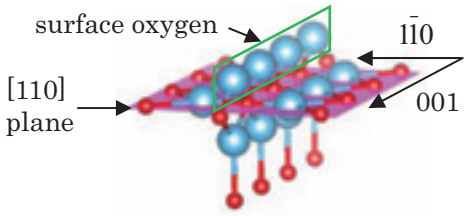

Fig. 2. Rutile TiO_2(110) surface (K. Momma et al., J. Appl. Crystallogr. **44** (2011) 1272.)

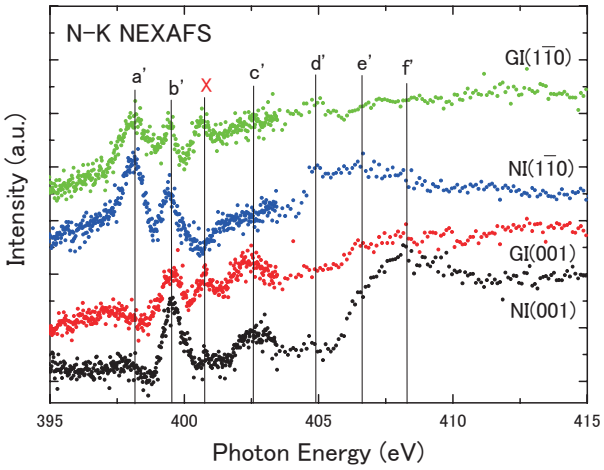

Fig. 3. N-K NEXAFS spectra of nitrogen dopant in rutile TiO_2(110) .

[1] J. G. Chen, Surface Science Reports **30** (1997) 1.
[2] E. Filatova *et al*., Phys. Status Solidi B **246** (2009) No.7, 1454.
[3] Y. Kim *et al*., J. Phys. Chem. C **115** (2011) 18618.

BL3B

Photoionization of Polyaromatic Molecules on the Surface of Ionic Liquids

T. Ishioka, K. Tomita, Y. Imanishi, S. Furukawa and A. Harata

Department of Molecular and Material Sciences, Kyushu University, Kasuga-shi, Fukuoka 816-8580, Japan

Ionic liquids are rapidly expanding topics of research because of their fovorable properties such as high ionic conductivity, negligible vapor pressure, and controllable hydrophobicity. Much effort has been made to understand the unique physical properties of ionic liquids. The dielectric constant is one of them because many theoretical approaches rely on dielectric continuum models.

Recently, some authors reported on bulk dielectric constants of various ionic liquids [1, 2]. However, interfacial property is also important to understand the characteristics of ionic liquid since that is related to many applications such as solvent extraction and batteries. Until now little is known on the interfacial dielectric properties of ionic liquids. Photoionization is a suitable technique for studying interfacial dielectric state because given threshold reflects the solvation energy at the surface. In this report, ionization threshold energies of polyaromotic molecules on various ionic liquids were measured and interfacial properties of ionic liquids are discussed.

Ionic liquids used: 1-butyl-3-methylimidazolium tetrafluoroborate, hexafluorophosphate ([bmim][BF_4] and [bmim][PF_6]), ethylammonium nitrate, and protonated betain bistrifluoromethane sulfonylimide ([Hbet][Tf_2N]) were synthesized as a usual method. Pure water and formamide was used as reference solvents. In a typical photoionization measurement, the light was emitted from the chamber to a He-purged cell through an MgF_2 window. The range of light energy was in 4-8 eV. The emitted light was reflected with an Al mirror and vertically irradiated on the sample surface. High voltage (400V) was applied between the mesh electrode that was 5 mm above the liquid surface and a Pt cell with 25 mm in diameter. Hexane solutions of aromatic molecules (naphthacene, perylene, pyrene) were prepared at the concentration of 10^{-4} M and added dropwisely on the surface of ionic liquids by 200 μL. After evaporation of hexane, the photoinduced current (~ 0.1 pA) was measured by a picoammeter (Keithley model 428).

Measured photoionization spectra were analyzed and threshold values were determined by fitting the spectra to the empirical formula of $I = (E - E_{th})^{2.5}$. Figure 1 shows the obtained photoionization threshold plotted against (1-1/ε), where ε is the relative permittibity of the liquid. The threshold energy lies higher in a vacuum for each aromatic carbon (naphthacene: 6.97 eV; perylene: 6.96 eV; pyrene: 7.43 eV) than in any other solvents because the threshold energy (E_{th}) satisfy the formula in the case of emitting electron into the air,

$E_{th} = I_p + P^+$ and P^+ where I_p and P^+ are the ionization potential and polarization energy of the photoionized molecule, respectively and P^+ is always negative since the polarization is exothermic.

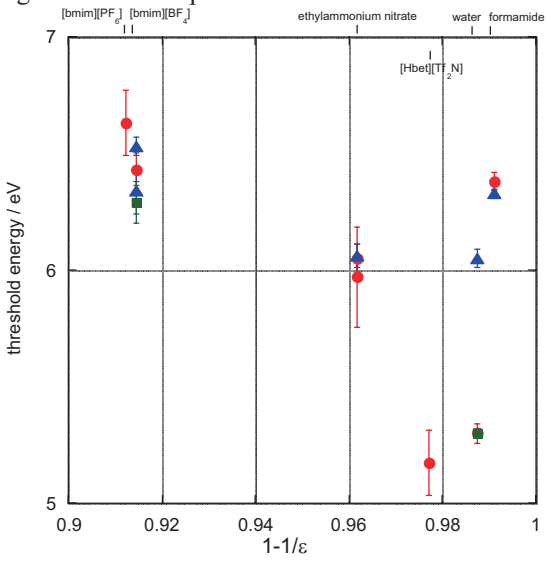

Fig. 1. Measured photoionization threshold plotted against a function of relative permitivity of each solvent. Round, triangle, and square plots are the results for perylene, pyrene, and naphtacene, respectively. Error bars are standard deviation for the measurement (n = 5).

Using Born's theory and making an assumption that each ionized molecule is spherically coordinated by surrounding solvent molecules, the polarization energy has a linear relationship with the value (1-1/ε). However, for some polyaromatic molecules and solvents, the linearity cannot be applied and the absolute polarization energy is far smaller than the value estimated by complete solvation. The result imply that surface polyaromatic molecule is not fully solvated by surrounding ionic liquids. Furthermore, the photoionization threshold of pyrene shows the weakest dependence on the changes of bulk relative permittibity. This result coinsides with our previous report using ionic liquid/water mixture [3] where the photoionization threshold of pyrene has a small dependence on solvent composition. The analysis of the different behavior of polyaromatic molecules at the ionic liquid surfaces are now in progress.

[1] C. Wakai *et al.*, J. Phys. Chem. B **109** (2005) 17028.
[2] I. Krossing *et al.*, J. Am. Chem. Soc. **128** (2006) 13427.
[3] T. Ishioka, N. Inoue and A. Harata, UVSOR Activity Report **36** (2009) 58.

BL4B

Huge Magnetic Anisotropy and Coercivity on Fe/W(110)

T. Nakagawa[1, 2], Y. Takagi[1, 2] and T. Yokoyama[1, 2]

[1]*Institute for Molecular Science, Okazaki 444-8585, Japan*

[2]*School of Physical Sciences, The Graduate University for Advanced Studies (SOKENDAI), Okazaki 444-8585, Japan*

Magnetic nanostructures have been an important subject both for application and fundamental researches. Materials with large coercivity and magnetic anisotropy are highly demanded for industrial uses. Single atomic layers, where magnetic features such as anisotropy, coercivity diverse from its bulk materials, give rise to extraordinary magnetic properties. Among magnetic single layers, Fe/W(110) has been one of the most extensively studied systems owing to its pseudomorphic growth mode, which results in 1x1 registry despite their large lattice mismatch ($a_{(W)}/a_{(Fe)}$~1.1). The large expansion of Fe lattice has been inferred to generate a large magnetic anisotropy. However, due to its extremely large value, the anisotropy energy has not been directly determined in spite of huge accumulation of experimental results on Fe/W(110) [1].

We have investigated magnetic anisotropy energy and coercivity of Fe nanoislands on W(110) (Fig.1(a)) using x-ray circular dichroism (XMCD). The experiment was done at BL4B using a low temperature cryostat and a split pair superconductive magnet. The spectra were taken at T_s = 5K under magnetic field up to 6 T. The samples were prepared *in situ* with thermal deposition of Fe onto W single crystals.

Figure 1 (b) shows magnetization curves taken along three directions (see Fig.1 (c) for the configurations) by measuring the Fe L_3-edge white-line intensity. Using a first order anisotropy formula, $f(\theta,\phi)=c_1\cos^2\theta + c_2\sin^2\theta \sin^2\phi - M$, we fits the magnetization curves. c_1 and c_2 are the magnetization anisotropy energies for [110] (out-of-plane) and [001] (in-plane) directions, respectively. The obtained anisotropy constants are plotted in Fig. 1 (d). The anisotropy energy is ~1 meV per Fe atom for the in-plane and out-of-plane directions as determined from magnetization curves, almost constant for the nanoisland below one monolayer. This anisotropy energy corresponds to an anisotropy field of 17 T. The coercivity, H_c, for the nanoislands at 0.25 ML is very large, ~5 T. With increasing the Fe coverage, giving larger island size, it rapidly decreases to 1 T at 0.6 ML, which follows $H_c \sim 1/r$ (radius of island).

The obtained largest coercivity is 1/3 of the anisotropy field, suggesting that the magnetization reversal process is via a domain wall creation, not a coherent rotation. In case of the coherent rotation at low temperature (~5 K), the coercivity should be close to the anisotropy energy.

Coercivity is limited by the smaller anisotropy energy since the magnetization reversal proceeds along the lower energy potential. Therefore, the large anisotropy both for the in-plane and out-of-plane directions is the origin of the huge coercivity on Fe/W(110).

[1] M. Pratzer, *et al*., Phys. Rev. Lett. **87** (2001) 127201.

Fig. 1. (a) Scanning tunneling microscopy image of Fe 0.3 ML deposited on W(110). (b) Magnetization curves on 0.4 ML Fe/W(110) for three directions (see (c)). (c) Experimental configurations for the XMCD measurements. (d) Anisotropy energies constant, c_1 and c_2 (see text) and (e) coercivity as a function of Fe coverage.

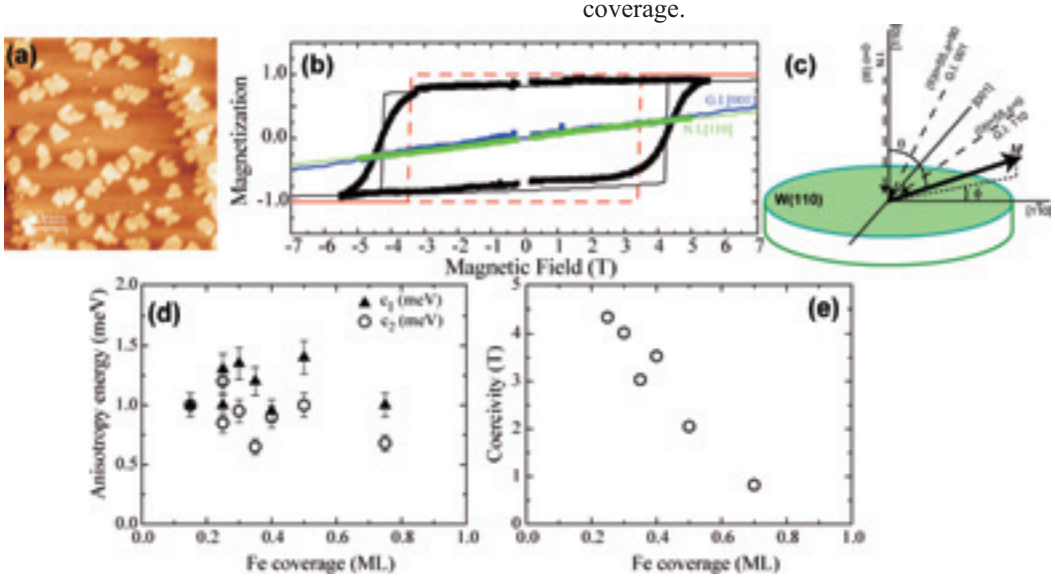

BL4B

Molecular Orientation and Magnetic Properties of Vanadyl Phthalocyanine on Si(111)

K. Eguchi[1], Y. Takagi[1, 2], T. Nakagawa[1, 2] and T. Yokoyama[1, 2]

[1]*The Graduate University for Advanced Studies (SOKENDAI), Okazaki 444-8585, Japan*

[2]*Institute for Molecular Science, Okazaki 444-8585, Japan*

It is important to understand the interactions of phthalocyanine compounds containing transition metals (TMPcs) with semiconductor substrates as well as metal ones for realizing molecular devices. Vanadyl phthalocyanine (VOPc) is one of TMPcs formed non-planer structure although TMPcs (M=Mn, Fe, Co, Ni, Cu and Zn) are planar structure. For non-planar structure, it is possible to adsorb on substrates with oxygen pointing up or down in a case of adsorption parallel to the surface. Actually, VOPc in the first layer adsorbs on HOPG [1] and Au [2] substrates with oxygen pointing up and a GaAs substrate [3] with oxygen pointing down to the surface. In this study, we investigated the molecular orientation and magnetic properties of vanadyl phthalocyanine (VOPc) deposited on a clean Si(111)-(7×7) surface by using x-ray absorption spectroscopy (XAS) and x-ray magnetic circular dichroism (XMCD).

Purified VOPc was deposited on Si(111)-(7×7) from homemade Knudsen cell at 570K under 3×10^{-9} Torr. During the sublimation deposition, the substrate was kept at room temperature. The deposition rate estimated by a quartz crystal oscillator was 0.1 ML/min. XAS and XMCD measurements were performed at 5 K by means of total electron yield (TEY) detect. In the XMCD measurement, the helicity of the circularly polarized x-ray was fixed positively while the magnetic field was reversed.

Figure 1 shows the π* resonance intensities of N *K*-edge x-ray absorption spectra for 0.9 and 15 ML VOPc deposited on clean Si(111) as a function of x-ray incident angle. It is found that the tilt angles of the phthalocyanine framework are about 26 deg and 37 deg for 0.9 ML and 15 ML VOPc, respectively. It is found that 15 ML VOPc does not form a molecular configuration with stand-up in comparison with a case of CuPc (β=66 deg) on Si(111) [4].

Figure 2 shows V *L*-edge and O *K*-edge XAS and XMCD spectra at the incident angle of 0 deg. The spectrum for 0.9 ML is broader than that for 15 ML because the energy resolution of the spectra for 0.9 ML was worse than that for 15 ML. However, it is clear that no additional peak is observed at V *L*-edge and the σ* resonance intensity of O *K*-edge is increased for 0.9 ML VOPc as compared with that for 15 ML VOPc. It is found that VOPc molecules of the first layer on the surface are absorbed with oxygen pointing down to the surface and interacted chemically with Si atoms.

For the magnetic properties of VOPc films, XMCD signals are obtained for 0.9 ML VOPc as well as 15 ML VOPc. The XMCD spectra for both 0.9 ML and 15 ML are similar shape although the intensities are different. It is found that the electron of central vanadium atom in d-orbital does not be lost for 0.9 ML VOPc.

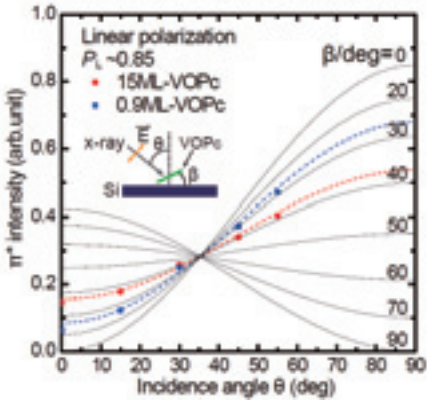

Fig. 1. The π* resonance intensities are plotted as a function of the incident angle of x-ray with respect to the surface normal. The dashed lines are fitting curves.

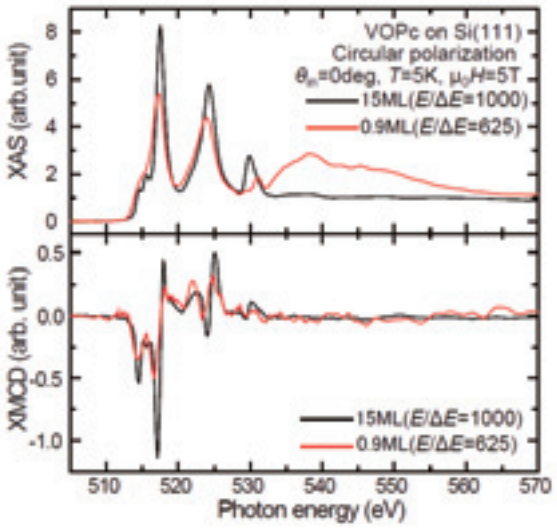

Fig. 2. V *L*-edge and O *K*-edge XAS and XMCD spectra for 0.9 and 15 ML VOPc/Si(111) taken at the incident angle of 0 deg from the surface normal at *T*=5 K and μ_0H=5 T.

[1] H. Fukagawa *et al.*, Phys. Rev. B **83** (2011) 085304.
[2] D.A. Duncan *et al.*, Surf. Sci. **604** (2010) 47.
[3] G. Mattioli *et al.*, J. Phys. Chem. Lett. **1** (2010) 2757.
[4] G. Dufour *et al.*, Surf. Sci. **319** (1994) 251.

BL4B

Magnetic Property of Iron Phthalocyanine Absorbed on Nitrogen-Modified Cu(001) Surface

Y. Takagi[1, 2], K. Eguchi[2], T. Nakagawa[1, 2] and T. Yokoyama[1, 2]
[1] *Institute for Molecular Science, Myodaiji-chio, Okazaki 444-8585, Japan*
[2] *The Graduate University for Advanced Studies, Okazaki, Aichi 444-8585, Japan*

The magnetic properties of molecules have attracted interest in recent years. The spin states of the magnetic metal-complex molecules containing 3d transition metal can be changed by an adsorbed molecule and a substrate under the molecular films. Iron (II) phthalocyanine (FePc) is one of interesting and fundamental compounds, because it takes an unusual intermediate triplet spin state and has a large orbital moment. In this study, we report on the magnetic property of FePc on nitrogen saturated Cu(001) surface [Cu(001)-c(2x2)N] by means of X-ray magnetic circular dichroism (XMCD) at BL4B, which equipped with a super conducting magnet system.

Sample preparation and XMCD measurement were carried out in UHV chambers. A Cu(001) single crystal was cleaned by repeated cycles of Ar^+ sputtering and annealing. The N adsorbed surface was made by N^+ bombardment and annealing at 520 K. Purified FePc was deposited on the substrate at room temperature (RT) by sublimation and the thicknesses of the films were monitored by a quartz crystal oscillator. The X-ray absorption spectra (XAS) and XMCD spectra were taken at 5 K and the XMCD spectra were recorded with reversal of the magnetic field.

Figure 1 (a) shows Fe L-edge XMCD spectra of 25 ML FePc on clean Cu(001) and 1 ML FePc on Cu(001)-c(2x2)N at incident angle θ = 0° from the surface normal at H = ±5 T. The spectra of FePc on Cu(001)-c(2x2)N is almost the same as that of 25 ML FePc. It seems that the inactivity of Cu(001)-c(2x2)N surface keep the same electronic state as FePc molecule in molecular plane. This result is different from the case of 1 ML FePc on the Co film [1]. The electronic state of FePc on Co films is modified by strong interaction between the FePc molecule and the Co layer.

In contrast to the result at θ = 0°, the spectrum of FePc film on Cu(001)-c(2x2)N at θ = 55° is different from that of 25 ML FePc [Fig. 1 (b)]. The peak at 707 eV in FePc film on Cu(001)-c(2x2)N is weak compare with that in 25 ML FePc. The peak at 707 eV in XAS spectra originates from the $3d_{z^2}$ orbital of the Fe ion. Because the $3d_{z^2}$ orbital is oriented perpendicular to molecular plane, it is affected by the substrate under the molecule. Therefore, the decrease of the peak is caused by the interaction between the Fe $3d_{z^2}$ orbital and the Cu(001)-c(2x2)N substrate under the FePc molecule. These results indicate that the electronic state of metal-complex molecules is modified only out of plane while that in in-plane is preserved the same electronic state of molecular.

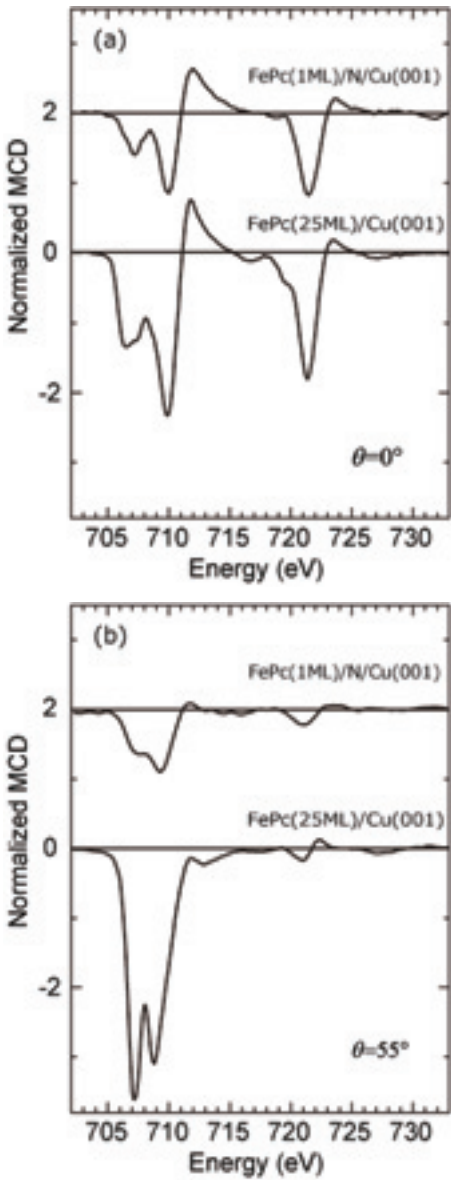

Fig. 1. Fe L-edge XMCD spectra of 25 ML FePc on clean Cu(001) and 1 ML FePc on Cu(001)-c(2x2)N at incident angle (a) θ=0°, (b) θ =55° from the surface normal at H = ±5 T.

[1] Y. Takagi *et al.,* UVSOR Activity Report **38** (2011) 67.

BL5B

Novel Beam Splitter for High-Order Harmonics with WO_3/TiO_2 Bilayer Grown on c-Plane Sapphire Substrate

H. Kumagai[1], Y. Sanjo[1], M. Murata[1], Y. Nabekawa[2], K. Midorikawa[2], T. Shinagawa[3] and M. Chigane[3]

[1]*Graduate School of Engineering, Osaka City University, Osaka 558-8585, Japan*
[2]*RIKEN Advanced Science Institute, Wako, Saitama 351-0198, Japan*
[3]*Inorganic Materials Lab., Osaka Municipal Technical Research Institute, Osaka 536-8553, Japan*

High-intensity high-order harmonics have been investigated intensively in recent years. In the construction of a beam line for the high-intensity high-order harmonics, however, use of a conventional beam splitter (BS) (Si or SiC) that absorbs the fundamental laser light has caused serious problems such as its thermal distortion. To solve these problems, we proposed and investigated a novel BS with transparent oxide materials that transmitted the fundamental laser light and then reflected the high-order harmonics. In BS for the high-order harmonics, reflection of the fundamental laser light should be minimized by entering the p-polarized fundamental light at the Brewster's angle, which could improve the separation between the fundamental laser light and the high-order harmonics at the same Brewster's angle.

We have fabricated WO_3/TiO_2 bilayers on c-plane sapphire substrates by controlled growth with sequential surface chemical reactions (SSCR) using sequentially fast pressurized pulses of the vapor sources. Our previous experimental results revealed that WO_3 (221) and rutile TiO_2 (200) thin films could be grown epitaxially on c-plane sapphire substrates by SSCRs. Then, in this study, we proposed a WO_3/TiO_2 bilayer grown on c-plane sapphire substrates, which could be utilized as a BS for the high-order harmonics. Reflectance characteristics were also investigated at the same Brewster's angle using monochromatized synchrotron radiation (SR) located at Ultraviolet Synchrotron Radiation Facility (UVSOR), Institute for Molecular Science, Okazaki, Japan.

Reflectivities for x-rays were measured with the beamline BL5B at UVSOR, and the current from a Si photodiode was used to determine the beam intensity reflected from the fabricated BS. The reflectivity was obtained dividing the intensity of the reflected beam by that of the incident. Figure 1 shows theoretical (dashed line) and measured (solid line) reflectivities of WO_3/TiO_2/c-plane sapphire BS at the Brewster angle for TiO_2 at the pump pulse at the wavelength range from 7 nm to 40 nm. The measured peak reflectivity was 37.0% at a wavelength of approximately 16.8 nm, which corresponded to the 47th-order harmonics of the 800-nm pump pulse, while theoretical peak reflectivity was 45.2% at a wavelength of approximately 16.1 nm, which corresponded to the 49th-order harmonics of the 800-nm pump pulse. Figure 2 also shows high reflectivity of WO_3/TiO_2/c-plane sapphire BS at the Brewster angle for TiO_2 at the pump pulse at the wavelength range from 30 nm to 100 nm.

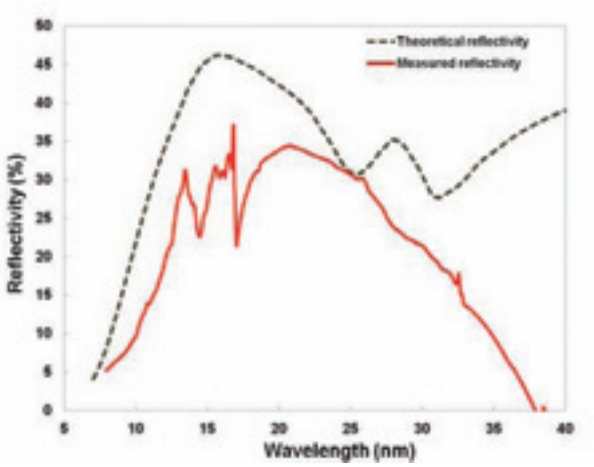

Fig. 1. Theoretical (dashed line) and measured (solid line) reflectivities of WO_3/TiO_2/c-plane sapphire BS at the Brewster angle for TiO_2 at the pump pulse at the wavelength range from 7 nm to 40 nm.

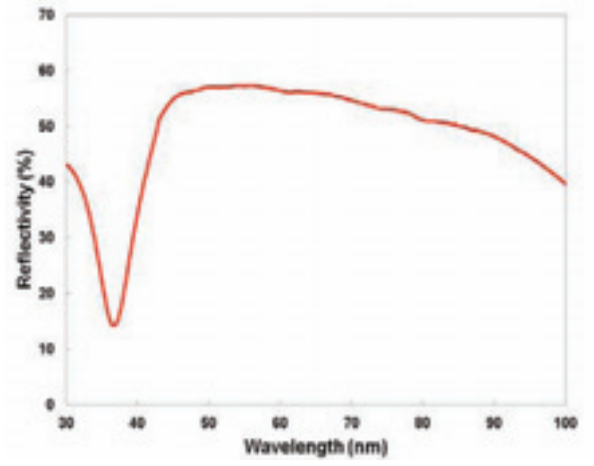

Fig. 2. Measured reflectivity of WO_3/TiO_2/c-plane sapphire BS at the Brewster angle for TiO_2 at the pump pulse at the wavelength range from 30 nm to 100 nm.

BL5B

Characterization of Silicon Carbide Coated Concave Mirrors for Generation of Intense EUV FEL Fields

M. Fushitani, A. Matsuda, T. Endo and A. Hishikawa
Graduate School of Science, Nagoya University, Nagoya 464-8602, Japan

Thanks to advances in free electron laser (FEL) technology, a high power coherent light source has been recently available in the extreme ultraviolet (EUV) region. This new light source makes it possible to investigate nonlinear optical phenomena induced by intense EUV laser fields. When atoms interact with EUV FEL, they undergo multiphoton multiple ionization as a typical nonlinear response to the EUV laser fields, but details of the ionization mechanism have remained to be clarified. Recently, we have carried out photoelectron measurements with EUV FEL pulses at the SCSS facility of the RIKEN HARIMA institute, and have revealed importance of resonance effects in three-photon double ionization of Ar [1] as well as double excitation of He [2] in intense EUV laser fields, demonstrating that single-shot photoelectron spectroscopy is a powerful tool for studies of multiphoton multiple ionization. In these experiments, the FEL field intensity available by using the Kirkpatrick-Baez optics installed at the SCSS facility was an order of ~10^{12} W/cm^2 due to the long focal length (~1 m), producing ions with at most doubly charged states. Therefore, to investigate the nonlinear response of atoms with highly charged states, mirrors with a high reflectivity as well as short focal length have to be employed for the focusing, thereby giving sufficiently large field intensities. Here, we investigate the reflectance property of a concave mirror (f = 75 mm) coated with silicon carbide (SiC) for the focusing of EUV FEL pules in the wavelength region of 50-61 nm.

The reflectance of a SiC coated concave mirror was measured at BL5B. The synchrotron radiation (SR) was dispersed by a grating and filtered in a confined region of 40-90 nm by a tin (Sn) foil (Fig. 1(a)) to suppress contributions from the higher order light due to the diffraction of the grating. The transmitted SR was detected at the normal angle by a Si photodiode (PD) suitable for the EUV region (AXUV100), which was used as a reference light. The SR light reflected by the SiC mirror at the angle of incidence of 7.5 degrees was measured with the same PD detector.

Figure 1 (b) shows a part of the reflectance of the SiC coated concave mirror. The reflectance increases from 40 nm and reaches the maximum of ~13 % around 65 nm. The wavelength region available for FEL at the SCSS facility is indicated by a double-headed arrrow. At 60 nm the reflectance is about 10 %, which is smaller than the throughput (30 %) of the focusing system at the SCSS, but the focal spot size of the SiC concave mirror is expected to be >10-times smaller. Therefore, based on comparisons of the focal areas, field intensities of EUV FEL pulses are expected to be improved by two orders of magnitudes, which results in intensities with an order of 10^{14} W/cm^2.

The present study strongly suggests that the SiC coated concave mirror with a short focal length is suitable for generating intense EUV laser fields with ~10^{14} W/cm^2. Such large field intensities allow us to investigate how multiple ionization takes place to produce highly charged ions by using EUV FEL pulses.

We are very grateful to the staff of the UVSOR facility.

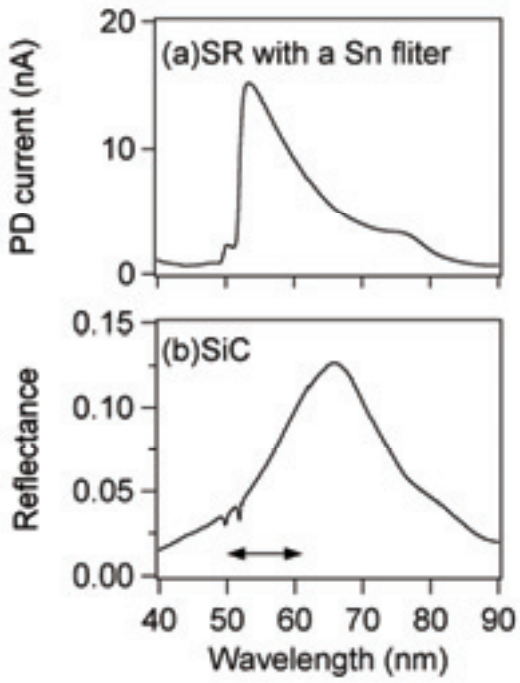

Fig. 1. (a) Synchrotron radiation dispersed by a grating and transmitted through a thin Sn filter, which is used as a reference light in the region of 40-90 nm. (b) Reflectance of a SiC coated concave mirror. The FEL wavelength region available at the SCSS facility is indicated by a double-headed arrrow.

[1] Y. Hikosaka *et al*., Phys. Rev. Lett. **105** (2010) 133001.
[2] A. Hishikawa *et al*., Phys. Rev. Lett. **107** (2011) 243003.

BL6U

Charge Transfer from Methyelthiolate Monolayers on Metal Substrates Studied by Core Hole-Clock Spectroscopy

K. Nakaya[1], H. Yamane[2], M. Nagasaka[2], N. Kosugi[2] and H. Kondoh[1]

[1] *Graduate School of Science and technology, Keio University, Yokohama 223-8522, Japan*

[2] *Department of Photo-Molecular Science, Institute for Molecular Science, Okazaki 444-8585, Japan*

Organic molecules adsorbed on solid substrates are potentially useful for sensors and electronic devices. Charge transfer from the molecules to the substrate is one of key factors which determine the electronic property of such devices [1]. However, the relation between adsorption structure and charge transfer has been unclear. The core-hole clock spectroscopy is a powerful technique to estimate charge transfer time scale from molecule to substrate. The metal-thiolate bond is often used as a covalent-bond linker between organic moiety and substrate. In this work we studied charge transfer time scale of methylthiolate (CH_3S) adsorbed on Ag(111) and Cu(111), which exhibit largely different adsorption structures, using the core-hole clock spectroscopy.

The experiments were carried out at beamline BL6U of UVSOR. Ag(111) and Cu(111) surfaces were cleaned by Ar^+ ion spattering and annealing. The methylthiolate monolayers were prepared by evaporation of dimethyldisulfide (CH_3S-SCH_3) onto the metal substrates at room temperature. These samples were irradiated by soft x rays with photon energies of 220-245eV, and we measured intensities of electrons emitted in the decay process of S2s→3p excitation by an electron energy analyzer. Obtained S $L_1L_{2/3}M_{1/2/3}$ Coster-Kronig autoionization spectra exhibit delocalized and localized final states, where exited electrons are transferring to the substrate and remaining within the molecule, respectively. Comparison between the intensities of the two final states enables to estimate the charge-transfer time constant [2].

Figure 1 shows intensities as a function of incoming photon energy and kinetic energy of the emitted electrons taken for the methylthiolate monolayer on Cu(111). Four different final states appear on the spectra: delocalized final states with constant kinetic energies *D* ($2p^{-1}3p^{-1}deloc^1$) and *d* ($2p^{-1}3s^{-1}deloc^1$) and localized final states with linear dispersion *L* ($2p^{-1}3p^{-1}3p^1$) and *l* ($2p^{-1}3s^{-1}3p^1$). A single spectrum taken with a photon energy of 235.0 eV is shown in Fig. 2. The spectrum was de-convoluted into the four components to estimate the charge-transfer time constant. Since the *L* final state is contributed from another decay channel (shake-up photoionization), we used *d* and *l* components for the estimation. Referring the S 2s core-hole life time (τ_c=0.5 fs), the charge transfer time constant τ_{CT} was obtained using a simple equation $\tau_{CT} = \tau_c \times I(l)/I(d)$. As a result, τ_{CT}(Cu(111)) is estimated to be 1.6 fs. In case of Ag(111), the component *l* was not clearly observed, and hence the charge transfer for CH_3S/Ag(111) is extremely fast. Considering the previous result (τ_{CT}(Au(111)) = 1.2 fs), it is concluded that τ_{CT}(Ag(111)) << τ_{CT}(Au(111)) < τ_{CT}(Cu(111)).

In the CH_3S/Ag(111) system, the S atoms are buried in the Ag adatom layer, while in the case of Cu(111), CH_3S molecules are simply adsorbed on the surface. The CH_3S/Au(111) system shows formation of a surface complex consisting of a Au adatom and CH_3S. Therefore, the metal adatoms generated on the surface may play a significant role in formation of strong bonding between the S atom of methyelthiolate and the surface metal atoms, leading to faster charge transfer.

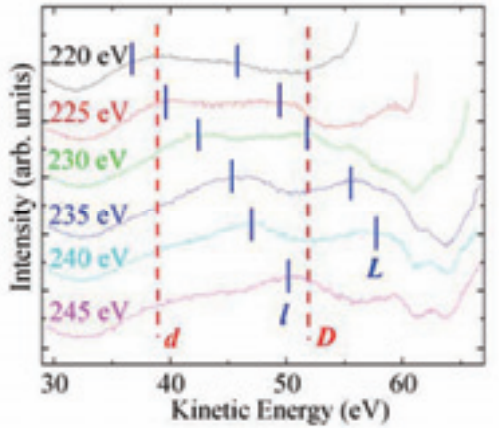

Fig. 1. Intensities of the emitted electrons taken for the methylthiolate monolayer on Cu(111).

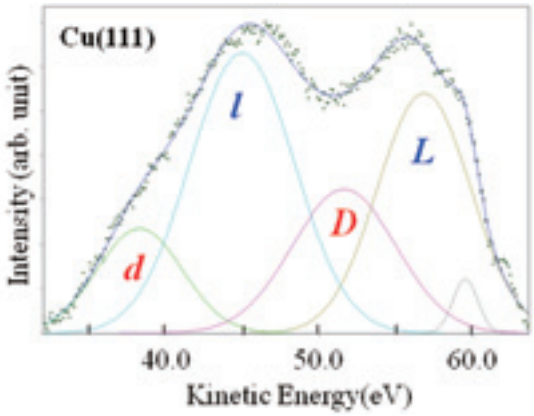

Fig. 2. Peak fitting of the spectrum at the photon energy of 235.0 eV.

[1] Li Wang, Wei Chen, Andrew Thye Shen Wee, Surf. Sci. Rep. **63** (2008) 465.

[2] A. Föhlisch *et al.,* Nature **436** (2005) 373.

BL6U

Giant Rashba Spin-Orbit Splitting of Pt Nanowires on Silicon

S. W. Jung[1], S. H. Jeon[1], H. Yamane[2], N. Kosugi[2] and H. W. Yeom[1]

[1] *Department of Physics and Center for Atomic Wires and Layers, Pohang University of Science and Technology, Pohang 790-784, Korea*

[2] *Department of Photo-Molecular Science, Institute for Molecular Science, Okazaki 444-8585, Japan*

The Rashba effect is one of important physical mechanisms to realize spintronic devices, where the spin degeneracy of conduction channels is lifted without an external magnetic field [1,2]. This effect is caused by breaking space inversion symmetry at crystal surfaces. Recent researches found a few systems with very large Rashba effect [3,4,5], called giant Rashba splitting and revealed unusual spin textures of Rashba bands [3,4]. Moreover, an one-dimensional conductor formed on a silicon surface was found to exhibit Rashba spin splitting, which has a great potential in spintronics applications [8].

In the present study, we performed angle-resolved photoelectron spectroscopy (ARPES) measurements, using BL6U of UVSOR, for a newly found nanowire system formed on a silicon surface, Si (110)-"6"x5-Pt. This nanowire structure was previously studied by scanning tunneling microscopy (STM) [6]. As shown in Fig. 1, well ordered wires are formed along [1 -1 0] on the Si(110) substrate [6]. Our own STM study showed a x3 periodic structure on the bright part of the wires along [1 -1 0], which is mixed with a x2 periodic structure on the dark valleys between wires. Since this structure is formed with the heavy element Pt, we expected a substantial spin-orbit interaction on its band structure.

Figure 2 shows the ARPES data along [1 -1 0] direction taken at 15 K with 46 eV photon. Two parabolic bands (at binding energy of ~ 0.2 eV) are split at the Γ point with symmetric dispersions. This band was shown to have one-dimensional dispersion along the wires and its periodicity along the wires is consistent with that observed in STM. Its dispersion is further consistent with the Rashba splitting picture with a Rashba energy of about 130 meV and a Rashba parameter of about 0.93 eVÅ. This Rashba splitting is much larger than that on the two dimensional system of Si(111)-$\sqrt{3} \times \sqrt{3}$-Bi [5,7] or the one dimensional system of Si(557)-Au [8], belonging to the category of giant Rashba systems. The spin structure of this system needs to be further confirmed by spin-polarized ARPES experiments and the atomistic origin of the Rashba band needs to be clarified in the forthcoming works including theoretical calculation. In any case, we believe that this is the first one dimensional system with a giant Rashba effect.

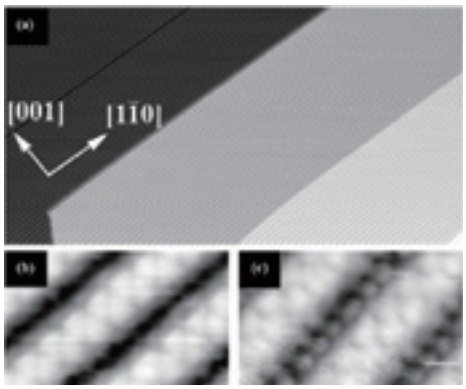

Fig. 1. STM topography of Si(110)-"6"x5-Pt taken from ref. [6]. (a) Wide region (300x150 nm^2 at filled state) and detailed images at (b) filled and (c) empty states.

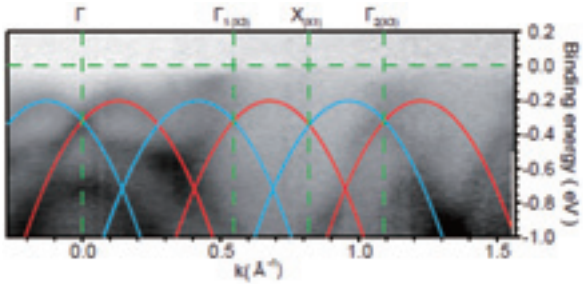

Fig. 2. Measured band dispersion of Si(110)-"6"x5-Pt along the wire ([1 -1 0]) direction. Red and blue solid lines indicate the major surface state band dispersions, which show Rashba type band splitting.

[1] Y. A. Bychkov and E. I. Rashba, Journal of Physics C: Solid State Physics **17** (1984) 6039.
[2] E. I. Rashba, Journal of Superconductivity **15** (2002) 13.
[3] C. R. Ast *et al*., Phys. Rev. Lett. **98** (2009) 186807.
[4] K. Ishizaka *et al*. , Nat. Mater. **10** (2011) 521.
[5] I. Gierz *et al*. , Phys. Rev. Lett. **103** (2009) 046803.
[6] A. Visikovskiy, M. Yoshimura and K. Ueda, Appl. Surf. Sci. **254** (2008) 7626.
[7] K. Sakamoto *et al*. , Phys. Rev. Lett. **103** (2009) 156801.
[8] D. Sánchez-Portal, S. Riikonen and R. M. Martin, Phys. Rev. Lett. **93** (2004) 146803.

BL7U

Warping Effects in the Band and Angular-Momentum Structures of the Topological Insulator Bi_2Te_3

W. S. Jung[1], Y. K. Kim[1], B. Y. Kim[1], Y. Y. Koh[1], Ch. Kim[1], M. Matsunami[2], S. Kimura[2], M. Arita[3], K. Shimada[3], J. H. Han[4], J. Kim[5], B. Cho[5] and C. Kim[1*]

[1]*Institute of Physics and Applied Physics, Yonsei University, Seoul, Korea*
[2]*UVSOR Facility, Institute for Molecular Science, Okazaki 444-8585 Japan*
[3]*HiSOR, Hiroshima University, Higashi-Hiroshima, Hiroshima 739-0046, Japan*
[4]*Department of Physics, Sungkyunkwan University, Suwon, Korea*
[5]*Department of Materials Science and Engineering, GIST, Gwangju 500-712, Korea*

The data from Bi_2Se_3 shows a large circular dichroism (CD), which stems from the existence of orbital angular momentum (OAM) [1]. It was found that the OAM is also locked to the electron momentum and its direction is antiparallel to the spin direction. Therefore, CD ARPES data may provide a way to measure the spin direction.

We report on our attempt to investigate the warping effect on the spin structures of the surface Dirac states of Bi_2Te_3 [2]. Our main goal was to obtain the systematic change in the OAM structure in the momentum space at a constant binding energy as a function of the energy from the Dirac point. Therefore, we performed ARPES experiments with circularly polarized light and obtained CD data. We observe the OAM direction from the dichroic ARPES data and find the spin structures. The results are consistent with the theoretical prediction, even in the high warping region.

To see how such a warping effect plays a role in the dichroism, we need to inspect the CD in the momentum space at a constant binding energy. Figure 1(b) plots constant energy CD data taken with 50 meV steps between 0 and 250 meV as marked by the dashed lines in Fig. 1(a). The plots show that the sign of the CD on a constant energy contour has binding energy dependence. Figure 1(c) shows CD data at 0, 100, and 250 meV binding energies. At 250 meV, which is close to the Dirac point, the shape of the constant energy contour is almost a circle. For 150 meV binding energy, the constant energy contour has a hexagonal shape. The Fermi contour at 0 meV binding energy has a strong warping effect, as manifested by its star shape. It is obvious that CD is also affected by the warping effect in Bi2Te3 and has a complex pattern.

CD plotted in Fig. 2 is very strong similar to CD results from Bi_2Se_3. We find that CD due to OAM is severely affected by the warping effect in the band structure. The OAM close to the Dirac point has an ideal chiral structure (sinθ) without the out-of-plane component. The CD shows a sin3θ effect in the weak warping effect region around 150 meV binding energy. Such θ dependence is compatible with the theoretically predicted spin structure for the case when the out-of-plane OAM component has a strong contribution to the θ dependence. In addition, CD gets an extra sin6θ term from modulation in the in-plane OAM component when the warping effect becomes very strong near the Fermi energy. This result is consistent with theoretical prediction, which considers higher order terms in our modified *kp* perturbation theory that incorporates OAM.

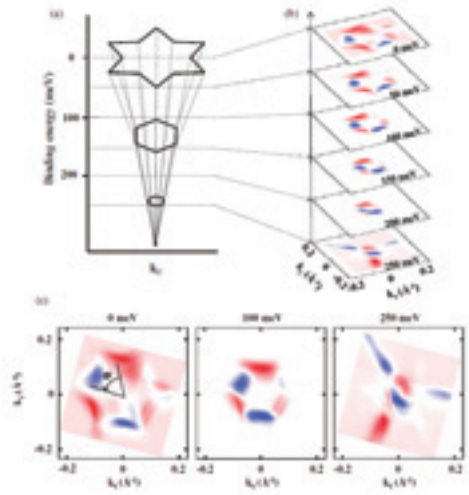

Fig. 1. (a) Illustration of Dirac cone of Bi_2Te_3. (b) Dichroism in the momentum space at various binding energies. (c) Constant dichroism map at selected binding energies of 0, 100, and 250 meV.

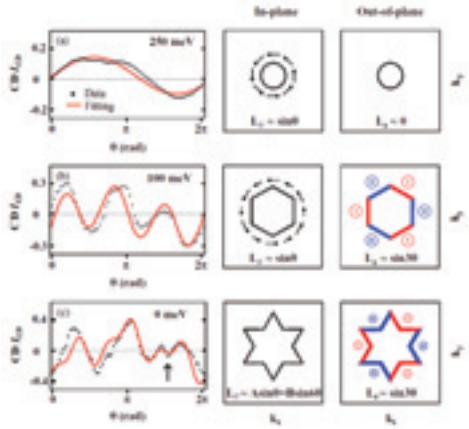

Fig. 2. CD and OAM direction along the constant energy contour at (a) 0 meV, (b) 100 meV, and (c) 250 meV.

[1] S. R. Park *et al.,* Phys. Rev. Lett. **108** (2012) 046805.
[2] W. Jung *et al.,* Phys. Rev. B **84** (2011) 245435.

BL7B

Reflection Spectroscopy of $KTa_{1-x}Nb_xO_3$ Thin Films by Reactive Sputtering

T. Goto, K. Nishimura, A. Yuasa, T. Tanaka and H. Matsumoto
School of Science & Technology, Meiji University, Kawasaki 214-8571, Japan

KTN ($KTa_{1-x}Nb_xO_3$) is a transparent optical crystal that is made of K, Ta, Nb, and O and exists as amorphous, pyrochlore, and perovskite crystal structures. Interestingly, it does not undergo a structural phase transition below its melting point temperature [1]. Furthermore, KTN having a perovskite crystal structure exhibits a very large electro-optic effect, wherein the refractive index changes by twice the magnitude of the applied voltage. The purpose of this study was to achieve optical responses for KTN thin film over a wide range of photon energies, and to investigate the electronic structures by comparing experimental data with theoretical calculations.

Thin films of $KTa_{1-x}Nb_xO_3$ ($0 \leq x \leq 0.7$) were deposited by radio frequency (RF) reactive sputtering onto fused quartz at a temperature of 500 °C. $KTaO_3$ and Nb plates were used as the target, and the sputtering was conducted in a mixture of argon and oxygen gases. The film thickness was about 150 nm. The chemical bonding states and crystallinity of the films were investigated by X-ray photoelectron spectroscopy (XPS) and X-ray diffraction (XRD) analyses. Reflection spectra of the films were measured in the vacuum ultraviolet region up to 40 eV with a 3 m normal incidence monochromator (gratings: G1, G2, and G3) using the BL7B beamline at UVSOR-II. A silicon photodiode sensor was used as the detector for the reflected light.

According to the analyses, all thin films are composed of polycrystalline KTN. When the impression electric power of Nb was measured at 0, 25, 50, 100, and 125 W, the value of x was set to 0, 0.10, 0.16, 0.47, and 0.59, respectively. The reflective measurement results using the beamline at UVSOR are shown in Fig. 1. As the value of x increased, the peaks at 5 eV and 10 eV shifted to the low energy side. To analyze the differences, a DV-Xα molecular orbital calculation was performed. The calculation results and the experimental measurements are in good agreement. The results of the calculation are shown in Figs 2 and 3, which are the energy level diagrams of $[M_7K_8O_{36}]$ (M = Ta, Nb) clusters embedded in Madelung potential is represented by the formal charges. In each oxide, the O_{2p} band comprises the valence band. The calculation results show that the peak shifts as x increases is the peak for the Nb_{4d} orbital.

[1] C. J. Lu , A. X. Kuang , G. Y. Huang and S. M. Wang , J. Materials Science **31** (1996) 3081.

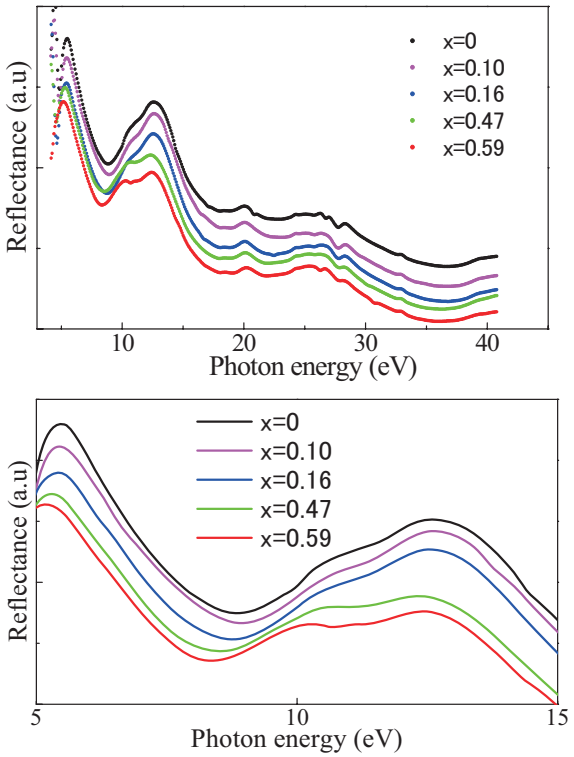

Fig. 1. Measurement results using the BL7B beamline at UVSOR

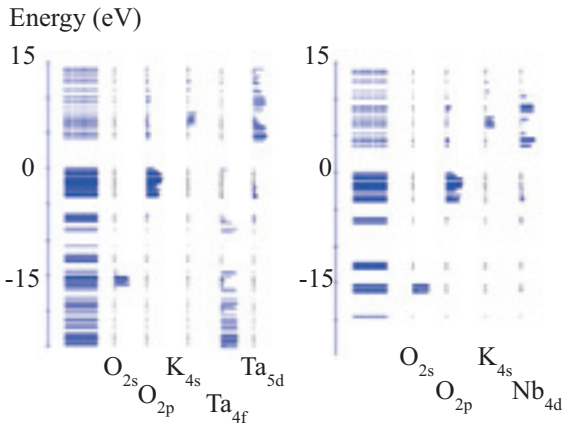

Fig. 2. $KTaO_3$ Fig. 3. $KNbO_3$

BL8B

Interface Electronic Structure of Diindenoperylene on Ag(111)

S. Kera[1], T. Hosokai[2], R. Kamiya[2], A. Gerlach[3] and N. Ueno[1]

[1]*Graduate School of Advanced Integration Science, Chiba University, Chiba 263-8522, Japan*

[2]*Faculty of Engineering, Iwate University, Morioka 020-8551, Japan*

[3]*Institut für Angewandte Physik, Universität Tübingen, Tübingen 72076, Germany*

Over the past decade, organic electronic devices have increased considerable attentions due to their potential applications. The adsorption of large π-conjugated organic molecules on metal surfaces is one of the key targets to understand the variety of peculiar interface properties. The molecule-substrate interaction crucially influences electronic and geometric properties at the interface.

Diindenoperylene (DIP: $C_{32}H_{16}$) (inset in Figure 1) is a typical organic semiconductor. The DIP monolayer films are prepared on graphite (HOPG) and Ag(111) substrate to reveal the interface electronic structure by using angle-resolved ultraviolet photoelectron spectroscopy (ARUPS).

ARUPS spectra were measured at photon incidence angle $\alpha=45^{o}$, hv=28 and 40 eV and T=295 K. The molecules were evaporated onto the graphite and Ag(111). The coverage/thickness of the monolayer was confirmed by the work function of the densely-packed monolayer (ML) film which shows a clear LEED pattern.

Figure 1 shows the UPS of DIP thin films on Ag(111) together with DIP monolayer (ML) on HOPG for the comparison. The DIP/HOPG spectrum (4) can be considered for the representative of physisorbed interface. The peaks A, B and C are ascribed to HOMO(π), HOMO-1(π) and HOMO-2(π), respectively. These valence features are appeared at high-binding energy (E_b) side by 0.35eV for DIP/Ag(111) (3). The peaks are suppressed and shifted to low-E_b side with decreasing the coverage. For the thinner films, the additional features are observed especially at band-gap region, which is denoted by I_1 – I_3. One may find other valence band features at around peak I_3 and at deeper E_b region, though it is hard to discuss the characteristics of each state due to coexistence a couple of orbital states. The features I_1 and I_2 would be related to the former LUMO and former HOMO of DIP as reported similarly in PTCDA/Ag(111), respectively [1]. Shockley surface state is completely disappeared for the film (1). The work function of the DIP(ML)/Ag(111) is decreased by 0.44 eV from Ag(111) and slightly recovered for other thicker films (2) and (3) by 0.1eV. The spectrum (1) is also obtained upon annealing the thicker films.

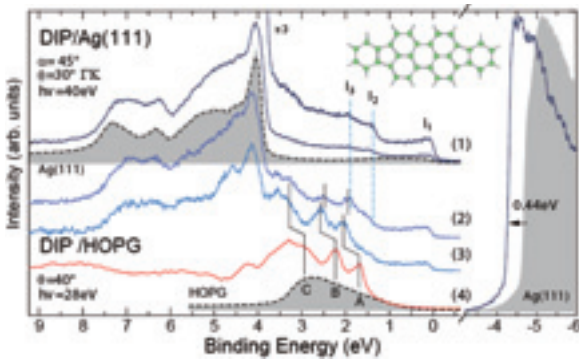

Fig. 1. Thickness dependence of DIP film prepared on a clean Ag(111), DIP(as-grown ML: 0.3 nm) (1), DIP(island film 0.6 nm) (2), and DIP(1 nm) (3) together with DIP(as-grown ML)/HOPG (4). UPS for each substrate are also shown. Work function shift (0.44 eV) is found for the secondary cut-off region.

Figure 2 shows ARUPS result for DIP(ML) /Ag(111) along Γ–K direction measured at hv=28 eV. The photoelectron angular distributions (PADs) of features I_1 and I_2 are slightly different each other. The PAD for molecular solids gives a momentum view of molecular orbital spread [2]. To reveal each orbital character beyond the energy resolution, a momentum map of the PAD is requested to be measured [3]. The adsorption distance evaluated by x-ray standing wave measurements remarks a closer distance for DIP than PTCDA on Ag(111). The relation between the adsorption distance and the degree of orbital hybridization to the metal, which may be appeared in the present UPS results, will be considered.

[1] J. Ziroff *et al.,* Phys. Rev. Lett. **104** (2010) 233004.

[2] S. Kera *et al.*, Chem. Phys. **325** (2006) 113.

[3] M. Dauth *et al.*, Phys. Rev. Lett. **107** (2011) 193002.

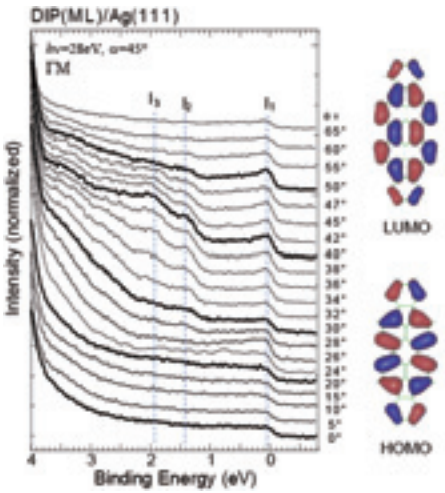

Fig. 2. ARUPS along Γ–K direction for DIP(as-grown ML)/Ag(111). HOMO and LUMO distribution on gas-phase are also shown.

BL8B

ARUPS Study of Anisotropic Molecular Orientation of Pentacene Thin Film on Microstructured Substrate

K. K. Okudaira, T. Ishii, K.Hotta and N. Ueno

Association of Graduate Schools of Science and Technology, Chiba Univererity, Chiba 263-8522, Japan

Recent progress in the field of organic thin-film transistors receives significant attention underscoring its importance for the microelectronic industry. In organic electronic devices, the electrical behavior is governed by not only the electronic states of the semiconducting molecules but also the morphology of their thin films. In-plane orientation of pentacene films has been performed in order to improve the transport properties in OFETs. Fabrication of oriented structure such as uniaxially oriented crystallites is important to obtain the oriented growth of materials as a substrate. In-plane orientation of pentacene films has been performed in order to improve the transport properties in OFETs. Fabrication of oriented structure such as uniaxially oriented crystallites is important to obtain the oriented growth of materials as a substrate. It has been shown that the uniaxially film growth of pentacene can be achieved by using micrsotructured substrate. In this study we show that a highly anisotropic growth of pentacene film on the uniaxially oriented poly (tetrafluoroethylene) (PTFE) onto the grating which have well-defined microstructure (such as groove period and depth).

ARUPS measurements were performed at the beamline BL8B of the UVSOR storage ring at the Institute for Molecular Science. The take-off angle (θ) dependencies of photoelectron spectra were measured at incident angle of photon (α) = 45° with the photon energy (hν) of 40 eV. All measurements were performed at room temperature. PTFE was deposited on brazed grating with different groove period (300line/mm (line space is 3.3 μm) and 1200 line/mm (line space is 830 nm) on which Cu has been deposited in advance. Pentacene thin film was obtained by deposition on PTFE film onto the grating (Pn/PTFE/grating).

We observed take-off angle (θ) dependence of HOMO peak in UPS of pentacene thin film (thickness of about 10 nm) on PTFE film deposited on grating Pn/PTFE/grating (300 lines/mm) and (1200 lines/mm) with parallel and perpendicular condition [Fig.1(a) and (b)]. In the parallel condition, the electrical vector of incidence photon is parallel to the direction of the groove. Photoelectron intensities from HOMO band show a sharp θ dependence with a maximum at θ = 50~60°. On the contrary, with parallel condition they show broader θ dependence. θ dependence for the pentacene thin film on grating (1200 lines/mm) is sharper than that on grating (300 lines/mm). They indicate that the anisotropy of molecular orientation of pentacene on the grating (1200 lines/mm) is higher than that on the grating (300 lines/mm). The narrower line space (below 800 nm) needs for the higher anisotropic molecular orientation of pentacene film.

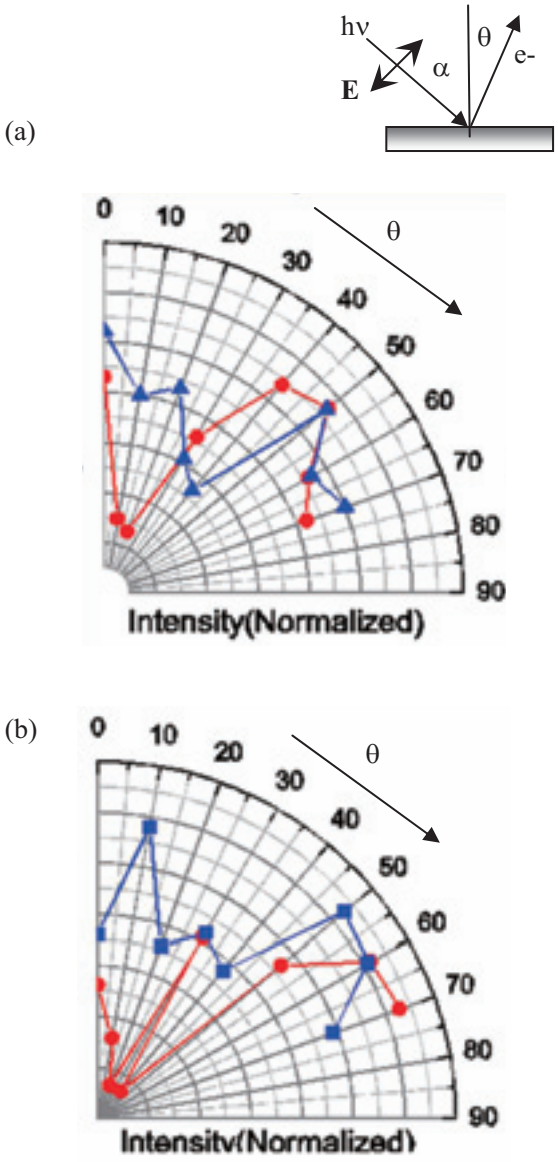

Fig.1. Take-off angle (θ) dependences of photoelectron intensities of HOMO peak of Pn/PTFE/grating (300 lines/mm) (a) and Pn/PTFE/grating (1200 lines/mm) (b) with parallel (●) and perpendicular condition (●).

BL1B

Electronic Structure and Correlation Effects in $K_{0.49}RhO_2$

R. Okazaki[1], Y. Nishina[1], Y. Yasui[1], S. Shibasaki[2] and I. Terasaki[1]
[1]*Department of Physics, Nagoya University, Nagoya 464-8602, Japan*
[2]*Department of Applied Physics, Waseda University, Tokyo 169-8555, Japan*

The layered cobalt oxide Na_xCoO_2 is a fascinating material because of its highly unusual transport properties, *i.e.*, a large Seebeck coefficient with low electrical resistivity [1], as well as a rich electronic phase diagram. With increasing Na content x, the system varies from a Pauli-paramagnetic metal to a Curie-Weiss metal through a charge-ordered insulator around x = 0.5. Furthermore, hydration induces a superconductivity near x = 0.3.

To elucidate the origin of such intriguing phenomena in this material, the knowledge of the detailed electronic structure is crucially important. The optical conductivity spectra in Na_xCoO_2 captured wide electronic structure [2,3], which can be assigned to the local density approximation (LDA) band structure. However, the LDA + Hubbard U calculations, which well explain the results of the angle-resolved photoemission spectroscopy studies on Na_xCoO_2, seriously worsen the consistency between the LDA and the optical conductivity spectra [4], puzzling a precise role of electron correlations for the electronic structure in this compound.

Here we investigate an optical property of isostructural 4*d*-electron Rh oxide $K_{0.49}RhO_2$ [5]. We used the beamline BL1B in UVSOR facility to measure the reflectivity spectra of $K_{0.49}RhO_2$ single crystals in an energy region of 2 – 30 eV, which enables us to evaluate the optical conductivity through the Kramers-Kronig analysis. In Fig. 1 (a), we show the optical conductivity spectrum below 8 eV. The peak locations are well defined near 0.9, 3.1, and 5.5 eV as labeled by γ′, β′, and α′, respectively. For comparison, we depict the room-temperature optical conductivity spectra of Na_xCoO_2 in Fig. 1 (b), which were taken from previous reports [2,3]. In Na_xCoO_2, three conductivity peaks labeled by γ, β, and α are clearly recognized at 0.5, 1.6, and 3 eV, respectively. Within the LDA scheme, the γ peak corresponds to the transition between t_{2g} bands and the β peak to t_{2g}-e_g transition. The α peak is responsible for the charge-transfer transition from occupied O 2*p* to unoccupied e_g states, as schematically illustrated in Fig. 1 (c). The peak positions in $K_{0.49}RhO_2$ are clearly shifted to higher energies relative to the spectra of Na_xCoO_2. It is also found that the peak widths are broader than those of Na_xCoO_2. These differences are naively captured by broader 4*d* orbitals in $K_{0.49}RhO_2$ as schematically shown in Fig. 1(d). A large crystal-field splitting pushes the α and β peaks in Na_xCoO_2 to higher energy α′ and β′ peaks in $K_{0.49}RhO_2$, respectively. The bandwidth of t_{2g} complex is expanded by broad orbitals of Rh 4*d* electrons, leading to a higher-energy shift of the γ peak as well. We also find that the effective mass of $K_{0.49}RhO_2$ is nearly half that of Na_xCoO_2 from a comparison of the spectrum weights. The electronic structure and correlation effects in $K_{0.49}RhO_2$ are well described by the difference between Co 3*d* and Rh 4*d* orbitals.

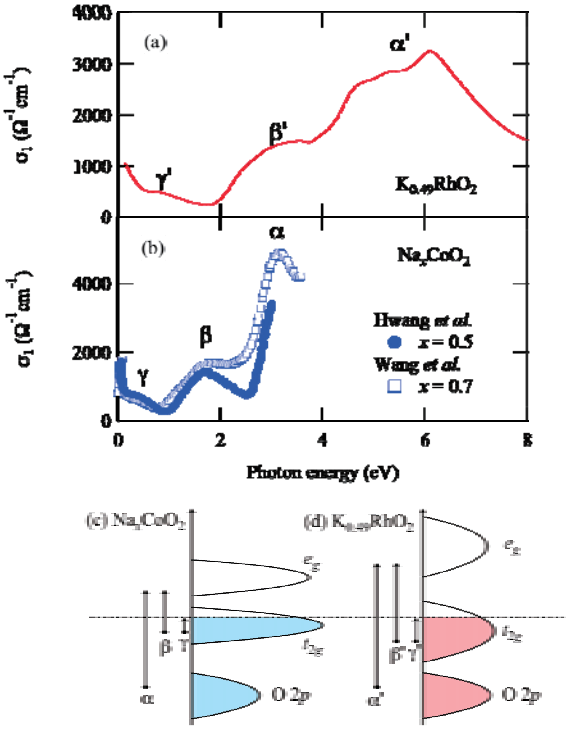

Fig. 1. Optical conductivity $\sigma_1(\omega)$ of (a) $K_{0.49}RhO_2$ and (b) Na_xCoO_2. The data for Na_xCoO_2 was taken from previous reports [2,3]. The peak locations in $K_{0.49}RhO_2$ (Na_xCoO_2) spectra are labeled by α′ (α), β′ (β), and γ′ (γ), which correspond to the O 2*p*-e_g, t_{2g}-e_g, and t_{2g}-t_{2g} transitions, respectively, as illustrated in schematic energy diagrams (c,d).

[1] I. Terasaki, Y. Sasago and K. Uchinokura, Phys. Rev. B **56** (1997) R12685.
[2] N. L. Wang *et al.*, Phys. Rev. Lett. **93** (2004) 237007.
[3] J. Hwang, J. Yang, T. Timusk and F. C. Chou, Phys. Rev. B **72** (2005) 024549.
[4] M. D. Johannes, I. I. Mazin and D. J. Singh, Phys. Rev. B **71** (2005) 205103.
[5] R. Okazaki *et al.*, Phys. Rev. B **84** (2011) 075110.

BL2A

Characterization of Phosphorus Doped Titanium Oxide

T. Kurisaki, M. Iwase, Y. Nagino, S. Yokoyama and H. Wakita

Department of Chemistry, Faculty of Science, Fukuoka University, Nanakuma, Jonan-ku, Fukuoka 814-0180, Japan

Doping TiO_2 with nonmetal such as nitrogen [1], carbon [2] and sulfur has received a lot of attention in recent years since it can extend the photoresponse of TiO_2 from ultra violet to the visible region, which is advantageous for using the sunlight as the energy source. As for Phosphorus-doped TiO_2 with visible-light photocatalytic activity, two kinds of P-TiO_2 [3,4] prepared using phosphate as precursor of P has been reported. However, some reports showed that P-TiO_2 prepared using phosphate cannot absorb visible-light. Thus, we attempted to prepare P-TiO_2 using phosphide as a new method. P-TiO_2 was synthesized through the hydrolysis of titanium tetraisopropoxide in suspension containing TiP compound [5], which was prepared by the treatment of titanium tetrachloride with cyclohexylphosphine. The synthesized P-TiO_2 nanoparticles exhibit a visible-light photocatalytic activity. However, the electronic structure of phosphorus in the P-TiO_2 nanoparticles is not well known.

For various light element compounds, we have studied the electronic structure by X-ray absorption spectroscopy [6]. These results suggested that there is a correlation between XANES spectra and the local structures.

In this work, we performed the XANES spectra measurement about various phosphorus doped titanium oxides and reference samples such as titanium phosphide (TiP). The obtained experimental XANES spectra are analyzed using the calculated theoretical spectra from DV-Xα calculations. The XANES spectra were measured at BL2A of the UVSOR in the Institute of Molecular Science, Okazaki [7]. The ring energy of the UVSOR storage ring was 750MeV and the stored current was 300 mA. P K-edge XANES spectra were recorded in the regions of 2125-2270eV by use of two InSb crystals. The absorption was monitored by the total electron yield using a photomultiplier. The samples were spread into the carbon tape on the first photodynode made of CuBe of the photomultiplier.

Figure 1 shows the observed P K-edge XANES spectra for the TiP and the phosphorus doped titanium oxide. The P K-edge XANES spectra of TiP and P-TiO_2 show different peak profiles at second peaks. The peaks that appear at approximately 2176 and 2185 eV on observed XANES spectrum of TiP are labeled A and B. The peak positions of A and B are estimated to the P^{-3} and P^{5+}. On the other hand, the observed XANES spectrum of P-TiO_2 showed only one peak at 2186 eV. The result suggests that phosphorus in the synthesized P-TiO_2 nanoparticle surface exists as phosphoric acid. We are going to try to analyze this change from comparison of P K-edge XANES and calculated spectra by DV-Xα molecular orbital calculations.

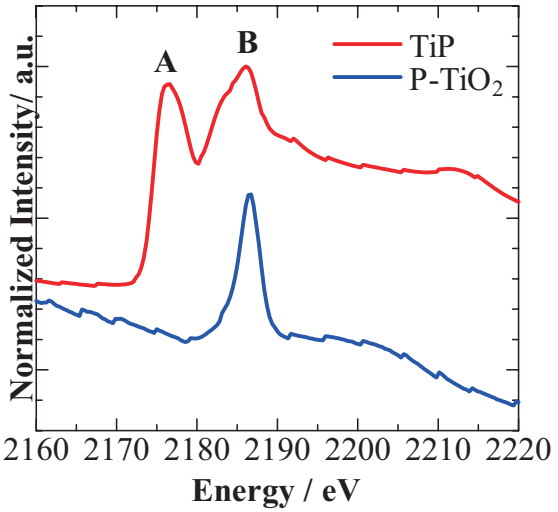

Fig. 1. Observed P K-edge XANES spectra of TiP and P-TiO_2.

[1] R. Asahi *et al*., Science **293** (2001) 269.
[2] Y. Nosaka *et al*., Sci. Tech. Adv. Mater. **6** (2005) 143.
[3] L. Lin and W. Lin, Chem. Lett. **34** (2005) 284.
[4] Q. Shi *et al*., J. Mol. B: Enzym. **43** (2006) 44.
[5] T. S. Lewkebandara *et al*., Chem. Mater. **7** (1995) 1053.
[6] T. Kurisaki *et al*., Anal. Sci. **24** (2008) 1385.
[7] S. Murata *et al*., Rev. Sci. Instrum. **63** (1992) 1309.

BL2A

Mg-K Edge XAFS Measurement of Mg Doped Hydroxyapatite by Fluorescence Mode

M. Sato[1], Y. Nishio[2], T. Nagayasu[2] and A. Nakahira[1, 2]

[1]*Kansai Center for Industrial Materials Research, Tohoku University, Osaka 599-8531, Japan*

[2]*Department of Material Science and Engineering, Osaka Prefecture University, Osaka 599-8531, Japan*

Hydroxyapatite ($Ca_{10}(PO_4)_6(OH)_2$, HAp) has been well understood as an alternate materials of our hard tissue because of their excellent osteoconductivity and biocompatibility. Furthermore, because HAp also has good protein adsorption ability and ion exchange ability, many studies for bioactivity and dissolution behavior of Mg, Mn, Fe, Si, Zn doped HAp have been performed. Since we could not obtain effective data of Mg doped HAp by total electron yield mode so far, we tried fluorescence mode and investigated a local structure of around Mg atom of Mg doped HAp. In this study, Mg doped HAp were prepared by microwave assisted hydrothermal process, respectively, and local structure of around P atom was investigated by XAFS measurement.

0.1 mol/l $Ca(NO_3)_2$, $(NH_4)_2HPO_4$ and $Mg(NO_3)$ solutions were used as starting materials. These solutions were mixed up each other becoming the ratio of Ca to P of 1.67 and the ratio of Mg from 1 to 15 mol% for Ca solution, respectively. Mixed solutions were set into autoclave and hydrothermally treated at 423 K for 60 min. with irradiation of microwave (2.45 GHz). After that, they were filtered and dried at 323 K for overnight. Mg-K edge XANES spectra of Mg doped HAp powders were measured by fluorescence method at room temperature using beryl double-crystal monochrometer at BL2A station of UVSOR and obtained spectra were compared to that obtained by a total electron yield mode.

Figure 1 shows a comparison of Mg-K edge XANES spectra of Mg doped HAp collected by total electron yield mode and fluorescence mode. Intensity of obtained spectra by total electron yield mode was too weak to analyze. Consequently, obtained spectrum is strongly affected by noise which is caused by a top-up. On the other hand, clear spectra can be obtained in the case of fluorescence mode.

From analysis using fluorescence mode and P-K edge XANES data, it is indicated that the Mg was replaced with the Ca (II) site. In addition, it is thought that the solid solubility limit of Mg ion into a HAp structure is approximately 15 mol%.

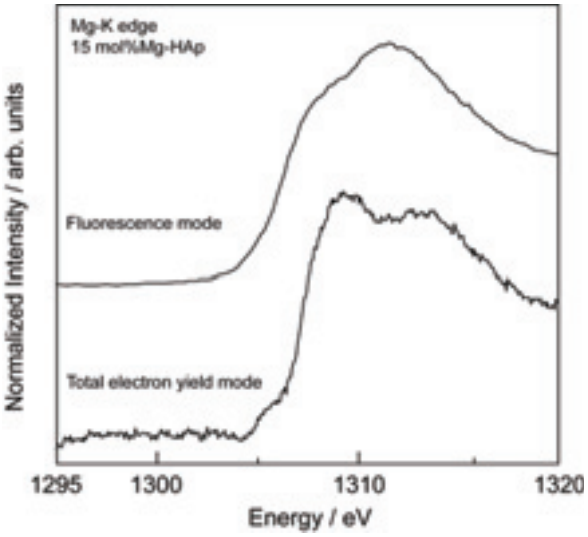

Fig. 1. Comparison of Mg-K edge XANES spectra of Mg doped HAp collected by total electron yield mode and fluorescence mode.

BL2A

Investigation of Local Structure of Si-K and Al-K Edge in Zeolites Prepared from Waste Materials

M. Sato[1], Y. Takamatsu[2], K. Kumadani[2] and A. Nakahira[1, 2]

[1]*Kansai Center for Industrial Materials Research, Tohoku University, Osaka 599-8531, Japan*

[2]*Department of Material Science and Engineering, Osaka Prefecture University, Osaka 599-8531, Japan*

The depletion of natural resources is one of the our serious problems. Therefore, the development of the novel recycling technology has been performed energetically. Blast furnace slag (BF slag) is one of the waste materials that the development of the effective recycling technology and establishment of recycle system become the urgent assignment. The BF slag has been produced approximately 25 million tons per year and recycled as Portland cement, base coarse materials, fine aggregate for concrete and ground improvement materials, etc. However, recycling rate of BF slag is insufficient by comparing to the amount of generation. In this study, A, P and Y type zeolite were prepared using BF slag as a starting material to reduce an emission of waste materials, and local structure of BF slag and its products were investigated.

Water cooled BF slag was ground to become their particle size less than 70 μm. Ground slag powder was undergone an acid treatment to remove a Ca component. And then, Ca removed slag powder was hydrothermally treated in 0.23 mol/l NaOH solution at 368 K for 48 h. In this study, the ratio of Si to Al was changed in the range from 0.5 to 2.4. Si-K and Al-K edge XANES spectra of samples were measured by a total electron yield mode at room temperature using KTP double-crystal monochromator at BL2A station of UVSOR.

Figure 1 shows Si-K edge XANES spectra of water cooled BF slag, acid treated BF slag and A type zeolite prepared using acid treated BF slag. The local structure around Si atom of BF slag is relatively amorphous and changed by acid treatment. Furthermore, the local structure of A type zeolite prepared using slag as a starting material differed from commercial A type zeolite and that synthesized using reagents.

Figure 2 shows Al-K edge XANES spectra of A and P type zeolites prepared using acid treated BF slag. Obtained spectra of A type zeolite prepared using BF slag was different from the result of Si-K edge spectra, and similar spectra to that of commercial A type zeolite was obtained. This result indicates that the local structure of around Al atom of sample is almost same.

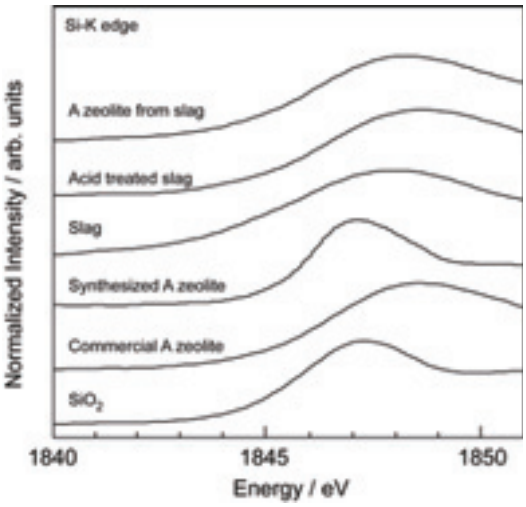

Fig. 1. Si-K edge XANES spectra of water cooled BF-slag and its products.

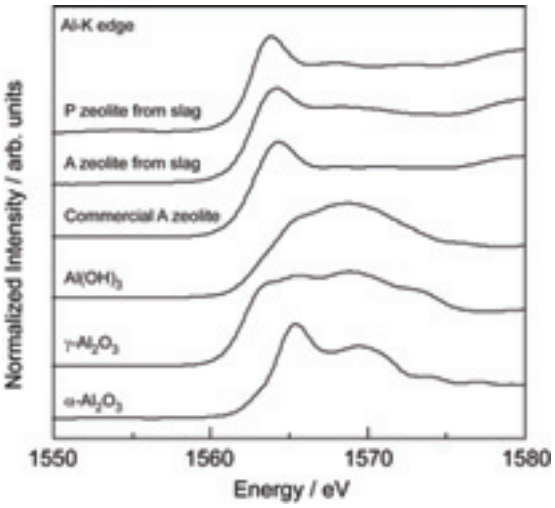

Fig. 2. Al-K edge XANES spectra of water cooled BF-slag and its products.

BL2A

Investigation of Local Structure of P-K Edge in Fe, Mg and Mn Doped Hydroxyapatite

M. Sato[1], Y. Kawabe[2], S. Misu[2], S. Hayashi[2] and A. Nakahira[1, 2]

[1]*Kansai Center for Industrial Materials Research, Tohoku University, Osaka 599-8531, Japan*

[2]*Department of Material Science and Engineering, Osaka Prefecture University, Osaka 599-8531, Japan*

Hydroxyapatite ($Ca_{10}(PO_4)_6(OH)_2$, HAp) has been well understood as a alternate materials of our hard tissue because of their excellent osteoconductivity and biocompatibility. Furthermore, because HAp also has good protein adsorption ability and ion exchange ability, many studies for bioactivity and dissolution behavior of Mg, Mn, Fe, Si, Zn doped HAp have been performed.

In this study, Fe, Mg and Mn doped HAp were prepared by conventional wet process, hydrothermal process and microwave assisted hydrothermal process, respectively, and local structure around P atom was investigated by XAFS measurement.

0.1 mol/l $Ca(NO_3)_2$, $(NH4)_2HPO_4$ and $FeCl_3$, $Mg(NO_3)$ and $MnCl_2$ solutions were used as starting materials. These solutions were mixed up each other becoming the ratio of Ca to P of 1.67 and the ratio of Fe from 0.1 to 1 mol%, Mg from 1 to 15 mol% and Mn from 1 to 5 mol% for Ca solution, respectively. In the case of wet process, mixed solution was aged for 1 h at room temperature. For the hydrothermal and microwave assisted hydrothermal process, mixed solutions were set into autoclave and samples were prepared at 423 K for each preparation time. After that, they were filtered and dried at 323 K for overnight. P-K edge XANES spectra of obtained HAp powders were measured in a total electron yield mode at room temperature using InSb double-crystal monochrometer at BL2A station of UVSOR.

From XRD measurement, obtained all samples had a HAp structure. Figure 1 shows P-K edge XANES spectra of Fe, Mg and Mn doped HAp powders. In the case of Mn and Fe doping, obtained P-K edge XANES spectra of Fe and Mn doped HAp samples were similar to that of commercial HAp, and a change of the spectral pattern was not clearly observed within any ratio of Fe and Mn. This result indicates that the local structure of around P atom of Fe doped HAp samples is almost same with commercial HAp. From this result, it is estimated that the doped Fe and Mn substitutes to Ca site. On the other hand, minimal peak shift and broadening of spectrum was observed for the 15 mol% Mg doped HAp. This result may be caused by the decrement of crystallinity and generation of $Mg_3(PO_4)_2$ phase.

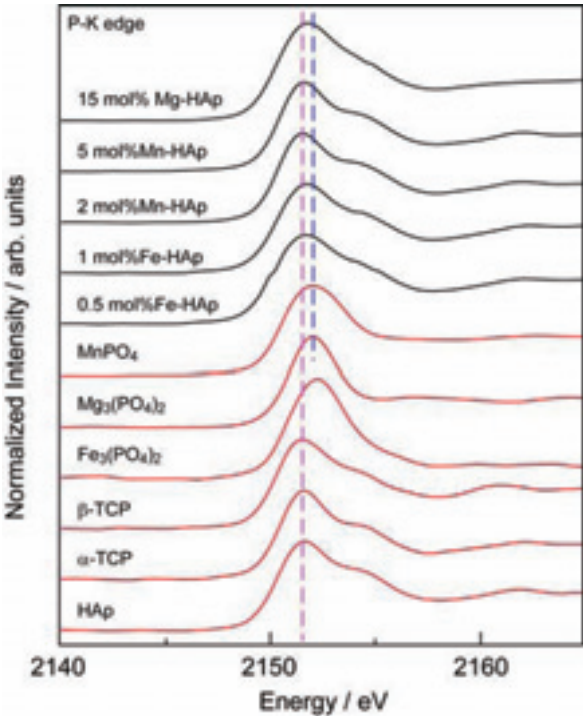

Fig. 1. P-K edge XANES spectra of Fe, Mn and Mg doped HAp (black line) and references (red line).

BL3B

Energy Transfer Caused by Emission Reabsorption in CsI:Ag^- Crystals

T. Kawai[1], S. Nagata[1] and T. Hirai[2]

[1]*Graduate School of Science, Osaka Prefecture University, Sakai 599-8531, Japan*

[2]*Faculty of Science and Engineering, Ritsumeikan University, Kusatsu 525-8577, Japan*

Energy transfer mechanism from host crystals to impurity ions has been widely studied from the viewpoint of applications of scintillators and/or phosphors [1]. In CsI crystals doped with Tl^+ or Na^+ ions, the hopping motion of self-trapped excitons or V_k centers plays an important role in the energy transfer. In this study, we have investigated luminescence properties of CsI:Ag^- crystals in order to reveal the energy transfer mechanism from the host CsI crystals to the impurity Ag^- ions.

Figure 1 shows the absorption and luminescence spectra of the Ag^- centers doped in the CsI crystals at 10 K. The C absorption band due to the Ag^- centers is observed at 3.76 eV. Excitation by the photon energy corresponding to the C absorption band on the CsI:Ag^- crystals induces luminescence bands peaking at 2.53 and 3.45 eV. These luminescence bands are attributed to the radiative transitions from the relaxed excited states of $^3T_{1u}$ and $^1T_{1u}$ in the Ag^- centers and are called the A' and C' luminescence bands, respectively [2].

Under excitation at 6.42 eV which is higher than the band-gap energy of CsI crystals, the broad luminescence bands peaking at 3.6 eV are observed in addition to the A' luminescence band. The 3.6 eV luminescence bands are attributed to the off-center self-trapped excitons (STEs) in CsI host crystals. Though the STE luminescence band usually has a standard Gaussian shape, the off-center STE luminescence band of the CsI:Ag^- crystals has a small shoulder at 3.45 eV and a slight dent around 3.70 eV. The small shoulder at 3.45 eV comes from the C luminescence band of the Ag^- centers. The dent at 3.70 eV in the off-center STE luminescence band is attributed to the reabsorption by the C absorption band, because the C absorption band located around 3.7 eV is covered with the off-center STE luminescence band. This fact implies that the Ag^- centers reabsorb the off-center STE luminescence.

Figure 2 shows the excitation spectra for the A' and off-center STE luminescence band up to the vacuum ultraviolet energy region. The excitation spectra for the A' luminescence bands exhibit a remarkable response at 3.78 eV which corresponds to the C absorption band. In general, luminescence bands due to the Tl^+-type centers doped in alkali halide crystals are not efficiently excited in the energy region above the band gap of the host crystal, because photo-excited carriers are immediately self-trapped owing to the strong electron-phonon interaction. However, the luminescence bands due to the Ag^- centers doped in CsI crystals are efficiently excited even in the energy range above the band gap of CsI host crystals. The excitation spectrum for the A' luminescence band exhibits the similar structure to that for the off-center STE luminescence band in this energy range above the band gap. These results indicate that the efficient energy transfer from the CsI host crystals to the Ag^- centers occurs through the reabsorption of the off-center STE luminescence by the C absorption band.

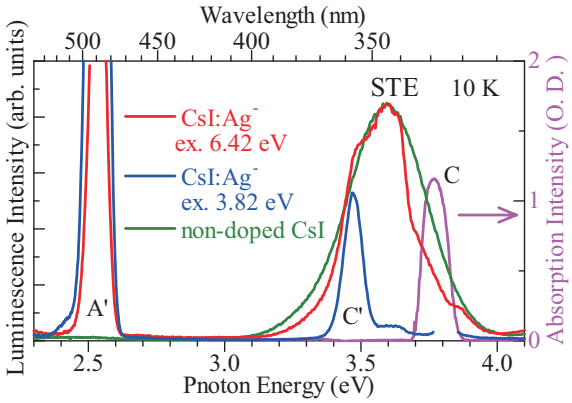

Fig. 1. Luminescence and absorption spectra of CsI:Ag^- and non-doped CsI crystals.

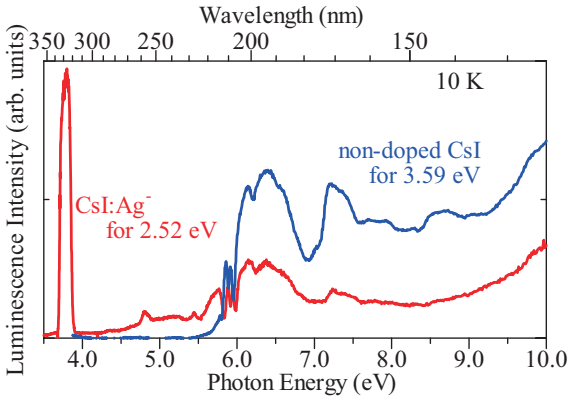

Fig. 2. Excitation spectra for the A' luminescence band of CsI:Ag^- and the off-center STE luminescence band of non-doped CsI crystals.

[1] M. J. Weber, J. Lumi. **100** (2002) 35.
[2] S. Shimanuki, M. Watanabe and T. Kawai, Phys. Stat. Sol. (b) **208** (1998) 105.

BL3B

Relaxed Exciton Luminescence of CsCl Heavily Doped with CsI

N. Ohno and A. Ohno

Graduate School of Engineering, Osaka Electro-Communication University, Neyagawa, Osaka 572-8530, Japan

Extensive studies have been made on luminescence arising from localized relaxed excitons in alkali chlorides containing iodine impurities. Stimulation in iodine absorption bands of dilute I^--doped alkali chlorides produces characteristic luminescence bands under excitation with UV light or with X-rays at low temperatures. These luminescence bands have been well explained in terms of localized relaxed excitons at ICl^- molecule (I^- monomer) and a complex of two iodine ions (I^- dimer) [1,2]. However, optical and luminescence properties of heavily iodine-doped alkali chloride crystals have not been examined sufficiently for applying to high efficient scintillation materials. The authors have reported luminescence properties of KCl heavily doped with KI so far [3]. The present report describes the results of CsCl heavily doped with CsI.

The crystals of CsCl:I were grown by the Bridgeman method from reagent grade CsCl added with an appropriate amount of CsI (up to 5 mol %). The optical measurements were made at 6 K.

The luminescence spectra excited with photons near the exciton absorption region of CsCl were almost the same as those of the previous studies [3]: two luminescence bands peaking at 3.95 eV (monomer emission) and 5.12 eV (dimer emission) are found at 6 K. Photoexcitation spectra detected at 5.11 eV for various CsI mol % of CsCl:I crystals are shown in Fig. 1. The each spectrum has been normalized at unity at the maximum. The excitation peaks at 6.50 and 6.65 eV of 0.01 mol % crystal move toward the lower energy side with increasing CsI concentration. The low energy shift of the excitation bands suggests that there coexist dimers, trimers and lager sizes of I^- ions (CsI cluster) in heavily-doped CsCl:I crystal as can been seen in the case of heavily-doped KCl:I [4].

The luminescence energies of the trimers and clusters of I^- ions in heavily doped CsCl:I crystals are expected to be different from that of I^- dimers. We have examined the photoluminescence spectra excited at various photon energies. The results for 1 mol % crystal are shown in Fig. 2. It is clearly confirmed that the peak energy of the luminescence band moves towards the low energy side when excited with lower photon energy. These luminescence bands are supposed to be the composite bands due to radiative annihilation of the relaxed exciton at dimers, trimers and clusters of I^- ions [4].

In CsCl crystals containing CsI above 1 mol %, there exists a small amount of dimer centers as compared with monomers, and moreover the amount of trimers and clusters of CsI is extremely smaller than those of monomers and dimers. However, the luminescence intensities of such large-sized centers are found to be comparable with that of the dimer emission. This fact suggests that the excitons trapped in CsI clusters in heavily doped CsCl:I crystals would give the high luminescence efficiency. The similar mechanism has been reported in and heavily-doped KCl:I [4] and CsI:Na systems [5], where the observed luminescence enhancement originates from excitons in small-sized KI or NaI particles in host crystals.

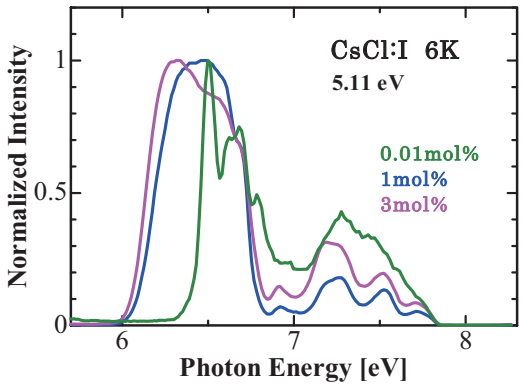

Fig. 1. Photoexcitation spectra of CsCl:I crystals detected at 5.11 eV for various CsI mol % at 6 K.

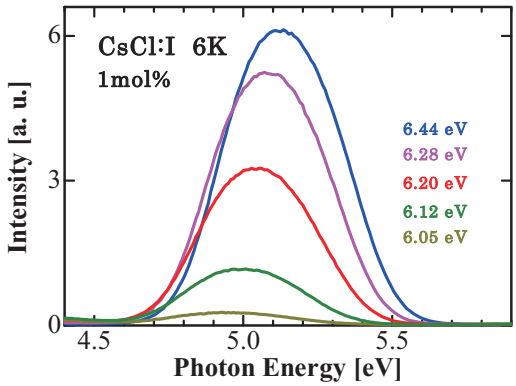

Fig. 2. Photoluminescence spectra of CsCl:I (1 mol %) excited at various photon energies at 6 K.

[1] N. Nagasawa, J. Phys. Soc. Jpn. **27** (1969) 1535.
[2] K. Kan'no, K. Tanaka and T. Hayashi, Rev. Solid State Sciences **4** (1990) 383, and references therein.
[3] M. Yoshida and N. Ohno, Proc. Int. Conf. on Excitonic Processes in Condensed Matter (1996) 231.
[4] A. Ohno and N. Ohno, Phys. Status Solidi C **8** (2011) 112.
[5] M. Nakayama, N. Ando, T. Miyoshi, J. Hirai and H. Nishimura, Jpn. J. Appl. Phys. **41** (2002) L263.

BL3B

Origin of Luminescence Bands in $NaBi(WO_4)_2$ Crystals

M. Kitaura[1], M. Fujita[2], A. Ohnishi[1], M. Sasaki[1] and Sangeeta[3]
[1]*Department of Physics, Facility of Science, Yamagata University, Yamagata 990-8560, Japan*
[2]*Japan Coast Guard Academy, Kure 737-8512, Japan*
[3]*Bhabha Atomic Research Center, Munbai 400 085, India*

$NaBi(WO_4)_2$ belongs to the family of double tungstates expressed by the chemical formula $NaT(WO_4)_2$, in which T is occupied by trivalent cations. This material attracts interest for practical use as Cerenkov radiator to detect ultra high-energy radiation and charged particles. Despite of such an important material in high-energy physics experiment, optical properties of $NaBi(WO_4)_2$ have not been much investigated, as compared to other metal tungstates. In the present study, reflectivity and photoluminescence spectra of $NaBi(WO_4)_2$ have been measured using synchrotron radiation.

The crystals of $NaBi(WO_4)_2$ were provided from Bhabha Atomic Research Centre, Mumbai, India. They were grown from melt by the Czochralski method. The samples used in our experiment were attached at the cold finger of a LHe flow-type cryostate, and cooled down at 10 K. The reflectivity spectra were measured using a calibrated silicon diode in the measurement chamber. The photo-luminescence spectra were measured for various excitation wavelength by the combination of a grating monochromator and a CCD detector.

Figure 1 shows the contour plot of excitation-emission spectra of $NaBi(WO_4)_2$ (lower part), together with reflectivity spectrum (upper part). These data were measured at 10 K. A prominent peak is observed at 312 nm in the reflectivity spectrum. An emission band appears at 538 nm under excitation with photons around 340 nm. As the excitation wavelength is decreased from 340 nm to 320 nm, the 538 nm band is weakened, and another band appears at 484 nm. This band is predominantly observed under excitation in shorter excitation wavelength. These results are almost agreement with the results by Tyagi *et al*. [1].

Two emission bands are observed at 484 and 538 nm in $NaBi(WO_4)_2$ excited by photons in the fundamental absorption region. The 484 and 538 nm bands are similar to the blue (443 nm) and green (551 nm) bands in $PbWO_4$, respectively. Itoh *et al*. [2] have explained the origin of these bands as follows: The blue band is ascribed to radiative decay of excitons self-trapped on regular WO_4 tetrahedra, while the green band is likely assigned to excitons localized on WO_6 octahedra of inclusions. $NaBi(WO_4)_2$ crystallizes in the scheelite structure in which W ions locate inside tetrahedrons of four O ions. It is thus more likely that the 2.65 eV band is linked to regular WO_4 tetrahedra. The 2.34 eV band may be due to WO_6 octahedra, because there is the possibility that sodium tungstates composed of WO_6 octahedra, e.g., $NaWO_3$ and $Na_2W_2O_7$, are included as low temperature phases. Decay kinetics of the 2.65 and 2.34 eV bands is now in investigation with Nd^{3+}:YAG laser system, in order to clarify excited state dynamics of the self-trapped excitons of complex molecular ion type.

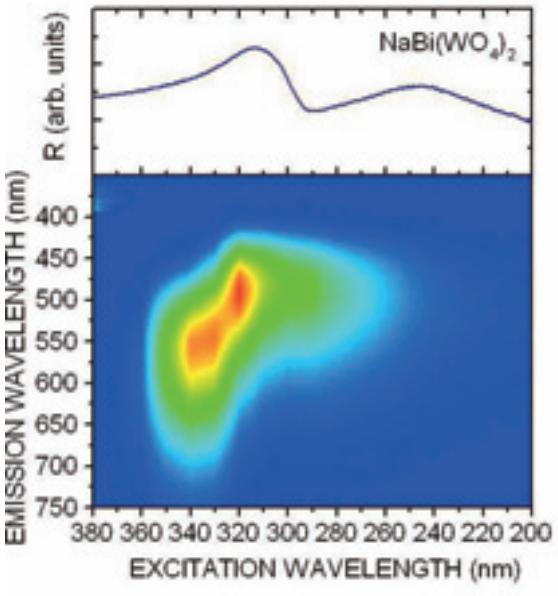

Fig. 1. Reflectivity spectra (upper part) and contour plot of excitation-emission spectra (lower part) of $NaBi(WO_4)_2$ measured at 10K.

[1] M. Tyagi *et al*., J. Lumi. **132** (2012) 41.
[2] M. Itoh *et al*., Phys. Rev. B **62** (2000) 12825.

BL4B

Valence State Analysis of Co Ions in $Pr_{1-x}Ca_xCoO_{3-\delta}$

T. Yoshioka[1] and T. Yamamoto[1, 2]

[1]*Faculty of Science and Engineering, Waseda University, Tokyo169-8555, Japan*
[2]*Institute of Condensed-Matter Science, Waseda University, Tokyo 169-8555, Japan*

Rare-earth cobaltates, $R_{1-x}A_xCoO_{3-\delta}$ (R = rare-earth, A = alkaline-earth), have been extensively studied for last fifty years because of their characteristic thermal, electrical, and magnetic properties [1-3]. For a thorough understanding of such properties, it is necessary to investigate the charge compensation mechanism due to the doping of the alkaline-earth ions in $RCoO_3$. However, the mechanisms of charge compensation have not yet been thoroughly understood for these rare-earth cobaltates with alkaline-earth ions. In this study, the valence state analysis of Co ions in $Pr_{1-x}Ca_xCoO_{3-\delta}$ (x=0, 0.5) are carried out by the Co-L_3 X-ray absorption near-edge structure (XANES) measurements at different temperature.

All $Pr_{1-x}Ca_xCoO_{3-\delta}$ samples were synthesized by the conventional solid-state reaction method. Co-L_3 XANES spectra were recorded at BL4B in UVSOR using the total-electron-yield (TEY) method. All the sample powders were mounted on carbon adhesive tape. Synchrotron radiation from the storage ring was monochromatized by a varied-line-spacing plane grating (800 lines/mm). The energy resolution of the incident beams ($E/\Delta E$) was set to 3000 by tuning the slit width at the upper and lower reaches of the grating. To see a temperature dependence of the Co-L_3 XANES spectra, all the spectra were collected at room temperature and 105 K.

Prior to the XANES analysis, all the samples were characterized by the X-ray diffraction (XRD). No extra peaks were found in the observed XRD patterns except for those of the perovskite structured $Pr_{1-x}Ca_xCoO_{3-\delta}$. Then the samples were determined to be crystallized in a single-phased orthorhombic perovskite structure (Pbnm).

Observed Co-L_3 XANES spectra of $PrCoO_3$ and $Pr_{0.5}Ca_{0.5}CoO_{3-\delta}$ are compared in Fig. 1. In order to investigate the difference in the spectral profiles among these two, the observed spectra were deconvoluted into three components by using Gaussian functions (dashed lines in Fig. 1). It is found that relative intensity of peak A to B increases and peak C to B decrease with doping Ca^{2+} ions both at room temperature and 105K. In order to see the change in spectral profiles of Co-L_3 XANES quantitatively, the relative intensities of peaks A and C to B, i.e., I_A/I_B and I_C/I_B, respectively, are plotted in Figs. 2(a) and (b), respectively.

As shown in Fig. 2, the relative intensities of peak A and C to B increase and decrease, respectively, with increasing of doped Ca^{2+} ions both at room temperature and 105K. Furthermore, if we compare the spectra at 105K to the spectra of room temperature, the relative intensity I_A/I_B and I_C/I_B is smaller and larger, respectively. These experimental results suggest that the distributions of Co 3d band of $Pr_{1-x}Ca_xCoO_{3-\delta}$ are different between at room temperature and 105K.

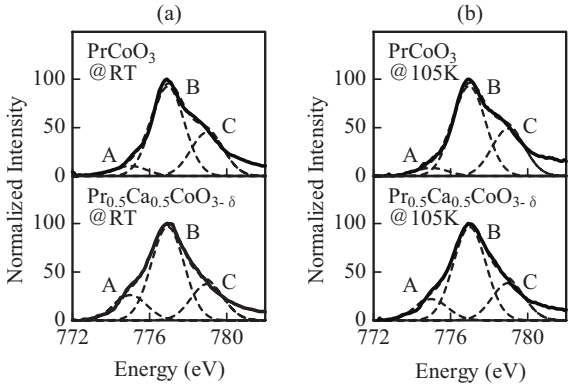

Fig. 1. Observed Co-L_3 XANES spectra of $PrCoO_3$ and $Pr_{0.5}Ca_{0.5}CoO_{3-\delta}$ (a) at room temperature and (b) at 105K. Dashed lines denote spectra deconvoluted into three components of the Gaussian function.

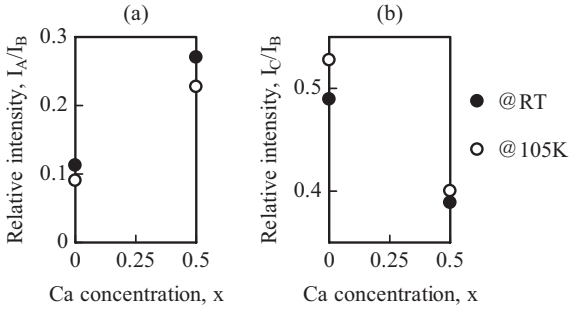

Fig. 2. Relative intensities of (a) Peak A to B, I_A/I_B, and (b) Peak C to B, I_C/I_B in Co-L_3 XANES spectra of $Pr_{1-x}Ca_xCoO_{3-\delta}$ (x=0, 0.5) as a function of the concentration of Ca^{2+} ions.

[1] G. Ch. Kostogloudis *et al.*, Solid State Ionics **106** (1998) 207.
[2] H. Masuda *et al.*, J. Phys. Soc. Jpn. **72** (2003) 873.
[3] S. Tsubouchi *et al.*, Phys. Rev. B **69** (2004) 144406.
[4] J. Zhou *et al.*, J. Phys.: Condens. Matter **20** (2008) 055222.

BL5U

Angle-Resolved Photoemission Spectroscopy of a Mixed Valence System $Sm_{1-x}Y_xS$

K. Imura[1], T. Hajiri[1, 2], M. Kaneko[2], Y. Nishi[3], H. S. Suzuki[4], N. K. Sato[3], T. Ito[2], M. Matsunami[1, 5] and S. Kimura[1, 5]

[1]*UVSOR Facility, Institute for Molecular Science, Okazaki 444-8585, Japan*
[2]*Graduate School of Engineering, Nagoya University, Nagoya 464-8603, Japan*
[3]*Graduate School of Science, Nagoya University, Nagoya 464-8602, Japan*
[4]*Nuclear Scattering Group, National Institute for Materials Science, Tsukuba 305-0047, Japan*
[5]*School of Physical Sciences, The Graduate University for Advanced Studies, Okazaki 444-8585, Japan*

Samarium monosulfide (SmS) is a prototypical compound that exhibits an insulator-to-metal transition by applying external pressure. This phase transition is accompanied by a color change from black to golden-yellow, namely B-G transition. The energy gap of about $E_g \sim 0.1$ eV evaluated by an electrical resistivity measurement at ambient pressure decreases forward a critical pressure of the B-G transition. Although angle resolved photoemission spectroscopy (ARPES) is one of powerful techniques to study electronic structure as well as a mechanism of this transition, unfortunately, pressure study is impossible.

On the other hand, it has been reported that the B-G transition is induced by site substitution [1]. Then we focused onto the $Sm_{1-x}Y_xS$ system and performed ARPES measurement in order to reveal the mechanism of the B-G transition.

Single crystals of $Sm_{1-x}Y_xS$ ($x = 0$, 0.17, 0.33) were grown by the Bridgman technique using a high-frequency induction furnace installed at NIMS [Figs. 1 (a) and 1 (b)]. ARPES measurement on these crystals was performed at the VUV-ARPES beamline BL5U of UVSOR. The obtained inner potential V_0 values 13.4 eV for $x = 0$, 13.7 eV for $x = 0.17$ and 15.2 eV for $x = 0.33$, by analyzing $h\nu$-dependence (27 - 84 eV) of energy distribution curve of highly-dispersive S 3*p* bands.

Figure 1 (c) shows the *x*-dependence of lattice constant. As increasing *x* up to 0.17, lattice constant decreases monotonically. At $x = 0.17$, the lattice constant suddenly shrinks by the B-G transition. This discontinuous volume change suggests a valence transition of Sm ions ($Sm^{2+} \rightarrow Sm^{3+} + e^-$), because the ionic radius of Sm^{3+} is smaller than that of Sm^{2+}.

The ARPES image of pure-SmS near the Γ point ($h\nu = 61$ eV) at 10 K is shown in Fig. 1 (d). The dispersive feature of the S 3*p* bands at the binding energy of about 3.2-6.5 eV is consistent with previous ARPES study and LDA band structure calculation [2, 3]. Flat bands in the binding energy below 2.5 eV originates from the multiplet structure of the Sm^{2+} 4*f* final state. The top of the flat Sm^{2+} 4*f* state is far from the Fermi level. This is consistent with the activation-type *T*-dependence of electrical resistivity $\rho(T)$ [4] and the absence of the Drude response of the optical conductivity $\sigma(\omega)$ [5].

In the golden phase of $x = 0.33$ shown in Fig.1 (e), on the other hand, the top of the Sm^{2+} 4*f* state shifts to the Fermi level. This result is consistent with the metallic property in the golden phase. The observation suggests that the insulator-to-metal transition occurs owing to the touch of the Sm^{2+} 4*f* state to the Fermi level.

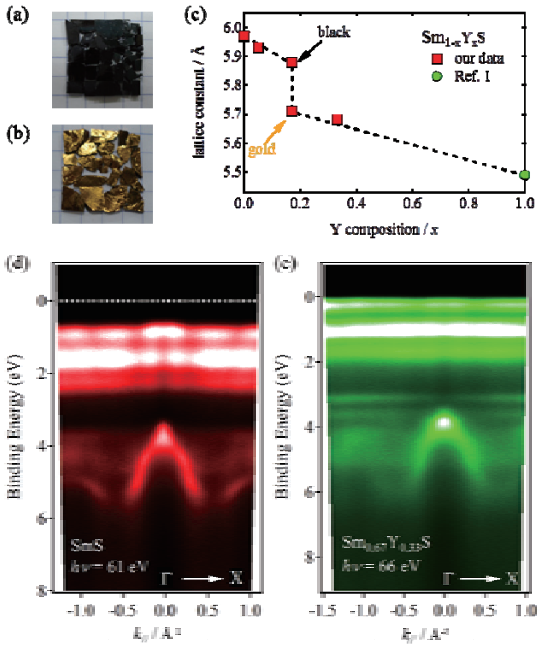

Fig. 1 Single crystals of (a) pure-SmS (black phase) and (b) $Sm_{0.67}Y_{0.33}S$ (golden phase). (c) Yttrium substitution dependence of lattice constant. Dotted lines are guide to the eye. ARPES images near the Γ point on the X-Γ-X line of (d) $x = 0$ ($h\nu = 61$ eV) and (e) $x = 0.33$ ($h\nu = 66$ eV) at 10 K.

[1] T. Penny and F. Holtzberg, Phys. Rev. Lett. **34** (1975) 322.
[2] T. Ito *et al.*, Phys. Rev. B **65** (2002) 155202.
[3] V. N. Antonov, B. N. Harmon and A. N. Yaresko, Phys. Rev. B **66** (2002) 165208.
[4] K. Matsubayashi *et al.*, J. Phys. Soc. Jpn. **76** (2007) 064601.
[5] T. Mizuno *et al.*, J. Phys. Soc. Jpn. **77** (2008) 113704.

BL5U

Valence-Band Electronic Structure of $Fe_{2-x}M_xVAl$ (M = Co, Ir)

T. Nomoto[1], K. Soda[2], H. Kondo[1], S. Harada[2], M. Kato[2], H. Miyazaki[3] and Y. Nishino[3]

[1]*Department of Physical Science and Engineering, Nagoya University, Nagoya 464-8603, Japan*

[2]*Graduate School of Engineering, Nagoya University, Nagoya 464-8603, Japan*

[3]*Graduate School of Engineering, Nagoya Institute of Technology, Nagoya 466-8555, Japan*

Heusler-type alloy Fe_2VAl is a half metal, the Fermi level E_F of which is located within a pseudo gap. Due to this electronic structure, small change in its composition or substitution of the fourth element may remarkably enhance its thermoelectric properties [1]. For $Fe_{2-x}M_xVAl$ (M = Co, Rh, Ir), their thermoelectric power negatively increases on the M substitution. In spite of Co belonging to the same group as Rh and Ir, however, the dependence of its thermoelectric power S on substituting amount x is different from those of the Rh and Ir substitutions [1]. In this report, we have studied electronic structures of $Fe_{2-x}M_xVAl$ by means of photoelectron spectroscopy and first principle calculation to clarify the origin of the difference in S.

Photoelectron spectroscopy was carried out in the angle-integrated mode for polycrystalline samples of $Fe_{1.96}M_{0.04}VAl$. Electronic structures were calculated with the Wien2k code [2] and a 2x2x2 super-cell of $Fe_{63}MV_{32}Al_{32}$. In the calculation, the lattice constant was set at an experimental one of Fe_2VAl without lattice relaxation and magnetic ordering.

Figure 1 shows typical valence-band photoelectron spectra of $Fe_{1.96}M_{0.04}VAl$ recorded at the excitation photon energy $h\nu$ of 44 eV, which is sufficiently lower than the Fe 3p-3d threshold, and so-called off-resonance (anti-resonance) spectra at $h\nu$ = 52 eV, where the Fe 3d photoemission is suppressed due to the Fe 3p-3d resonance. Thus the off-resonance spectra show the partial density of states (DOS) for other than the Fe 3d states, while the difference spectra between those recorded at $h\nu$ = 44 and 52 eV represent the Fe 3d partial DOS. The spectra for Co substitution resemble quite well ones for the Ir substitution but show a small hump around the binding energy E_B of 0.4 eV.

Calculated total and partial DOS of $Fe_{63}MV_{32}Al_{32}$ are presented near E_F in Fig. 2. Compared to Fe_2VAl, the overall shape of total DOS is little changed but is shifted towards the high binding energy side as a whole on the Co and Ir substitutions. This explains the observed negative S, since S may be proportional to the energy gradient of DOS at E_F. For both Ir and Co substitutions, the Ir 5d and Co 3d states form a common band; the Ir 5d states dominate the higher binding energy side of the main Fe-V 3d band, while the Co 3d states are well hybridized with the whole 3d band. Most noticeable spectral difference between Co and Ir substitutions is the appearance of a peak just above E_F, derived from the Co 3d impurity-like states. These differences are ascribed to the difference in the spatial extent and energy position of the Co 3d and Ir 5d states, and hence their hybridization with surrounding elements. The calculated DOS suggests that the thermoelectric power for $Fe_{63}CoV_{32}Al_{32}$ (-110 μVK^{-1} at 300 K) may be larger in magnitude than that for $Fe_{63}IrV_{32}Al_{32}$ (-70 μVK^{-1}), which is, however, inconsistent with the experimental results [1]. The peak in the present spin-independent calculation would split in the ferromagnetic phase, which might reduce S for $Fe_{2-x}Co_xVAl$. Such in-pseudogap states are not clear in the present experimental spectra, since the spectra are suffered from modification by surface.

[1] Y. Nishino, Mater. Sci. Eng. **18** (2011) 142001.
[2] P. Blaha *et al*., Comput. Phys. Comun. **59** (1990) 399.

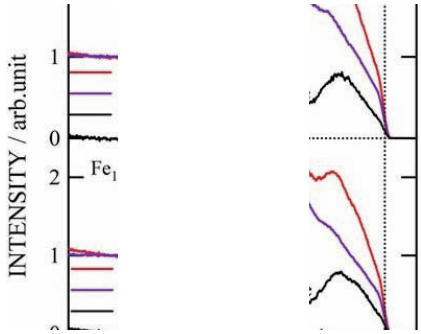

Fig. 1. Valence-band spectra of $Fe_{1.96}M_{0.04}VAl$.

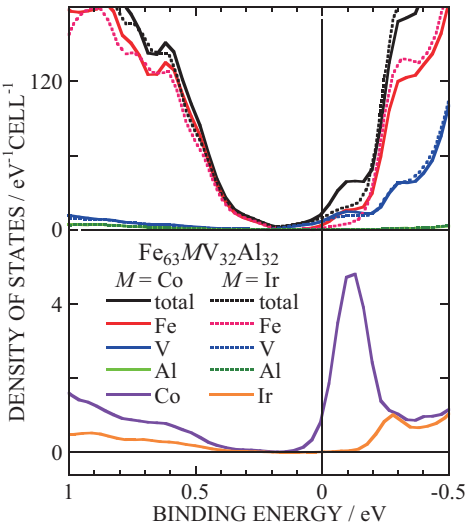

Fig. 2. Calculated density of states of $Fe_{63}MV_{32}Al_{32}$.

BL5U

Fabrication of Single-Crystalline EuO Thin Films with SrO Buffer Layer

H. Momiyama[1], H. Miyazaki[2], T. Hajiri[3, 4], M. Matsunami[4, 5], T. Ito[3] and S. Kimura[4, 5]

[1]*Department of Frontier Materials, Nagoya Institute of Technology, Nagoya 466-8555, Japan*

[2]*Center for Fostering Young and Innovative Researchers, Nagoya Institute of Technology, Nagoya 466-8555, Japan*

[3]*Graduate School of Engineering, Nagoya University, Nagoya 464-8603, Japan*

[4]*UVSOR Facility, Institute for Molecular Science, Okazaki 444-8585, Japan*

[5]*School of Physical Sciences, The Graduate University for Advanced Studies (SOKENDAI), Okazaki 444-8585, Japan*

Europium monoxide (EuO), a ferromagnetic semiconductor, with Curie temperature (T_c) of 69 K, is attracting attention due to its anomalous magneto-optical and transport properties [1, 2]. In the case of electron doping, T_c increases to as high as 200 K. Therefore EuO is one of candidate compounds for next-generation spintronics applications such as spinfilter [3, 4]. To growth high quality ultrathin films, it is important to satisfy small lattice mismatch between EuO and substrate or buffer layer. Then we adopt SrO as buffer layer in between EuO thin film and $SrTiO_3$ substrate, as shown in Fig. 1. SrO forms a rock-salt type crystal structure with a lattice constant of 0.5144 nm, which is the same crystal structure and similar lattice constant as EuO (The lattice mismatch between SrO and EuO is 0.3 %). Due to the quite small lattice mismatch, EuO ultrathin films with a few atomic layers are expected to be epitaxially grown on the SrO buffer layer. To check the existence of the impurity, such as Eu_2O_3 Eu-metal and Eu valence number of the surface of the thin films, we performed photoemission spectroscopy (PES) measurements of the fabricated thin films.

Single-crystalline EuO ultrathin films and SrO buffer layer with thickness of about 2 and 5 nm, respectively, were grown using a molecular beam epitaxy (MBE) method onto 0.05 wt% Nb-doped $SrTiO_3$ (001) single-crystalline substrates. The PES measurements were performed at the beamline BL5U of UVSOR-II combined with the MBE system. The EuO ultrathin films were prepared in the growth chamber and were transferred to a 3D-ARPES chamber under UHV condition.

Figure 2 shows the PES spectra of EuO 2 nm / SrO 5 nm / $SrTiO_3$ [Fig. 2 (a)] and EuO 5 nm / $SrTiO_3$ [Fig. 2(b)] measured at $h\nu = 38$ eV at 10 K. In the case of EuO 2 nm / SrO 5 nm/ $SrTiO_3$ in Fig. 2 (a), only Eu^{2+} 4*f* and O^{2-} 2*p* exist, in spite that the Eu^{3+} 4*f* and metallic states originating from Eu_2O_3 and Eu metal, respectively, are observed in EuO 2 nm / $SrTiO_3$ in Fig. 2(b) [5]. These results suggest that the SrO buffer layer protects the oxygen diffusion from $SrTiO_3$ substrate to the EuO thin film. Due to the quite small lattice mismatch at the interface and protect the oxygen diffusion, we successfully fabricated single crystalline EuO ultrathin films with a few atomic layers. The technique is useful for next generation spintoronics devices such as a spin filter.

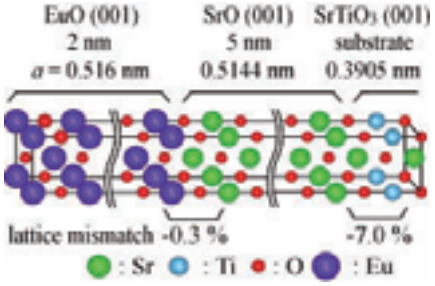

Fig. 1. Atomic structure of EuO (001) thin film with SrO buffer layer onto $SrTiO_3$ substrate. Lattice constant of $SrTiO_3$, SrO and EuO and lattice mismatch between $SrTiO_3$–SrO and SrO–EuO are shown in the figure.

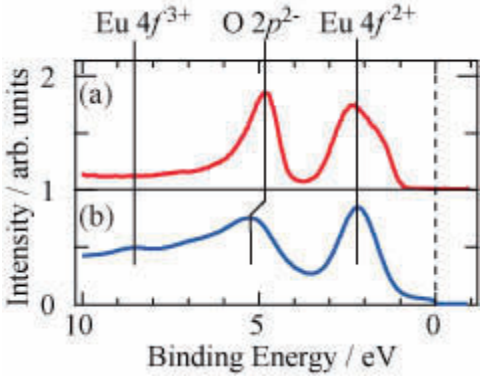

Fig. 2. Photoemission spectra of EuO 2 nm / SrO 5 nm / $SrTiO_3$ (a), EuO 5 nm / $SrTiO_3$ (b) at the temperature of 10 K with the photon energy of 38 eV, respectively.

[1] N. Tsuda *et al.*, *Electronic Conduction in Oxides* (Springers College) (1976).
[2] A. Mauger *et al.*, J. Phys. (paris) **39** (1978) 1125.
[3] A. Schmehl *et al.*, Nature Mater. **6** (2007) 882.
[4] M. Müller *et al.*, J. Appl. Phys. **105** (2009) 07C917.
[5] H. Lee *et al.*, J. Appl. Phys. **102** (2009) 053903.

BL5U

Angle-Resolved Photoemission Study on YbPtSb

Y. Shimura[1], R. Niwa[1], T. Ito[1, 2], T. Hajiri[1], S. Kimura[3, 4], M. Matsunami[3, 4] and H. S. Suzuki[5]

[1]*Graduate School of Engineering, Nagoya University, Nagoya 464-8603, Japan*

[2] *Nagoya University Synchrotron Radiation Research Center, Nagoya University, Nagoya 464-8603, Japan*

[3]*Editorial Board, UVSOR Facility, Institute for Molecular Science, Okazaki 444-8585, Japan*

[4]*School of Physical Sciences, The Graduate University for Advanced Studies (SOKENDAI), Okazaki 444-8585, Japan*

[5]*National Institute for Materials Science, Tsukuba 305-0047, Japan*

A topological insulator, whose physical properties at the bulk of the system are characterized as insulating or semimetal, while those at the surface as an anomalous metal, attracts much attention as a new spintronics device. It becomes central issue to investigate the anomalous metallic surface states, which appears as the linear dispersions intersecting each other between the bulk energy gap ('so called Dirac-corn'). So far, angle-resolved photoemission spectroscopy (ARPES) plays a dominant role to establish the 3D topological insulating nature and to probe the topology of their surface states especially in the binary Bi-based series of compounds [1].

Recently, half-Heusler ternary compounds XYZ (XY: transition or rare-earth metal, Z: pnictogen) have been expected to be a new platforms for topological quantum phenomena as spintronic utilization with tunable multifunctionalities (superconductivity, magnetism, heavy-fermion etc.), since the ground state changes from topologically trivial (semiconducting) to topologically nontrivial (semimetallic) as the characteristic energy difference between the Γ_6 and Γ_8 energy levels changes from negative to positive by changing combination of X, Y, and Z atoms [2, 3].

Among half-Heusler ternary compounds, YbPtSb with mostly localized Yb^{3+} ions [4] might be categorized as a border between the nontrivial and the trivial case as a reference compound LuPtSb. Furthermore, the exceptionally large specific heat coefficient γ = 8 J/mol K^2 as well as a very tiny ordered moment below T_c = 0.4 K has been observed on YbPtSb suggest its additional functionalities due to strong electron correlation effects [5].

In the present study, we have performed ARPES measurements on YbPtSb to clarify the existence of a topologically nontrivial state as well as its relation with extremely heavy carriers.

Figure 1 (a) shows the band structure along the ΓKX symmetry line of YbPtSb obtained by plotting the intensity of ARPES spectra with hν = 30 eV photons. Fig. 1(b) shows the result of LDA band calculation of LuPtSb, referred as the localized Yb^{3+} ground state, with spin-orbit coupling using the WIEN2k code for comparison. We found that the valence electronic structure around the G point can be qualitatively reproduced by the band calculation though the bandwidth in the experiment seems to be narrower by twice than the calculation, possibly due to electron correlation effect. On the other hand, we found qualitative discrepancies near the Fermi level. For example, while the calculation on LuPtSb expects only one zero-gap semiconducting nature, two types of Fermi surfaces (FSs), suggesting the semimetallic nature, have been observed by ARPES. One is light FSs at the Γ point and the other is a heavy FS at the X point. Though the origin of the observed differences is not clear yet, one possibility is a sizable hybridization effect of the Yb 4f states with conduction electrons. To elucidate the character of the observed FSs as well as the symmetry of the energy dispersions, further studies using polarization dependent ARPES and systematic studies on LuPtSb are intended.

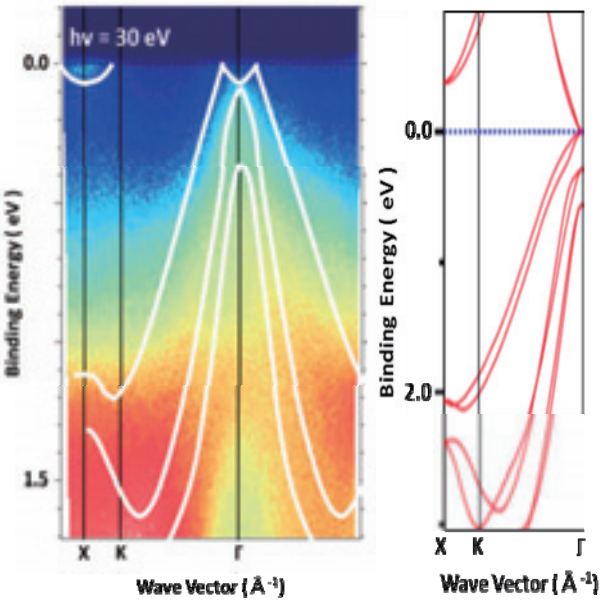

Fig. 1. (a) ARPES image along the ΓKX symmetry line. White lines are guide for eyes. (b) Band structure calculation of LuPtSb.

[1] For example, M. Z. Hasan and C. L. Kane, Rev. Mod. Phys. **82** (2010) 3045.
[2] S. Chadov *et al*., Nature Mat. **9** (2010) 541.
[3] H. Lin *et al*., Nature Mat. **9** (2010) 546.
[4] T. Koyama *et al*., J. Phys. Soc. Jpn. **80** (2011) SA097.
[5] Y. Nakanishi *et al*., Phys. Status Solidi B **247** (2010) 754.

BL5U

Temperature Dependent Photoemission Spectra of $CaCu_3Ti_4O_{12}$

H. J. Im[1], T. Sakurada[1], M. Tsunekawa[2], K. Kawata[1], T. Watanabe[1], H. Miyazaki[3] and S. Kimura[4, 5]

[1]*Department of Advanced Physics, Hirosaki University, Hirosaki 036-8561, Japan*
[2]*Faculty of Education, Shiga University, Shiga 522-8522, Japan*
[3]*Department of Environmental and Materials Engineering, Nagoya Institute of Technology, Japan*
[4]*UVSOR Facility, Institute for Molecular Science, Okazaki 444-8585, Japan*
[5]*School of Physical Sciences, The Graduate University for Advanced Studies, Okazaki 444-8585, Japan*

A-site ordered perovskite $CaCu_3Ti_4O_{12}$ (CCTO) has been attracted much attention due to an extremely high dielectric constant (ε) and its intriguing properties [1]. Particularly, the temperature dependence of physical properties has been of interest. For example, the absence of any structural phase transition around the temperature of 100 K, where the high ε dramatically drops, is quite a different point with the typical perovskites, the so-called ferroelectrics, where the crystal structural phase transition usually causes the large change of ε. In addition, the electrical resistivity measurements have showed the variable range hopping conductivity in the insulator phase below about 150 K. To clarify the mechanism of such unusual physical properties, we have carried out the temperature dependent photoemission (PES) experiments on a single crystal CCTO.

PES measurements have performed at BL5U. The used photon energy is 90 eV. The sample surface in the (100) plane was prepared by cleaving *in situ* in the ultra-high vacuum. The measurement temperatures are from 150 to 300 K. A wide acceptable angle-integrated mode (±16°) was used to accumulate the data. The Fermi level was referred to that of gold thin film electrically connected with the sample. In PES experiments of an insulator sample, one should take care of the possibility of charging in the sample during measurement. Therefore, we have investigated the intrinsic properties of CCTO by comparing with spectra obtained by controlling the photon flux with the slit size of the beamline.

Figure 1 (a) shows PES spectra in valence band regime at hv = 90 eV and T = 300 K with various slit sizes. The mainly Cu 3d peak is observed around 4 eV with intense intensity. The broad peak of mainly O 2p states is observed around 5 - 8 eV. Small broad shoulder of mainly Cu 3d – O 2p hybridized states is observed around 2 eV as in our previous results [2]. It is found that the whole shapes of spectra are almost the same in the various slit sizes. However, the small shift of Cu 3d peak is observed in the slit sizes larger than 70×70 μm^2. We recognize that the typical behavior of the charging is the decease of the intensity of 2 eV peak with increasing the photon flux as shown in the inset of Fig. 1 (a). This can be a good standard point in analyzing the PES spectra.

Figure 1 (b) is the plot of temperature dependent PES spectra in the valence band regime at hv = 90 eV with the slit size of 30×30 μm^2 where the sample is not charged up safely as in the above photon flux dependent PES experiments. We find that the whole spectra shapes are almost the same over whole temperature. There is a small shift of Cu 3d peak around 4 eV to the higher binding energy with decreasing the temperature. And the PES spectra reveal that the intensity of Cu 3d – O 2p hybridized states around 2 eV increases with decreasing the temperature, particularly below T = 200 K. This is completely the opposite behavior to the typical case of the charging, indicating the intrinsic property of CCTO. It should be also noted that this temperature is roughly consistent with the temperature where the type of the transport property is changed as mentioned above. The physical meaning and the relation with the high ε are not clear yet and should be studied further.

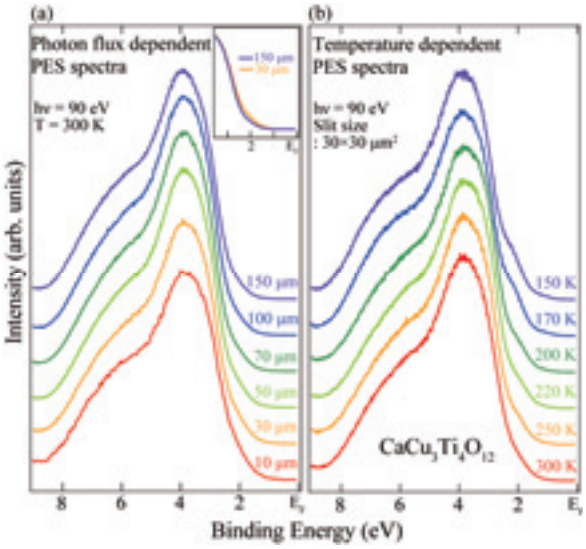

Fig. 1. (a) Photon-flux dependent and temperature dependent photoemission spectra of $CaCu_3Ti_4O_{12}$ in the valence band regime, obtained with the photon energy of 90 eV.

[1] M. A. Subramanian *et al.*, J. Solid State Chem. **151** (2000) 323.
[2] H. J. Im *et al.*, UVSOR Activity Report **38** (2011) 87.

BL6B

Electric Field Effect on Superionic Conductor

T. Awano

Department of Electronic Engineering, Tohoku Gakuin University, Tagajo 985-8537, Japan

Ionic conductivity of superionic conductors is as large as those in liquids. Movement of ions in superionic conductors is not in phase bout random as in liquids. However, existence of correlative movement of conduction ions by Coulomb repulsive interaction has been expected for a long time. Recently calculation simulation has been showing attractive interaction between conduction ions by electronic effect. Low energy spectral characteristics indicate such collective motion of conducting ions[1,2]. If coherent excitation of ionic movement occurs by coherent external electric field, ionic conductivity seems to increase drastically. In this study, I have investigated far-infrared and millimeter wave spectra of superionic conducting crystal $RbAg_4I_5$ in external electric field.

Fig. 1 shows reflectivity deviation at far-infrared region of $RbAg_4I_5$ applied electric field. Reflectivity around 74 and 91 cm^{-1} were increased by applying 1kHz sinusoidal wave of amplitude of 3.0 V_{pp}. This spectral change disappeared after removing the applied electric field. These peaks seem to be due to deformed breathing modes of Ag-I tetrahedron. Such enhancement of breathing mode seems to be due to increase of the number of silver and iodine tetrahedron pairs. Contrary to this result, in my previous experiment of silver atom doping, absorption bands at 45 and 70 cm^{-1} decreased [3].

Fig. 2 shows change of reflectivity ratio at submillimeter region of $RbAg_4I_5$ applied electric field. The ratio means reflectivity divided by that before applying the electric field. Red line shows that in applying 1kHz sinusoidal wave of amplitude of 3.0 V_{pp}. Intensity of "attempt mode" around 19 cm^{-1} increased. This spectral change disappeared after removing the applied electric field. The attempt mode is a motion of silver ion trying to escape surrounding tetrahedron. Such enhancement of attempt mode seems to be due to increase of the collective movement of silver ions. Contrary to this result, in my previous experiment of silver or iodine doping, the dielectric constants decreased by silver addition and increased by iodine addition in the spectral region below 20cm^{-1}[3].

In Raman scattering spectra of the doped $RbAg_4I_5$, drastic spectral changes were reported previously[4,5]. The scattering intensity in terahertz region (under 50cm^{-1}) increased by silver addition and decreased by iodine addition. Moreover fine structures at low temperature disappeared in the case of iodine addition. Reflectivity results of this study described above were contrary to those of the Raman spectroscopic study.

A part of the spectral change by applying electric field seems to be interpreted as change of local density of silver ion or iodine ion. (The latter means silver ion vacancy.)

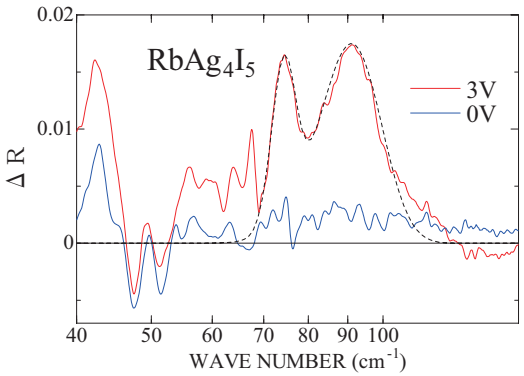

Fig. 1. Reflectivity change of $RbAg_4I_5$ by applying electric field. Red line shows that in applying AC1kHz, 3V. Blue line shows that after reducing the voltage to zero. The dotted line shows Gaussian curves at 74 and 91 cm^{-1}. Small peaks are due to remaining interference fringes.

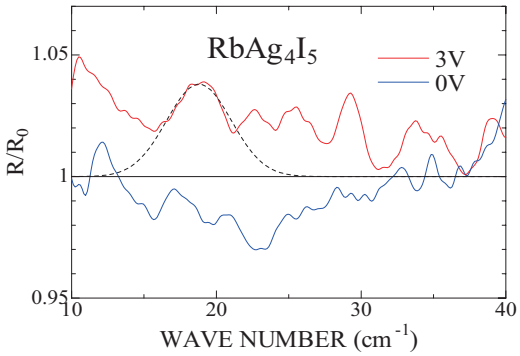

Fig. 2. Change of reflectivity ratio of $RbAg_4I_5$ by applying electric field. Red line shows that in applying AC1kHz, 3V. Blue line shows that after reducing the voltage to zero. R_0 means the reflectivity before applying the electric field. The dotted line shows Gaussian curve at 19cm^{-1}. Small peaks are due to remaining interference fringes.

[1] T. Awano, Infrared Phys. and Tech. **51** (2008) 458.
[2] T. Awano and T. Takahashi, J. Phys. Soc. Jpn. **79** Suppl. A (2010) 118.
[3] T. Awano, UVSOR Activity Report **36** (2009)100.
[4] S. Bredikhin, T. Hattori and M. Ishigame, Solid State Ionics **67** (1994) 311.
[5] S. Bredikhin, N. Kovaleva, T. Hattori and M. Ishigame, Solid State Ionics **74** (1994) 149.

BL7U

Temperature Dependences of Electronic Structure and Chemical Potential of $FeSb_2$

T. Takeuchi[1, 2, 3, 4] and T. Shimada[4]

[1]*EcoTopia Science Institute, Nagoya University, Nagoya 464-8603, Japan*
[2]*Department of Crystalline Materials Science, Nagoya University, Nagoya 464-8603, Japan*
[3]*PRESTO, Japan Science and Technology Agency, Saitama 332- 0012, Japan*
[4]*Department of Applied Physics, Nagoya University, 464-8603, Japan*

$FeSb_2$ is known to possess an extremely large magnitude of Seebeck coefficient reaching -40 mV/K, which is 200 times larger than that of practical thermoelectric materials [1]. The mechanism leading to this huge Seebeck coefficient has not been well understood yet. Therefore, in this study, by emoplying high-resolution angle resolved photoemission spectroscopy (ARPES), we investigated the characteristics of electronic structure near the chemical potential because it is the main factor to determine the electron transport properties including Seebeck coefficient.

Single grained $FeSb_2$ samples were grown in the Sb-flux, and we succeeded in obtaining $FeSb_2$ single crystals of ~1x1x1 mm^3 in dimension. The sample possesses a large evolution of Seebeck coefficient at around 10~30 K as it was reported previously, though the magnitude of Seebeck coefficient is slightly smaller than the reported value.

ARPES measurements were conducted at BL7U of UVSOR using photon energy of 22 eV. This photon energy was selected so as the measurable momentum area to cover the whole first Brillouin zone. The orientation of samples were determined by taking Laue pictures, and the clean surface was prepared by cleaving samples in the ultra high vacuum chamber of APRES apparatus just before the measurement.

Figure 1 shows temperature dependence of EDC spectrum measured at Γ point. The peak intensity and spectrum weight increases with decreasing temperature, and it becomes evident especially at low temperatures where the large magnitude of Seebeck coefficient is observable. Since the peak was located at the energy 200 meV below the chemical potential, it is naturally understood that the evolution of the peak in measured EDC cannot contribute the increasing magnitude of Seebeck coefficient. The observed evolution of peak suggests the presence of the similar increase of peak intensity near the chemical potential in the conduction band to cause the large increase in the magnitude of Seebeck coefficient with negative sign. In such a case, the chemical potential must possess drastic variation with temperature in the same manner as the significant variation of Seebeck coefficient. Thus, in the next step, we focused on the chemical potential shift.

The temperature dependence of chemical potential $\mu(T)-\varepsilon_F$ estimated from the peak energy in EDC was plotted in Fig.2 (a). We also plotted the contribution of chemical potential on Seebeck coefficient, $(\mu(T)-\varepsilon_F)/(|e|T)$ [2], together with the measured Seebck coefficient in Fig. 2 (b). The temperature dependence of $(\mu(T)-\varepsilon_F)/(|e|T)$ shows extremely good consistency with the measured value. This fact unambiguously indicates that the large magnitude of Seebeck coefficient is brought about by the electronic structure effect rather than the phonon-drag effect.

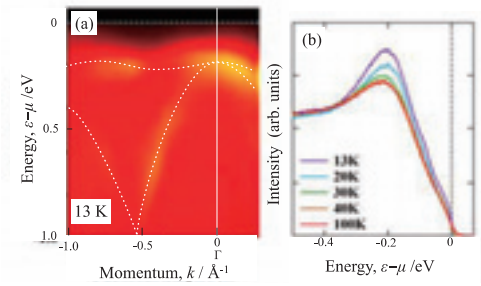

Fig. 1. (a) ARPES intensity $I(\boldsymbol{k},\varepsilon)$ of $FeSb_2$ measured at 13 K near the Γ point. The energy distribution curves $I(\Gamma,\varepsilon)$ measured at various temperatures are shown in (b). Evolution of the Peak intensity is observable with decreasing temperature especially below 30 K, where the magnitude of Seebeck coefficient increases.

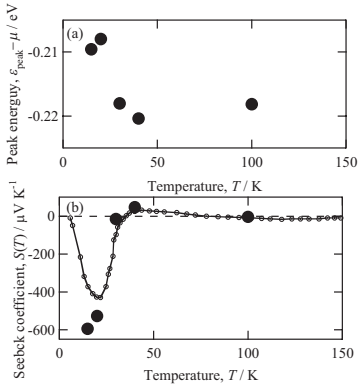

Fig. 2. Temperature dependence of (a) peak energy, (b) Seebeck coefficient and $(\mu(T)-\varepsilon_F)/(|e|T)$. The peak energy at 0 K is assumed to be –0.219 meV. The characteristic temperature dependence of Seebeck coefficient was clearly reproduced by that calculated from the chemical potential shift.

[1] A. Bentien, *et al.*, EPL **80** (2007) 17008.
[2] T. Takeuchi *et al.*, Mat. Trans. **51** (2010) 421.

BL7U

Observation of Anomalous Peaks in the Photoelectron Spectra of Highly Oriented Pyrolytic Graphite: Folding of the Band due to the Surface Charge Density Wave Transition

S. Tanaka[1], M. Matsunami[2,3] and S. Kimura[2,3]

[1]*The Insititue of Scientific and Industrial Research, Osaka University, Mihogaoka, Ibaraki 567-0047, Japan*

[2]*UVSOR Facility, Institute for Molecular Science, Okazaki 444-8585, Japan*

[2]*School of Physical Sciences, The Graduate University for Advanced Studies, Okazaki 444-8585, Japan*

Graphite has been regarded as a "textbook" system for solid state physics for many years because of its unique characteristics. In this study, the angle-resolved photoelectron spectroscopy (ARPES) with low-photon energy (7-16eV) is used for the investigation of HOPG (Highly Oriented Pyrolytic Graphite) at a low temperature. We observed for the first time peaks in the low binding energy region (from the Fermi level to 0.7 eV) of the surface normal photoelectron spectra at 11K, which disappear above ~30K. Based on the dispersion along both the parallel and normal to the surface, the peaks are ascribed to the emission from the K(H)-point that is backfolded into the Γ-point as a result of the two-dimensional superperiodicity. The surface charge density wave (CDW) transition is proposed for the driving mechanism of the superperiodicity based on the temperature-dependence of the photoelectron intensity[1].

The ARPES experiments were carried out at the BL7U SAMRAI of the UVSOR-II. Figure (a) shows a series of normal-emission photoelectron spectra of HOPG at 11K using the photon energies from 7.3 to 16eV (0.3eV-step). A distinct peak just below the Fermi level and a smaller peak at the binding energy (E_B) ~0.7eV are visible when the photon energy is near 11.5eV with a relatively high intensity. In the normal emission, only the electron states along the Γ-A line of the Brillouin zone (BZ) can be observed. Therefore, the peaks at E_B~0eV and 0.7eV in the ARPES spectra [Fig. (a)] are paradoxical since the π-band of the graphite crosses E_F near the K-point, and no corresponding bands near E_F have been reported at the center of the BZ.

In order to obtain the information about the two anomalous peaks, we measured the band dispersion by using ARPES at 11K. In Fig. (b), the dispersions of these peaks as a function of $k_{//}$ (inverse vector parallel to the surface) are displayed. The color map shows photoelectron intensity taken at hν=13eV. The dispersions of the two peaks closely resemble those of the π-bands around the K-point in the graphite. According to the photon-energy dependence of the surface normal photoelectron emission, it is also shown that the dispersion of these peaks along the k_z (surface normal) direction is similar to that along the K-H line. Therefore, these peaks cannot be assigned to the defect, edge, or surface states, but are

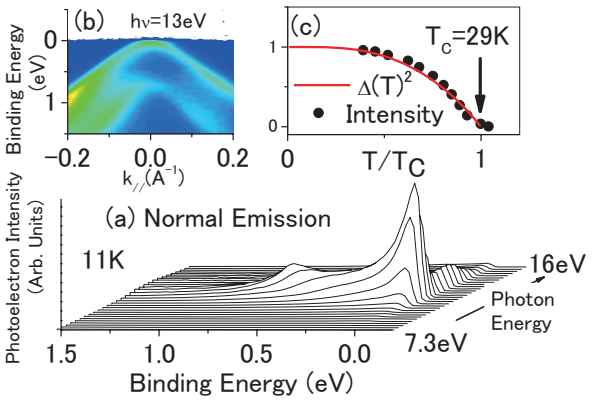

unambiguously ascribed to the electron emission from the π-band at the K(H)-point of the graphite. Then, we can conclude that the K-point of HOPG at 11K is backfolded into the Γ-point as a result of the formation of the $p\left(\sqrt{3}\times\sqrt{3}\right)R30^\circ$ or larger superperiodicity. The detection of the photoelectron emission from the K-point at the surface normal can be provided by the diffraction (scattering) by the reciprocal lattice vector of the 2D superlattice.

We measured the sample-temperature dependence of the photoelectron spectra in order to reveal the condition for the superperiodicity formation. In Fig. (c), the photoelectron intensity at E_B=0.016eV (solid circles) in the surface normal PES at hν=11.5eV is plotted as a function of the reduced temperature (divided by the critical temperature T_C=29K). This temperature-dependence is very similar to that of the X-ray reflection intensity of some materials corresponding to the superlattice formation as a result of the charge density wave (CDW) transition, which is well described with the square of the order-parameter Δ predicted by the BCS-law (solid line). Consequently, it is strongly suggested that the formation of the superlattice in HOPG is caused by the CDW transition. This observation demonstrates the advantage of the photoelectron spectroscopy with the tunable photons of the low energy.

[1] S. Tanaka, M. Matsunami and S. Kimura, Phys. Rev. B **84** (2011) 121411 (R) .

BL7U

Three-Dimensional Fermi Surface of $YbAl_2$ Studied by Angle-Resolved Photoemission Spectroscopy

M. Matsunami[1, 2], T. Hajiri[1], H. Miyazaki[1], M. Kosaka[3] and S. Kimura[1, 2]

[1]*UVSOR Facility, Institute for Molecular Science, Okazaki 444-8585, Japan*

[2]*School of Physical Sciences, The Graduate University for Advanced Studies (SOKENDAI), Okazaki 444-8585, Japan*

[3]*Graduate School of Science and Engineering, Saitama University, Saitama 338-8570, Japan*

The topology of the Fermi surface (FS) in the heavy-fermion systems directly reflects the degree of the hybridization between conduction band and 4*f* state (*c*-*f* hybridization) as a key concept for describing the heavy-fermion nature. Angle-resolved photoemission spectroscopy (ARPES) is a powerful tool to probe the *c*-*f* hybridized electronic structures. However, most of ARPES measurements have been performed on the basis of the surface Brillouin zone or by using the 4*d*-4*f* resonant process, in which the k_z dependence of the electronic structure and FS are ignored. Since the heavy-fermion systems generally have three-dimensional electronic structure and FS, ARPES measurements should be done along the bulk Brillouin zone.

$YbAl_2$, which crystallizes in the cubic Laves $MgCu_2$ structure, is a prototypical valence fluctuation system. The Yb mean valence has been estimated to be ~ +2.2 by the hard x-ray photoemission spectroscopy [1]. It strongly suggests that a strong *c*-*f* hybridization effect can be realized in $YbAl_2$. Hence $YbAl_2$ is well-suited system for studying the *c*-*f* hybridized electronic structures and the FS, particularly in comparison with the band structure calculations.

In this work, we have performed a three dimensional mapping of the FS for $YbAl_2$ by means of ARPES. The ARPES experiment was carried out at the undulator beamline BL7U "SAMRAI" in UVSOR-II [2]. The crystal orientation was determined by Laue x-ray diffraction. The single crystals of $YbAl_2$, which were grown by the Lithium flux method, were cleaved *in situ* along the (111) plane. The LDA band structure calculations were performed using the WIEN2k code.

Figure 1 (a) shows the bulk Brillouin zone of $YbAl_2$. Comparing the photon-energy dependence (16-29 eV) of ARPES data leading to the FS in the k_x-k_z plane with the LDA calculations as shown in Fig. 1 (b), the inner potential in this system was estimated to be 13.7 eV. Thus, the photon energy of $h\nu = 20$ eV are chosen so as to obtain the FS in the k_x-k_y plane as shown in Fig. 1 (c). Two FSs around Γ point in both the k_x-k_z and the k_x-k_y planes are well described by the LDA calculations. The results suggest the small renormalization effect in $YbAl_2$, which can be provided by the strong *c*-*f* hybridization, consistent with the extremely high Kondo temperature (above 2000 K).

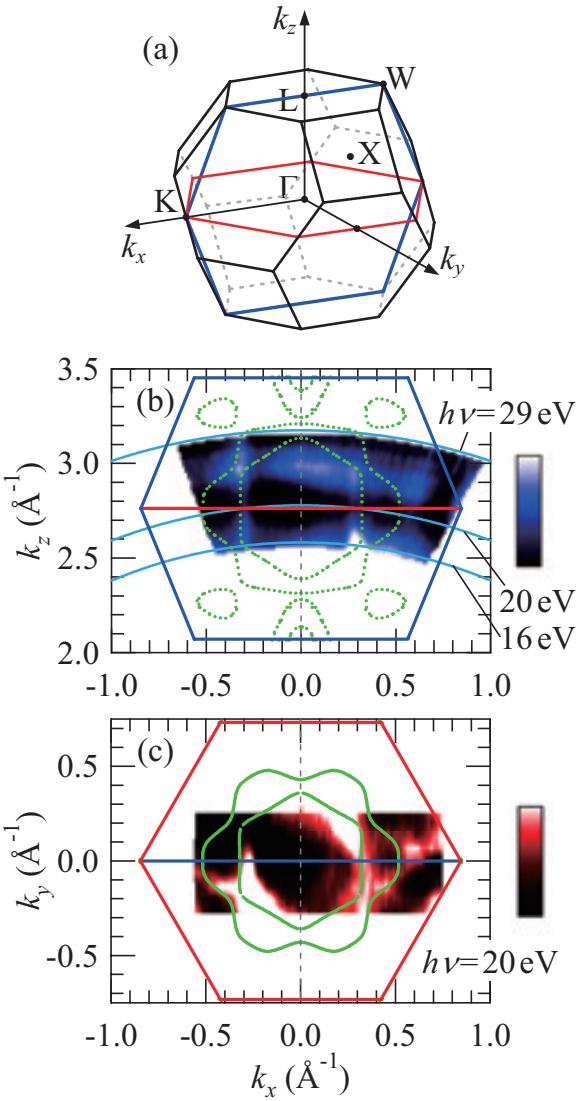

Fig. 1. (a) Brillouin zone of $YbAl_2$, in which the k_z corresponds to the (111) direction of the fcc Brillouin zone. (b) and (c) Fermi-surface (FS) mapping of $YbAl_2$ in the k_x-k_z plane and the k_x-k_y plane, respectively. The green dots and lines indicate the FSs obtained by the LDA band structure calculations.

[1] M. Matsunami *et al.*, J. Phys. Soc. Jpn. **81** (2012) 073702.

[2] S. Kimura *et al.*, Rev. Sci. Instrum. **81** (2010) 053104.

BL7U

The Orbital Characters of Low-Energy Electronic Structure in the Iron-Chalcogenide Superconductor $K_xFe_{2-y}Se_2$

F. Chen[1], Q. Q. Ge[1], M. Xu[1], Y. Zhang[1], X. P. Shen[1], M. Matsunami[2], S. Kimura[2] and D. L. Feng[1]

[1]*State Key Laboratory of Surface Physics, Department of Physics, and Advanced Materials Laboratory, Fudan University, Shanghai 200433, People's Republic of China*

[2]*UVSOR Facility, Institute for Molecular Science, Okazaki 444-8585, Japan*

The newly discovered $K_xFe_{2-y}Se_2$ superconductor exhibits many distinct properties from other iron-based superconductor [1], such as its parent compound and electronic structure [2, 3]. Since the electronic structures of iron-based superconductors are dominated by multiple *3d* orbitals [4, 5], to understand the unique properties of $K_xFe_{2-y}Se_2$, one needs to understand its orbital characters.

The intrinsic phase separation in $K_xFe_{2-y}Se_2$ superconductor leads to relatively lower concentration of superconducting phase compared to other iron-based superconductors, however, the strong photon intensity and variable polarizations of beamline BL7U at the ultraviolet synchrotron orbital radiation facility (UVSOR) enable us to successfully resolve the orbital characters of low-energy electronic structure.

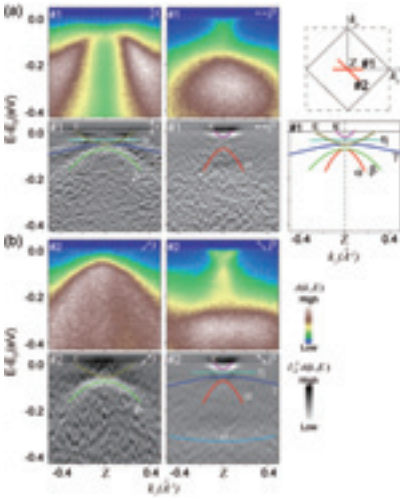

Fig. 1. The polarization-dependent APRES data around Z taken with 30 eV photon. (a) The photoemission spectra and their corresponding second derivatives with respect to energy taken in the s and p geometries, respectively, along Z-A direction. (b) is the same as panel a, but taken along Z-R direction.

Figure 1 shows the photoemission spectra around the *Z* point. In Fig. 1(a), the upper panels are the photoemission spectra taken along Z-A (#1) direction in the *s* and *p* geometries, respectively, and the lower panels are the corresponding second derivatives with respect to energy. Fig. 1(b) is similar to Fig. 1(a), except that the data were taken along Z-R (#2) direction. We could resolve three hole-like bands, α, β, and γ, two electron-like band, κ and ε, and two rather flat bands, ω and ω', around Z in Fig. 1.

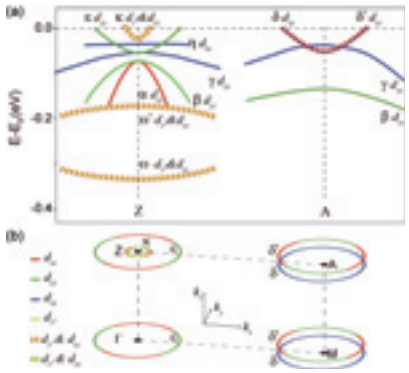

Fig. 2. (a) The summary of the orbital characters of low-energy electronic structure in $K_xFe_{2-y}Se_2$ superconductor along Z-A direction. (b) The illustration of the orbital characters on the Fermi surface sheets around Γ, M, Z, and A. The almost overlapping δ and δ' Fermi surface sheets around M and A are separated for a better illustration.

Exploiting the polarization-dependent angle-resolved photoemission spectroscopy (ARPES), we have determined the orbital characters of the low-energy electronic structure of $K_xFe_{2-y}Se_2$ superconductor (Fig. 2) by considering the spatial symmetries of Fe *3d* orbitals and their matrix element effects mentioned in refs.4 and 5. We found that the small electron pocket near the Z point is mostly dominated by the dz^2 orbitals, while the large Fermi cylinders around the zone corner are dominated by the *dxz*, *dyz*, and *dxy* orbitals. Moreover, we find that the Fermi cylinders are actually composed of two highly degenerate ones, indicating negligible interactions between them.

To a large extent, the $K_xFe_{2-y}Se_2$ superconductor shares similar orbital characters with other iron-based superconductors [4, 5], but with its own characteristics. The determined orbital characters would help to construct realistic model for $K_xFe_{2-y}Se_2$.

[1] J. G. Guo *et al*., Phys. Rev. B **82** (2010) 180520.
[2] Y. Zhang *et al*., Nature Mater. **10** (2011) 273.
[3] F. Chen *et al*., Phys. Rev. X **1** (2011) 021020.
[4] Y. Zhang *et al*., Phys. Rev. B **83** (2011) 054510.
[5] Y. Zhang *et al*., Phys. Rev. B **85** (2012) 085121.

BL7U

Angle-Resolved Photoemission Study on Non-Superconducting $Li_{1+x}FeAs$

T. Hajiri[1,2], T. Ito[1,3], R. Niwa[1], S. Hirate[1], M. Matsunami[2,4], B. H. Min[5], Y. S. Kwon[5] and S. Kimura[2,4]

[1]*Graduate School of Engineering, Nagoya University, Nagoya 464-8603, Japan*
[2]*UVSOR Facility, Institute for Molecular Science, Okazaki 444-8585, Japan*
[3]*Nagoya University Synchrotron radiation Research Center, Nagoya University, Nagoya, 464-8603, Japan*
[4]*School of Physical Sciences, The Graduate University for Advanced Studies (SOKENDAI), Okazaki 444-8585, Japan*
[5] *Department of Emerging Materials Science, DGIST, Daegu 711-873, Republic of Korea*

LiFeAs is an intriguing iron pnictide superconductor because it shows superconductivity (T_C = 18 K) without any structural and SDW/AFM transitions [1]. In pristine LiFeAs, we have demonstrated that the electronic structure can be fundamentally explained by a LDA band structure calculation. We have also pointed out the importance of the interband scattering between hole and electron Fermi surfaces in terms of the appearance of superconductivity [2]. In this system, the excess or deficiency of Li-ions from the stoichiometry has been reported to suppress the superconductivity [3] and enlarges spin fluctuation [4]. However, the reason of the suppression of the superconductivity owing to the off-stoichiometry has not been clarified yet.

To elucidate the effect of the Li excess or deficiency to the electronic structure, we performed a polarization-dependent three-dimensional angle-resolved photoemission spectroscopy (3D-ARPES) of a Li-excess LiFeAs ($Li_{1+x}FeAs$) without superconducting transition at BL7U, UVSOR-II.

Figure 1 shows a normal emission (k = 0 Å^{-1}) ARPES image of $Li_{1+x}FeAs$ measured at T = 12 K along the Z-A direction. The blue line indicates the trace of the peak positions of the momentum distribution curves (MDCs) and the green dashed lines indicate the dispersion curves derived from an LDA band calculation. The obtained band dispersion is strongly renormalized below 100 meV. The renormalized bare band is assumed as the green solid line in Fig. 1. The obtained band dispersion has kink structure that is away from the assumed bare band at about 20 meV and 100 meV.

In order to argue about the kink structure qualitatively, we performed the self-energy analysis. Figure 2 shows the real part of the self-energy ReΣ(ω), which is obtained by the subtraction of the assumed bare band dispersion from the MDC dispersion. The ReΣ(ω) spectrum clearly has two peaks; one is located at about 20 meV and the other at about 100 meV. The former is consistent with phonon energy position as shown by the dashed lines reported by Raman spectroscopy [5] and theory [6]. However, the later peak cannot be explained by the phonon origin. A recent inelastic neutron scattering (INS) study indicated that the spin excitation peak appears at around 100 meV as shown by a blue line [7], which is consistent with the observed higher-energy kink. This suggests that the higher-energy kink originates from magnetic excitations.

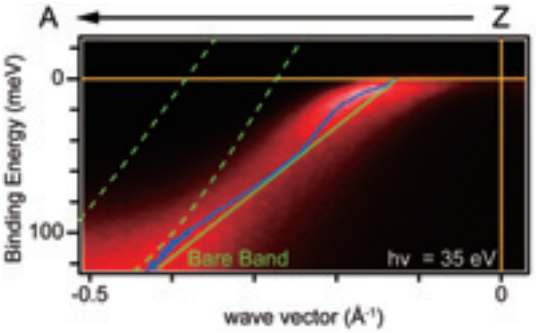

Fig. 1. ARPES image of $Li_{1+x}FeAs$ measured at T = 12 K along the Z-A direction.

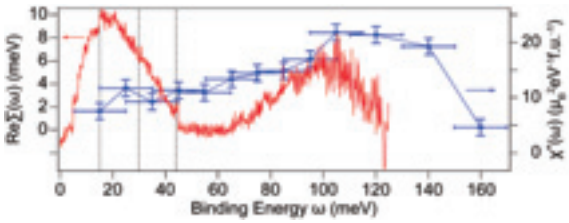

Fig. 2. The real part of the self-energy ReΣ(ω) indicated by a red solid line. Vertical dashed lines indicate the phonon energy position [5, 6] and blue line indicates the energy dependence of the local susceptibility of $Li_{0.94}FeAs$ obtained by INS [7].

[1] X. C. Wang *et al*., Solid State Commun. **148** (2008) 538.
[2] T. Hajiri *et al*., Phys. Rev. B **85** (2012) 094509.
[3] M. Wang *et al*., Phys. Rev. B **83** (2011) 220515(R).
[4] L. Ma *et al*., Phys. Rev. B **82** (2010) 180501(R).
[5] Y. J. Um *et al*., arXiv:1109.5797.
[6] R. A. Jishi *et al*., Adv. Condens. Matter Phys. **2010** (2010) 804343.
[7] M. Wang *et al*., Phys. Rev. B **83** (2011) 220515(R).

BL7U

Angle-Resolved Photoemission Study on Quasi-One-Dimensional Organic Conductor $(TMTSF)_2AsF_6$

S. Hirate[1], T. Hajiri[1], T. Ito[1, 3], S. Kimura[2, 4] and T. Nakamura[4, 5]

[1]*Graduated School of Engineering, Nagoya University, Nagoya 464-8603, Japan*
[2]*UVSOR Facility, Institute for Molecular Science, Okazaki 444-8585, Japan*
[3]*Nagoya University Synchrotron Radiation Research Center, Nagoya University, Nagoya 464-8603, Japan*
[4]*School of Physical Sciences, The Graduate University for Advanced Studies (SOKENDAI), Okazaki 444-8585, Japan*
[5]*Institute for Molecular Science, Okazaki 444-8585, Japan*

The Bechgaard salts $(TMTSF)_2X$ (TMTSF: tetramethyl-tetraselenofulvalene, X=AsF_6, PF_6, ClO_4, *etc*.) are the well-known models of quasi-one-dimensional systems. Owing to the stacks of planar TMTSF molecules in columns, quasi-one-dimensional conductivity appears. At low temperatures, this quasi-one-dimensionality results in an intriguing ground state such as a spin-density-wave (SDW) state, or a superconducting state, depending on anion X and pressure [1]. For $(TMTSF)_2AsF_6$, the SDW transition occurs at 12 K at ambient pressure.

In this study, we have performed angle-resolved photoemission spectroscopy (ARPES) on single-crystalline $(TMTSF)_2AsF_6$ to clarify the electric state and its relation to the anomalous properties. By utilizing the bulk-sensitive microfocus low-energy photons ($h\nu$ = 8 eV, 15×100 μm^2) at the BL7U, we have succeeded in directly observing the intrinsic electronic structure of $(TMTSF)_2AsF_6$.

Figure 1 shows the ARPES image near E_F along the ΓX high-symmetry line measured at T = 30 K. At the Γ point, the hole-like dispersive feature, which can be assigned to the TMTSF band [2], was clearly observed. In order to clarify the relation between the observed dispersive feature and the anomalous property, we analyzed the electronic structure near E_F around the Fermi/Luttinger surface in detail.

Figure 2 shows the second derivative of the ARPES image (Fig. 1) with enlarged scales. The weak dispersions (b) and (c) other than the main feature (a) appear at the low-binding energies. The origin of anomalous multiple dispersive features are not clear yet. Two separated excitations of spin and charge in one-dimensional electron systems has been expected by so called spin-charge separation model, which has recently been demonstrated on $SrCuO_2$ by the ARPES experiments [3]. Furthermore, an additional low-energy excitation due to the electron-photon coupling has been predicted by the recent theory [4]. To elucidate the present observation of the anomalous multiple dispersive features on $(TMTSF)_2AsF_6$, further studies are intended.

[1] T. Ishiguro *et al*., *Organic Supercondutors* (Springer-Verlag, Berlin, 1998).
[2] S. Ishibashi, Sci. Techonol. Adv. Mater. **10** (2009) 024311.
[3] B. J. Kim *et al*., Nat. Phys. **2** (2006) 397.
[4] F. F. Assaad, Phys. Rev. B **78** (2008) 155124.

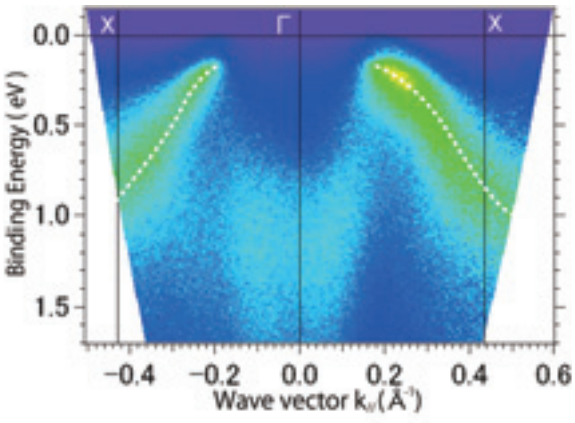

Fig. 1. ARPES image of $(TMTSF)_2AsF_6$ along the ΓX high-symmetry line measured at T = 30 K. Dashed lines are guide for eyes to trace a main dispersive feature.

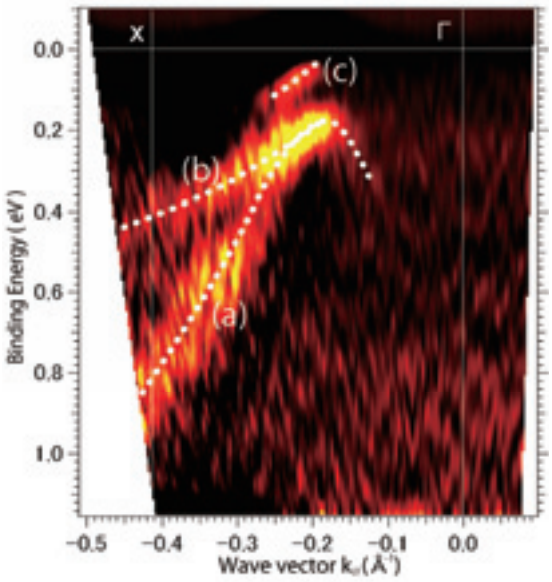

Fig. 2. Second derivative of ARPES image (Fig. 1) of $(TMTSF)_2AsF_6$ enlarged near E_F around the Fermi/Lutinger surface. Dashed lines (a), (b) and (c) are guide for eyes to trace the observed dispersive features.

BL7B

Optical Characterization and Computational Chemical Evaluation of Electronic Localized States in Polyolefin

T. Arai[1], M. Hosobuchi[1], N. Fuse[2], K. Takeda[1] and Y. Ohki[1]
[1]*Waseda University, 3-4-1 Ohkubo, Shinjuku-ku, Tokyo 169-8555, Japan*
[2]*Central Research Institute of Electric Power Industry, 2-6-1 Nagasaka, Yokosuka-shi, Kanagawa 240-0196, Japan*

Optical absorption spectra and photoluminescence spectra were obtained for eight kinds of polyolefin sheet samples using photons in a range from visible to vacuum ultraviolet. Almost all samples were found to exhibit an absorption peak at around 6.5 eV and a luminescence band at around 4.3 eV as shown in Figs. 1 and 2. The luminescence was found to be induced by the absorption. Furthermore, it was found that successive absorption of ultraviolet photons weakens the luminescence intensity [1, 2]. It is assumed from these results that α, β-unsaturated carbonyls are luminous and that the carbonyls are decomposed through the Norrish type II reaction by absorbing ultraviolet photons [3, 4]. In Norrish type II reaction, α, β-unsaturated carbonyls change to β, γ-unsaturated carbonyls, which are then separated into pure carbon double bonds and pure carbonyls by main chain scissions.

Quantum chemical calculations were carried out using polyethylene models with and without an unsaturated carbonyl to verify the above-mentioned assumption. From the calculation results, the model with an unsaturated carbonyl was found to have localized electronic states in the forbidden band as shown in Fig. 3. One of the differential energies between the states is close to the photon energy, by which the luminescence is induced. The bond length of a double bond, which is next to the carbonyl, was found to be longer at the excited singlet state than at the ground state. These results obtained by the quantum chemical calculations support the above-mentioned assumption of the luminescence center and its decomposition.

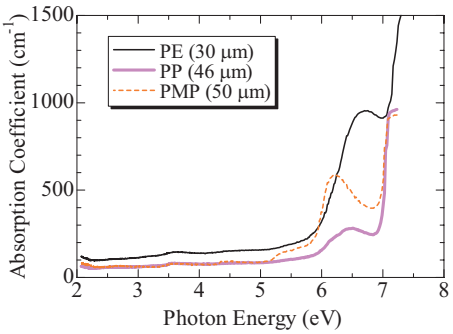

Fig. 1. Absorption spectra measured by vacuum ultraviolet spectroscopy observed for PE, PP and PMP. The numerals in parentheses are the thicknesses of the samples.

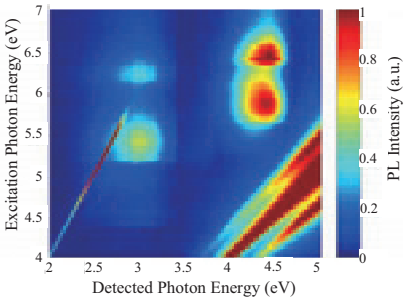

(a) PE

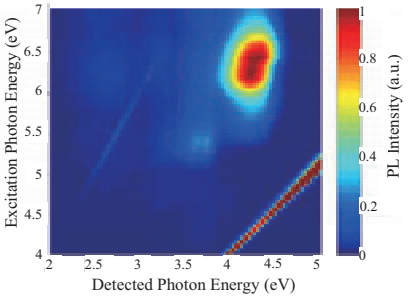

(b) PP

Fig. 2. Two-dimensional intensity distributions of various PL peaks observed for PE (a) and PP (b) at 10 K.

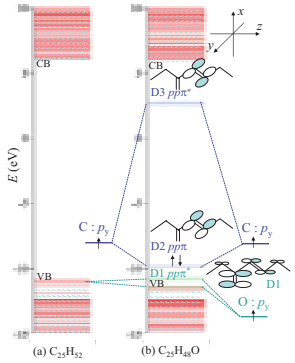

Fig. 3. The energy levels of $C_{25}H_{52}$ (a) and $C_{25}H_{48}O$ (b).

[1] T. Ito *et al.*, IEEJ Trans. FM **121** (2001) 865 (in Japanese).
[2] T. Ito, N. Fuse and Y. Ohki, IEEJ Trans. FM **124** (2004) 624.
[3] N. S. Allen, J. Homer and J. F. McKellar, J. Appl. Polym. Sci. **21** (1977) 2261.
[4] N. S. Allen and J. F. McKellar, J. Appl. Polym. Sci. **22** (1978) 3277.

BL7B

Optical Investigation on K_2NiF_4-Type Cobalt-Oxides in Vacuum Ultra-Violet Region

J. Fujioka[1], K. Ueda[1], M. Uchida[1], J. S. Lee[2] and Y. Tokura[1]

[1] *Department of Applied Physics, University of Tokyo, Tokyo 113-8656, Japan*

[2] *Department of Photonics and Applied Physics, Gwangju Institute of Science and Technology (GIST), Gwangju 500-712, Korea*

Spin state of the Co ions, particularly Co^{3+}, in cobalt-oxides has long been a controversial issue. Depending on the relative magnitude of the crystal field splitting against the Hund's rule coupling, the spin state for Co^{3+} with six 3d electrons can be low spin (LS, S=0), high spin (HS, S=2), or even intermediate spin (IS, S=1). Although this additional degree of freedom complicates the problem in understanding magnetic and relevant properties, it can also provide a chance to invoke novel functionality, such as the large thermoelectric power or spin state dependent charge transport.

For the half-doped layered perovskite $La_{1.5}Ca_{0.5}CoO_4$, a checkerboard-type charge order of Co^{2+} and Co^{3+} is realized with a high transition temperature T_{CO}~850 K, and the magnetic order occurs at comparably low temperature (T) around 30 K. Concerning the local spin state, Co^{2+} is usually considered to be in the HS state. As for Co^{3+}, Hollmann *et al*. recently proposed the temperature-induced spin-state transition by examining high-temperature magnetic susceptibility [1], although the high-temperature spin state is not determined between IS and HS.

In this article, we report the spin-state issue in the layered perovskite cobaltate based on the optical spectroscopy. From the temperature dependency of infrared-active optical phonons, we observed clear signatures of the temperature-induced spin-state transition particularly to IS around 400 K.

We measured reflectivity spectra for single crystals of $La_{1.5}Ca_{0.5}CoO_4$ between 12 meV and 5 eV using Fourier-transform spectrometer and grating-type spectrometer in temperature range between 300 K and 850 K. We obtained the reflectivity between 5 and 30 eV at room temperature by using synchrotron radiation at BL7B in UVSOR. We determined complex optical constants through the Kramers-Kronig transformation with proper extrapolations of reflectivity in the low and high energy regions.

Figure 1 (a) shows the reflectivity spectra up to 30 eV. Sharp peaks below 0.1 eV are assigned to infrared active optical phonons. A peak structure in energy range from 0.1-4 eV is assigned to charge transfer type transition between O-2p band and Co-3d band, or Co-3d interband transition. In the following, we focus the temperature dependence of the phonon spectra. Figure (b) shows optical conductivity spectra in the energy range between 20-50 meV. At 300 K, three peaks are visible around 33, 37 and 44 meV. These peaks are assigned to the Co-O bond bending mode. With increasing temperature, the peaks gradually broadens, as expected by structural anharmonicity. It should be noted that there are additional modes developing as temperature increases above 400 K around 30 meV (indicated by red triangles). This indicates that there is an additional structural distortion going on with an increase of temperature, and such a distortion should be understood differently from the structural distortion related to the charge order. Considering that the mode itself, supposing the tetragonal symmetry, is an apical oxygen bending mode, it would be reasonable to assume that the corresponding structural distortion is related to the apical oxygen, and the most plausible candidate should be Jahn-Teller distortion. It is of importance to note that among possible spin states of Co^{3+}, it is only the IS state that involves the Jahn-Teller distortion. This leads us to suggest that while the LS state of Co^{3+} would be dominant at the low temperature, the IS becomes populated as T increases across 400 K, which is substantially lower than the charge ordering transition temperature (850 K) .

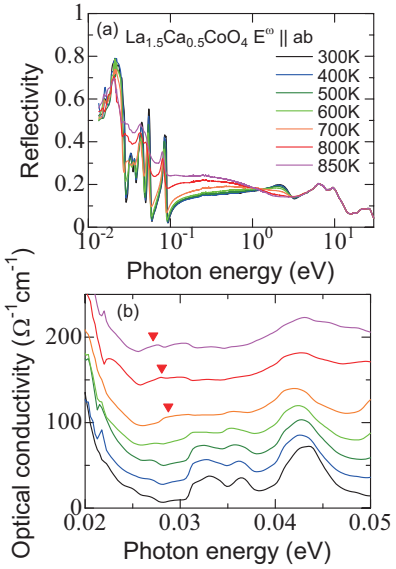

Fig. 1. (a) Reflectivity and (b) optical conductivity spectra for $La_{1.5}Ca_{0.5}CoO_4$ at various temperatures.

[1] N. Hollmann *et al.*, Phys. Rev. B **83** (2011). 174435.

BL7B

Decay Behaviors of Auger-Free Luminescence in Cs_2ZnCl_4

A. Ohnishi[1], M. Saito[1], M. Kitaura[1], M. Sasaki[1] and M. Itoh[2]

[1]*Depeartment of Physics, Yamagata University, Yamagata 990-8560, Japan*

[2]*Department of Electrical and Electronic Engineering, Shinshu University, Nagano 380-8553, Japan*

The crystal of Cs_2ZnCl_4 is composed of anionic $ZnCl_4$ tetrahedra separated from each other and interstitial Cs cations between them [1]. In the previous work [2], we have investigated optical properties of Cs_2ZnCl_4 crystals with the use of synchrotron radiation as a light source, and observed Auger-Free luminescence (AFL) resulting from a radiative transition between the Cl 3*p* valence band and the Cs 5*p* outermost core band. In the present study, we have studied decay behaviors of AFL using a time-correlated single-photon counting method under the single bunch operation.

Cs_2ZnCl_4 crystals were prepared by evaporating a stoichiometric mixture of solutions of CsCl and $ZnCl_2$. Experiments were performed at the BL7B beamline of UVSOR. Luminescence from samples was dispersed by a grating monochromator and detected by a microchannel-plate photomultiplier.

When Cs_2ZnCl_4 is excited at 10 K at 21.4 eV, three AFL bands peaking at 3.2 4.1 and 4.8 eV are observed. In Fig. 1, decay curves of AFL measured at 3.2, 4.1 and 4.8 eV are shown in semi-logarithmic scale, where decay curves are vertically displaced for comparison. The photo-excitation was made at 21.4 eV at 10 K. Three decay curves are parallel with each other. That is, the decay profile is fundamentally the same for each band. This result suggests that the life time is governed by that of the holes created on the outermost core band. We can see a somewhat fast component in the earlier stage of the decay curves. If we estimate the lifetime from a least-square fit to the single exponential decay by neglecting the component, the decay time is about 2.0 ns. The red straight line drawn on the experimental data of the 3.2 eV AFL shows a single exponential curve with lifetime of 2.0 ns. Figure 2 shows decay behaviors of the 4.1 eV band at 10 and 300 K. The decay time at 300 K is estimated to be 1.6 ns. The decay time is a little shorter than that at 10 K. This temperature dependence was the same for the AFL at 3.2 and 4.8 eV.

The life time of AFL is much longer compared to the lattice relaxation time. Thus, it is probable that the core hole induces some lattice distortion within the life time and interacts with the lattice vibrations. In fact, the AFL spectrum observed was red-shifted than the energy range expected within the rigid band model. Furthermore, the linewidths of AFL bands were found to be gradually broadened as increasing the sample temperature, though the overall structures of AFL spectrum were not very sensitive to the sample temperature between 10 and 300 K. These details will be reported somewhere.

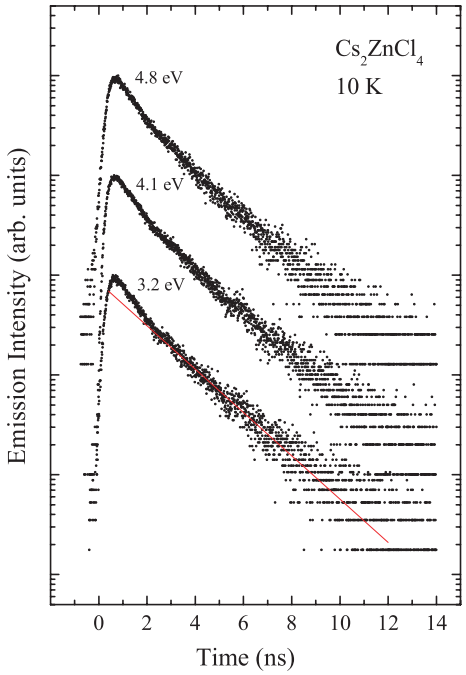

Fig. 1. Decay behaviors of AFL detected at 3.2, 4.1, and 4.8 eV in Cs_2ZnCl_4.

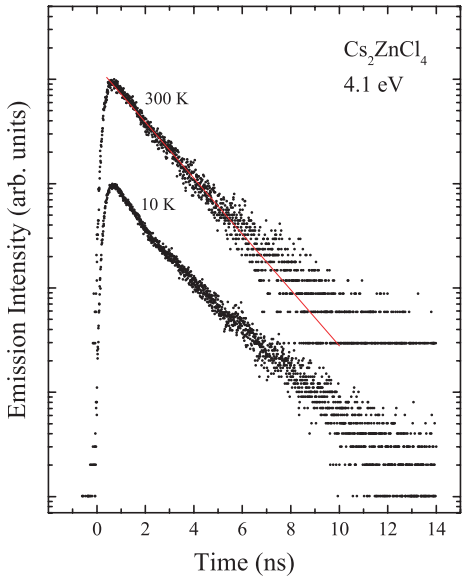

Fig. 2. Decay behaviors of AFL detected at 4.1 eV at 10 and 300 K in Cs_2ZnCl_4.

[1] J. A. Mcginnery, Inorg. Chem. **13** (1974) 1057.
[2] A. Ohnishi, T. Otomo, M. Kitaura and M. Sasaki, J. Phys. Soc. Jpn. **72** (2003) 2400.

BL7B

Electronic Status of Rare-Earth Ion in Glass Host by Characterizing Photoluminescence of Rare-Earth Doped APLF Glass Scintillator

M. Tsuboi[1], M. Kouno[1], K. Takeda[1], T. Nakazato[1], T. Shimizu[1], M. Cadatal-Raduban[1], K. Yamanoi[1], K. Sakai[1], R. Nishi[1], Y. Minami[1], Y. Arikawa[1], N. Sarukura[1], T. Norimatsu[1], M. Nakai[1], H. Azeti[1], T. Murata[2], S. Fujino[3], H. Yoshida[4], T. Suyama[5], K. Fukuda[5], A. Yoshikawa[6], N. Sato[7], H. Kan[7] and K. Kamada[8]

[1]*Inst. Laser Engineering, Osaka Univ.* ,[2]*Kumamoto Univ.* ,[3]*Kyushu Univ.* ,[4]*Ceramic Research Center of Nagasaki,* [5]*Tokuyama Corp.* ,[6]*Inst. Materials Research, Tohoku Univ.* ,[7]*Hamamatsu Photonics K.K.* ,[8]*Furukawa Co., Ltd.*

The realization of nuclear fusion is highly expected to satisfy the energy demand in the future. Fusion plasma diagnostics at higher plasma areal density than 3 g/cm^2 is one of the biggest breakthrough in nuclear fusion research. Scattered-neutron diagnostics [1] utilizing Pr^{3+}-doped $20Al(PO_3)_3$-80LiF (APLF+Pr) glass scintillator is expected to achieve plasma areal density measurement in fusion core. APLF+Pr, which have high sensitivity for scattered neutrons and fast response time about 5.4 ns, is the key factor of the measure.

In this work, we report the luminescence properties of APLF+Pr at different Pr^{3+} concentrations (0.5mol%～3mol%).

We have measured Photoluminescence (PL) spectra and Photoluminescence Excitation (PLE) spectra of APLF+Pr at 30K, 50K, 150K, 200K, 250K, and 300K. The experiment was conducted at BL7B utilizing G2 grating. PL spectra are measured with excitation wavelength at 80nm, 120nm, 150nm, 180nm, and 200nm. The APLF+Pr samples, having Pr+ density at 0.5mol%, 1mol%, 2mol%, and 3mol%, and cut into 10 mm × 10 mm × 10 mm, were prepared. PL and PLE spectra of Pr^{3+}-doped $LiCaAlF_6$ (Pr:LiCAF) was measured as well for comparison.

The PL spectra of APLF+Pr and Pr:LiCAF excited by 180 nm radiation are shown in Fig. 1. The green colored lines are corresponding to spectra of APLF+Pr with Pr^{3+} density at 0.5mol%, 1mol%, 2mol% and 3mol% and red line to that of Pr:LiCAF. The UV luminescence around 250 nm are observed for each samples.

The PLE spectra of APLF+Pr monitoring 240 nm, 400 nm, and 480 nm are illustrated in Fig. 2. The 240 nm emission is attributed to 4f5d→4f^2 transition. In the other hand, the 400 nm emission occurs from both 4f5d and $^1S_0$.

These consequences indicate that 5d state of Pr^{3+} in APLF glass host vary in wide range as shown in Fig. 3.

[1] M. Moran *et al.*, Rev. Sci. Instrum. **75** (2004) 3592.

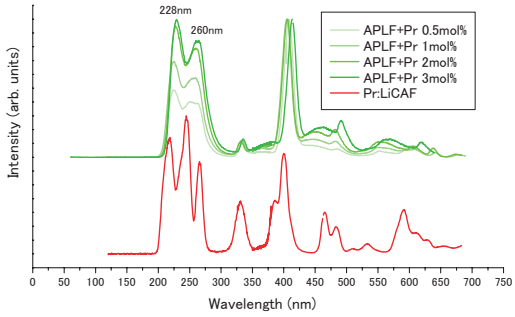

Fig. 1. PL spectra of APLF+Pr and Pr:LiCAF.

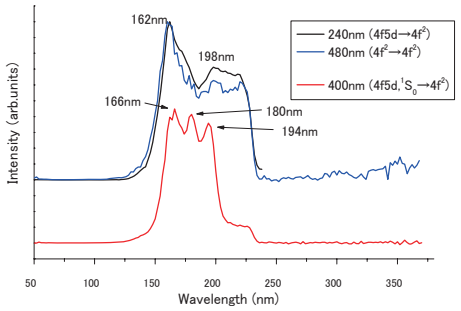

Fig. 2. PLE spectra of APLF+Pr.

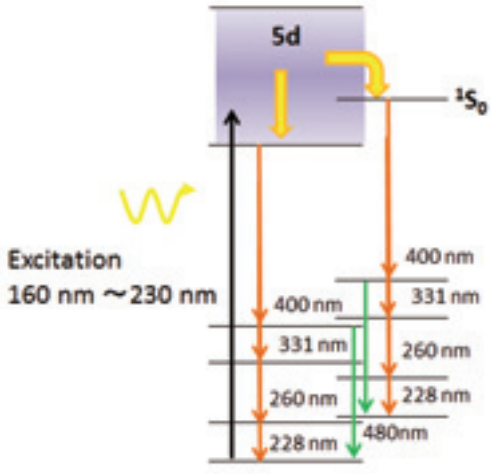

Fig. 3. Energy status of Pr^{3+} in APLF glass host.

BL7B

Vacuum UV Reflectance Spectrum of Diamond

H. Okamura
Graduate School of Science, Kobe University, Kobe 657-8501, Japan

Diamond is one of the most familiar and classical materials of all, with its well known crystal structure and the covalent bonding. Accordingly, its band structure has been studied extensively since the early stage of the band calculation technique. To examine the energy dependent band structure of a material, it is very useful to compare the dielectric function ε(ω) derived from the calculated band structure with that derived from the measured optical spectra. The Kramers- Kronig analysis is often used to derive ε(ω) from a reflectance spectrum $R(\omega)$ measured over a wide photon energy range.

In spite of the familiarity of this material in the condensed matter and materials physics, experimental studies of its optical properties above the fundamental absorption edge have been only reported by a small number of papers [1-5]. Namely, several papers on the UV and vacuum UV (VUV) reflectance measurements of diamond appeared in the 1960's, but since then, no further measurements seem to have been reported [6], in spite of the persisting interest from the theoretical point of view [6-8].

In view of the above situation, we have measured the reflectance of diamond in the VUV using the synchrotron radiation source at BL7B of UVSOR. The diamond sample used was a diamond anvil used for high pressure optical experiments in our laboratory at Kobe University. The anvil was of type IIa with low density of impurities, and had a table diameter of 3.1 mm, a culet diameter of 0.4 mm, and a height of 1.7 mm. The light beam was incident on the table side of the diamond. Below the fundamental absorption edge, there may have been reflection from the back (culet) surface, but this should not occur above the absorption edge.

Figure 1 shows the measured reflectance spectrum $R(\omega)$ of diamond at room temperature. It has a high reflectance band at 12-22 eV and peaks at 7 and 12.5 eV, which had been observed previously [1-5]. The weak structure at 5.5 eV is due to the fundamental absorption edge of diamond. This structure is only weak since the fundamental absorption edge is due to an indirect band gap. The peak at 7 eV is due to the smallest direct band gap, which was studied in detail including its temperature dependence [4]. However, the shoulder at 10 eV and the dip at 23 eV were not clearly observed in the previous works [1-5]. In the old measurements made in the 1960's, discrete lines from discharge lamps were used as the light source, and then the measured reflectance at the discrete photon energies were interpolated. This resulted in poor spectral resolution, and these structures had probably been overlooked. We plan further measurements in the future, including the temperature dependences, to make available more complete optical spectra of this important material for comparison with the results of band calculations.

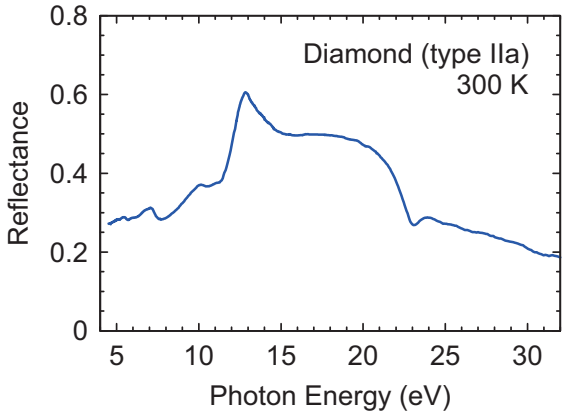

Fig. 1. Reflectance spectrum a type IIa diamond anvil at room temperature.

[1] H. R. Philipp and E. A. Taft, Phys. Rev. **127** (1962) 159.
[2] W. C. Walker and J. Osantowski, Phys. Rev. **134** (1964) A153.
[3] H. R. Philipp and E. A. Taft, Phys. Rev. **136** (1964) A1445.
[4] R. A. Roberts, D. M. Roessler and W. C. Walker, Phys. Rev. Lett. **17** (1966) 302.
[5] R. A. Roberts and W. C. Walker, Phys. Rev. **161** (1967) 730.
[6] V. V. Sobolev, A. P. Timonov and V. Val. Sobolev, Optics and Spectroscopy **88** (2000) 255.
[7] A. D. Papadopoulos and E. Anastassakis, Phys. Rev. B **43** (1991) 5090.
[8] S. Logothetidis, J. Petalas, H. M. Polatoglou and D. Fuchs, Phys. Rev. B **46** (1992) 4483.

BL7B

Photoluminescence - Photoluminescence Excitation Spectra of *a*-Plane AlN

R. Ikematsu, H. Iwai, K. Ozaki and K. Fukui
Fac. Engi., Univ. Fukui, Fukui 910-8507, Japan

The uppermost of the valence band (VB) at the Γ point of the AlN is split into three bands, LH, HH, and CH bands. These splits are due to the crystal-field splitting and the spin-orbit splitting. However, both the crystal-field splitting energy (Δcr) and the spin-orbit splitting energy (Δso) of the AlN are different from those of the GaN [1]. Then, the uppermost VB ordering at the Γ point of the AlN and GaN are CH-HH-LH (top-to-bottom order) and HH-LH-CH, respectively. The important point is that the transition from CH band, and HH and LH bands to the conduction band (CB) are allowed for $\boldsymbol{E} \parallel \boldsymbol{c}$ and $\boldsymbol{E} \perp \boldsymbol{c}$, respectively, where $\boldsymbol{E}$ represents the electric field vector of the excitation light and $\boldsymbol{c}$ the crystal axis. It means that it is not easy to measure the minimum bandgap of AlN, because the AlN samples are usually thin films and the $\boldsymbol{c}$ axis are perpendicular to the surfaces (*c*-plane AlN). On the other hand, the $\boldsymbol{c}$-axis is parallel to the sample surface in the case of *a*-plane AlN (See Fig. 1). Then, we can measure the optical anisotropy of AlN by the in-plane rotating. In this report, we present the photoluminescence (PL) - PL excitation (PLE) spectra of the *a*-plane AlN single crystalline film.

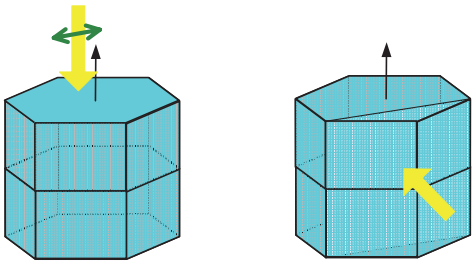

Fig. 1. c-plane (left) and a-plane (right) of the wurtzite AlN

The AlN single crystalline film was grown on the *r*-plane sapphire substrate by the MOVPE method [2]. All measurements have been performed at BL7B. The PL from the sample at about 20 K is measured by the conventional 0.3 m monochromator with the Liq. N_2 cooled CCD.

Figure 2 shows the PL-PLE spectrum of the *a*-plane AlN at 20 K with $\boldsymbol{E} \perp \boldsymbol{c}$ (above) and $\boldsymbol{E} \parallel \boldsymbol{c}$ (below) configurations. The horizontal and the vertical axes represent the photon energy of the PL and the excitation energy, respectively. The vertical straight-line like trajectory at 6.05 eV in each configuration represents the well-known PL peak due to the free and bound excitons of the AlN, and are strongly excited at 6.3 – 6.35 eV (red and white regions) in $\boldsymbol{E} \perp \boldsymbol{c}$ configuration. The white region at the lower photon energy side and the white slant line at the higher photon energy show the impurity PL and Rayleigh scattering of the excitation light, respectively. In the $\boldsymbol{E} \parallel \boldsymbol{c}$ configuration, the PL - PLE spectrum shows at least three slant line like trajectory parallel to that of the Rayleigh scattering. The energy differences among these lines are always 1, 2 or 3 × 110 meV. Here the photon energy difference, 110 meV, is in good agreement with the LO photon energy of the AlN. Then, we consider that these lines are attributed to the resonance Raman lines.

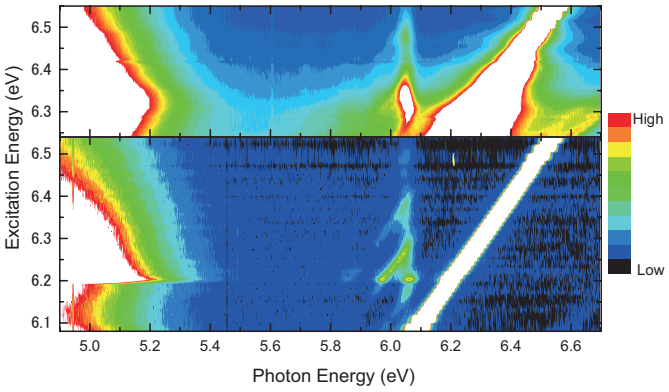

Fig. 2. The photoluminescence – photoluminescence excitation (PL – PLE) spectra at 20 K of a-plane AlN thin film with $\boldsymbol{E} \perp \boldsymbol{c}$ (above) and $\boldsymbol{E} \parallel \boldsymbol{c}$ (below) configurations.

[1] T. Onuma, S. F. Chichibu, T. Sota, K. Asai, S. Sumiya, T. Shibata and M. Tanaka, Appl. Phys. Lett. **81** (2002) 652.
[2] N. Okada, N. Kato, S.Sato, T. Sumii, N. Fujimot, M. Imura, K. Balakrishnan, M. Iwaya, S. Kamiyama, H. Amano, I. Akasaki, T. Noro and A. Bandoh, J. Cryst. Growth **300** (2007) 141.

BL7B

Refractive Index of Heavily Boron Doped Diamond with Impurity Band

T. Inushima[1], Y. Ota[1] and K. Fukui[2]

[1]*Department of Electronics, Tokai University, 4-1-1 Kitakaname, Hiratsuka 259-1292, Japan*

[2]*Department of Electrical and Electronics Eng., University of Fukui, Bunkyo, Fukui 910-8507, Japan*

Since the discovery of superconductivity in boron-doped diamond, its impurity band structure has been a key issue for the understanding of the superconductivity. Recently we reported that when the boron concentration exceeds N_B=4×10^{18}cm^{-3}, an impurity band forms at the first excited levels (2p) of the impurity boron at 0.06 eV above the valence band maximum. At higher N_B, the wave functions of the 2P states begin to overlap and the impurity band spreads in the *k*-space. Simultaneously, Fermi level rises to the impurity band and a variable range hopping is realized [1]. When the impurity band has *k*-space dependence, the refractive index should change, especially in the visible region. However, precise refractive index measurement was not been reported. Hence we measure the refractive index of boron doped diamond with impurity band using BL7B and compare it with that obtained by the density functional first principle calculation.

Figure 1 shows the refractive index of 5000 ppm boron doped diamond measured at 300 K by a combination of G3 grating (1.2~7.7 eV) and a photo-diode detector of BL7B. The value of 5,000 ppm corresponds to N_B=1×10^{19}cm^{-3}. The reflection spectrum shown in the inset shows weak sinusoidal interference fringes caused by the interference of the transmitting light of the homo-epitaxial diamond film. Using the film thickness of 1.6 μm, the refractive index is obtained from the oscillatory order of the interference so as to fit the optimum refractive index of 2.4 at 1.8 eV, where the oscillation disappears. The observed refractive index is much smaller than that of the bulk diamond (n~2.4), and shows a continuous decrease as the photon energy decreases and becomes less than 1 around 1.2 eV.

Figure 2 shows the refractive index of boron doped diamond obtained by *ab initio* calculation. The used program is Advance/PHASE and the cutoff wavefunction energy is 25 Hartree. The calculation model is the diamond $C_{63}B$ super cell, where the Bravais unit cell of diamond is expanded to 2×2×2 and one carbon atom is replaced by a boron, which corresponds to N_B=2.7×10^{21}cm^{-3}. For comparison, refractive indices of single unit cell diamond and $C_{53}B$ super cell are also plotted. The calculated refractive index is in good agreement with that obtained in Fig. 1, which indicates that the impurity band forming in the boron doped diamond with N_B=1×10^{19}cm^{-3} is similar to that with a boron concentration two orders of magnitude larger.

In conclusion, when the impurity band is established in boron doped diamond when N_B> 4×10^{18}cm^{-3}, it has *k*-space dependence and changes the refractive index in the visible region.

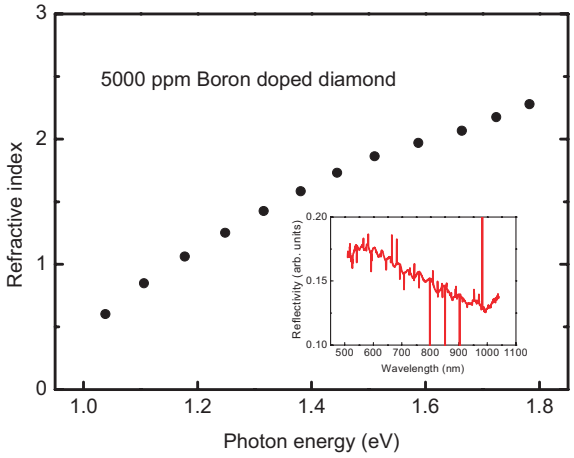

Fig. 1. Refractive index of 5000 ppm boron doped diamond. Inset shows the sinusoidal oscillation of the reflection spectrum caused by interference of the transmitted light.

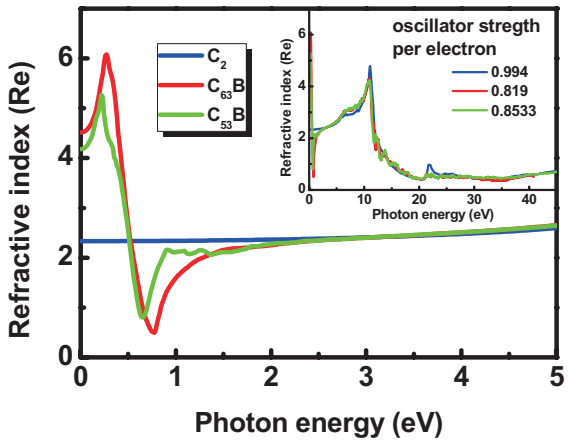

Fig. 2. Refractive indices of diamond, $C_{63}B$ and $C_{58}B$ super cells obtained by *ab initio* calculations.

[1] T. Inushima, R. F. Mamin and H. Shiomi, Phys. Rev. B **79** (2009) 045210.

BL8B

Photoelectron Spectroscopy of $Sc_3N@C_{78}$*

S. Hino[1], M. Zenki[1], T. Zaima[1], Y. Aoki[1], S. Okita[1], T. Ohta[1], H. Yagi[1], T. Miyazaki[1], R. Sumii[2, 3], H. Okimoto[4], Y. Ito[4] and H. Shinohara[4]

[1]*Graduate School of Science and Engineering, Ehime University, Matsuyama 790-8577, Japan*
[2]*UVSOR, Institute for Molecular Science, Okazaki 444-8585, Japan*
[3]*Research Center for Materials Science, Nagoya University, Nagoya 464-8602, Japan*
[4]*Graduate School of Science, Nagoya University, 464-860, Japan*

Extensive ultraviolet photoelectron spectroscopic studies of single metal atom entrapped metallofullerenes, $M@C_{82}$, established an empirical rule that the cage structure principally governs the electronic structure of these metallofullerenes and a difference in the amounts of transferred electrons to the cage is another factor to modify it. A similar relationship was found in the UPS of endohedral fullerenes encapsulating multiple atoms, such as $Sc_2C_2@C_{82}$ [1], $Y_2C_2@C_{82}$ [2] and $M_3N@C_{80}$ (M = Sc, Tm and Dy) [3]. However, the UPS of $La_2@C_{78}$ and $Ti_2C_2@C_{78}$ were significantly different [4], even though their cage symmetry was the same D_{3h}. Isolation of another C_{78} cage endohedral fullerene, $Sc_3N@C_{78}$, has also been reported. Since its absorption spectrum is significantly different from those of $La_2@C_{78}$ and $Ti_2C_2@C_{78}$, it is highly plausible that their electronic structure might be mutually different. We measured the ultraviolet photoelectron spectra of $Sc_3N@C_{78}$ and compared them with the UPS of $La_2@C_{78}$ and $Ti_2C_2@C_{78}$. Density functional theory (DFT) calculation was also performed to elucidate the plausible geometry of $Sc_3N@C_{78}$.

The valence band UPS of $Sc_3N@C_{78}$ obtained with hν = 20 – 60 eV photon energy. The spectral onset was 0.75 eV below the Fermi level. There are 8 explicit structures labeled A to H in the UPS of $Sc_3N@C_{78}$. Approximate peak positions of the structures are indicated with dotted lines.

The UPS of $La_2@C_{78}$, $Ti_2C_2@C_{78}$ and $Sc_3N@C_{78}$ obtained with hν = 40 eV photon energy are shown in Fig. 1. These three endohedral fullerenes have the same cage symmetry of D_{3h} (78:5). For the electronic structures located in the 5 - 11 eV binding energy region, there is a fairly good correspondence among these three UPS, although there are slight deviations in the corresponding structure peak positions (indicated by dotted lines) and slight difference in their relative intensity. Since the structures in this region are due to σ-electrons, the present findings suggest that the σ-electronic structures of these three endohedral fullerenes do not differ significantly. On the other hand, there is a significantly large difference in the upper valence band UPS (between the Fermi level and BE = 5 eV), which is against the empirical rule. X-ray photoelectron spectra of these endohedral fullerenes and the DFT calculation revealed that there was a critical difference in these fullerenes in the amounts of transferred charge from the entrapped species to the cage.

DFT geometry optimization of $Sc_3N@C_{78}$ gave three possible structures and one of them reproduced the UPS very well (Fig. 2). Therefore, we concluded that $Sc_3N@C_{78}$ took the geometry shown in the inset of Fig. 2.

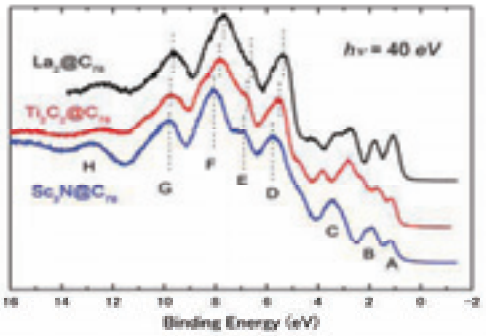

Fig. 1. UPS of $La_2@C_{78}$, $Ti_2C_2@C_{78}$ and $Sc_3N@C_{78}$.

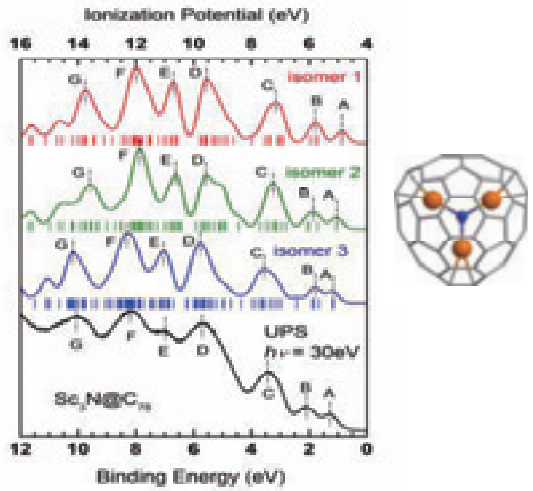

Fig. 2. DFT calculated simulation spectra and the UPS of $Sc_3N@C_{78}$ and its estimated structure.

*This work was publiushed in J. Chem. Phys. C **116** (2012) 165.

[1] T. Pichler e*t al,*. PRB **62**, (2000) 13196.
[2] S. Hino *et al*., PRB **72** (2005) 195424.
[3] H. Shiozawa *et al*., PRB **72** (2005) 195409.
[4] S. Hino *et al*., PRB **75** (2007) 125418.

BL8B

Ultraviolet Photoelectron Spectra of $Er_2@C_{82}$ (I), $Er_2@C_{82}$ (III), $Er_2C_2@C_{82}$ (I) and $Er_2C_2@C_{82}$ (III)

T. Miyazaki[1], R. Sumii[2, 3], H. Umemoto[4], H. Okimoto[4], Y. Ito[4], T. Sugai[4], H. Shinohara[4], T. Zaima[1], H. Yagi[1] and S. Hino[1]

[1] *Graduate School of Science and Engineering, Ehime University, Matsuyama 790-8577, Japan*
[2] *Institutes for Molecular Science, Okazaki 444-858, Japan*
[3] *Research Center for Materials Science, Nagoya University, Chikusa-ku, Nagoya 464-8602, Japan*
[4] *Graduate School of Science, Nagoya University, Chikusa-ku, Nagoya 464-8602, Japan*

Fullerenes cages often encapsulate metal atoms and metal-carbide clusters, and entrapped metal atoms donate electrons to the cage so that the electronic structure of the fullerene cage is altered by the encapsulation. Recently, erbium atoms and erbium carbide encapsulated C_{82} fullerenes, $Er@C_{82}$ (I), $Er_2@C_{82}$ (I), $Er_2@C_{82}$ (III), $Er_2C_2@C_{82}$ (I) and $Er_2C_2@C_{82}$ (III), have been isolated. The NMR study revealed their cage symmetry as follows, C_{2v} (82:9) for $Er@C_{82}$ (I), C_s (82:6) for $Er_2@C_{82}$ (I) and $Er_2C_2@C_{82}$ (I), C_{3v} (82:8) for $Er_2@C_{82}$ (III) and $Er_2C_2@_{82}$ (III). It is worthwhile to examine what kind of change entrapped multiple Er atoms bring to the electronic structure of the C_{82} cage. In this report, ultraviolet photoelectron spectra (UPS) of $Er_2@C_{82}$ (I), $Er_2@C_{82}$ (III), $Er_2C_2@C_{82}$ (I) and $Er_2C_2@C_{82}$ (III) are presented and compared with the valence band electronic structure of their endohedral C_{82} fullerenes.

$Er_2@C_{82}$ (I), $Er_2@C_{82}$ (III), $Er_2C_2@C_{82}$ (I) and $Er_2C_2@C_{82}$ (III) were synthesized and isolated from the soot containing them. Specimens for photoelectron spectra measurement were prepared by vacuum deposition onto a gold deposited molybdenum disk from a quartz crucible under 5×10^{-7} Pa. The temperature of the crucible during vacuum deposition of endohedral fullerenes was 650°C ~ 700°C. The UPS was measured at the beamline BL8B of Ultraviolet Synchrotron Orbital Radiation Facility of Institute for Molecular Science. The base pressure of the UPS measurement chamber was 4×10^{-8} Pa and the pressure during the measurement was about 6×10^{-8} Pa. The measured UPS were referenced against the Fermi level (EF) of gold and were plotted as a function of binding energy relative to E_F. All UPS were normalized by the peak height of a structure appeared at around 5.5 eV. The energy resolution of the UPS was 110meV, which was estimated from the width of the Fermi edge of gold.

The UPS of these endohedral fullerenes taken by 40eV photon energy are collected in Figure 1 for comparison. The spectral onset energy of these endohedral fullerenes is around 0.8 ~ 0.9 eV, which is larger than that of $Er@C_{82}$ (I) of 0.4 eV [1]. As for the deeper binding energy region (structures labeled by α – ε), the electronic structure of these endohedral fullerenes seems to be almost analogous although there are minute differences among them: A large structure 'α' appears at around 5.4 ~ 5.6 eV, a series of structures β, γ, δ appear between 6.7 and 8.6 eV with a slight intensity variation and a difference in their intervals. These peak positions of structure β and δ do not shift so much, but peak top position of structure γ moves in slightly wider range. These findings indicate that the skeletal C–C σ-bonds in endohedral fullerenes are similar in these endohedral fullerenes and they are not seriously affected by entrapped species. As for the upper valence band UPS of these endohedral fullerenes, the situation is quite different. The electronic structure is principally dependent on the cage structure, and entrapped species do not bring serious change to the electronic structure of endohedral fullerenes. That means the empirical rule that the electronic structure of mono-metal entrapped endohedral fullerenes is principally governed by the cage structure seems to be held in multiple atoms encapsulated fullerenes. The difference spectrum between the UPS of $Er_2@C_{82}$ (III) and $Er_2C_2@C_{82}$ (III) has the same C_{3v} structure reveals two excess electrons on the cage of $Er_2@C_{82}$.

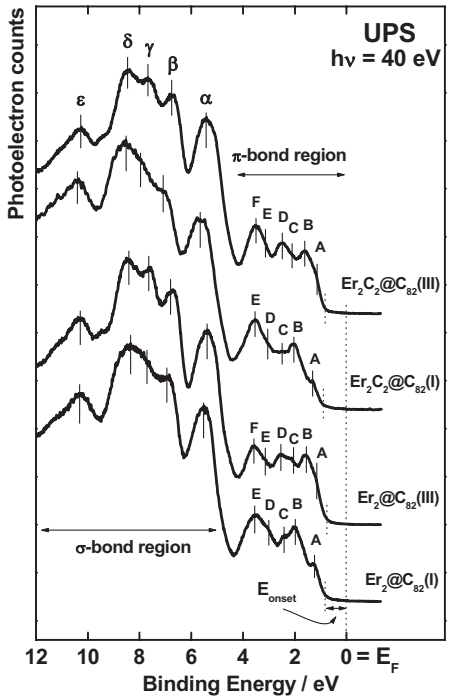

Fig. 1. UPS of Er atoms encapsulated fullerenes were measured by incident photon energy of 40 eV.

[1] T. Miyazaki *et al*., Chem. Phys. **378** (2010) 11.

BL2A

The Measurement of Soft X-Ray Excited Optical Luminescence of a Ge^+ Implanted Silica Glass Sample

T. Yoshida[1], S. Muto[2] and H.Yoshida[3]

[1]*EcoTopia Science Institute, Nagoya University, Nagoya 464-8603, Japan*

[2]*Department of Materials, Physics and Energy Engineering, Nagoya University, Nagoya 464-8603, Japan*

[3]*Department of Applied Chemistry, Graduate School of Engineering, Nagoya University, Nagoya 464-8603, Japan*

The discovery of room temperature photoluminescence (PL) from indirect band gap materials has generated important interest in this field. In particular, Ge doped silica glass is expected to apply to a light emission source for communication in a LSI chip as well as to single electron devices, since it shows blue and violet electroluminescence around 3.1 eV [1, 2]. Although the Ge doped silica glass has been studied extensively, the origin of the 3.1 eV PL and the emission mechanism still remain controversial. The purpose of this paper is to discuss the relation between the optical properties and the chemical state of Ge atoms in a silica glass, applying X-ray absorption fine structures (XAFS).

The sample used in this study was a synthesized silica glass (T-4040, OH content: 800ppm) produced by Toshiba Ceramics, Japan, 13 mm in diameter and 2 mm in thickness. Mass analyzed Ge^+ ions of 30 keV were injected into the samples at room temperature normal to the sample surface. The Ge^+ fluence ranged from 2 x 10^{14} to 2 x 10^{16} cm^{-2}. The measurement of luminescence of the samples induced by soft X-ray irradiation was carried out on the beamline BL1A and BL2A at UVSOR, Institute for Molecular Science. The luminescence was focused by a lens in the UHV chamber to the monochromator (CP-200, JOBIN YVON) and detected by a multi-channel analyser (OMA III, EG&G PRINCETON APPLIED RESEARCH).

PL spectra before and after the Ge^+ implantation were measured at room temperature using a Hitachi F-4500 spectrometer.

Fig. 1 shows PL spectra excited by 5 eV light before and after Ge^+ implantation. A weak and broad band is observed before implantation, while a new emission band around 2.7 eV appears after the implantation of 2 x 10^{15} cm^{-2}. This PL band was ascribed to the $B_{2\alpha}$ oxygen deficient centers [3] associated with the displacement damages. When the fluence is more than 2 x 10^{16} cm^{-2}, a sharp and intense 3.1 eV PL band replaces the 2.7 eV band.

We tried to measure Ge $L_{2,3}$-edge XANES spectra of the 2 x 10^{16} cm^{-2} implanted sample in the total electron yield mode (TEY), but the concentration of Ge atom were too low to measure. On the other hand, we found that an intense soft X-ray induced luminescence of this sample is observed at 3.1 eV. Therefore, we measured the excitation spectra of the 3.1eV band by changing the incident energy of the soft X-ray, and show the spectra in Fig. 2 together with Ge $L_{2,3}$-edge XANES of a Ge (0) powder sample recorded in the TEY mode. It is interesting to see good correspondence among them, and this result may indicate that the Ge (0) species relate to the generation of 3.1 eV PL.

[1] L. Rebohle, J. von Borany, R. A. Yankov, W. Skorypa, I. E. Tyschenko, H. Froeb and K. Leo, Appl. Phys. Lett. **71** (19) (1997) 2809.

[2] M. L. Brongersma, A. Polman, K. S. Min, E. Boer, T. Tambo, H. A. Atwater, Appl. Phys. Lett. **72** (1998) 2577.

[3] Skuja L. N. and Etzian W., Phys. Status Solidi A **96** (1986) 191.

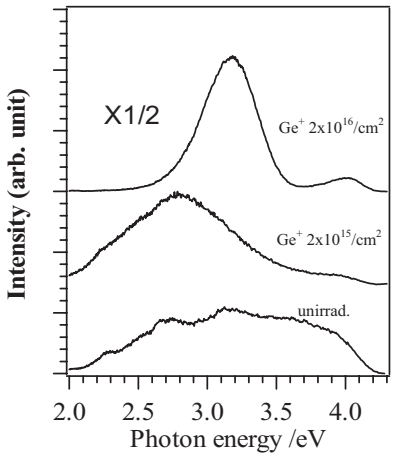

Fig. 1. PL spectra excited by 5 eV light for silica glass before and after Ge^+ implantation.

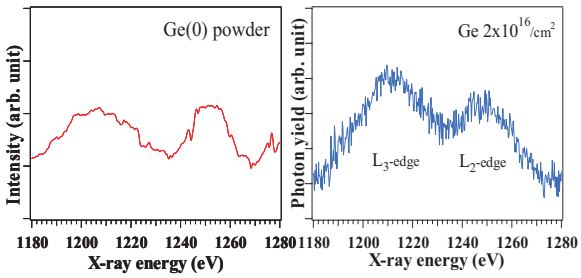

Fig. 2. Comparison between the luminescence yield spectrum of the 3.1 eV band for a silica glass irradiated by Ge^+ and Ge $L_{2,3}$-edge XANES spectrum of a Ge powder.

BL2A

Local-Structures of P of $LiMnFePO_4$ Doped with Mn

A. Nakahira[1, 2], S. Hayashi[1], M. Sato[2], Y. Takamatsu[1], Y. Nishio[1], Y. Kawabe[1], S. Misu[1], K. Kumadani[1], T. Shirai[1] and H. Aritani[3]

[1]*Faculty of Engineering, Materials Science and Engineering Dept, Osaka Prefecture University, 1-1 Gakuen-cho, Naka-ku, Sakai 599-8531, Japan*

[2]*Kansai Center, Institute of Materials Research (IMR), Tohoku University, 1-1 Gakuencho, Naka-ku, Sakai 599-8531, Japan*

[3]*Faculty of Engineering, Saitama Institute of Technology, 1690 Fusai-ji, Fukaya 369-0293, Japan*

$LiFePO_4$ (lithium iron phosphate) is an interesting alternative positive electrode material for lithium and lithium-ion rechargeable batteries application because of due to its low cost and good specific capacity. Although these $LiFePO_4$ (lithium iron phosphate) materials have some advantages in terms of environmental benignity, potential low-cost synthesis, cycling stability, and high temperature capability, the major drawback point for $LiFePO_4$ is the poor lithium ion conductivity, which have limited its power-demanding applications such as hybrid electric vehicles and other power generating equipments.

A number of various efforts has been made in the past decade to solve the conductivity problem for $LiFePO_4$. Nowadays, the main problems for $LiFePO_4$ is still the poor lithium ions conductivity caused by the low intrinsic electronic conductivity. Therefore, the modification of $LiFePO_4$ added with Mn have been attempted. In this study, $LiFePO_4$ added with Mn ($LiMnFePO_4$) was synthesized through the chemical synthesis of $LiFePO_4$ materials by the solution processing process and the heat-treatments in order to improve the specific capacity and cycling stability etc. The purpose of this study is to investigate the P-*K* edge local structures for $LiFePO_4$ added with Mn ($LiMnFePO_4$).

The synthesis of $LiFePO_4$ and $LiFePO_4$ added with Mn ($LiMnFePO_4$) was carried out using LiOH, $(NH_4)_2HPO_4$, $MnSO_4$ and $FeSO_4$, and the ascorbic acid was used as a carbon source. These stock solutions were prepared for 1 mol/L LiOH, 0.5 mol/L $(NH_4)_2HPO_4$, 0.5 mol/L $FeSO_4$ and 0.5 mol/L $MnSO_4$. The synthetic reaction was carried out through the hydrothermal treatments in autoclave bomb at various temperatures. The products were aged for various times and filtered with Buchner funnel. The products were dried at 323K for 24 hours and ground with alumina mortar. The products were characterized by XRD and FT-IR and their microstructures by SEM and TEM. The local structures around P-*K* edge for the powders of $LiFePO_4$ added with Mn ($LiMnFePO_4$) were evaluated and characterized by measuring X-ray adsorption near edge structure (XANES) at BL2A at UVSOR in Okazaki.

The components of products of $LiFePO_4$ added with Mn ($LiMnFePO_4$) were evaluated by XRD and the products were identified to be olivine type $LiFePO_4$. Figure 1 shows the results of P-*K* edge for the powders of $LiFePO_4$ added with Mn ($LiMnFePO_4$). The P-*K* edge of $(NH_4)_2HPO_4$ was measured as a reference material. The peaks of $LiFePO_4$ and $LiFePO_4$ added with Mn ($LiMnFePO_4$) were higher than $(NH_4)_2HPO_4$ as a reference material. Furthermore, $LiFePO_4$ added with Mn ($LiMnFePO_4$) had the higher energy of P-*K* edge peak, compared to monolithic$LiFePO_4$. It is obvious that the peak shift of P-*K* edge for $LiFePO_4$ added with Mn ($LiMnFePO_4$) was attributed to the addition of Mn into $LiFePO_4$.

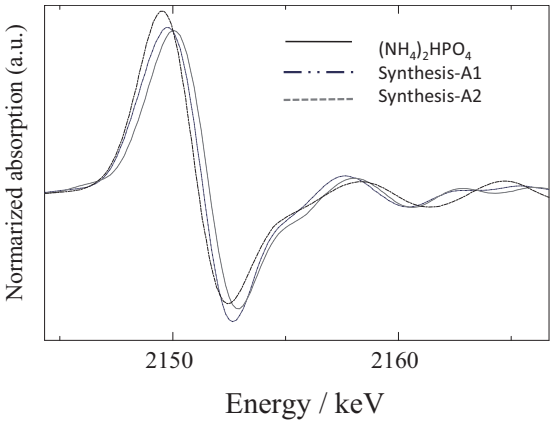

Fig. 1. XANES results of P-*K* edge for $LiFePO_4$ added with Mn ($LiMnFePO_4$).

BL2A

Evaluation of Al Local Structure of Cu-Al based Talcite Clay

A. Nakahira[1, 2], S. Hayashi[1], M. Sato[2], Y. Takamatsu[1], S. Misu[1], K. Kumadani[1] and H. Aritani[3]

[1]*Faculty of Engineering, Materials Science and Engineering Dept, Osaka Prefecture University, 1-1 Gakuen-cho, Naka-ku, Sakai 599-8531, Japan*

[2]*Kansai Center, Institute of Materials Research (IMR), Tohoku University, 1-1 Gakuencho, Naka-ku, Sakai 599-8531, Japan*

[3]*Faculty of Engineering, Saitama Institute of Technology, 1690 Fusai-ji, Fukaya 369-0293, Japan*

Hydrotalcite is one of unique clay minerals among the layered double hydroxide (LDH) materials, which are composed of double layered structures, its composition formula of $[M^{2+}_{1-X}\ M^{3+}_{X}\ (OH)_2 \cdot A^{n-}_{X/n} \cdot nH_2O]$. These materials are expected to be useful due to wide potentials as filers, catalysis, drug delivery system (DDS) and adsorption materials. "MgAl-talcie basically composed of Mg^{2+} and Al^{3+}, which is called hydrotalcite, is most popular among LDH materials .

In order to improve various properties of LDH, especially Mg-Al LDH (hydrotalcite), recently, the developments of novel LDH materials modified with the substitution of Mg^{2+} and Al^{3+} sites with another M^{2+} and M^{3+}, are attempted for expanding the new application fields. We also have developed the new types of LDH materials modified with the addition of Zn^{2+}, Ni^{2+}, Fe^{3+} and other cations of M^{2+} and M^{3+}. In this study, we successfully synthesized the novel LDH materials composed of Cu^{2+}-Al^{3+} based hydrotalcite by the soft solution process (co-precipitation processing). Therefore, we, here, attempted to investigate the Al local structure of Cu^{2+}-Al^{3+} based hydrotalcite with the X-ray adsorption near edge structure (XANES) measurements to clarify of the fine structure.

The stock solutions of 0.2 mol/dm^3 $CuCl_2$ aqueous solution. 0.1 mol/dm^3 $AlCl_3$ aqueous solution, and 0.05 mol/dm^3 $NaHCO_3$ were prepared. The pH of mixing solution was controlled with the NaHCO3 solution and aqueous NaOH solution. The products were synthesized by the co-precipitation method as a soft chemical process. CuAl-talcite with M^{2+}/M^{3+} =2~4 were synthesized by adding mixing solution into 0.05 mol/dm^3 $NaHCO_3$ at RT. 1 mol/dm^3 NaOH was simultaneously added into the aqueous solution under pH 10. The precipitation was aged at room temperature for a few hours for Cu^{2+}-Al^{3+} based hydrotalcite. The products were filtered with Buchner funnel. They were separated and sufficiently washed by deionized water and dried at 50 ℃ for 24 hours.

The products of Cu^{2+}-Al^{3+} based hydrotalcite were characterized with various methods. The local structures around Al for Cu^{2+}-Al^{3+} based hydrotalcite were evaluated by measuring X-ray adsorption near edge structure at BL2A in UVSOR with KTP.

For the comparison, Mg-Al hydrotalcite samples prepared by the co-precipitation method were similarly evaluated. Cu^{2+}-Al^{3+} based hydrotalcite samples synthesized by the co-precipitation method was powdered. the results of powder X-ray diffraction analysis showed that all samples for Cu^{2+}-Al^{3+} based hydrotalcite with different Cu^{2+}/Al^{3+} ratio of 2 to 4 were identified to be a layered double hydroxide. Figure 1 shows the results of XANES of Al-*K* edge for Cu^{2+}-Al^{3+} based hydrotalcite and the commercial Mg-Al hydrotalcite and Mg-Al hydrotalcite samples prepared by the co-precipitation method. The spectrum of Cu^{2+}-Al^{3+} based hydrotalcite products were similar to one of commercial Mg-Al hydrotalcites. The difference between the peak positions of P-*K* edge of Cu^{2+}-Al^{3+} based hydrotalcite with different Cu^{2+}/Al^{3+} ratio of 2 to 4 was confirmed by XANES This differences was caused by the content of Cu in hydrotalcite structures.

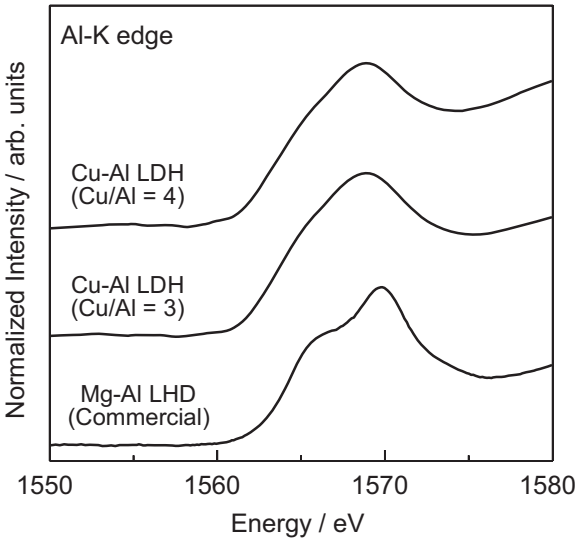

Fig. 1. Results of XANES of Al-*K* edge of the Cu^{2+}-Al^{3+} based hydrotalcite.

BL2A

Mo L_{III}-Edge XANES Study of Silylated Mo/H-MFI Catalysts for Methane Dehydroaromatization

H. Aritani[1], F. Ohya[1], K. Kuramochi[1], T. Sugawara[1], N. Naijo[1], K. Takanashi[1] and A. Nakahira[2]

[1]*Department of Life Science & Green Chemistry, Saitama Institute of Technology, Fukaya 369-0293, Japan*
[2]*Graduate School of Engineering, Osaka Prefecture University, Sakai 599-8531, Japan*

As a typical GTL (Gas-To-Liquid) catalyst in a direct conversion process of LNG, MoO_x-modified H-MFI zeolite (Mo/H-MFI) catalyst shows high activity for methane dehydroaromatization to produce benzene and naphthalene in the absence of oxygen. The important problem on the Mo/H-MFI catalysts is a rapid deactivation by coking and/or carbon contamination on the catalyst surface, and thus, highly active GTL catalysts with durable activity have been called for. Many workers have been revealed that reduction of Mo species is brought about in contact with methane in initial step. Reduced Mo ions tend to react methane to form carbide and/or oxycarbide species in next step [1]. The carbide species is active for methane dehydroaromatization, however, it is difficult to avoid the deactivation due to carbon deposition on the H-MFI surface. The carbon deposition proceeds mainly on the acid sites of H-MFI extraframework. On H-MFI interpores, appropriate acid sites shows durable activity with low deactivation rate. In the present study, silylated Mo/H-MFI catalysts were prepared in order to cover the acid sites of H-MFI extraframework. By silylation using organosilane regents, coking sites in extraframework can be covered selectively. In fact, the silylated Mo/H-MFI showed durable activity in the reaction with CH_4-H_2 at 973 K. To characterize the bare- and sylilated Mo-H-MFI catalysts, Mo L_{III}-edge XANES studies were applied. Red-ox states of the active Mo species on H-MFI with/without silylation were evaluated before/after the methane dehydroaromatization.

Catalysts were prepared by impregnation of H-MFI support with $MoO_2(acac)_2$–$CHCl_3$ solution, and followed by drying overnight and calcination at 773 K for 3 h. The amount of MoO_3-loading is 5.0 wt% in this study. H-MFI supports with Si/Al_2 = 20-72 were synthesized hydrothermally at 413 K for a week, and followed by ion-exchanging with NH_4Cl and calcination at 873 K. Silylation was carried out by impregnating triethoxyphenylsilane-heptane solution (Mo/Si=5) with Mo/H-MFI, and dried at 353 K for onernight. The catalytic activity of methane dehydroaromatization was evaluated by means of fixed bed flow reaction, as described in a separate paper [2]. Mo L_{III}-edge XANES spectra were measured in BL2A of UVSOR-IMS in a total-electron yield mode using InSb double-crystal monochromator. Photon energy was calibrated by using Mo metal-foil at Mo L_{III}-edge, and normalized XANES spectra and their second derivatives are presented. REX-2000 (Rigaku) software was used by normalization of each XANES spectrum.

Figure 1 shows the XANES spectra of bare- (shown in top) and silylated (in bottom) Mo/H-MFI catalysts (pretreated with CO(2%)-He) reacted with CH_4(20%)-He at various temperatures. Reduction of Mo species reflects the shift of lower edge energy. After reaction at 973-1023 K, Mo species on silylated Mo/H-MFI are reduced easier than that on bare one. At 1073 K, Mo^{2+} species due to Mo_2C are formed definitely in both catalysts. The silylated catalyst showed a maximum activity at 973 K, and thus, the silylation relates to the enhancement of Mo species to form partially carbonized (Mo-oxycarbonates, in major) ones. At the same time, carbon deposition was inhibited. These results suggest the inhibition of carbon coking and formation of active Mo species at lower temperature at 973K by silylation (Mo/Si=5).

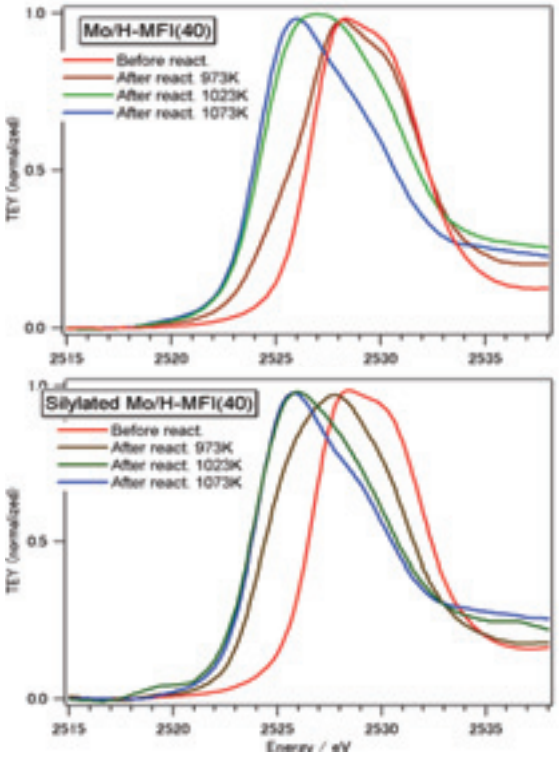

Fig. 1. Mo L_{III}-edge XANES of Mo/H-MFI (Si/Al_2=40) catalysts before and after silylation with phenylsilane (Mo/Si=5) reacted at various temperatures.

[1] H. Aritani, S. Shinohara, S. Koyama, K. Otsuki, T. Kubo and A. Nakahira, Chem. Lett. **35** (2006) 416.
[2] H. Aritani, H. Shibasaki, H. Orihara and A. Nakahira, J. Environm. Sci. **21** (2009) 736.

BL2A

Mg-*K* XANES Study of Mg-Doped Hydroxyapatite

H. Murata[1], K. Shitara[1], F. Oba[1] and I. Tanaka[1, 2]

[1]*Department of Materials Science and Engineering, Kyoto University, Kyoto 606-8501, Japan*
[2]*Nanostructures Research Laboratory, Japan Fine Ceramics Center, Nagoya 456-8587, Japan*

Hydroxyapatite (HAp) is a main inorganic component of human bones and teeth. HAp in human bodies contains various kinds of defects such as Ca vacancies, excess H and impurities. They affect biological properties of HAp [1] and thus it is important to understand their electronic and atomistic structures.

Mg is one of the essential elements for human bodies and a major impurity in human bones. It is considered to have an important role for bone re-modeling [1]. In this study, we investigated the local environments of Mg in HAp by Mg-*K* X-ray absorption near edge structure (XANES).

Undoped and Mg-doped HAp samples were synthesized using the solution-precipitation method. Starting materials were 0.1 mol/L solutions of $Ca(NO_3)_2{\cdot}4H_2O$, $Mg(NO_3)_2{\cdot}6H_2O$ and $(NH_4)_2HPO_4$. Precipitations were matured at 353 K for 5 hours in Ar atmosphere. Nominal Mg/(Ca+Mg) ratio was set to 0, 2, 5 and 20 at%. Mg-*K* XANES was measured at BL2A in UVSOR. The incident X-ray beam was monochromatized by beryl double crystals. XANES signals were collected with GaAsP photo-diodes (HAMAMATSU G-1127-02). Pellets of samples were mounted on carbon tapes. For a detailed analysis of Mg-*K* XANES, theoretical spectra were obtained by the first-principles supercell method with a core-hole effect [2].

Mg-doped HAp samples were characterized by XRD. No secondary phases were observed. The XRD patterns showed peak shifts and broadening by Mg doping. This indicated that Mg was incorporated into the HAp crystals.

The Mg-*K* XANES spectra of these samples were measured at BL2A. Usually, XANES signals in a soft X-ray region are collected by the total electron yield (TEY) method. However, our samples had a tendency to be charged up and we could not obtain high-quality spectra by the TEY method. Therefore, the fluorescent yield (FY) method with GaAsP photodiodes was employed. Figure 1 shows Mg-*K* XANES of the Mg-doped HAp samples measured by the FY method. The FY method gives good spectra for Mg with small concentrations.

It is found that the Mg-*K* XANES for 2, 5 and 20 at%Mg have the same features. In order to elucidate the local environments of Mg in HAp via the interpretation of Mg-*K* XANES, theoretical spectra were obtained. HAp has two non-equivalent Ca site, i.e., the Ca-1 (columnar) site and Ca-2 (triangular) site. We considered models in which one Mg was substituted for the Ca-1 or Ca-2 sites. However, neither model reproduced the experimental Mg-*K* XANES spectra. This indicated that Mg in HAp is not simply located at these sites. Our previous study suggested that the XANES of dopants in HAp is affected by association with the Ca vacancy and excess H [3]. Mg in HAp is likely to be associated with other defects as well. A detailed analysis of the defective structures is in progress.

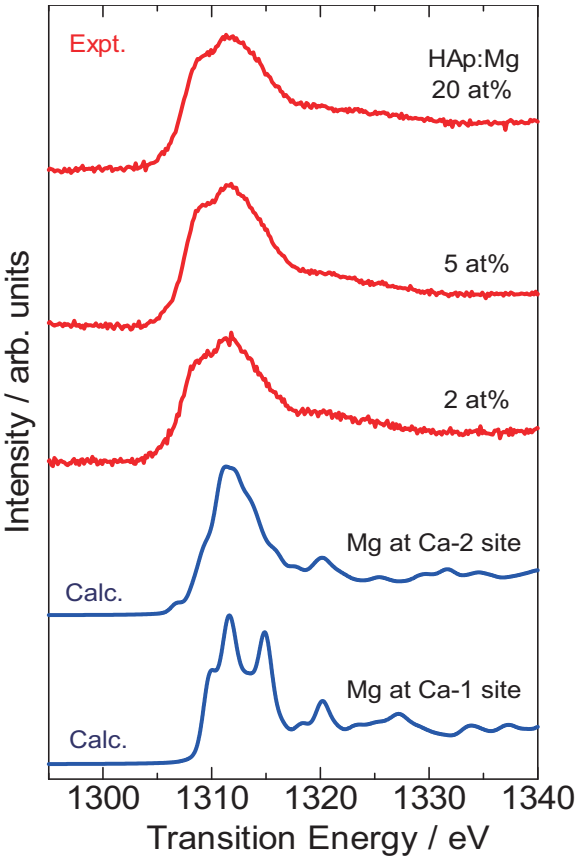

Fig. 1. Experimental and calculated Mg-*K* XANES of Mg-doped Hap.

[1] A. Boanini *et al.*, Acra Biomater. **6** (2009) 1882.
[2] I. Tanaka *et al.*, J. Am. Ceram. Soc. **88** (2005) 2013.
[3] H. Murata *et al.*, J. Phys.: Condens. Matter **22** (2010) 384213.

BL3U

Hybridized Electronic States near E_F of Potassium-Doped Picene Probed by Soft X-Ray Emission Spectroscopy

H. Yamane and N. Kosugi

Department of Photo-Molecular Science, Institute for Molecular Science, Okazaki 444-8585, Japan
School of Physical Sciences, The Graduate University for Advanced Studies, Okazaki 444-8585, Japan

Recently, a new organic superconductor has been discovered for a Potassium (K)-doped picene [see, Fig. 1(a)], with high transition temperatures (< 18 K), which depend on the K concentration [1]. In order to elucidate the nature of the superconductivity in the K-doped picene, detailed information on the electronic structure is required. It has been suggested from theoretical calculations that the dopant (K) orbitals are higher in energy and weakly hybridized with the molecular states close to the Fermi energy (E_F) [2]; however, experimental proofs for the formation of hybridized electronic states of the K-doped picene have not yet been reported.

In this work, in order to understand the local electronic structure of the K-doped picene, soft X-ray spectroscopies were applied at BL3U. The K-doped picene was prepared by the co-evaporation of picene (99.9% purity, NARD inst. Ltd) and K (SAES getters) on SiO_2/Si(111) at the fixed deposition rates with the post-annealing at 370 K. The K concentration and the crystallinity of the K_xPicene (x = 0, 3) were confirmed by CuKα X-ray diffraction (XRD) and fluorescence-yield X-ray absorption spectroscopy (FY-XAS).

Figure 1(a) shows the XRD scans of the K_xPicene (x = 0, 3), which agree well with the earlier study [1]. For the K-doped picene, the K atoms are intercalated in the stacked picene molecules.

Figure 1(b) shows FY-XAS spectra of the K_xPicene (x = 0, 3) at the normal incidence. The strong XAS peaks, originating from the C 1s → LUMO (π*) and LUMO+1 (π*) transitions [3,4], appear at the incident photon energy ($h\nu_{in}$) of 284–285 eV. These peaks are shifted to the lower $h\nu_{in}$ side and broadened upon the K doping due to the electron transfer from K 4s to LUMO and LUMO+1 of picene.

Figure 2 shows the selected soft X-ray emission (XES) spectra of the K_xPicene (x = 0, 3) at various $h\nu_{in}$. The elastic peak shows linear dispersion to the higher emission energy ($h\nu_{out}$) side with increasing $h\nu_{in}$. At $h\nu_{in}$ = 310.0 eV, the fluorescence feature in XES ($h\nu_{out}$ < 290 eV) for the K-doped picene shows a doping-induced peak near E_F at $h\nu_{out}$ = 288 eV very weakly, as indicated by the downed arrow, which is not observable for the undoped picene. From the $h\nu_{in}$ dependence of the XES spectra, we found that the doping-induced peak near E_F is pronounced after the K 2p excitation, $h\nu_{in} \geq$ 295 eV [see, Fig. 1(b) and 2].

These FY-XAS and XES results indicate that the molecular states of picene are hybridized with K 4s near E_F upon the K doping.

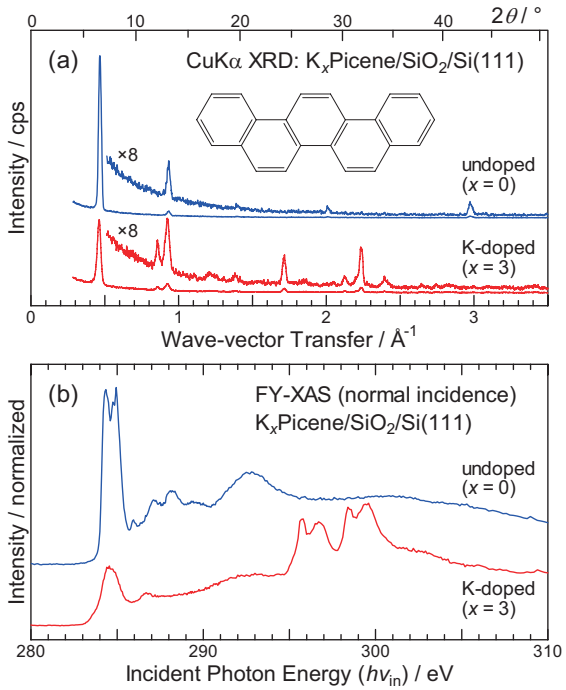

Fig. 1. (a) CuKα XRD and (b) FY-XAS spectra of K_xPicene (x = 0 and 3) films on SiO_2/Si(111).

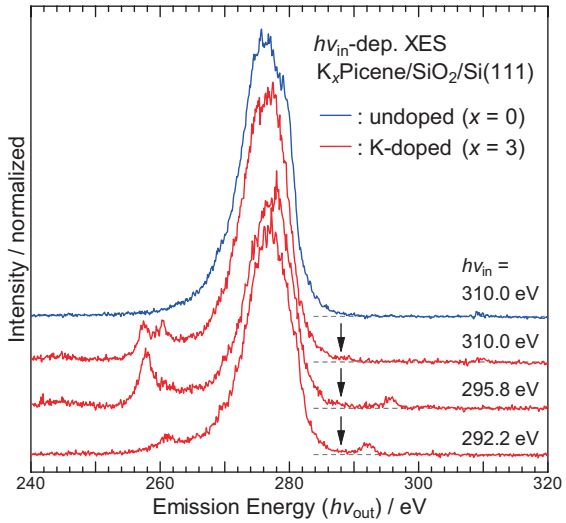

Fig. 2. XES spectra of K_xPicene (x = 0 and 3) films as a function of incident photon energy ($h\nu_{in}$).

[1] R. Mitsuhashi *et al.*, Nature **464** (2010) 76.
[2] G. Giovannetti and M. Capone, Phys. Rev. B **83** (2011) 134508.
[3] H. Ågren *et al.*, Chem. Phys. **196** (1995) 47.
[4] M. Obst *et al.*, Environ. Sci. Tech. **45** (2011) 7314.

BL3B

Optical Spectroscopy of ZnO:Al Thin Films

N. Kashiwagura, T. Hashida and T. Takeya
Department of Mathematical and Design Engineering, Gifu University, Gifu 501-1193, Japan

Today the most widely adopted TCO (transparent conductive oxides) films for use as electrodes of solar cell and liquid crystal display is ITO (Indium Tin Oxides) films. However, ITO films include so sparse Indium that the substitutive materials are expected. ZnO thin films are one of the hopeful materials as TCO films.

ZnO thin films were deposited on a fused silica glass (10 mm x 20 mm x 0.5 mm) by the DC sputtering method. The induced electric power, the substrate temperature were 12 W, 200 ℃, respectively, for all samples in common. The sputtering gas (Ar) pressure was 0.125, 0.2 and 0.3 Torr. for sample 1, sample 3 and sample 5, respectively.

Optical absorption, luminescence and excitation spectra were measured using the BL3B beam in the temperature range of 8-300 K.

Figure 1 shows the optical absorption spectra for ZnO thin films. The sharp edge at 150 nm (8.3 eV) for sample 1 is due to the absorption of fused silica substrate. The several broad bands below 360 nm (3.3 eV) are due to the band-to-band transition of ZnO. All the samples are efficiently transparent as TCO thin film above 380 nm (visible light region).

Figure 2 shows the luminescence spectra with various excitation wavelengths in sample 1 at 300 K. The band-to-band excitation below 360 nm produces several broad luminescence bands at 405 nm, at 425 nm and at 440-490 nm. In these spectra, the additional peaks around 540 and 590 nm are the influence from outer ceiling lights, which could not be perfectly eliminated. As the excitation wavelength increases (the excitation energy decreases), the intensity of luminescence bands decreases as a whole.

Figure 3 shows the luminescence spectra in sample 5 at 300 K. The spectra exhibit several broad luminescence bands at 405 nm, at 425 nm and at 440-490 nm. The spectra are very similar to that of sample 1. With increasing the excitation wavelength, the luminescence intensities decrease as a whole.

The band around 425 nm is estimated to be intrinsic luminescence (for example, self-trapped exciton). The broader band around 470 nm is estimated to be the luminescence associated with defects (for example, donor/acceptor recombination).

The relation between the luminescence and electrical conductivity will be examined. In this study, optical properties of Al doped ZnO thin films were investigated. It seems to be important to investigate the exact Al concentration in thin films which are made by sputtering with the target including 2% Al nominally.

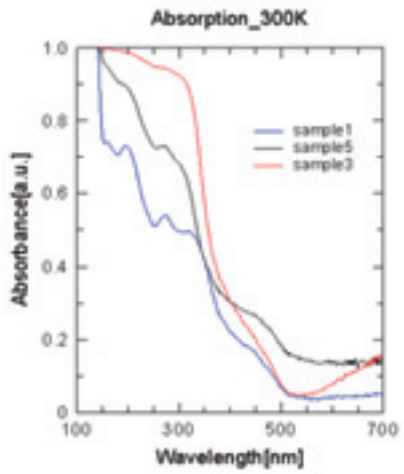

Fig. 1. Absorption spectra in ZnO thin films at 300 K.

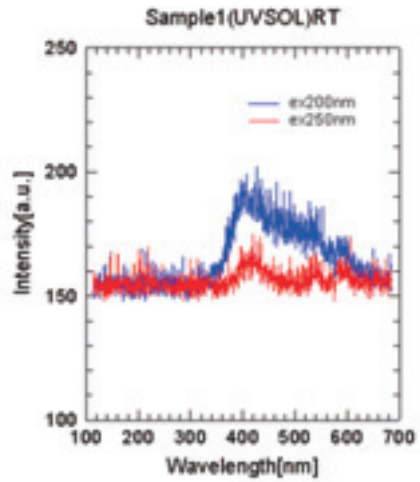

Fig. 2. Luminescence spectra in sample 1 at 300 K.

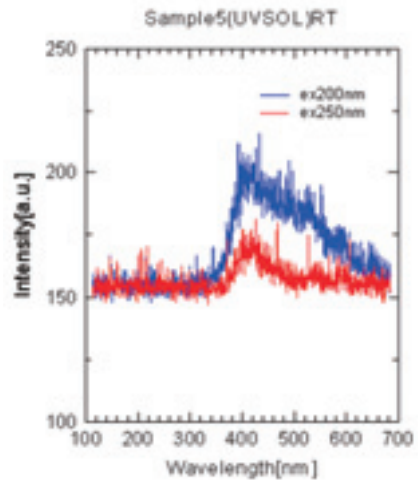

Fig. 3. Luminescence spectra in sample 5 at 300 K.

BL3B

Optical Spectroscopy of $Cd_{1-x}Mn_xTe$ Crystals

M. Yamaga, Y. Ogoshi, A. Kanetake, S. Takano, T. Nohisa, S. Tsuda and H. Tsuzuki
Department of Material and Design Engineering, Gifu University, Gifu 501-1193 Japan

$Cd_{1-x}Mn_xTe$ crystals have magneto-optical properties induced by Mn^{2+} ions. They are very useful as applications to an optical isolator.

In a previous activity report [1], optical properties of $Cd_{1-x}Mn_xTe$ crystals (x=0.5) were reported. In this report, the composition x is extended from 0.1 to 0.9 in the whole range of the composition. $Cd_{1-x}Mn_xTe$ crystals were grown by the vertical Bridgeman method. The compositions, x, of the crystals are 0.1, 0.25, 0.3, 0.5, 0.75, 0.9 being equal to the melting compositions [2].

Figure 1 shows the absorption spectra observed in $Cd_{1-x}Mn_xTe$ (x=0.1, 0.25, 0.3, 0.5, 0.75, 0.9) at 300 K. The band gap energy related to the absorption edge of the crystal increases with an increase of x up to 0.5 and slightly decreases above 0.6. This result suggests that the phase transition of the crystal $Cd_{1-x}Mn_xTe$ occurs around x=0.6 from zinc blende to hexagonal phases. The sample temperature is decreased from 300 K, the band edge is shifted to the short wavelength, resulting in the large band gap.

Figure 2 shows temperature dependence of the luminescence spectra for $Cd_{0.9}Mn_{0.1}Te$. The peak of the luminescence is around 720 nm and just below the band edge energy observed at 20 K. The luminescence peak is shifted to the longer wavelength and the intensity markedly decreases with an increase of temperature. The intensity is negligibly small above 140 K. In the same way, Fig. 3 shows the luminescence spectra of $Cd_{0.25}Mn_{0.75}Te$ at various temperatures. The luminescence peak is shifted to the short wavelength compared with that for $Cd_{0.9}Mn_{0.1}Te$. However, the line width for $Cd_{0.25}Mn_{0.75}Te$ is the largest for all crystals with the compositions of x=0.1, 0.25, 0.3, 0.5, 0.75, 0.9.

We consider the origin of the luminescence from $Cd_{1-x}Mn_xTe$ (x=0.1, 0.25, 0.3, 0.5, 0.75, 0.9) crystals. The luminescence may be assigned to weakly localized excitons. The line width has the maximum for x=0.75. This result is consistent with the ESR results of Mn^{2+} in $Cd_{1-x}Mn_xTe$ (x=0.1, 0.25, 0.3, 0.5, 0.75, 0.9) that the ESR line width has also the maximum at x=0.75. The line broadening is due to local magnetic field created by Mn^{2+} cluster in the $Cd_{1-x}Mn_xTe$ crystals.

[1] M. Yamaga, UVSOR Activity Report **38** (2010) 117.
[2] M. Prakasam, O. Viraphong, L. Teule-Gay, R. Decourt, P. Veber, E. G. Villora and K. Shimamura, J. Crystal Growth **318** (2011) 533.

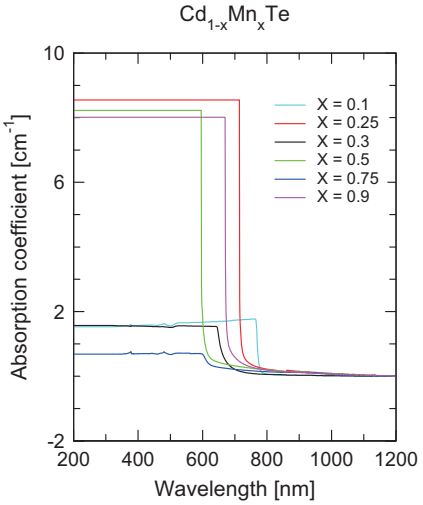

Fig. 1. Absorption spectra of $Cd_{1-x}Mn_xTe$.

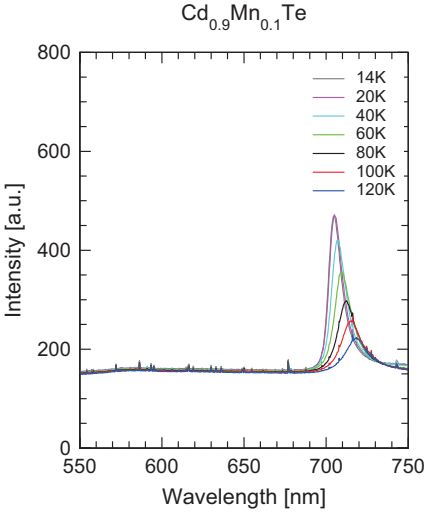

Fig. 2. Luminescence spectra in $Cd_{0.9}Mn_{0.1}Te$.

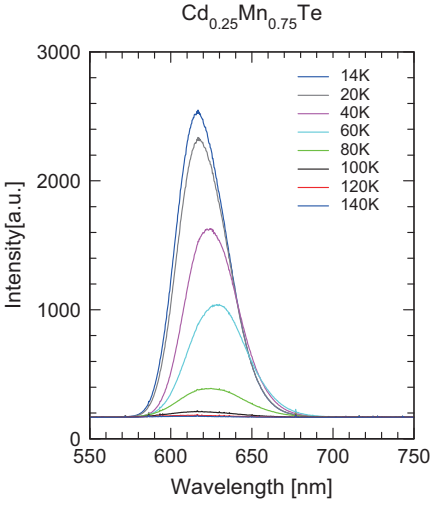

Fig. 3. Luminescence spectra in $Cd_{0.25}Mn_{0.75}Te$.

BL4B

Annealing Effect on Local Structure of Diamond-Like Carbon and Tungsten-containing Diamond-Like Carbon Films

A. Fujimoto and K. Kanda

Laboratory of Advanced Science and Technology for Industry, University of Hyogo Kamigori, Ako, Hyogo 678-1205, Japan

Diamond-like carbon (DLC) film is expected to use as various industrial fields, because of its some excellent properties such as hard, low friction coefficient, low surface energy and so on. Recently, incorporation of Tungsten (W) into DLC films was proposed because it was known that this incorporation improved the film's thermal durability. In the present study, the effect of annealing on DLC and tungsten containing DLC (W-DLC) films in vacuum was investigated from the measurement of the annealing temperature dependence on the carbon K-edge near-edge x-ray absorption fine structure (NEXAFS) spectra of the commercial DLC and W-DLC films fabricated by various methods for industrial use.

Sample commercial DLC and W-DLC films were prepared on the Si substrate with ≈200 nm film thickness using several deposition methods: 1) DLC and W-DLC films by unbalanced magnetron sputtering (UBMS) (KOBELCO Co., Ltd.), 2) DLC film fabricated by ion plating (IP) (NANOTEC Co., Ltd.), 3) DLC film fabricated by plasma-enhanced CVD (PE-CVD) (Nippon-ITF Inc.). These samples were annealed in a furnace (Thermo RIKO Co. Ltd; GFA430) under vacuum conditions ($<10^{-4}$ Pa). The annealing temperature was 673, 773, or 873 K, and the annealing time was 32 h. C-K NEXAFS spectra were measured at the BL4B of UVSOR and BL09A of NewSUBARU. The NEXAFS spectra were measured in the energy range 275-320 eV with 0.5 eV FWHM resolution in the total electron yield mode.

In the C-K NEXAFS spectra of DLC films, sharp peak, which is assignable to the transitisons from the C 1s level to the unoccupied π* levels of the sp^2 (C=C) and/or sp (C≡C) sites, is observed at 285.4 eV. The intensity of this peak increased with the annealing temperature, which indicated the increase of sp^2 ratio in the film. The procedure used to estimate the $sp^2/(sp^2+sp^3)$ ratio is described elsewhere [1]. Figure 1 shows the dependence of the $sp^2/(sp^2+sp^3)$ ratios of the films on the annealing temperature. The $sp^2/(sp^2+sp^3)$ ratios of the commercial W-DLC and DLC films as deposited were estimated to be 0.3-0.4. The $sp^2/(sp^2+sp^3)$ ratios of all the W-DLC and DLC films increased with the annealing temperature indicating that a graphite structure had formed[2]. Therefore, the onset of increase in $sp^2/(sp^2+sp^3)$ ratio was positioned at higher temperature indicated that the film had strong thermal durability. In short, thermal durability of these films was stronger in the order of IP DLC, UBMS W-DLC, UBMS DLC, and PE-CVD DLC films

As a result, the present study confirmed following facts from local structure level by the measurement of NEXAFS spectra: 1) Thermal stability of DLC films was varied on the deposition method of film. 2) Incorporation of W improves the film's thermal durability.

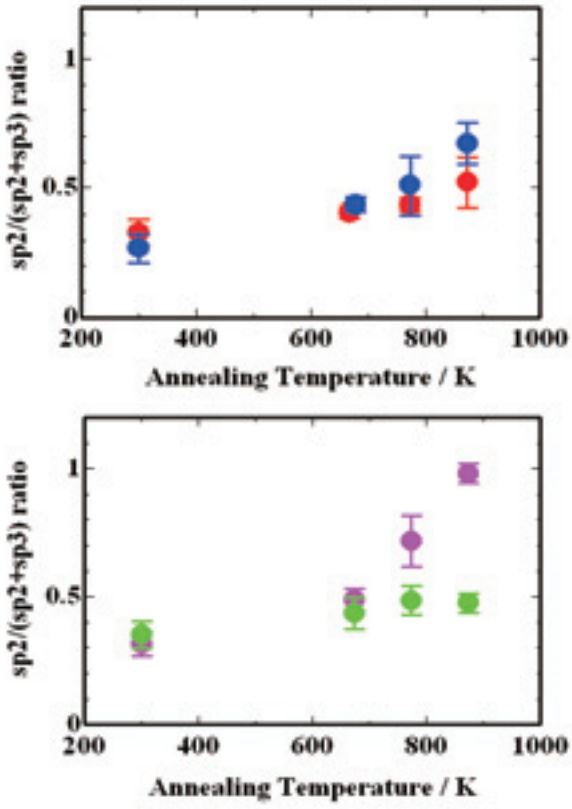

Fig. 1. Dependence on annealing temperature of $sp^2/(sp^2+sp^3)$ ratio:. a): UBMS W-DLC and : UBMS DLC films;. b): PE-CVD DLC and : IP DLC films. Points at 273 K indicate $sp^2/(sp^2+sp^3)$ ratio as deposited.

[1] K. Kanda, T. Kitagawa, Y. Shimizugawa, Y. Haruyama, S. Matsui, M. Terasawa, H. Tsubakino, I. Yamada, T. Gejo and M. Kamada, Jpn. J. Appl. Phys. **41** (2002) 4295.

[2] K. Kanda, J. Igaki, N. Yamada, R. Kometani and S. Matsui, Diamond Relat. Mater. **18** (2009) 490.

BL4B

Electronic Structural Changes of $LiNi_{0.5}Mn_{1.5}O_4$ during Lithium-Ion Intercalation/Deintercalation

T. Okumura, M. Shikano and H. Kobayashi

Research Institute for Ubiquitous Energy, National Institute of Advanced Industrial Science and Technology (AIST), Midorigaoka 1-8-31, Ikeda, Osaka 563-8577, Japan

Lithium-ion batteries (LIB) with high energy density, safety, and durability are required for electric vehicles (EV), hybrid electric vehicles (HEV), and plug-in hybrid electric vehicles (PHEV) as their power sources. Lithium nickel manganese spinel oxide $LiNi_{0.5}Mn_{1.5}O_4$ is one of the candidates for the positive electrode materials for LIBs as an alternative to the conventional $LiCoO_2$ cathode because of its low cost and low toxicity[1]. Moreover, its specific capacity above 4.5 V is suitable for designing the next-generation LIB with the high energy density. In order to get the guide to improve the superior electrochemical properties, understanding the detailed electronic structural changes in $Li_xNi_{0.5}Mn_{1.5}O_4$ during lithium-ion intercalation/deintercalation process is essential as reported in other electrode materials[2].

The $Li_xNi_{0.5}Mn_{1.5}O_4$ samples with various lithium concentrations have been picked up from the batteries after intercalation or deintercalation as shown in Fig. 1. Ni L_3-edge, Mn L_3-edge and O K-edge XANES spectra were measured with total electron yield mode. The Ni and Mn L_3-edge spectra at various lithium contents (shown in Fig. 2 (a) and (b), respectively) correspond to the electronic transitions from the $2p_{3/2}$ states to an unoccupied 3d state. At $x < 1$, the absorption edge peak at the right shoulder of Ni L_3-edge peaks clearly appeared with the decrement of the lithium-ion contents although the significant change could not be observed in Mn L_3-edge peaks. This result indicates that the charge variation during lithium-ion deintercalation was compensated by the redox reaction of the Ni^{2+}/Ni^{4+} couple[3]. On the other hand, at $x > 1$, the absorption edge energy of Mn L_3-edge peaks shifted towards lower energy levels with an increase of lithium content while Ni L_3-edge peaks were mostly maintained. This result indicates that the charge variation during lithium-ion intercalation was compensated by the redox reaction of the Mn^{3+}/Mn^{4+} couple [3]. The large voltage gap between $x < 1$ and $x > 1$ in Fig. 1 results from the difference of the redox-ion species.

The O K-edge spectra were shown in Fig. 2 (c). The absorption edge peaks appeared around 528-535 eV particularly indicate the transition from O 1s to hybridized orbital of O 2p with transition-metal 3d[2]. At $x > 1$, the shape of the peaks changed with the increase of the lithium content as well as the shape of Mn L_3-edge peaks changes as written above, although it maintained at $x > 1$.

These results indicated that both manganese and oxide ions contributed on the redox reaction at $x < 1$, and the only nickel ion affect the redox reaction at $x > 1$. Thus, the electronic structural change of oxide ion is also crucial for considering redox reaction at charging/discharging batteries, and the contribution of the oxide ion on redox reaction differs in various redox cation species.

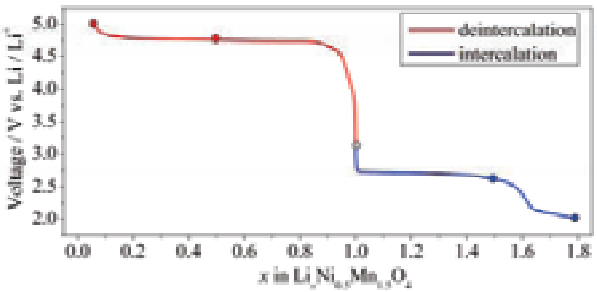

Fig. 1. Lithium-ion intercalation/deintercalation behavior in $LiNi_{0.5}Mn_{1.5}O_4$ spinel oxide. Circles indicate lithium content of samples measured XANES spectra.

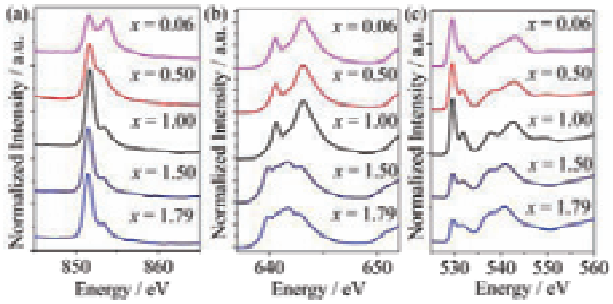

Fig. 2. XANES spectra of Ni L_3-edges (a), Mn L_3-edges (b), and O K-edges (c) in $Li_xNi_{0.5}Mn_{1.5}O_4$.

[1] Q. Zhong *et al.*, J. Electrochem. Soc. **144** (1997) 205.
[2] *for example*, T. Okumura *et al.*, Dalton Trans. **40** (2011) 9752.
[3] Y. Terada *et al.*, J. Solid State Chem. **156** (2001) 286.

BL5U

Valence-Band Electronic Structure of N-Implanted TiO_2

K. Soda[1], T. Owada[2], K. Morita[2], S. Harada[1], E. Kuda[1] and T. Yoshida[3,1]

[1]*Graduate School of Engineering, Nagoya University, Nagoya 464-8603, Japan*

[2]*Department of Physical Science and Engineering, Nagoya University, Nagoya 464-8603, Japan*

[3]*EcoTopia Science Institute, Nagoya University, Nagoya 464-8603, Japan*

TiO_2 is well-known as a photocatalyst with a band gap of ~3 eV [1]. Recently, Yoshida *et al*. have found that TiO_2 gains the photoactivity for visible light by N^+ ion implantation and that N occupying at the O site is responsible for the visible-light activity by the N *K*-edge near-edge X-ray absorption fine structure (NEXAFS) measurement [2]. In this study, we have investigated valence electronic structure of such N^+ implanted TiO_2 to clarify the origin of the visible-light photoactivity.

Photoelectron measurement were carried out at room temperature in the angle-integrated mode with total energy resolution of ~0.1 eV. Specimens were rutile TiO_2 (100) plates, which were first *in situ* cleaned by 5-keV Ar^+ ion sputtering and then implanted with 5-keV N^+ or N_2^+ ions. The origin of the binding energy E_B was set to the Fermi energy E_F of a gold plate on a sample holder.

Figure 1 shows typical photoelectron spectra recorded before and after the N^+ implantation with the excitation photon energy $h\nu$. In the figure, the background due to the secondary electrons are subtracted from the measured spectra and their intensity is normalized with the integrated intensity from E_F up to E_B = 12 eV. In the upper panel, spectra after the Ar^+ sputtering and subsequent N^+ implantation of ~8 x 10^{20} ions m^{-2} are compared by shifting the spectrum after the implantation towards the high binding energy side so that the valence band bottom (E_B = 8 ~ 9 eV) may coincide with each other. The N *K*-edge NEXAFS measurement for this sample confirms the formation of visible-light active N species. After the sputtering, a broad hump appears in the upper part of the gap around E_F. This is due to the reduction of Ti or defect formation, induced by the sputtering, which also leads to the increase in electrons in the Ti 3*d* conduction band. Observed apparent shift of the Fermi edge towards the high binding energy side after the implantation implies the decrease in defects and conduction electrons, which may be caused by the recovery of the chemical bond, *i.e.* new Ti-N bond formation. Spectral increase due to the N 2*p* states derived from the Ti-N bond appears in the upper part of the O 2*p* valence band and in the lower region of the gap (E_B = 3 ~ 6 eV). The assignment of these new bands after the implantation is also confirmed by the Ti 3*p*-3*d* resonance behavior around $h\nu$ = 50 eV, which is shown in the lower panel of the figure for the spectra after the implantation. At $h\nu$ = 50 eV, the hump around 0.5 eV, Ti 3*d* conduction band or defect states, and the O 2*p*-Ti 3*d* bonding valence band at E_B ~ 7 eV are enhanced due to the resonance photoemission of the Ti3*d* electrons [3], while the states at E_B = 3 ~ 6 eV show no prominent increase, because they are mainly derived from O 2*p* and N 2*p* states. These are consistent with a band calculation for TiO_2 and N-substituted $TiO_{2-x}N_x$ [1].

Similar results have already reported by Batzill *et al*., who concluded that the impurity states just above the valence band without the band-gap narrowing were formed by N doping [3]. However, the present results together with the NEXAFS ones suggest that the implanted N occupies the O site and forms a common valence band extending into the band gap in the surface region; the top of the valence band is located at E_B ~ 2.5 eV, which is comparable with reported threshold of the photoactivity in the decomposition of methylene blue for the N-doped TiO_2 [1]. The Ti 3*d* defect states just below the conduction band also induce visible-light absorption but are not responsible for the photoactivity.

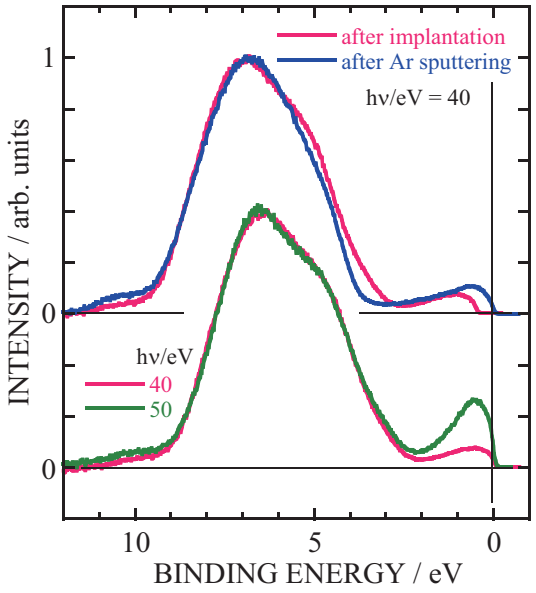

Fig. 1. Valence-band spectra of N-implanted TiO_2.

[1] R. Asahi *et al.*, Science **293** (2001) 269.
[2] T. Yoshida *et al.*, Mater. Sci. Forum **561-565** (2007) 567.
[3] M. Batzill *et al.*, Phys. Rev. Lett. **96** (2006) 026103.

BL5U

Effects of Periodicity Imperfection on Mini-Bands in Semiconductor Superlattice

K. Hashimoto[1], D. Shimura[1], M. Kuwahara[2], S. Harada[1], T. Ujihara[1], M. Matsunami[3] and S. Kimura[3]

[1]*Graduate School of Engineering, Nagoya University, Nagoya 464-8603, Japan*
[2]*EcoTopia Science Institute, Nagoya University, Nagoya 464-8603, Japan*
[3]*UVSOR Facility, Institute for Molecular Science, Okazaki 444-8585, Japan*

Recently a highly-optimized intermediate band solar cell, of which a high conversion efficiency can reach 74.6% theoretically, is proposed [1]. The concept is to utilize intermediate bands in the carrier excitation in order that the band structure is adjusted to the solar light spectrum. As intermediate bands, the mini-band due to a periodic quantum structure (superlattice structure) is used. But there is a problem that it is presently impossible to produce quantum dots of equal size and perfect periodicity.

In this study, the effects of periodicity imperfection on the mini-band structure, especially hole mini-bands, were investigated. We examined a superlattice structure which consists of multiple quantum wells because the preparation method has been established.

Figure 1 shows the detailed structures of each sample: A GaAs bulk sample, a periodic superlattice and a disordered superlattice of which second well layer was made thinner. Amorphous arsenic layers were deposited on the sample surfaces to suppress oxidation, and they were removed just before the measurements by heat-treatment. On the evaluation of the mini-band structure, the synchrotron-radiation photoemission measurements were performed at BL5U of the UVSOR facility.

Figure 2 shows the electron density mappings in a valence band around Γ point. The red dots and green dots indicate the band structure determined from the peak values of the second order differential. They are a heavy hole band and a light hole band, respectively. In the case of bulk GaAs, the band structures are quadric curves. In addition, they are doubly-degenerated at $k_z = 0$. On the other hand, the band structures of the periodic superlattice and the disordered superlattice are not degenerated at $k_z = 0$. Moreover, they are also folded symmetrically on the white arrows, which indicate the interval of the Brillouin zone due to the periodic structure of superlattice. Therefore, their band structures are mini-bands.

The mini-band structures are characterized by the width of band splitting between the heavy hole mini-band and the light hole mini-band. Figure 3 shows the width of band splitting as a function of the wavenumber. The width of the disordered superlattice is wider than that of of the periodic superlattice. This is attributed to the following discussion: Due to the thinner well, the heavy hole band and the light hole band of the disordered superlattice were lower than those of the periodic superlattice. The band shift amount of the light hole band is larger than that of the heavy hole band by a difference in the effective mass. As a result, the width of the disordered superlattice is wider.

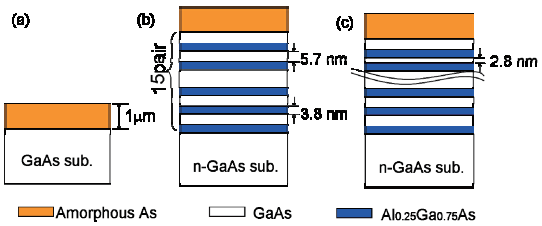

Fig. 1. Schematic images of the sample structure. (a) GaAs, (b) periodic superlattice and (c) disordered superlattice.

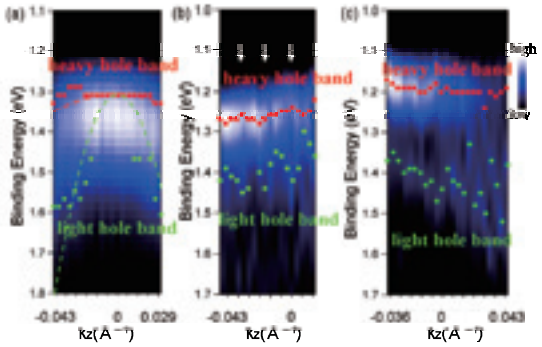

Fig. 2. Electron density mappings of (a) GaAs, (b) periodic superlattice and (c) disordered superlattice.

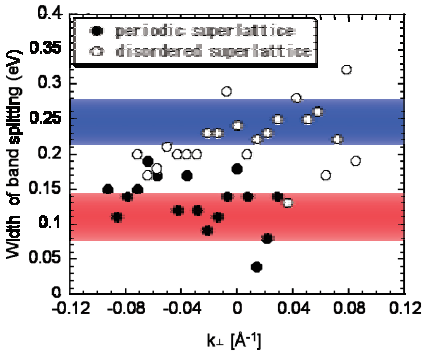

Fig. 3. Width of band splitting between heavy hole mini-band and light hole mini-band.

[1] T. Nozawa and Y. Arakawa, Appl. Phys. Lett. **98** (2012) 171108.

BL5B

Photodegradation in Amorphous Chalcogenide Semiconductor Films by Vacuum Ultraviolet Absorption Spectroscopy

K. Hayashi

Department of Electrical and Electronic Engineering, Gifu University, Gifu 501-1193, Japan

It is well known that amorphous chalcogenide semiconductor materials show a variety of photoinduced effects [1-4]. The prominent photoinduced phenomenon in these materials is a time-dependent decrease in photocurrent during and after irradiation of bandgap (BG) light [3,4]. This phenomenon is usually called photodegradation and is explained in terms of light-induced metastable defects (LIMD). In the device application of these materials, LIMD creation is a serious problem. Although a number of models have been proposed for LIMD creation [4], details of the mechanism underlying LIMD creation in these materials are still not clear. Understanding the physical mechanism underlying metastability is one of the important fundamental problems related to these materials.

Recently, I found a new phenomenon that photocurrent by irradiation of BG light increased in amorphous chalcogenide films. This phenomenon is not explained in terms of LIMD creation. These photoinduced phenomena can in general be either irreversible, i.e. the photoinduced changes are permanent after irradiation, or reversible, in which case the changes can be removed by annealing to the glass-transition temperature. The new phenomenon was an irreversible change. The photoinduced changes by BG light of the x-ray diffraction and the volume have directly shown that these phenomena are due to a change of the local structure of the amorphous network. However, several previous studies of photoinduced phenomena have reported that there is no direct correlation among photodegradation, photodarkening and photoinduced volume change.

Our recent studies have focused on the photoinduced energy structure changes in the vacuum ultraviolet (VUV) region by irradiation of BG light. Few studies have examined whether the photoinduced change of the chemical bonds contributes to photodegradation and photodarkening. To understand the dynamics and the correlation of photoinduced structure changes in the VUV region and the photoinduced change of photocurrent in amorphous chalcogenide semiconductors, real time in-situ measurements are required. In previous report, those dynamics and correlations are examined by measuring the total photoelectron yield (TPEY) that can measure the optical property in the VUV region. However, the beam position, brightness, and the energy stability were insufficient in the observation of the dynamics of TPEY by irradiation of BG light in UVSOR. In this report, I will discuss the stability of light source.

Samples used for the measurement of the transmission spectrum were amorphous chalcogenide (a-As_2S_3 and a-As_2Se_3) semiconductor thin films prepared onto aluminum thin films. Typical thickness of the sample and the aluminum films were around 200nm and 100nm respectively. The aluminum film was also used in order to eliminate the higher order light from the monochromator in the VUV region. The measurements were performed at room temperature. A pinhole of 1.5mm in a diameter was inserted between the monochromator and sample to remove stray light. The intensity of the VUV light was monitored by measuring the TPEY of a gold mesh.

Figure 1 shows the spectra of the light source under the same condition monitored by measuring the TPEY of a gold mesh. As shown in the figure, the spectrum reproducibility in the top-up operation is not good. We are examining the method to increase the accuracy of measurement at present.

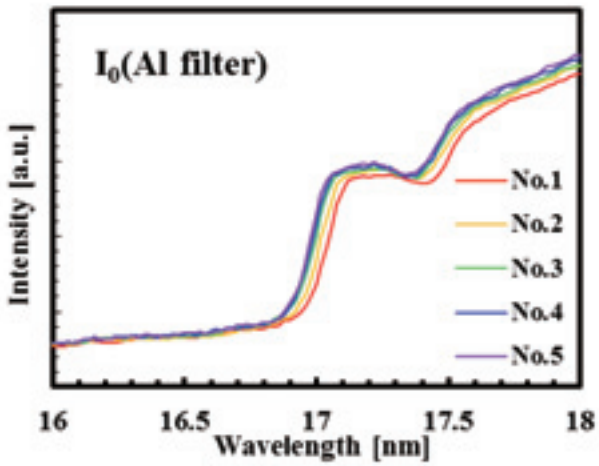

Fig.1. Spectra of the light source under the same condition monitored by measuring the TPEY of a gold mesh.

[1] K. Tanaka, Rev. Solid State Sci. **4** (1990) 641.
[2] S. R. Elliot, J. Non-Cryst. Sol. **81** (1986) 71.
[3] D. L.Staebler and C. R. Wronski, Appl. Phys. Lett. **31** (1977) 292.
[4] K. Shimakawa, A. Kolobov and S. R. Elliott, Adv. Phys. **44** (1995) 475.

BL6U

Extended Electronic States in Crystalline Guanine-Cytosine Watson-Crick Multilayers

R. Friedlein[1], Y. Wang[1], H. Yamane[2] and N. Kosugi[2]

[1] *School of Materials Science, Japan Advanced Institute of Science and Technology, Ishikawa 923-1292, Japan*

[2] *Dept. of Photo-Molecular Science, Institute for Molecular Science, Okazaki 444-8585, Japan*

In order to elucidate the role of intermolecular interactions in the pre-biotic assembly of RNA precursor oligomers, it is crucial to understand, if and in which way one-dimensional, stacked assemblies of Watson-Crick (WC) pairs may be formed without the presence of a backbone. With scanning tunneling microscopy studies limited to monolayer assemblies [1], the nature of the stacking between individual nucleic acids as well as of WC pairs has so far only been studied theoretically [2].

In recent home-based experiments we have found that the two nucleic acids guanine and cytosine assemble into an ordered multilayer film based on the hydrogen bonding within WC pairs (Fig. 1). The stability of WC pairs is high such that a macroscopic phase separation does not occur. Thin mixed films, about 2-3 nm thick, have been prepared under ultra-high vacuum conditions by co-deposition of guanine and cytosine molecules, at equal rates with respect to the amount of molecules, on the surface of highly-oriented pyrolytic graphite, HOPG(0001), held at 25 °C. The samples have then been exposed to water vapor *in situ*, and transferred in air to the experimental set-up at BL6U of the UVSOR facility.

Photon-energy dependent valence band photoelectron spectra obtained in the normal emission direction are shown in Fig. 1. The onset of the spectra is related to the highest occupied molecular orbital (HOMO) of guanine. It shows a clear dispersion with the photon energy which is consistent with the formation of extended electronic states related to the guanine HOMO similar to those in guanine multilayer films [3]. This demonstrates a quasi-columnar arrangement of the guanine molecules oriented in the direction normal to the surface and an anti-parallel stacking with two molecules per repeat unit along the stacks. Non-dispersing states at higher binding energy, denoted “A” and “B”, are related to cytosine molecules that have a significantly smaller intermolecular π-π overlap.

In order to accomplish an anti-parallel stacking in a layered arrangement, subsequent WC pairs must be flipped with respect to each other. As verified by quantum-chemical calculations [4], in this configuration, the cytosine molecules stack with those from neighboring WC pairs. This is in stark contrast to the arrangement realized in RNA which indicates an important role of the backbone sugars in preventing otherwise preferred anti-parallel stacking configurations.

Financial support from the SHIBUYA and MARUBUN Foundations is acknowledged.

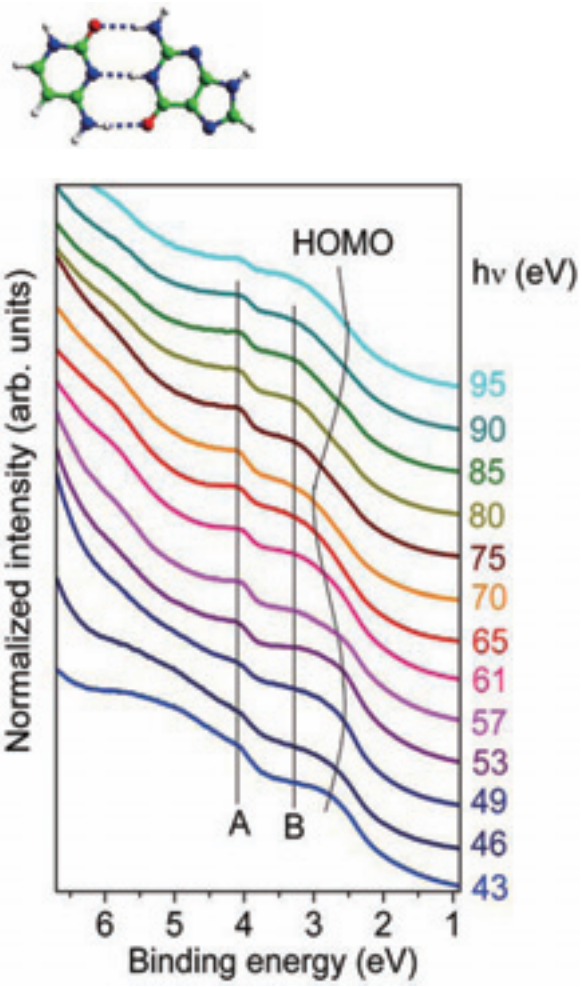

Fig. 1. The structure of a cytosine-guanine WC pair (top), and photon-energy-dependent photoelectron spectra of the mixed film (bottom). The dispersion of the guanine-derived HOMO is indicated by a solid line.

[1] S. Xu, M. Dong, E. Rauls, R. Otero, T. R. Linderoth and F. Besenbacher, Nano Lett. **6** (2006) 1434.

[2] C. Acosta-Silva, V. Branchadell, J. Bertran and A. Olivia, J. Phys. Chem. B **114** (2010) 10217.

[3] R. Friedlein, Y. Wang, A. Fleurence, F. Bussolotti, Y. Ogata and Y. Yamada-Takamura, J. Am. Chem. Soc. **132** (2010) 12808.

[4] Y. Wang, F. Negri, H. Yamane, N. Kosugi and R. Friedlein, in preparation.

BL6U

Band Alignment at CNT/n-Type 4H-SiC Interface Formed by Surface Decomposition of SiC

T. Maruyama[1], S. Sakakibara[1], Y. Ishiguro[1], H. Yamane[2] and N. Kosugi[2]
[1]*Department of Materials Science and Engineering, Meijo University, Nagoya 468-8502, Japan*
[2]*Institute for Molecular Science, Okazaki 444-8585 Japan*

Carbon nanotube (CNT) growth by surface decomposition of SiC is a synthesis method for self-organized CNT films only by heating SiC(000-1) carbon-face in a high vacuum [1]. By this method, high-density, well-aligned zigzag-type CNTs can be produced perpendicular to the substrate surfaces. In addition, CNTs were atomically bonded to SiC without any interlayers [2]. Previously, we reported both electrical property and electronic structure for CNT/n-type 6H-SiC and showed the presence of Schottky barrier at the interface [3]. In this study, we performed photoemission spectroscopy (PES) experiments for CNT/n-type 4H-SiC interface and determined the band alignment.

CNT films formed by surface decomposition of n-type 4H-SiC(000-1) were used as samples. For PES measurements, we prepared three kinds of samples with different CNT thicknesses; CNTs (~300 nm) on 4H-SiC, CNTs (several nm) on 4H-SiC and 4H-SiC(000-1) substrate. The PES measurements were carried out in a high-resolution angle-resolved PES system at BL6U. All PES spectra were measured at normal emission with the incident photon energy of 60 and 350 eV. The overall energy resolution was below 100 meV at room temperature (~300K).

Figure 1 (a) shows PES spectrum near valence band maximum (VBM) of CNTs (~300 nm) formed on 4H-SiC with that of Au. The Fermi edge is observed in the spectrum of CNTs, confirming that they were metallic, as reported for CNT films on 6H-SiC [3]. The band alignment at the CNT/SiC interface can be evaluated by measuring the binding energy of C 1s core level at the CNT/4H-SiC interface, the energy separation between the VBM and the C 1s core level of 4H-SiC and that between the Fermi edge and the C 1s level of CNTs [3]. Figure 1 (b) shows PES spectrum of the C 1s core level of CNT/SiC interface. By peak fitting, the energy separation in the C 1s core level between CNT and 4H-SiC was estimated to be 1.36 eV. From the PES measurements, we also determined the binding energy of C 1s peaks of CNTs (~300 nm) to be 284.35 eV and the energy separation between the VBM and C 1s core level of SiC to be 279.30 eV.

From these values, the band alignment at the CNT/4H-SiC interface was obtained, which is shown in Fig. 2. It should be noted that, in contrast with the CNT/n-type 6H-SiC interface, Schottky barrier was not formed at the CNT/4H-SiC interface. This result is consistent with recent experimental results about the current-voltage (I-V) characteristics of CNT(~300 nm)/n-type 4H-SiC heterojunction, which showed Ohmic behavior [4].

This work was supported in part by the Joint Studies Program (2011) of the Institute for Molecular Science (IMS).

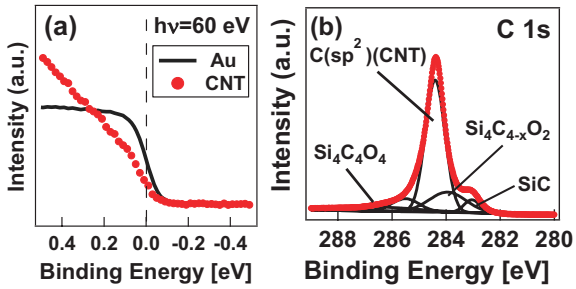

Fig. 1. PES spectra of (a) VBM of CNTs with the Fermi edge of Au (hν = 60 eV), and (b) C 1s core spectrum of CNT(several nm)/4H-SiC (hν = 350 eV).

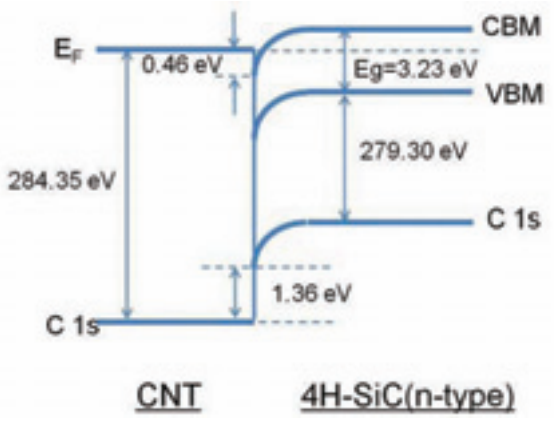

Fig. 2. Band alignment of CNT/n-type 4H-SiC heterojunction.

[1] M. Kusunoki *et al.*, Appl. Phys. Lett. **77** (2000) 531.
[2] M. Kusunoki *et al.*, Chem. Phys. Lett. **366** (2002) 458.
[3] T. Maruyama, S. Sakakibara, H. Ito, H. Yamane, E. Shigemasa and N. Kosugi, UVSOR Activity Report **38** (2011) 127.
[4] S. Sakakibara, Unpublished master's thesis. Meijo University (2012).

BL6U

Valence-Band Dispersion of Metal Phthalocyanines (I): *Intra*molecular and *Inter*molecular Electron-Phonon Coupling in Crystalline Films of Zinc Phthalocyanine (ZnPc)

H. Yamane and N. Kosugi

Department of Photo-Molecular Science, Institute for Molecular Science, Okazaki 444-8585, Japan
School of Physical Sciences, The Graduate University for Advanced Studies, Okazaki 444-8585, Japan

It has been predicted by theoretical studies that local/nonlocal electron-phonon (e-ph) couplings play a crucial role in the charge transport mechanism in organic molecular solids [1]. In order to examine the evidence for the e-ph coupling in organic molecular solids experimentally, the temperature dependence of the electronic structure of well-crystallized samples should be taken into account.

In this work at BL6U, we prepared a crystalline film of zinc phthalocyanine (ZnPc), a promising material for organic electronics, with a flat-lie orientation on the Au(111) surface, wherein the intermolecular π-π interaction exists along the surface normal direction. The crystallinity of the ZnPc film was confirmed by the incident-angle dependence of X-ray absorption spectroscopy, the low-energy electron diffraction, and the CuKα X-ray diffraction. From the angle-resolved photoemission spectroscopy (ARPES) experiments on the crystalline ZnPc film on Au(111), we observed an intermolecular valence-band dispersion [$E(\boldsymbol{k})$] and the clear evidence for the e-ph coupling as a function of the temperature.

Figure 1 (a) shows the $E(\boldsymbol{k})$ relation of the ZnPc crystalline film prepared on Au(111), which is obtained from the incident photon energy dependence of normal emission ARPES spectra at 15 K. The highest occupied molecular orbital [HOMO (π, a_{1u})], Zn3d (b_{1g}), and π's derived peaks show a dispersive shift with the same periodicity. This periodicity corresponds well with the Γ and Y points, estimated from the lattice constant of 3.32 Å determined by the X-ray diffraction [Fig. 1 (b)]. This correspondence indicates that the observed $E(\boldsymbol{k})$ is ascribed to the intermolecular interaction. The tight-binding fitting to the $E(\boldsymbol{k})$ relation gives a HOMO transfer integral (t) of 25 meV and hence a HOMO bandwidth (= 4t) of 100 meV, which is the same order as a reorganization energy for local phonons of CuPc [2].

In order to examine the e-ph coupling in crystalline ZnPc film, we measured the temperature dependence of ARPES at the Γ and Y points with the 60 and 90 eV incident photons, respectively. As seen in Fig. 1 (c), the Γ-point HOMO energy shifts depending on the temperature, while the Y-point HOMO energy seems independent on the temperature. From the lineshape analysis, we found that both the HOMO bandwidth (i.e., energy difference between the Γ- and Y-HOMO) and the Γ-HOMO peakwidth are narrowed with increasing the temperature, which is an opposite trend in a remanent Au(111) Fermi edge. This is the distinct indication of the local/nonlocal e-ph interaction; that is, band narrowing due to the interaction with local phonons (intramolecular vibrations) and band widening due to interaction with nonlocal phonons (intermolecular lattice vibrations) [1]. Thus, it is considered that a transition between incoherent hopping transport associated with the local e-ph coupling and coherent band transport associated with the nonlocal e-ph coupling occurs within the energy scale of 100 meV in the crystalline ZnPc. From the $E(\boldsymbol{k})$ relation, in the coherent band transport at the low temperature, the effective mass and the mobility of the HOMO hole are 13.8m_0 and 28.9 cm^2/Vs at 15 K, respectively.

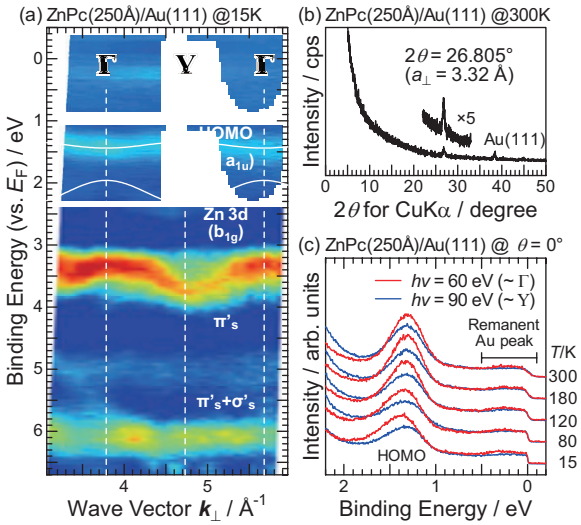

Fig. 1. (a) Intermolecular $E(\boldsymbol{k})$ relation of the crystalline ZnPc film on Au(111) at 15 K, wherein the second derivative of the ARPES spectra were used for mapping out. White curves for the HOMO and Zn 3d derived bands are the best-fit results in the tight-binding model. (b) CuKα X-ray diffraction of the crystalline ZnPc film on Au(111) at 300 K. (c) Temperature dependence of ARPES in the HOMO-band region at the Γ and Y points, measured with 60 and 90 eV incident photons, respectively.

[1] C. A. Perroni, V. M. Ramaglia, and V. Cataudella, Phys. Rev. B **84** (2011) 014303, and refs therein.
[2] S. Kera, H. Yamane, and N. Ueno, Prog. Surf. Sci. **84** (2009) 135.

Valence-Band Dispersion of Metal Phthalocyanines (II): Phase Reversal of the Intermolecular HOMO-Band Dispersion between Crystalline Films of Non- and Per-Fluorinated Zinc Phthalocyanines

H. Yamane and N. Kosugi

Department of Photo-Molecular Science, Institute for Molecular Science, Okazaki 444-8585, Japan
School of Physical Sciences, The Graduate University for Advanced Studies, Okazaki 444-8585, Japan

The energy band dispersion [$E(\boldsymbol{k})$] is a fundamental basis to understand electric properties of solids such as hole mobility (μ_h). In the field of organic solids, the study of the intermolecular $E(\boldsymbol{k})$ shows a rapid progress due to the needs of the interpretation of the charge transport mechanism in organic electronic devices. However, due to the weak intermolecular interaction and the difficulty in preparing crystallized films for the $E(\boldsymbol{k})$ measurement, the intermolecular $E(\boldsymbol{k})$ has been observed for high-μ_h materials. In order to elucidate and control the functionality of organic semiconductors, a systematic experiment on the intermolecular $E(\boldsymbol{k})$ can play a crucial role.

Recently, we have observed the intermolecular $E(\boldsymbol{k})$ in a crystalline zinc phthalocyanine (ZnPc) film on Au(111) using the angle-resolved photoemission spectroscopy (ARPES) at BL6U [1]. One of the key points of this observation is that the $E(\boldsymbol{k})$ relation of ZnPc can be a benchmark for the systematic study on the intermolecular interaction in terms of the intermolecular distance and/or the orbital symmetry by changing terminal groups or central metals in the molecule. In this work, we have studied the effect of the fluorination of ZnPc (*i.e.*, F_{16}ZnPc) on the $E(\boldsymbol{k})$.

Figure 1 (a) and (b) show the *ex situ* CuKα X-ray diffraction (XRD) and the *in situ* incident-angle (α) dependence of N-K X-ray absorption spectra (XAS), taken by the sample-current mode, measured for a 150-Å-thick F_{16}ZnPc film on Au(111), respectively. A F_{16}ZnPc-derived XRD peak appears at 2θ = 27.565°, which gives a lattice constant of 3.23 Å. This value is in good agreement with the molecular orientation estimated from XAS, wherein the sharp π^* peaks at 397–400 eV are strongest at α = 60°. From these results, we found that the molecules form a well-known β-bilayer (β_{BL})-crystalline structure, which is similar to α-crystalline ZnPc, with their molecular plane parallel to the Au(111) surface.

Figure 1 (c) shows the incident photon energy ($h\nu$) dependence of ARPES at the normal emission for the β_{BL}-crystalline F_{16}ZnPc film on Au(111). A highest occupied molecular orbital (HOMO)-derived peak shows a clear periodic shift with $h\nu$. From the $E(\boldsymbol{k})$ relation for the HOMO band of F_{16}ZnPc and ZnPc in Fig 1 (d), we found that the bandwidth of F_{16}ZnPc (120 meV) is larger than that of ZnPc (100 meV), which is consistent with their intermolecular distance. Moreover, the dispersion phase for the HOMO band of F_{16}ZnPc is flipped from that of ZnPc. This reversal may originate from the π···F 2p interaction, which is under theoretical consideration.

[1] H. Yamane and N. Kosugi, a separate page in this volume.

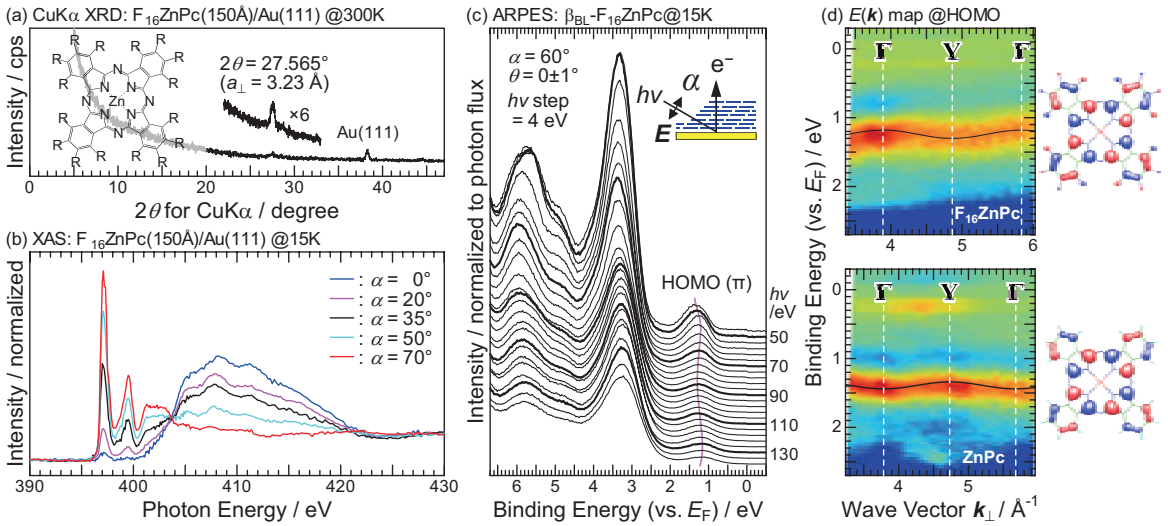

Fig. 1. (a) CuKα XRD of F_{16}ZnPc films (150 Å) on Au(111). Inset is a molecular structure of ZnPc (R = H) and F_{16}ZnPc (R = F). (b) Incident-angle (α) dependence of N-K X-ray absorption spectra for the crystalline film of F_{16}ZnPc on Au(111) at 15 K. (c) Photon energy ($h\nu$) dependence of ARPES for the crystalline film of F_{16}ZnPc on Au(111) at 15 K. (d) Comparison of the HOMO-band dispersion of β_{BL}-F_{16}ZnPc (top) and α-ZnPc (bottom).

Valence-Band Dispersion of Metal Phthalocyanines (III): Dimerization of Mn-3d-Derived Band in Crystalline Films of Manganese Phthalocyanine (MnPc)

H. Yamane and N. Kosugi

Department of Photo-Molecular Science, Institute for Molecular Science, Okazaki 444-8585, Japan
School of Physical Sciences, The Graduate University for Advanced Studies, Okazaki 444-8585, Japan

Metal phthalocyanines (MPc) have attracted much attention due to their unique electronic and magnetic properties in terms of organic electronics/spintronics. In this work, we have examined the intermolecular interaction in a crystalline film of MnPc, a promising organic spintronic material, by using angle-resolved photoemission spectroscopy (ARPES) at BL6U.

Figure 1 (a) shows the CuKα X-ray diffraction (XRD) for a 200-Å-thick MnPc film on Au(111). A MnPc-derived XRD peak appears at 2θ = 27.250°, which gives a lattice constant of 3.27 Å. In the N-K X-ray absorption spectra (XAS) for the crystalline MnPc film on Au(111) [Fig. 1 (b)], sharp transition peaks appear at 397–403 eV. Among these, peak X at 398 eV shows a broad incident angle (α) dependence, which may originate from the hybridization between the N p and Mn d states. Other peaks are ascribed to the N 1s → π* transitions. A sharp α dependence of these π* peaks indicates the flat-lie orientation, which is consistent with XRD.

Figure 1 (c) shows the incident photon energy ($h\nu$) dependence of ARPES at the normal emission for the crystalline MnPc film prepared on Au(111) at 15 K. The highest occupied molecular orbital (HOMO) of ZnPc is derived from the C 2p orbital; on the other hand, the HOMO of MnPc is derived from the Mn 3d orbital [1]. The HOMO (Mn 3d) and HOMO-1 (C 2p) derived peaks of MnPc show a clear periodic shift with $h\nu$. Moreover, we have found that the Mn 3d derived peak consists of two components with the different dispersion, indicating the relatively strong interaction at the Mn site.

Figure 1 (d) shows the valence band dispersion $E(\boldsymbol{k})$ map for the crystalline MnPc film on Au(111), wherein the symmetric Γ and Y points are estimated from the lattice constant of 3.27 Å from the XRD data. The agreement between the periodicity of C 2p peak and the symmetric points indicates that the observed $E(\boldsymbol{k})$ is ascribed to the intermolecular interaction. For the Mn 3d peak, the peak split and its dispersion are clearly seen in the $E(\boldsymbol{k})$ map. Furthermore, the periodicity of the Mn 3d dispersion is 1/2 times of that of the C 2p dispersion as labeled Y_{2a}. A possible origin of the Mn 3d dispersion is dimerization of the Mn d_π state.

Moreover, various band dispersions are observed in the energy region of 3–4 eV. There is a possibility of the deconvolution of the broad photoemission peak into individual molecular orbitals by the combination with theoretical calculations.

[1] *e.g.*, M.-S. Liao and S. Scheiner, J. Chem. Phys. **114** (2001) 9780; M.-S. Liao, J.D. Watts and M.-J. Huang, Inorg. Chem. **44** (2005) 1941.

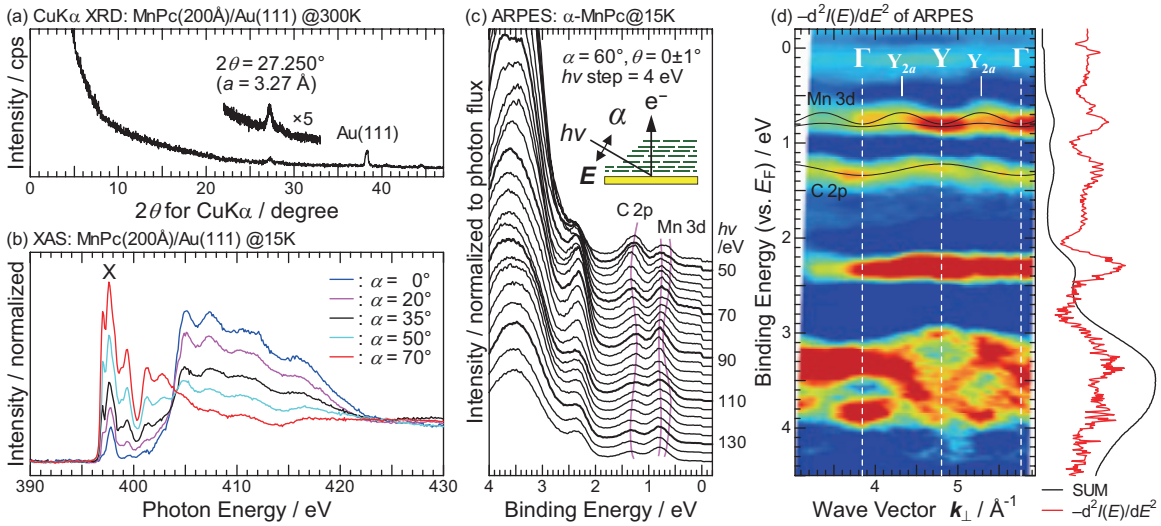

Fig. 1. (a) CuKα XRD of MnPc films (200 Å) prepared on Au(111). (b) The incident angle (α) dependence of N K-edge XAS of crystalline films of MnPc on Au(111) at 15 K. (c) The photon energy ($h\nu$) dependence of ARPES and (d) the intermolecular $E(\boldsymbol{k})$ relation, which is obtained from the second derivative of the raw ARPES data, of the crystalline film of MnPc prepared on Au(111) at 15 K.

BL6B

Far-Infrared Reflective Study of Alkali Niobate Ceramics

T. Nishi, T. Hayakawa, H. Yamada and K. Kakimoto

Graduate School of Engineering, Nagoya Institute of Technology Nagoya 466-8555, Japan

Alkali niobate is one of the promising candidates of lead-free piezoelectric materials. Especially, Li-doped (Na,K)NbO_3 (LNKN) solid solution shows excellent piezoelectric properties. Although it was expected that the distortion of NbO_6 unit would contribute to the good ferroelectric properties, the details are still unclear. Thus, the knowledge of the relation between the vibration of NbO_6 unit and ferroelectric properties is strongly needed. The vibration of the NbO_6 is observed as a ferroelectric soft mode in the infrared (IR) spectrum. So, this study was aimed to the analysis of the ferroelectric soft mode of $Na_{0.5}K_{0.5}NbO_3$ which is a base material of the LNKN.

The $Na_{0.5}K_{0.5}NbO_3$ ceramic sample was synthesized by a solid-state reaction method. The surface of $Na_{0.5}K_{0.5}NbO_3$ ceramic was polished and used for IR reflectivity study. The reflectivity far-infared spectram was obtained in the range of 20 – 8000 cm^{-1} at room temperature using a synchrotron radiation source, then the spectra were corrected by using a Michelson interferometer (Bruker, IFS66v).

Figure 1 shows the reflectance spectram of $Na_{0.5}K_{0.5}NbO_3$ ceramics at room temperature. The spectrum was analyzed using the following formula,

$$\varepsilon(\omega) = \varepsilon_\infty \prod_{j=1}^{n} \frac{\omega_{jLO}^2 - \omega^2 + i\omega\gamma_{jLO}}{\omega_{jTO}^2 - \omega^2 + i\omega\gamma_{jTO}} \qquad (1).$$

Figure 2 shows the infrared reflectance spectram around the wavenumber of the soft mode and the fitting curve. Table 1 shows the fitting parameters of the soft mode. The soft mode frequency obtained from the IR spectroscopic analysis was 255 cm^{-1}. Relative permittivity ε_r calculated from the soft mode wavenumber was ε_r of 520. This result was different from the measured value (capacitance method, ε_r of 555 at 1kHz). The permittivity in the range of THz, which was the observed soft mode, is contributed a ionic polarization. On the other hand, the permittivity in the range of kHz was due to ionic and orientation polarizations. This suggested that the ionic polarization contributed the NbO_6 unit accounted for 94 % of the total permittivity of $(Na_{0.5}K_{0.5})NbO_3$. Thus, the relation between the distortion of the NbO_6 units and a ferroelectric property can be evaluated by using the IR spectroscopy analysis. We will investigate the relation between a ferroelectric property and the amount of a distortion of the NbO_6 by analyzing the IR spectra of Li-doped (Na,K)NbO_3 solid solution.

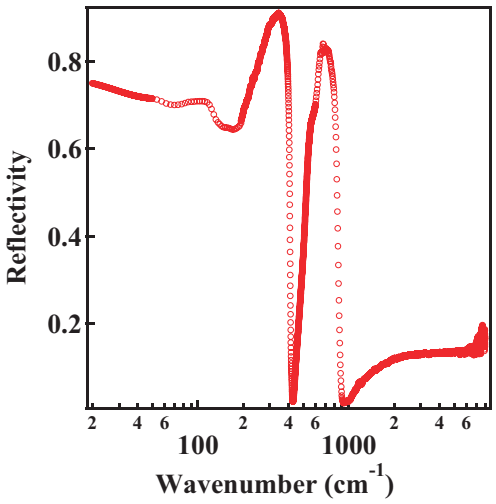

Fig. 1. Infrared reflectance spectra of $Na_{0.5}K_{0.5}NbO_3$ ceramics at R.T..

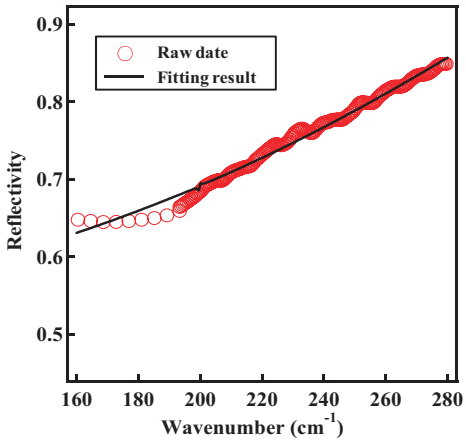

Fig. 2. Infrared reflectance spectra around the soft mode.

Table 1. Fitting parameters of the soft mode.

Fitting parameter	IR
ω_{TO}	254.51
ω_{LO}	434.34
γ_{TO}	163.80
γ_{TO}	568.14

This research was supported by the Industrial Technology Research Grant Program in 2007 from the New Energy and Industrial Technology Development Organization (NEDO) of Japan.

BL7B

Luminescence Decay of Organic-Inorganic Perovskite Compounds

M. Koshimizu, N. Kawano and K. Asai

Department of Applied Chemistry, Graduate School of Engineering, Tohoku University, Sendai 980-8579, Japan

Quantum confinement in semiconductors has been a subject of great interest from the viewpoint of the applications for optical devices, as well as the basic science. Among various materials having low-dimensional quantum confinement structure, Pb-based organic-inorganic perovskite-type compounds have attracted much attention due to their unique optical properties. The crystal of these compounds composed of alternating inorganic and organic layers. The inorganic and organic layers are composed of PbX_6^{2-} octahedra and organic amine, respectively. Due to the large difference in band-gap energy and dielectric constant in the organic and inorganic layers, an exciton in the inorganic layer is tightly confined, resulting in huge binding energy (several hundreds of meV) and large oscillator strength.

We have been developing scintillation materials using these compounds. In recent years, the demand for fast scintillation materials has increased for applying in radiation detectors with an excellent timing property and the ability to operate at a high counting rate. The large binding energy and oscillator strength of the exciton enables us to fabricate scintillation materials with excellent timing response [1]. During the course of the development, we found that the scintillation properties largely depend on the amine molecules used in the organic layer, in which no luminescence or scintillation occurs. In order to reveal the origin of this dependence, the luminescence decay characteristics should be obtained under excitation (1) only in the inorganic layers and (2) both in the inorganic and the organic layers. In this report, we show that the excitation in the organic layers has little influence on the luminescence behavior.

The chemical formula of the sample compound is $(C_6H_5C_2H_4NH_3)_2PbBr_4$. The single crystals of the compound were grown by solvent diffusion technique. The photoluminescence spectra and time profiles were measured using vacuum ultraviolet (VUV) light as an excitation source at UVSOR BL7B operated in single bunch mode.

Figure 1 shows the photoluminescence spectrum. The prominent peak at 410 nm is ascribed to free excitons. A small shoulder at 440 nm may be ascribed to excitons trapped at some defects or impurities, because the intensity of this shoulder has been different in different crystals. The shape of the spectra was quite similar for the excitation wavelength range of 50 – 300 nm.

Figure 2 shows the photoluminescence time profiles at 410 nm under excitation at 300 nm and 180 nm. In the case of the excitation at 180 nm, both the inorganic layer and the organic layer were excited. The decay characteristics were also quite similar. Hence, these results indicate that the excitation in the organic layer has little influence on the luminescence and scintillation behavior.

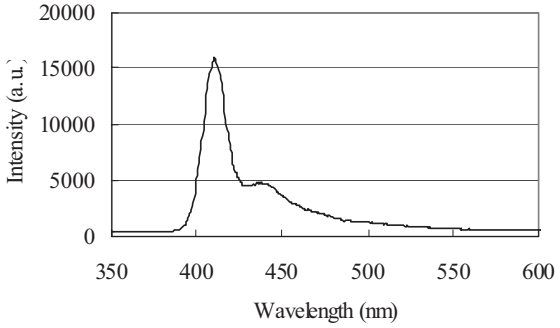

Fig. 1. Luminescence spectrum of the sample excited at 300 nm.

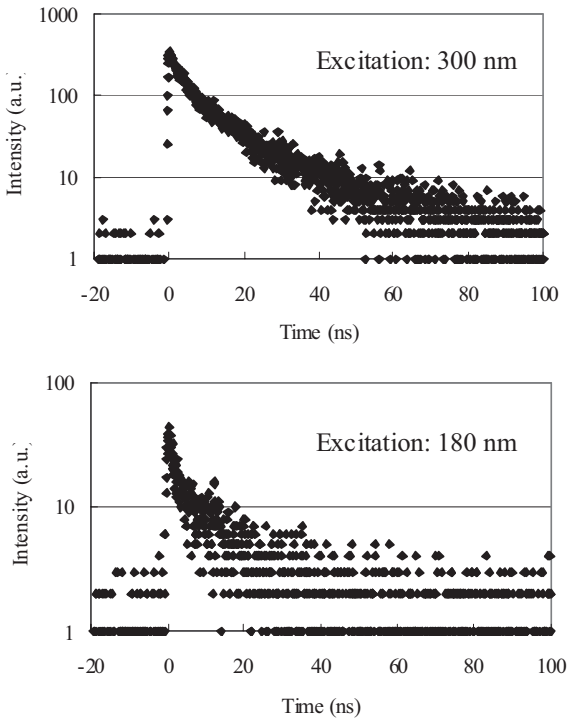

Fig. 2. Luminescence time profiles at 410 nm.

[1] K. Shibuya *et al.,* Appl. Phys. Lett. **84** (2004) 4370.
[2] K. Shibuya *et al.,* Jpn. J. Appl. Phys. Part2 (Express Letter) **43** (2004) L1333.
[3] S. Kishimoto *et al.,* Appl. Phys. Lett. **93** (2008) 261901.

BL7B

Photoluminescence upon Vacuum Ultraviolet Excitation in Pr^{3+} ion doped Inorganic Materials

Y. Inaguma, H. Horiguchi, S. Sasaki and D. Mori
Department of Chemistry, Faculty of Science, Gakushuin University, Tokyo 171-8588, Japan

Pr^{3+} ion doped inorganic materials has been extensively investigated in relation with various applications [1]: laser materials utilizing visible emission from the $^3P_0$ and $^1D_2$ states (blue-green and red emission, respectively), or infrared emission from the $^1G_4$ state of Pr^{3+}, field emission display (FED) devices utilizing red $^1D_2$ emission, scintillators or tunable ultraviolet (UV) lasers utilizing UV emission from the 4f5d state. The emission color or energy in Pr^{3+} ion doped inorganic materials is strongly related to the electronic structure, especially, the band gap energy of host materials. Therefore the emission color can be controlled by the choice of host materials [2].

Recently phosphor materials emitting UV light upon vacuum ultra violet (VUV) excitation are desired as the substitutes of mercury lamp due to the toxicity of mercury. As mentioned above, since the UV emission from the 4f5d state in Pr^{3+} can be observed, Pr^{3+} ion doped compounds are expected to be candidates of the UV phosphors. The UV emission from the 4f5d state would be observed when the band gap energy of the host material is in the VUV region. In this study we then chose Pr^{3+} ion doped alkaline-earth phosphates with the band gap energy in the VUV region and investigated their luminescence properties. Herein, we report on the photoluminescence upon VUV excitation of $Ca_3(PO_4)_2$:Pr among them.

The polycrystalline samples were synthesized by a conventional solid state reaction at elevated temperature. The mixture of starting materials: alkaline-earth carbonate such as $CaCO_3$, $(NH_4)H_2PO_4$ and Pr nitrate solution were calcined at 1000°C in air. The calcined powder was pressed into pellets and sintered at 1000-1200°C in air. The phase identification for the samples was carried out by the laboratory powder X-ray diffraction (XRD) using a Rigaku RINT 2100 diffractometer with a Bragg Brentano geometry (graphite-monochromatized CuKα radiation). The emission and excitation spectra were recorded in the beamline BL7B at the UVSOR facility.

The obtained sample was crystallized to be the hexagonal β-type form of tricalcium phosphates composed of isolated PO_4 tetrahedra and Ca^{2+} ions, which was confirmed by a powder XRD experiment. Figure 1 shows the emission spectrum upon excitation of 173 nm (right side) and excitation spectrum emission monitored at 280 nm (left side) for $Ca_3(PO_4)_2$:Pr 2% at room temperature. Here, the emission spectrum was not corrected, while the excitation spectrum was corrected for the spectral distribution of excitation light source. As seen in Fig. 1, the UV emission peaks at 240 and 280 nm were observed, which correspond to the transitions from the 4f5d state to the $4f^2$ (^3H_J) state of Pr^{3+}. In the excitation spectrum, the peaks around 175 nm and 200-220 nm were observed, which correspond to the host absorption band, i.e. the intra charge transfer of PO_4^{3-}[3] and the transition from the ground state of $4f^2$($^3H_4$) to the 4f5d state of Pr^{3+}, respectively.

It was found that $Ca_3(PO_4)_2$:Pr exhibits the UV emission corresponding to the transition from the 4f5d state of Pr^{3+} and the Pr^{3+} ion doped alkaline–earth phosphates are candidates of UV phosphors.

The luminescence properties upon VUV excitation in other Pr^{3+} ion doped alkaline phosphate will be reported in the near future.

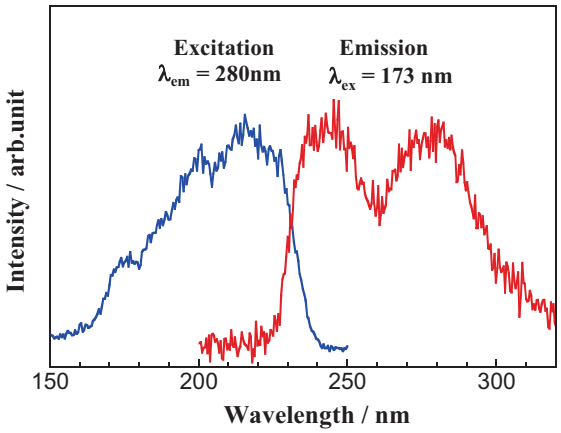

Fig. 1. Emission spectrum upon excitation of 173 nm (right side) and excitation spectrum emission monitored at 280 nm (left side) for $Ca_3(PO_4)_2$:Pr 2% at room temperature.

The authors thank Mr. M. Hasumoto and Prof. S. Kimura for their experimental supports and helpful advices.

[1] E. Van der Kolk *et al.*, Phys. Rev. B **64** (2001) 195129.
[2] Y. Inaguma *et al.*, Inorg. Chem. **50** (2011) 5389.
[3] H. Ling *et al.*, J. Solid State Chem. **177** (2004) 901.

BL8B

Photoelectron Spectrum of Zn-Phthalocyanine/C_{60} Interface under the Light Irradiation

S. Tanaka, K. Fukuzawa and I. Hiromitsu

Interdisciplinary Faculty of Science and Engineering, Shimane University, Matsue 690-8504 Japan

The electronic structure at the organic/organic and organic/metal interfaces plays an important role for the photovoltaic properties of the organic solar cell (OSC). The photoelectron spectroscopy is the one of the powerful methods to investigate the electronic structure of the organic/organic and organic/metal interfaces [1]. We have recently reported the electronic structures of the organic thin films under the light irradiation which were investigated by using the photoelectron spectroscopy with an external light source. In the previous report, we reported the photoinduced shift in the photoelectron spectra of the Zinc-phthalocyanine (ZnPc)/C_{60} interface [2]. The shift direction of the photoelectron spectrum was corresponded to the polarity of the photovoltaic effect at the ZnPc/C_{60} interface. In this report, the progress of the experimental results of the photoelectron shift under the light irradiation is reported.

The organic films were fabricated by the vacuum deposition technique. Two kinds of sample were fabricated: the planer hetero-junction (PHJ) sample and the bulk hetero-junction (BHJ) sample. The PHJ sample had a planer interface of ZnPc and C_{60} on the indium-tin oxide substrate. The BHJ sample was fabricated by the co-deposition of ZnPc and C_{60}. For the observation of the photoinduced effect on the electronic structure, the photoelectron spectra under the light irradiation were compared with that under dark. A solar simulator was used as the light source for the irradiation. The simulated airmass 1.5 solar illumination was exposed to the sample in a vacuum chamber through a viewport. All the photoelectron measurements were carried out with a photon energy of 40 eV at room temperature.

The photoelectron spectrum of the ZnPc/C_{60} interface was shifted toward higher kinetic energies by the light irradiation (Fig.1 (a)). The C_{60} thickness dependence of the photoinduced shift on the photoelectron spectrum is shown in Fig. 1 (b). The shift value was saturated at around 10nm of the C_{60} layer thickness and was approximately 60 meV. The photoinduced shift was caused by the photovoltaic effect at the ZnPc/C_{60} interface. The photogenerated electrons were accumulated in the C_{60} layer, causing the acceleration of the photoelectrons (Fig. 1(b) inset). The increase of the shift value in the initial stage of the C_{60} deposition was probably related to the increase of the interfacial area of the ZnPc/C_{60}. However, the saturated shift value of 60 meV was approximately one order smaller than the open circuit voltage of the ZnPc/C_{60} PHJ OSC. The reason of this discrepancy is still an open question.

It is known that the OSC with a BHJ layer shows higher energy conversion efficiency than that with a PHJ OSC [3]. However, the photoelectron spectrum of ZnPc:C_{60} (volume ration = 1:1) BHJ sample showed no significant photoinduced shift under the light irradiation. The present results indicate that semipermeable membranes for the electric charges are required on both sides of the BHJ layer to generate a charge current flowing in the OSC.

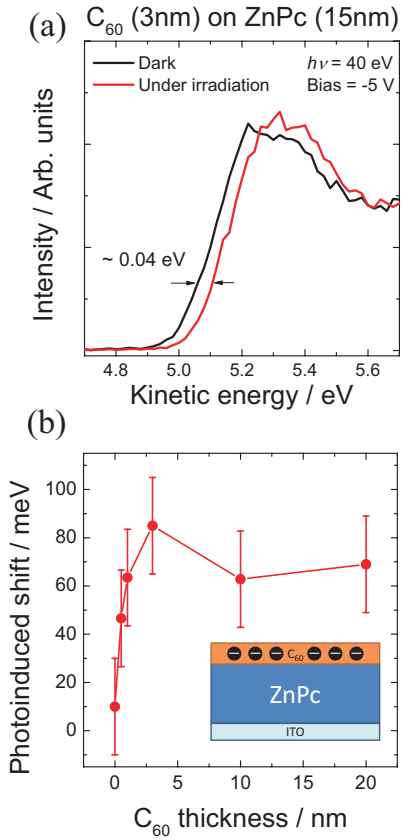

Fig. 1. (a) Photoelectron spectra of the C_{60} (3 nm) on the ZnPc layer at the secondary electron cutoff region. The red (black) curve indicates the photoelectron spectrum under the light irradiation (dark). (b) C_{60} thickness dependence of the photoinduced shift of the photoelectron spectrum. Inset shows the schematic image of the charge distribution at the sample surface under the light irradiation.

[1] H. Ishii *et al.*, Adv. Mater. **11**(1999) 605.
[2] S. Tanaka *et al.*, UVSOR Activity Report **38** (2010) 136.
[3] T. Taima *et al.*, Appl. Phys. Lett. **85** (2004) 6412.

BL8B

Influence of Growth Conditions on the Interface Electronic Structure at Planar Organic Donor/Acceptor Heterojunctions of Sexithiopheneand C_{60}

U. Hörmann[1], Y. Nakayama[2], Y. Ozawa[3], W. Brütting[1] and H. Ishii[2, 3]
[1]*Institute of Physics, University of Augsburg, Augsburg 86135, Germany*
[2]*Center for Frontier Science, Chiba University, Chiba 263-8522, Japan*
[3]*Faculty of Engineering, Chiba University, Chiba 263-8522, Japan*

On the way to high performance organic solar cells tremendous effort has been put into increasing the short circuit current by structural device optimization. Little attention has, however, been paid to the influence of morphology on the open circuit voltage (V_{oc}).

Here we investigate the electronic structure at sexithiophene (6T)/C_{60} hetero interfaces under different preparation conditions. In solar cells this system yields a V_{oc} of 0.5 V for room temperature grown films. Accompanied by morphological changes, this voltage is reduced to 0.37 V if C_{60} is deposited onto a high temperature grown 6T film.

In high vacuum 6T layers of 10 nm and 5 nm thickness have been deposited onto PEDOT:PSS (Clevios AI4083) covered indium tin oxide substrates at substrate temperatures of 100 °C (HT) and 30 °C (RT), respectively. In both cases, the deposition rate was set to 0.3 – 0.8 Å/s. C_{60} was deposited stepwise onto the 6T films at a rate of 0.3 Å/s at room temperature. Ultraviolet photoelectron spectroscopy (UPS) was performed at BL8B at UVSOR. The photon energy, incident angle and photoelectron emission angle were set to 30 eV, 45° and 0°, respectively throughout this study. For valence-band region (VB) spectra a bias of +5 V was applied to the sample in order to avoid charging, whereas -13 V wasapplied for secondary electron cutoff (SECO) measurements.

As expected from previous studies, heating in vacuum increases the work function of PEDOT:PSS, from 5.0 eV to 5.3 eV. Figure 1 shows the recorded UPS spectra of the 6T films and C_{60} overlayers on them. For direct comparison RT (black) and HT (red) data are shown in one plot. Both the SECO and VB spectra of the neat 6T film remain energetically unchanged by substrate heating. However, the features become sharper for the HT grown film. This can probably be attributed to the presence of two different crystalline 6T phases in the RT film as indicated by x-ray diffraction (XRD) measurements [1].

Interestingly the whole spectrum (VB and SECO) is shifted by $\Delta = 0.12$ eV towards higher binding energies, when 0.3 nm of C_{60} are deposited onto the HT 6T film. This indicates the occurrence of band bending at the C_{60}/6T(HT) interface as illustrated in Figure 2. By contrast, no band bending is observed in the RT case, where the energetic position of the overall spectrum remains unchanged by 0.3 nm of C_{60} (even though the HOMO onset shows a slight downshift due to spectral broadening).

In both cases the SECOs shift towards higher vacuum level energies with increasing C_{60} coverage. This can possibly be ascribed to mutual polarization of the molecules.The RT shift of +0.15 eV is in accordance with Ref. [2]. In the HT case the vacuum level recovers to the neat 6T value of 4.6 eV. Note, however, that 6T features are still present in the VB spectrum in this case. This suggests that the SECO shift probably has not reached its maximum and might stem from an incomplete C_{60} coverage on the extremely rough 6T(HT) surface observed by AFM.

Comparison of the 5 nm VB spectra reveals that growing C_{60} on HT 6T shifts the C_{60} HOMO to larger binding energies from 1.9 eV to 2.0 eV. This shift results in a reduction of the 6T/C_{60} charge transfer gap for the HT sample (indicated in Fig.2), which is in accordance with the reduced V_{oc} observed for 6T(HT)/C_{60} solar cell devices.

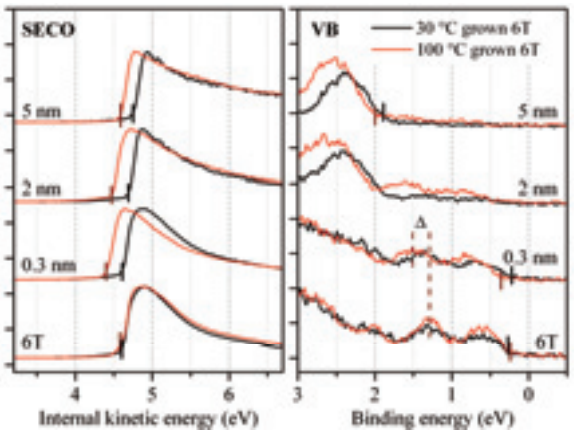

Fig.1. SECO (left) and VB (red) spectra of C_{60} grown on the RT (black) and HT (red) grown 6T.

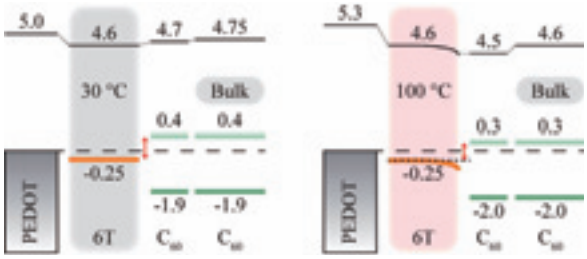

Fig.2. Schematic energy diagram of C_{60} grown on RT (left) and HT (right) grown 6T. Values are energy relative to the PEDOT:PSS Fermi level (units: eV).

[1] A. Hinderhofer and F. Schreiber (UniTübingen), unpublished.
[2] A. Wilke and N. Koch (HU Berlin), *in prep*.

List of Publications

M. Adachi, M. Katoh, H. Zen, T. Tanikawa, M. Hosaka, Y. Takashima, N.Yamamoto, Y. Taira, **"Status and Prospects of Coherent Light Source Developments at UVSOR-II"**, AIP Conf. Proc. **1234** (2010) 491.

S. Chikada, K. Hirose and T. Yamamoto, **"Analysis of Local Environment of Fe Ions in Hexagonal $BaTiO_3$"**, Jpn. J. Appl. Phys. **49** (2010) 91502.

M. Fushitani, A. Matsuda, A. Hishikawa, **"EUV and Soft X-Ray Photoelectron Spectroscopy of Isolated Atoms and Molecules Using Single-Order Laser High-Harmonics at 42 eV and 91 eV"**, J. Electron Spectrosc. Relat. Phenom. **184** (2012) 561.

M. Fushitani, A. Matsuda and A. Hishikawa, **"Time-Resolved EUV Photoelectron Spectroscopy of Dissociationg I_2 by Laser Harmonics at 80 nm"**, Opt. Exp. **19 (**2011) 9600.

T. Gejo, T. Tamura, K. Honma, E. Shigemasa, Y. Hikosoka, and Y. Tamenori, **"Angle-Resolved Metastable Fragment Yields Spectra of N2 and CO in the Innershell Excitation Energy Region"**, J. Chem. Phys. **136** (2012) 54201.

T. Hajiri, T. Ito, R. Niwa, M. Matsunami, B. H. Min, Y. S. Kwon and S. Kimura, **"Three-Dimensional Electronic Structure and Interband Nesting in the Stoichiometric Superconductor LiFeAs"**, Phys. Rev. B **85** (2012) 94509.

S. Hino, M. Zenki, T. Zaima, Y. Aoki, S. Okita, T. Ohta, H. Yagi, T. Miyazaki, R. Sumii, H. Okimoto, Y. Ito and H. Shinohara, **"Photoelectron Spectroscopy of $Sc_3N@C_{78}$"**, J. Phys. Chem. C **116** (2012) 165.

T. Hirahara, G. Bihlamyer, Y. Sakamoto, M. Yamada, H. Miyazaki, S. Kimura, S. Blu¨gel, and S. Hasegawa, **"Interfacing 2D and 3D Topological Insulators: Bi(111) Bilayer on Bi_2Te_3"**, Phys. Rev. Lett. **107** (2011) 166801.

T. Iizuka, T. Mizuno, B. H. Min, Y. S. Kwon and S. Kimura, **"Existence of Heavy Fermions in the Antiferromagnetic Phase of $CeIn_3$"**, J. Phys. Soc. Jpn. **81** (2012) 043703.

T. Inushima, D. K. Maude, H. Lu, W. J. Schaff, T. Iizuka, S. Kimura, A. Yamamoto and K. Fukui, **"Superconducting Properties of InN with Low Carrier Density near the Mott Transition"**, J. Phys. Soc. Jpn. **82** (2012) 44704.

M. Itoh, **"Luminescence Study of Self-Trapped Excitons in $CdMoO_4$"**, J. Lumin. **132** (2012) 645.

W. Jung, Y. Kim, B. Kim, Y. Koh, Chul Kim, M. Matsunami, S. Kimura, M. Arita, K. Shimada, J. H. Han, J. Kim, B. Cho and C. Kim, **"Warping Effects in the Band and Angular-Momentum Structures of the Topological Insulator Bi_2Te_3"**, Phys. Rev. B **84** (2011) 245435.

I. Katayama, H. Shimosato, M. Bito, K. Furusawa, M. Adachi, M. Shimada, H. Zen, S. Kimura, N. Yamamoto, M. Hosaka, M. Katoh and M. Ashida, **"Electric Field Detection of Coherent Synchrotron Radiation in a Storage Ring Generated Using Laser Bunch Slicing"**, Appl. Phys. Lett. **100** (2012) 111112.

H. S. Kato, H. Yamane, N. Kosugi and M. Kawai, **"Characterization of An Organic Field-Effect Thin-Film Transistor in Operation Using Fluorescence-Yield X-Ray Absorption Spectroscopy"**, Phys. Rev. Lett. **107** (2011) 147401.

M. Katoh, M. Adachi, H. Zen, J. Yamazaki, K. Hayashi, A. Mochihashi, M. Shimada, and M. Hosaka, **"Full Energy Injection and Top-up Operation at UVSOR-II"**, AIP Conf. Proc. **1234** (2010) 531.

T. Kawai and T. Hirai, **"Luminescence Properites of KCl:Ag- Crystals Excited near the Fundamental Absorption Edge"**, J. Lumin. **132** (2012) 513.

S. Kimura, T. Iizuka, H. Miyazaki, T. Hajiri, M. Matsunami, T. Mori, A. Irizawa, Y. Muro, J. Kajino and T. Takabatake, **"Optical Study of Charge Instability in $CeRu_2Al_{10}$ in Comparison with $CeOs_2Al_{10}$ and $CeFe_2Al_{10}$"**, Phys. Rev. B **84** (2011) 165125.

M. Koshimizu, K. Onodera, F. Nishikido, R. Haruki, K. Shibuya, S. Kishimoto and K. Asai, **"X-Ray Detection Capability of a $BaCl_2$ Single Crystal Scintillator"**, J. Appl. Phys. **111** (2012) 24906.

T. Miyazaki, R. Sumii, H. Umemoto, H. Okimoto, Y. Ito, T. Sugai, H. Shinohara, T. Zaima, H. Yagi and S. Hino, **"Ultraviolet Photoelectron Spectra of $Er_2@C_{82}$ (I), $Er_2@C_{82}$ (III), $Er_2C_2@C_{82}$ (I) and $Er_2C_2@C_{82}$ (III) "**, Chem. Phys. **397** (2012) 87.

K. Nakajima, K. Ohta, H. Katayanagi and K. Mitsuke, **"Photoexcitation and Electron Injection Processes in Azo Dyes Adsorbed on Nanocrystalline TiO_2 Films"**, Chem. Phys. Lett. **510** (2011) 228.

F. Nakamura, Y. Kousa, A. A. Taskin, Y. Takeichi, A. Nishide, A. Kakizaki, M. D'Angelo, P. Lefevre, F. Bertran, A. Taleb-Ibrahimi, F. Komori, S. Kimura, H. Kondo, Y. Ando and I. Matsuda, **"Topological Transition in $Bi_{1-x}Sb_x$ Studied as a Function of Sb-Doping"**, Phys. Rev. B **84** (2011) 235308.

T. Nakazato, Y. Furukawa, M. Cadatal-Raduban, M. Pham, T. Tatsumi, A.Saiki, Y. Arikawa, N. Sarukura, H. Nishimura, H. Azechi, K. Mima, T. Fukuda, M. Hosaka, M. Katoh and N. Kosugi, **"Systematic Study on Ce:LuLiF$_4$ as a Fast Scintillator Using Storage Ring Free-Electron Lasers"**, Jpn. J. Appl. Phys. **49** (2010) 122602.

K. Okada, T. Nakashima, M. Sakai, A. Suemitsu, C. Huang, H. Yagi, H. Katayanagi, K. Mitsuke and K. Tabayashi, **"Dissociative Photoionization of Perfluorocyclobutane and *cis*-1,1,2,2,3,4-Hexafluorocyclobutane"**, J. Phys. Conf. Ser. **288** (2011) 12021.

R. Okazaki, Y. Nishina, Y. Yasui, S. Shibasaki and I. Terasaki, **"Optical Study of the Electronic Structure and Correlation Effects in $K_{0.49}RhO_2$"**, Phys. Rev. B **84** (2011) 75110.

T. Okazaki, T. Yoshioka, Y. Kusakabe, T. Yamamoto and A. Kitada, **"Valence state analysis of Mn and Fe Ions in Room-Temperature Ferromagnetic Mn- and Fe-Codoped In_2O_3"**, Solid State Commun. **151** (2011) 1749.

M. Shikano, H. Kobayashi, S. Koike, H. Sakaebe, Y. Saito, H. Hori, H. Kageyama and K. Tatsumi, **"X-ray Absorption Near-Edge Structure Study on Positive Electrodes of Degraded Lithium-Ion Battery"**, J. Power Sources **196** (2011) 6881.

C. Szwaj, S. Bielawski, M.-E. Couprie, C. Bruni, M. Hosaka, A. Mochihashi, and M. Katoh, **"Remaining noise-induced spatiotemporal dynamics in a free electron laser stabilized by feedback control"**, Eur. Phys. J. D **59** (2010) 451.

Y. Taira, M. Adachi, H. Zen, T. Tanikawa, M. Hosaka, Y. Takashima, N. Yamamoto, K. Soda and M. Katoh, **"Feasibility Study of Ultra-Short Gamma Ray Pulse Generation by Laser Compton Scattering in an Electron Storage Ring"**, Nuc. Instrum. Methods. Phys. Res. A **637** (2011) S116.

S. Tanaka, M. Matsunami and S. Kimura, **"Observation of Anomalous Peaks in the Photoelectron Spectra of Highly Oriented Pyrolytic Graphite: Folding of the Band Due to the Surface Charge Density Wave Transition"**, Phys. Rev. B **84** (2011) 121411(R).

J. Wagner, M. Gruber, A. Wilke, Y. Tanaka, K. Topczak, A. Steindamm, U. Hörmann, A. Opitz, Y. Nakayama, H. Ishii, J. Pflaum, N. Koch and W. Brütting **"Identification of Different Origins for S-Shaped Current Voltage Characteristics in Planar Heterojunction Organic Solar Cells"**, J. Appl. Phys. **111** (2012) 54509.

M. Yamaga, T. Ishikawa, M. Yoshida, T. Hasegawa, E. G. Villora and K. Shimamura **"Polarization of Optical Spectra in Transparent Conductive Oxide β-Ga_2O_3"**, Phys. Status Solid **C8** (2011) 2621.

M. Yamaga, T. Nakamura, Y. Oda, J.-P. R. Wells and T. P. J. Han **"Dynamics and Energy Transfer of Sm^{2+} in KY_3F_{10} Crystals"**, J. Ceram. Processing Res. **12**, special issue 3 (2011) s241.

M. Yamaga, Y. Ohsumi, T. Nakayama and T. P. J. Han **"Persistent Phosphorescence in Ce-Doped Lu_2SiO_5"**, Opt. Mater. Exp. **2** (2012) 413.

H. Yamane, T. Hatsui, K. Iketaki, T. Kaji, M. Hiramoto, and N. Kosugi, **"Site-Specific Intermolecular Interaction in α-Phase Crystalline Films of Phthalocyanines Studied by Soft X-Ray Emission Spectroscopy"**, J. Chem. Phys. **135** (2011) 34704.

Y. Zhang, L. X. Yang, M. Xu, Z. R. Ye, F. Chen, C. He, H. C. Xu, J. Jiang, B. P. Xie, J. J. Ying, X.F. Wang, X. H. Chen, Jiangping Hu, M. Matsunami, S. Kimura, D. L. Feng, **"Nodeless Superconducting Gap in $A_xFe_2Se_2$ (A = K,Cs) Revealed by Angle-Resolved Photoemission Pectroscopy"**, Nat. Mater. **10** (2011) 273.

UVSOR Users Meeting

Date: Nov 18-19, 2011
Place: Okazaki Conference Center, Okazaki, Japan

Nov 18th (Thu)

<Session A, 13:00-14:30>

A1 K. Soda (Nagoya Univ.)
Opening remarks

A2 M. Kato (UVSOR)
Prface

A3 M. Matsunami (UVSOR)
Present status of photoemission beamlines BL5U and BL7U

A4 E. Shigemasa (UVSOR)
Plan for BL4U

Coffee break, 14:30-14:40

<Session B, 14:40-16:20 >

B1 S. Tanaka (Osaka Univ.)
Charge density wave transition on the HOPG surface: Observation of the band folding by using the ARPES

B2 T. Hirahara (Tokyo Univ.)
Electronic structure and transport property for ultrathin films of topological insulators

B3 H. Miyazaki (Nagoya Inst. of Technology)
Electronic structure of EuO ultrathin films studied by three-dimensional angle-resolved photoemission spectroscopy

B4 T. Iizuka (SOKENDAI)
Pressure dependent reflectivity spectroscopy on $CeIn_3$ at low temperature

B5 H. Aritani (Saitama Inst. of Technology)
Mo L-edge XANES study of GTL catalysts measured at BL2A beamline

<Poster Session, 16:30-18:00>

P01 M. Tuboi (Osaka Univ.)
Electronic status of rare-earth ion in glass host by characterizing photoliminescence of rare-earth doped APLF glass scintillator

P02 S. Nagata (Osaka Pref. Univ.)
Energy transfer from CsI host crystals to Ag- centers in CsI:Ag-

P03 T. Yamamoto (Waseda Univ.)
Local environment analysis of dilute dopants by XANES

P04 Y. Imoto (Univ. Fukui)
Build of the VUV spectroscopic beamline BL3B

P05 K. Eguchi (IMS)
Magnetic properties of iron nanoparticles on β-Si_3N_4(0001)/Si(111)

P06 M. Sawa (Nigata Univ.)
Developments of a multi-electron coincidence spectrometer and a light chopper

P07 Y. Takagi (IMS)
Magnetic property of iron phthalocyanine on Co/Cu(001)

P08 K. Nakaya (Keio Univ.)
Charge transfer from methyelthiolate monolayers on metal substrates studied by Core Hole-Clock spectroscopy

P09 K. Nakagawa (Kobe Univ.)
Fluorescence spectra of solid films of amino acids

P10 K. Soda (Nagoya Univ.)
Valence Band Electronic Structure of N-implanted TiO_2

P11 T. Nomoto (Nagoya Univ.)
Electronic structure of $Fe_{2-x}M_xVAl$ (M = Co, Rh, Ir)

P12 H. Momiyama (Nagoya Inst. of Technology)
Fabrication and evaluation of single crystalline EuO thin films with SrO buffer layer
P13 R. Niwa (Nagoya Univ.)
Charge density wave formation in $GdTe_2$
P14 H. Iwayama (UVSOR)
Dissociative pathways of CF_4 studied by a double toroidal electron analyzer and ion momentum spectrometer
P15 M. Saito (Yamagata Univ.)
New Auger-free luminescence in molecular ionic crystals A_2ZnCl_4 (A=Cs,Rb)
P16 T. Wakamatsu (Yamagata Univ.)
Luminescence properties of Ag-Y phostimulable phosphor excited with VUV light
P17 Y. Suzuki (Yamagata Univ.)
Determination of the threshold energy for e-h multiplication in $SrGa_2S_4:Eu^{2+}$
P18 Y. Nakamura (Fukui Univ.)
Development of spectroscopic ellipsometry for UV-VUV region
P19 S. Naruse (Fukui Univ.)
Polarization properties of optical reflectance, photoluminescence and photoluminescence excitation spectra from a-plane AlN
P20 M.Yamaguchi (Fukui Univ.)
Infrared reflectance spectra from InAlN mixed crystal thin-films
P21 Y. Ota (Tokai Univ.)
Dielectric function of impurity band of boron doped diamond
P22 T. Hajiri (Nagoya Univ.)
Polarization-dependent three-dimensional angle-resolved photoemission spectroscopy on LiFeAs
P23 K. Ogawa (Nagoya Unv.)
Carrier concentration dependence of super conducting gap in $Bi_2(Sr,La)_2CuO_{6+\delta}$
P24 T. Shimada (Nagoya Univ.)
High-resolution angle-resolved photoemission spectroscopy of $FeSb_2$
P25 H. J. Im (Hirosaki Univ.)
Angle-resolved photoemission study of the electronic structure of $CaCu_3Ti_4O_{12}$
P26 Y. Nakayama (Chiba Univ.)
Interface electronic structures of pn hetero-junctions in organic light emitting diodes
P27 P. K. Sarker (Yokohama National Univ.)
Photostability of free-amino acids and their precursor molecules exposed to simulated space radiation
P28 H. Zen (Kyoto Univ.)
Stabilization of injector and injection kicker in UVSOR-II
P29 Y. Taira (Nagoya Univ.)
Generation of ultra-short gamma ray pulses and application to positron annihilation lifetime study

Banquet, 18:15-

Nov 19th (Fri)

<Session C, 09:00-10:00 >
C1 M. Nagasaka (IMS)
Soft X-ray absorption spectroscopy of liquids and aqueous solutions at BL3U
C2 H. Yamane (IMS)
Recent progress of solid-&-surface ARPES system at BL6U
C3 K. Mitsuke (IMS)
Valence structures of thin-film sumanene and azo dyes and the mechanism of extreme UV photodissociation in gaseous aromatic hydrocarbons

<Session D, 10:10-12:00>
D1 H. Murata (Kyoto Univ.)
Measurements of soft X-ray absorption spectra with silicon drift detector

D2 T. Nakagawa (IMS)
XMCD study of giant coercivity in Fe/W(110)

D3 H. Kobayashi (AIST)
Investigation on the structural changes of the Li_2MO_3-$LiMO_2$ positive electrode materials with a high capacity in Li de-intercalation/intercalation process

D4 N. Narukage (ISAS/JAXA)
Overview of chromospheric Lyman-Alpha SpectroPolarimeter (CLASP) and its development with UVSOR BL7B

D5 S. Kera (Chiba Univ.)
Molecular orbital energy and symmetry of 3*d*-2*p* hybridized state for metal phthalocyanine

D6 K. Hayashi (Gifu Univ.)
Observation of photoinduced phenomena in amorphous semiconductor materials by total photoelectron yield

<Session E, 12:00-12:30>

E1 K. Fukui (Fukui Univ.)
Present status of BL3B

E2 S. Kimura (UVSOR)
Next plan of BL5U

E3 **Discussion**

Topical Meeting for FEL and High Power Radiation

Date: Dec 5-6, 2011
Place: Seminar room (#201) of main building, Institute for Molecular Science, Okazaki, Japan

Dec 5th (Mon)

13:30-13:40 Opening Remarks

<Session 1: Short wavelength single pulse FEL and its application>
13:40-14:10 K. Togawa (RIKEN)
Present status of beam comissioning at X-ray free electron laser facility SACLA
14:10-14:30 T. Hara (RIKEN)
Beam orbit correction in the undulator to the oscillation of SACLA
14:30-14:50 T. Sato (RIKEN)
Status of beam line development at XFEL SACLA
14:50-15:20 E. Shigemasa (UVSOR)
Atomic and Molecular processes in high power XUV laser field

15:20-15:40 Coffee break

<Session 2: Storage Ring FEL>
15:40-16:00 N. Sei (AIST)
Research and development of higer harmonic free electron laser
16:00-16:20 M. Hosaka (Nagoya Univ.)
Seeding of storage ring FEL and its application
16:20-16:40 D. Tonaka (LASTI)
Present status of laser Compton scattering gamma ray source at New SUBARU
16:40-17:00 T. Kaneyasu (SAGA-LS)
Generation of laser Compton scattering gamma ray at SAGA-LS
17:00-17:20 Y. Taira (Nagoya Univ.)
Generation of ultra-short gamma ray pulse via laser Compton scattering and its application to lifetime measurement of positron annihilation
17:20-17:40 T. Hayakawa (JAEA)
Feasibility of application study on laser Compton scattering gamma ray using FEL

18:00-19:00 Visit to UVSOR
19:00-21:00 Banquet

Dec 6th (Tue)

<Session 3: Short wavelength single pulse FEL and application>
09:00-09:20 M. Adachi (UVSOR)
Coherent light source developments at UVSOR
09:20-09:40 M. Kumaki (Waseda Univ.)
THz-CSR and CTR sources using S-band compact electron linac
09:40-10:10 S. Kimura (UVSOR)
Application of high power THz Radiation

10:10-10:30 Coffee break

10:30-10:50 R. Kato (Osaka Univ.)
Simulation on ISIR FEL oscillation using FELO
11:00-11:20 J. Shen (Osaka Univ.)
Spectral measurement of THz FEL

11:20-11:40 M. Fujimoto (Osaka Univ.)
Evaluation of FEL gain from measurement of temporal evolution of FEL power
11:40-12:00 A. Irizawa (Osaka Univ.)
Development and use of high power THz FEL light source with L-band linac
12:00-12:20 H. Zen (Kyoto Univ.)
Present status and prospects of KU-FEL (2011)
12:20-12:40 K. Ishida (Kyoto Univ.)
Characteristic prediction of KU-FEL after installation of 1.8-m undulator

12:40-12:50 Closing Remarks
13:00-14:00 Banquet